UNIVERSIDAD NACIONAL AUTÓNOMA DE MÉXICO
Posgrado en Ciencias Físicas
Instituto de Física
Laboratorio de Materia Ultrafría

Time-averaged optical potentials for trapping and manipulating ultracold quantum ^{6}Li gases

T E S I S

que para optar por el grado de:

maestro en ciencias (física)

P R E S E N T A :

José Eduardo Padilla Castillo

tutor principal

Dr. Jorge Amin Seman Harutinian
Instituto de Física, UNAM

comité tutor

Dra. Rosario Paredes Gutiérrez
Instituto de Física, UNAM
Dr. Daniel Sahagún Sanchez
Instituto de Física, UNAM

Ciudad Universitaria, Cd. Mx., 21 de marzo del 2021

Hoja de Datos del Jurado

1. Datos del alumno
José Eduardo Padilla Castillo
Correo electrónico: eduardopadilla@ciencias.unam.mx
Teléfono: 55 77 24 42 42
Universidad Nacional Autónoma de México
Posgrado en Ciencias Fisicas
Instituto de Física
Laboratorio de Materia Ultrafria
Número de cuenta: 309152648

2. Datos del tutor
Dr. Jorge Amin Seman Harutinian

3. Datos del sinodal 1

4. Datos del sinodal 2

5. Datos del sinodal 3

6. Datos del sinodal 4

7. Datos de la tesis
Time-averaged optical potentials for trapping and manipulating ultracold quantum ^{6}Li gases
142 p.
2021

Resumen

Este trabajo presenta el diseño e implementación de un sistema óptico que permite la creación de potenciales ópticos promediados en el tiempo (TAP) para la captura y manipulación de gases cuánticos ^{6} Li.

La implementación de la técnica TAP nos permite crear una trampa óptica moldeable (ODT). En esta trampa se lleva a cabo la última etapa de enfriamiento, el enfriamiento evaporativo, que nos permite obtener un gas fermiónico ultrafrío (≈ 20 nK). El enfriamiento evaporativo fue optimizado y complementado con TAP, que se documenta y caracteriza en esta tesis.

Las diferentes geometrías para ODT que TAP nos permite crear son casi arbitrarias, desde un pozo doble hasta una caja de potencial o un potencial armónico. En esta tesis se desarrolla un algoritmo, con el cual fue posible obtener estas trampas con geometrías arbitrarias.

Una vez seleccionada la geometría, también es posible escalar sus dimensiones. Esto nos permite controlar el tamaño y el volumen de la trampa. Por ejemplo, usando geometría armónica, es posible manipular la cintura ODT para pasar de 40.0 (26) μm a 128.6 (26) μm de manera continua.

Un resultado importante de esta tesis es el diseño y estudio de un experimento cuyo objetivo es observar la transición de fase BEC disminuyendo el volumen, pero manteniendo constante la temperatura y el número de átomos. Este experimento, además de mostrar la utilidad del TAP, proporciona una nueva perspectiva de lo que se suele hacer en el campo de los átomos ultrafríos, donde se disminuye el volumen en lugar de la temperatura para lograr la condensación de Bose-Einstein. Este experimento también nos da una primera idea de cómo medir el volumen de una trampa armónica tridimensional.

Finalmente, se prueba la trampa de geometría de doble pozo en los átomos, lo que nos permite obtener dos muestras cuánticas cuya separación podemos controlar finamente, mostrando la versatilidad de TAP. Con esta configuración fue posible realizar un experimento en el que concluimos definitivamente que tenemos muestras en régimen cuántico. Esto se logró dejando las dos muestras interaccionar en tiempo de vuelo y, debido a que éstas se comportan como ondas de materia, se observó un patrón de interferencia.

Abstract

This work presents the design and implementation of an optical system that allows the creation of time-averaged optical potentials (TAP) for the capture and manipulation of ^{6}Li quantum gases.

The implementation of the TAP technique allows us to create a moldable optical dipole trap (ODT). In this trap the last stage of cooling is carried out, the evaporative cooling, which allows us to obtain an ultracold fermionic gas ($\approx$ 20 nK). Evaporative cooling was optimized and complemented with TAP, which is documented and characterized in this thesis.

The different geometries for the ODT that TAP allows us to create are almost arbitrary, from a double well to a box or a harmonic potentials. In this thesis an algorithm is developed, with which it was possible to obtain these traps with arbitrary geometries.

Once the geometry is selected, it is also possible to scale its dimensions. This allows us to control the size and volume of the trap. For example, using harmonic geometry, it is possible to manipulate the ODT waist to go from 40.0(26) μm to 128.6(26) μm in a continuous way.

An important result of this thesis is the design and study of an experiment whose objective is to observe the BEC phase transition decreasing the volume, but keeping the temperature and the number of atoms constant. This experiment, in addition to showing the usefulness of TAP, provides a new perspective on what is usually done in the field of ultracold atoms, where the volume is lowered instead of the temperature to achieve the Bose-Einstein condensation. This experiment also give us a first insight of how to measure the volume of a three dimensional harmonic trap.

Finally, the double-well geometry trap is tested on the atoms, which allows us to obtain two quantum samples whose separation we can finely controlled, showing the versatility of TAP. With this configuration it was possible to carry out an experiment in which we definitively concluded that we have samples in the quantum regime. This was achieved by allowing the two samples to interact in time-of-flight and, since they behave like matter waves, an interference pattern was observed.

Contents

Agradecimientos

A mis padres, Efraín Padilla y Vianey Castillo, quienes me han enseñado a andar en el gran camino de la vida, sin ustedes no sería ni una ínfima parte del hombre que soy ahora. A mis hermanos, Samir, Evelin e Isaack, grandes colegas de la infancia quienes me han acompañado en tantas aventuras, mostrándome distintas y bellas percepciones del mundo. A ustedes, mi gran familia nuclear, estas pequeñas palabras de este párrafo no bastan para describir el gran amor y cariño que les tengo. Tantos recuerdos y vivencias sellan en mi ser un lazo incondicional hacia ustedes que jamás podrá romperse. Siempre buscaré llenarlos de orgullo y ser un ejemplo para ustedes.

A l'Ari, la meva xicota, que sempre admiraré per la seva positivisme cap a la vida. Al costat de tu puc riure i plorar, ballar, nedar, menjar ric i gaudir de la simple existència, que amb tu és meravellosa. Gràcies per ser la meva companya incansable tants anys, per estimar-me i suportar-me, per escoltar-me, per compartir-me la teva vida, pel teu amor. T'estimo molt amor meu.

A Jorge Seman, quien agradezco enormemente por darme la oportunidad de trabajar con él. Muchas gracias por permitirme formar parte de un equipo tan increíble. Para mí siempre serás más que un tutor, eres un gran amigo y mentor que siempre se preocupó por mí a través de justos regaños. Una disculpa por todas esas ocasiones que te saque de quicio. Añoro esas largas sobremesas casuales mientras comíamos en Química y espero con ansias cualquier oportunidad para repetirlas. Ha sido y seguirá siendo un gusto trabajar contigo, no solo por tu gran capacidad académica sino por tu gran calidad de persona que siempre he admirado.

A Jackson Poveda, quien nunca se rinde. Muchas gracias por presionar hasta los límites, siempre recordare como una lección aquella noche del 24 de octubre de 2018, cuando logramos el BEC a las 23:53 en medio de la cena con pizzas. Gracias por todas esas enseñanzas tanto de la física como en la vida, mientras comíamos en Química o cenábamos gran variedad de porquerías.

A Asaf Paris, por permitirme hacer ese servicio social en OCR, ese laboratorio tan lejano. Gracias por dejarme ser tu ayudante y gracias por todos esos chistes espontáneos.

A Diego Hernández y Andrés Gutiérrez, mis colegas en el laboratorio del noveno circulo detrás de las Puertas del Infierno. Sin duda, este proyecto no hubiera sido posible sin su ayuda. Gracias por compartir conmigo esas inconmensurables cantidades de café, junto con esas risas, pláticas y un congreso.

A Manuel Mendoza, Ernesto Carro, Eduardo Ibarra, Sebastián Morales, Alejandra del Rio, Melanie Bautista, Iván Barrientos, Javier Carcamo, Karen Cuervo, Sandy

Quinllin, Juan David, Viani Morales, Patricio Vargas y demás compañeros con los cuales compartí, comparto o compartiré trabajo en algún momento en el laboratorio.

A los Rydberg, astutos compañeros del laboratorio vecino. A Eduardo Esquivel, por la locura en nuestras charlas y esos soundtracks formidables en el laboratorio. A Giovanni Torres por su ayuda con muchas figuras y seriedad apacible. A Leonardo Uhthoff por mostrarme la maravilla del Pencil y el aventón ilegal para ir por ramen.

A compañeros de clase durante la carrera y maestría. Con especial énfasis a los colegas teóricos que trabajan en la misma área como Juan García Nila, Alexis Domínguez y Juan Carlos Obeso.

A Carlos Alberto Gardea Flores, Rodrigo Alejandro Gutiérrez Arenas y Maira Gloria Pérez Vielma, nuestros técnicos electrónica, por ayudarme a desarrollar el sumador electrónico prototipo y luego el definitivo dentro de la caja x, que es fundamental para realizar este proyecto.

A mis sinodales: Víctor Romero, Daniel Sahagún, Héctor Cruz y Alexander Franco. Gracias por su rápida respuesta al aceptar leer este trabajo y por el tiempo que dedicaron para ayudarme a mejorarlo.

To Giacomo Roati, our LENS collaborator, for his advice, help and that little push to carry out this project. To Giacomo Valtolina, for inviting me to take the next step in his laboratory in Berlin. Both are invaluable to me, grazie mille.

A Rosario Paredes y Daniel Sahagún, mi comité tutor, estoy agradecido por su tutoría, calidez humana y paciencia hacia mí. Gracias por tener siempre abierta la puerta para mí.

A Víctor Romero, mi educador, una sino la más grande influencia en mi vida académica, quien me ha inspirado desde aquellas magistrales clases a ser el científico que me gustaría llegar ser. Muchas gracias por darme ese necesario empujón a la física experimental.

A Rocío Jáuregui responsable técnica del Laboratorio Nacional de Materia Cuántica, que con su incansable labor logro traer a México en el LMU su primer BEC. Pero personalmente estoy más agradecido por su tutoría, calidez humana y paciencia hacia mí para prepararme a ese predoctoral de cuántica.

Y finalmente, al Instituto de Física y UNAM amada, por la oportunidad de hacer ciencia y por su cafetería del décimo piso, fuente inconmensurable de café y conocimiento.

El desarrollo de esta tesis no hubiera sido posible sin el financiamiento de los siguientes proyectos de investigación:

- Beca de maestría por parte de CONACyT del programa 000306 - MAESTRÍA EN CIENCIAS (FÍSICA)
- Los siguientes proyectos de DGAPA-PAPIIT (UNAM):
  – IA101716, IN111516, IN107014, IN103818, IN109021 y IN109619.
- Los siguientes proyectos del Instituto de Física (UNAM):
  – PIIF-8 y PIIF-9.

- Apoyo de la Coordinación de la Investigación Científica (CIC-UNAM) No.LANMAC-2019.
- Los siguientes proyectos de CONACyT:
  – Redes Tématicas "Tecnología Cuántica".
  – Ciencia Básica grants 255573, 254942 y A1-S-39242.
  – CONACyT y CIC-UNAM, a través del programa de Laboratorios Nacionales: LN232652, LN260704, LN271322, LN280181, LN293471 y LN299057.
  – CONACyT - 314860, "Mantenimiento de infraestructura del Laboratorio Nacional de Materia Cuántica: Materia Ultrafría e Información Cuántica".
  – CONACyT - 315838, "Mantenimiento del Laboratorio Nacional de Materia Cuántica: Materia Ultrafría e Información Cuántica"
- Ayuda para la impresión de tesis, clausula 99 del CCT UNAM.

Introduction

"Many years later, facing the firing squad, Colonel Aureliano Buendía was to remember that distant afternoon when his father took him to discover [the great invention of their time] ...
the chest gave off a glacial exhalation. Inside there was only an enormous, transparent block with infinite internal needles in which the light of the sunset was broken up into colored stars. Disconcerted, knowing that the children were waiting for an immediate explanation, José Arcadio Buendía ventured a murmur:
'It is the largest diamond in the world.'
'No,' the gypsy corrected him, 'it is ice."

Gabriel García Márquez, *One Hundred Years of Solitude*

Why are physicists interested in cooling atoms? Why do we want to cool atomic gases to lower and lower temperatures? Well, before we answer these questions we have to stop and think about how fast atoms are moving at room temperature. The mean speed of air molecules at standard conditions[1] is around 422 meters per second, which is comparable to the speed of a supersonic jet aircraft flying at Mach 1.5. Then, if we want to study atoms more carefully, wouldn't it be better if they moved slower or even stood (nearly) motionless? Certainly, at lower speeds one could study atoms in greater detail and determine their properties with much higher precision. Of course, this is exactly what cold atom physics has allowed us to do.

A typical application of the precision measurements that have now become a reality are atomic clocks which, to this date, are the most precise clocks known to humanity. Put in layman's terms, a clock is able to measure time by counting something that ticks, but the ticking mechanism of regular clocks (such as the swing of a pendulum or the oscillations of a quartz crystal) is not nearly as reproducible as the *ticking* of an atom. Therefore, atomic transition frequencies provide the time and frequency standards which have been adopted worldwide as the definition of the second itself [1, 2].

Using laser light to slow down the motion of atoms was first proposed by Hänsch and Schawlow in 1975 [3]. A laser is generally thought of as something that heats

[1] Using the most likely speed according to $v_p = \sqrt{\frac{2kT}{m}}$ for diatomic nitrogen N_2, the primary component of air, at room temperature (300 K).

up matter because they are commonly used for welding and metal cutting. However this is not always the case, it only proves that there exists an energy transfer process between atoms and light. If somehow we could reverse the energy transfer process, then light would be able to remove energy from matter cooling it down. This process is exactly what occurs with lasers in dilute atomic gases.

When an atom transitions to an excited (unstable) state by absorbing a photon, it has no other choice but to eventually re-emit it. If the frequency of the absorbed light is less than the frequency of the emitted light, this frequency difference is equivalent to energy loss i.e. cooling. That is, irradiating atoms with light of a carefully controlled frequency can cool them by a small amount at every absorption-emission process which itself normally occurs many millions of times per second. This allows us to reach extraordinarily low temperatures by means of simply irradiating matter with laser light.

After this ideas were put forward, the scientific community became interested in trapping cooled atoms in containers which we now call atom traps. Naturally, these are not physically tangible receptacles, they are made up of laser beams and magnetic fields in which cooled atoms at the millikelvin and microkelvin temperatures can be held. For the development of laser cooling and trapping methods, W.D. Phillips, S. Chu and C. Cohen-Tannoudji received the Nobel Prize in 1997 [4, 5, 6]. Among other things, these techniques helped to improve the precision of atomic clocks.

The pursuit for even lower temperatures didn't stop there and researchers began to wonder what would happen if we could cool atoms even further. Well, when we reach lower temperatures (in the nanokelvin range) with a gas of particles, we arrive to the quantum regime and the gas becomes degenerate. At this point, statistical mechanics plays a crucial role, it makes a big difference whether the atoms are bosons (particles that have integer spin) or fermions (particles that have half odd integer spin). If they are fermions, they form a quantum degenerate Fermi gas (DFG), on the other hand, if they are bosons they transition to a state known as a Bose-Einstein condensate (BEC).

With this in mind, physicists developed all kinds of laser cooling based techniques trying to create a quantum degenerate gas without success. Eventually, they realized that the key to reach the required temperatures is actually a relatively simple process known as evaporative cooling, which happens in everyday life. Surprisingly, evaporative cooling is easier to explain than laser cooling, because it works under the same principle as blowing into a cup of coffee to cool it down. When one does this the most energetic water molecules escape from the coffee in the form of vapor, and those which stay behind have (on average) less energy, in other words, the coffee has cooled down.

So by selectively removing the hottest particles one effectively cool down the ensemble. And that's exactly what we do when we apply evaporative cooling on the atoms. We let the most energetic atoms escape so that the remaining ones cool down and eventually rethermalize to nanokelvin temperatures, reaching the quantum regime.

Nevertheless in the early 90's it wasn't obvious how to combine laser and evaporative cooling to achieve quantum degeneracy since these two methods work best in very different regimes. Laser cooling is more efficient at very low atomic densities, because

at high densities a photon emitted by an atom gets absorbed again by another atom and, on average, this heats up the gas. On the contrary, evaporative cooling requires collisions between particles to allow the sample to reach thermal equilibrium throughout the evaporation process.

Because of this, the initial consensus of the scientific community was that it would not be possible to use both methods. But, through the use of very clever schemes, they eventually learned how to combine both techniques in sequence to reach the quantum regime. Part of this thesis will show precisely how they achieved this and how we have implemented it in our laboratory.

The groups led by E. Cornell and C. Wiemann, W. Ketterle, and R. Hulet successfully created the first Bose-Einstein condensates in 1995 using dilute atomic alkali vapours and magnetic traps [7, 8, 9]. This achievement earned E. Cornell, C. Wiemann and W. Ketterle the Nobel prize in 2001.

On the other hand, the creation of the first quantum degenerate Fermi gas had to wait until 1999 when D.S. Jin's group [10] achieved the complex feat. Nowadays, these innovative techniques have become the standard method to produce Bose-Einstein condensates and quantum degenerate Fermi gases. But additionally to these phase transitions, quantum gases exhibit other fascinating phenomena such as superfluidity and macroscopic quantum excitations [11, 12], making ultracold atomic gases an attractive research topic all by itself.

Furthermore, these systems exhibit a high degree of control, and for this reason, they can be understood and modeled with unprecedented clarity. Therefore, ultracold atoms are considered to offer a unique scenario to implement quantum simulators of many-body Hamiltonians [13]. The idea behind a quantum simulator can be explained as follows: if there are two systems which are described by the same equations (Hamiltonians), but one is very difficult to experimentally study and the other is simple, then the physics can be studied in the simple system and extrapolated (mapped) to the complex one. In condensed matter there are many systems which are not yet fully understood but can be simulated with ultracold atoms. Among these we have high-T_c superconductors [14], the Josephson effect [15], strongly correlated materials, quantum phase transitions [16, 17], and so on. Ultracold atoms can be used to explore the underlying physics of many of these condensed matter systems.

But what do we mean when we say these experiments have a *high degree of control*? Well, we mean that many of the fundamental parameters of the system can be finely tuned experimentally. For instance, the dimensionality and geometry of the system can be manipulated by tailoring optical and magnetic trapping potentials [18]. As a consequence, control over the trapping potentials also allows to easily change thermodynamic properties of the gas such as density, temperature and volume. Another parameter that can be precisely controlled is the interaction strength between particles which we can manipulate through Feshbach resonances for bosons [19] and fermions [20] by simply changing an external magnetic field. Moreover, the quantum statistics of the system itself can be selected by using fermionic or bosonic atoms in the experiment.

0.1 Ultracold Matter Laboratory

In this context, the Ultracold Matter Laboratory (LMU, for its acronym in Spanish) at UNAM's Institute of Physics was created in Mexico. LMU's objective is the production and study of quantum atomic gases, using both fermionic and bosonic isotopes of lithium (^{6}Li and ^{7}Li respectively). The main reason for using these atomic species is their broad magnetic Feshbach resonances [21, 22]. As we have already mentioned, this allows us to manipulate the intensity and sign of interatomic interactions between particles by applying an external magnetic field. Which in turn allows us to access very different regimes, from an almost ideal gas, where atoms interact very weakly, to a strongly interacting system with attractive or repulsive interactions.

In the particular case of ^{6}Li, if the interactions are repulsive, a molecular bound state with bosonic statistics is formed, which can lead to Bose-Einstein condensation of molecules [23, 24]. On the contrary, if the interactions are attractive, a bound state is formed in momentum space, corresponding to the analog of the Cooper pairs described by BCS theory [25].

Since it is possible to continuously change the value of the applied magnetic field, it is also possible to continuously move the system from the BEC side to the BCS side through the so-called "BEC-BCS crossover" [26]. These systems have been used in other experiments with the goal of studying phenomena such as collective excitations [27], the Josephson effect [28] and the existence of quantized vortices [12], through the BEC-BSC crossover.

The main research line at the LMU is the study of different types of excitations in atomic superfluid. We are particularly interested in exploring them in Fermi superfluids across the BEC-BCS crossover. As a first experiment, we have started to study parametric excitations generated by modulating the trapping potential. We have identified the generated excitation with the so-called Faraday waves [REFERENCIA]. This experiment is currently in progress, so we only mention it in the Perspectives section 6.2.1 of this thesis.

As a next step, we plan to study more complex excitations. We have special interest in exploring the phenomenon of turbulence in superfluid gases. The study of quantum turbulence arises from the interest in understanding turbulence at different scales. This is still an open problem and is considered one of the most important problems in modern physics. To study quantum turbulence, the formation of vortices whose angular momentum is quantized is necessary. These have been produced and studied in Bose-Einstein condensates [11] and in particular across the BEC-BCS crossover [12]. It should be noted that quantum turbulence has already been observed in bosonic ^{4}He and fermionic ^{3}He liquid superfluids [29]. However, these systems have disadvantages when trying to analyze the dynamics of the vortices because they have diameters smaller than 1 nm in contrast with 1 μm presented in ultracold gases. Quantum turbulence was first observed in ultracold gases in a Bose-Einstein condensate [30, 31], however, it has not been observed in fermionic gases yet.

Finally, in the medium term, we plan to carry out a study of the thermodynamic properties of these systems, with special emphasize in the critical behavior of the

superfluid-gas phase transition. To do so, we intend to employ a novel formalism in terms of global thermodynamic variables. This theory was proposed by V. Romero Rochin et al. [32, 33, 34] to address the problem of thermodynamics in systems where the concept of rigid walls does not exist and the system becomes inhomogeneous. In this case, defining variables such as pressure or volumes becomes difficult and a different thermodynamic approach is necessary.

0.2 This thesis

As discussed before, in order to achieve quantum degeneracy, we need to implement the last cooling stage, the evaporative cooling. This process consist in transfer the atoms into a conservative potential and then reduce dynamically the height of potential removing selectively the hottest particles.

Then, this trapping potential has exceptional properties, like there is no energy exchange between the potential and the atoms, but there is still some interaction to trap the atoms. Also, this potential needs to be able to be dynamically changed.

This thesis is centered in the theoretical concepts and experimental implementation of this exceptional atom trap, the optical dipole trap (ODT), for the capture of ^{6}Li quantum gases.

This work also presents the time-averaged optical potential (TAP) technique, which allows us to create a moldable geometry ODT to have better trap properties control. The design and implementation of the optical system which allows the creation of TAP for the manipulation of ^{6}Li quantum gases is also documented in this thesis.

The TAP basic idea to control the size and geometry of the beam waist involves rapidly modulating the position of the laser beam focus. The timescale of the modulation is much faster than the radial trap frequency. By doing so the atoms do not respond to the "instantaneous" motion of the beam and instead "see" a potential proportional to the time-averaged intensity profile.

This thesis is organized as follows:

- In Chapter 1, a brief theoretical introduction to interacting Fermi gases is given. Here, we discuss how it is possible to change the interaction between the two-component spin of a Fermi gas using a Feshbach resonance. This results in different interaction regimes which make possible to generate different superfluid states, such as a BEC or a BCS-like system, or even transit between them through the so-called BEC-BCS crossover.

- In Chapter 2 we discuss theoretically how to use lasers and magnetic fields to cool and trap ^{6}Li atoms. We distinguish between two principal light-produced forces, the radiation force used to create the MOT, optical molasses and sub-Doppler cooling, and the dipole force used to create the ODT. At the end of the chapter, we describe theoretically the evaporative cooling process.

- In Chapter 3 we describe our experimental setup and methods to produce quantum gases. We detail the experimental process to transfer the atoms from the previous cooling stages (Doppler and sub-Doppler cooling) to the ODT. Also, the evaporative cooling was optimized and complemented with TAP,

which allows us to produce quantum degenerate superfluid samples containing about 6×10^4 atoms at a temperature of approximately 20 nK and a phase-space density of the order of 10.

- In Chapter 4, the theoretical concepts and experimental implementation of the TAP is presented. Additionally, a theoretical treatment for TAP is developed summarizing into an algorithm, with which it was possible to obtain almost any desirable geometry for the ODT. The different geometries for ODT that TAP allows us to create go from a double well to a box or a harmonic potentials. Also, once the geometry is selected, it is also possible to scale its dimensions. This allows us to control the size and volume of the trap.

- In Chapter 5 we present the results of manipulate geometrically the quantum gases. For example, using harmonic geometry, it is possible to manipulate the ODT waist to go from 40.0(26) μm to 128.6(26) μm in a continuous way.

  An important result of this thesis is the design and study of an experiment whose objective is to observe the BEC phase transition decreasing the volume, but keeping the temperature and the number of atoms constant. This experiment has a new perspective on what is usually done in the field of ultracold atoms, where it is the temperature the control parameter to achieve the Bose-Einstein condensation.

  Finally, the double-well geometry trap is tested on the atoms, which allows us to obtain two quantum samples whose separation we can finely controlled, showing the versatility of TAP. With this configuration it was possible to carry out an experiment in which we definitively concluded that we have samples in the quantum regime. This was achieved by allowing the two samples to interact and since they behave like matter waves, an interference pattern was observed.

- In Chapter 6 we present the conclusions and perspectives. As a perspective, we present the effects of modulating the trap at a much slower rate, in such a way that the "time-average" condition is not fulfilled. In this way, the trap geometry dynamically varies, generating collective excitations in the sample. We present some very preliminary results on the study of this specific type of parametric excitation that we identify as Faraday waves.

Chapter 1

Interacting atomic gases

1.1 Ideal Fermi gas in a harmonic trap

In our experiment, fermionic ^{6}Li atoms are cooled down. To understand how this is done we need to review the theory of ultracold Fermi gases. For that purpose we will now follow the derivation presented in a review by Stringari *et al.* [35]. Let us consider the simplest model, the ideal Fermi gas model in a harmonic potential of the form

$$V = \frac{1}{2}m(\omega_x^2 x^2 + +\omega_y^2 y^2 + \omega_z^2 z^2). \tag{1.1}$$

Since the number of atoms N is very large ($N \gg 1$) the semi-classical approach can be used. Considering this description and using the local-density approximation for the Fermi distribution function [34] of a given spin species we have

$$f(\mathbf{r}, \mathbf{p}) = \frac{1}{e^{\beta[p^2/2m + V(\mathbf{r}) - \mu]} + 1}, \tag{1.2}$$

where $\beta = 1/k_B T$ and μ is the chemical potential. Integrating the Fermi distribution over spatial and momentum coordinates we obtain

$$N = \frac{1}{(2\pi\hbar)^3}\int d\mathbf{r}d\mathbf{p} f(\mathbf{r}, \mathbf{p}) = \int_0^\infty \frac{g(\epsilon)d\epsilon}{e^{\beta[\epsilon-\mu]} + 1}, \tag{1.3}$$

Here we have introduced the density of states $g(\epsilon) = \epsilon^2/2(\hbar\bar{\omega})^3$ where the geometric mean of the trapping frequencies is $\bar{\omega} = (\omega_x\omega_y\omega_z)^{1/3}$.

In the limit where $T = 0$, the integral in equation (1.3) can be analytically solved to obtain the Fermi energy (the Fermi distribution becomes a step-function which is zero when the energy is larger that the chemical potential). The resulting Fermi energy is

$$N = \frac{1}{2(\hbar\bar{\omega})^3}\int_0^{E_F} \epsilon^2 d\epsilon \rightarrow E_F = (6N)^{1/3}\hbar\bar{\omega} \tag{1.4}$$

and we set this energy to be equal to the chemical potential μ when $T = 0$.

We can then define a useful set of variables in terms of the Fermi energy, such as the Fermi temperature T_F and the Fermi wave-vector k_F

$$T_F \equiv \frac{E_F}{k_B} = \frac{(6N)^{1/3}}{k_B}\hbar\bar{\omega}, \tag{1.5}$$

$$k_F \equiv \frac{\sqrt{2mE_F}}{\hbar} = \sqrt{\frac{2m(6N)^{1/3}\bar{\omega}}{\hbar}}. \tag{1.6}$$

Moreover, the Fermi energy (1.4) can be used to define the length scales characterizing the Fermi distribution in coordinate space in the following way, $R_{F_i} = \sqrt{2E_F/m\omega_i^2}$ gives the width of the density distribution at $T = 0$, which can be calculated by integrating the distribution function (1.2) in momentum space,

$$n(x, y, z) = \frac{8}{\pi^2}\frac{N}{R_{F_x}R_{F_y}R_{F_z}}\left(1 - \frac{x^2}{R_{F_x}^2} - \frac{y^2}{R_{F_y}^2} - \frac{z^2}{R_{F_z}^2}\right)^{3/2} \tag{1.7}$$

To make physical sense, this quantity is defined to be strictly positive and hence it is equal to zero for every point where it results in a negative value. This formula is often referred to as the Thomas-Fermi distribution as we will discuss later in this chapter.

As we explain in the next section, ultracold identical fermions are nearly non-interacting systems due to Pauli blocking. Therefore, the ideal Fermi gas is an excellent approximation to describe them. Additionally, in the next section we also introduce a theoretical treatment to analyze a two-component spin mixture with interactions.

1.2 Interactions by two-body collisions

As we will discuss later in section 1.2.2, we have two distinguishable half-spin particles in our experiment which correspond to the lowest energy hyperfine states of ^{6}Li. These states are nearly equally populated. Each species does not interact with itself due to Pauli blocking, but they do interact with each other. Therefore it is necessary to introduce a theoretical treatment to describe the two-component spin mixture with interactions.

One of the main results of this treatment is that at very low temperatures one finds that the collision can be parameterized by a single constant which is the scattering length a_s. The absolute value of a_s determines the interaction strength and its sign defines if the interaction is effectively repulsive ($a_s > 0$) or attractive ($a_s < 0$).

In the next subsection we elaborate on the main results of the theory of elastic scattering in the $s-$wave channel [36, 37] and in the subsequent subsection we discuss about Feshbach resonances which is the mechanism that allows us to control the value of the scattering length to access different interaction regimes, from weakly to strongly interacting systems, from a repulsive to an attractive gas.

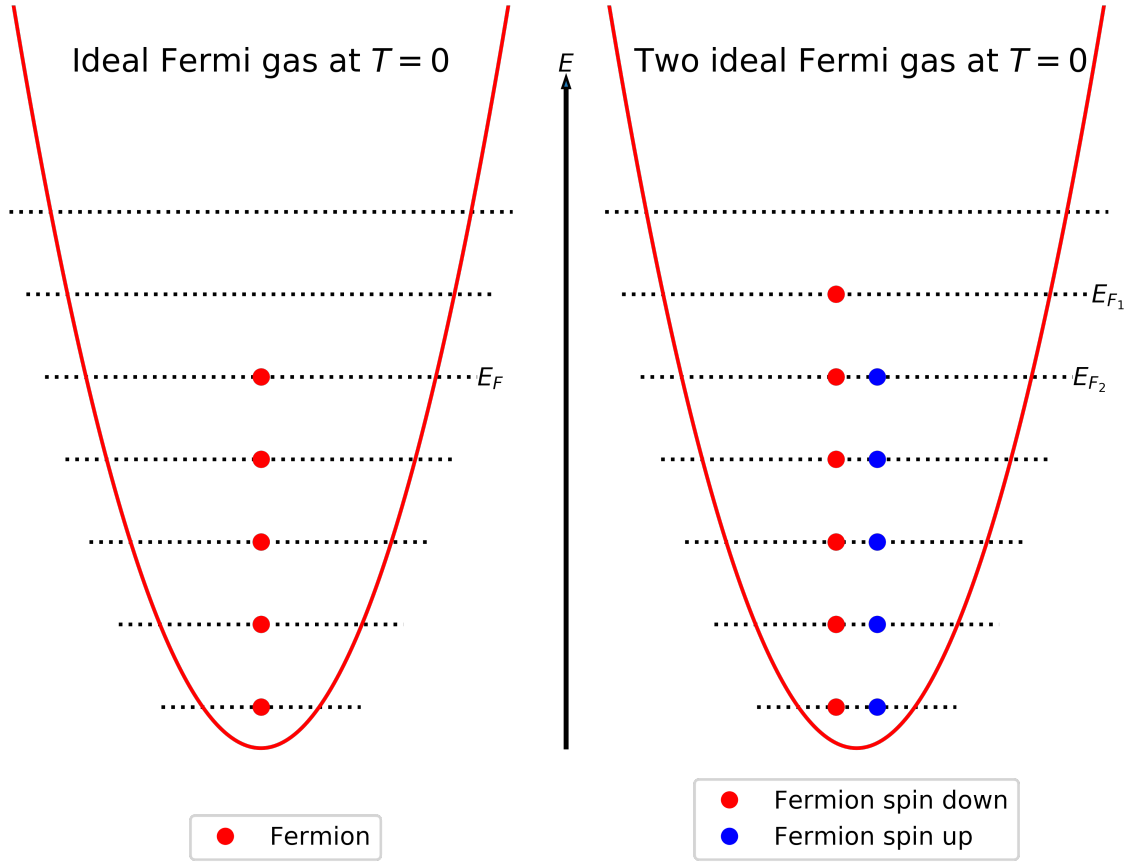

Figure 1.1: Left: pictorial representation of an ideal Fermi gas in a harmonic trap at $T = 0$. As a consequence of the Pauli exclusion principle, fermions form a Fermi sea in which each energy state up to the Fermi energy E_F is occupied. Right: pictorial representation of two ideal Fermi gases in a harmonic trap at $T = 0$. Each Fermi gas has different spin, which we portray by using two different colors. We assume there is not interaction between the spin components, and therefore each of them can be treated as a Fermi sea with its own Fermi energy E_{F_i}

1.2.1 Scattering

Interaction effects in quantum degenerate, dilute Fermi gases can be accurately modeled by a small number of parameters characterizing the physics of two-body collisions. The parameter which determines the quantum degeneracy of a sample is known as the phase space density (PSD) and is given by

$$\rho(n,T) = n\lambda_T^3 = n\left(\frac{\hbar^2}{2\pi m k_B T}\right) \tag{1.8}$$

where λ_T is the de Broglie thermal wavelength associated to the atoms, and n the atom density. The PSD measures the number of atoms inside a cube whose side is λ_T. When $\rho > 1$, i.e. low temperature and large density n, the system is degenerate.

Under these conditions, the spatial range r_0 of the interatomic potential is much smaller than both λ_T and the inverse Fermi wave vector k_F^{-1}

$$r_0 \ll \lambda_T, \quad r_0 \ll k_F^{-1}, \tag{1.9}$$

then, two interacting atoms cannot be considered as point-like particles anymore. They need to be treated as two wave-packets which have a two-body wave function that describes the collision.

According to Cohen-Tannoudji *et al.* [36], the problem of describing the collision process between two wave-packets reduces to solving the Schrödinger equation

$$i\hbar\frac{\partial\Psi(\mathbf{r},t)}{\partial t} = \left(-\frac{\hbar^2}{2m_r}\nabla^2 + V(\mathbf{r})\right)\Psi(\mathbf{r},t) \tag{1.10}$$

in the well known center of mass coordinate system, where m_r is the reduced mass and $\mathbf{r} = \mathbf{r}_1 - \mathbf{r}_2$ is the relative coordinate of the two particles. This describes the evolution of the incident wave-packet in the presence of a potential $V(\mathbf{r})$ whose center can be considered as the scattering center in the problem.

Using the stationary states, the solution is of the form $\Psi(\mathbf{r},t) = \psi(\mathbf{r})e^{-iEt/\hbar}$ where $\psi(\mathbf{r})$ is the solution to the time-independent Schrödinger equation

$$E\psi(\mathbf{r}) = \left(-\frac{\hbar^2}{2m_r}\nabla^2 + V(\mathbf{r})\right)\psi(\mathbf{r}) \tag{1.11}$$

where $E = \frac{\hbar^2\mathbf{k}^2}{2m_r}$ is the kinetic energy of the incident wave-packet before the collision. This equation is subject to the condition that the incoming component of the wave function is a plane wave $e^{i\mathbf{k}\cdot\mathbf{z}}$ because we assume that the wave-packet has a well-defined energy E (and hence it also has a well defined momentum $\hbar\mathbf{k}$) before the collision.

When the plane wave reaches the region of influence of the potential $V(\mathbf{r})$, it is scattered. Near the scattering center, the evolution of the system is very complex but (fortunately) we are not interested in describing it with detail. However, far from this region, at $r \gg r_0$, the stationary scattering state $\psi(\mathbf{r})$ can be considered

as a superposition of a transmitted plane wave $e^{i\mathbf{k}\cdot\mathbf{z}}$ which continues to propagate along $\hat{\mathbf{z}}$ and a scattered wave with the shape of an "outgoing" spherical wave e^{ikr}.

This spherical wave needs to have two additional factors to satisfy the equations. The first one is a $1/r$ factor that satisfies the radial component of (1.11) in spherical coordinates because $(\frac{1}{r}\frac{\partial^2}{\partial r^2}r + k^2)\frac{e^{ikr}}{r} = 0$. The second factor is the so-called scattering amplitude f which contains all of the information of the collision, therefore it depends on the shape of the potential $V(\mathbf{r})$ and the kinetic energy associated to the wave vector k. Assuming that $V(\mathbf{r}) = V(r)$ is a central potential, f depends only of the scattering direction θ, because the problem is symmetric with respect to the incident wave axis (the $z-$axis).

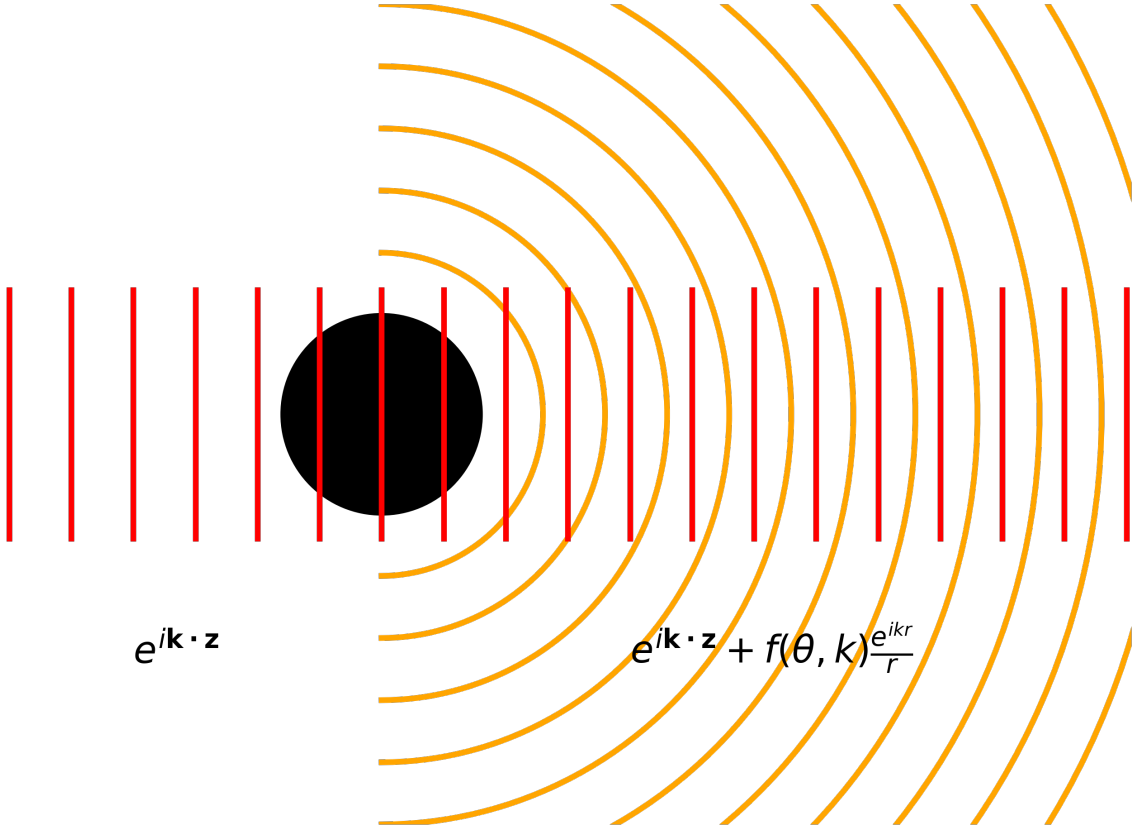

Figure 1.2: Representation of the scattering process. The incident plane wave $e^{i\mathbf{k}\cdot\mathbf{z}}$ is represented by red parallel lines. The scattering center (a potential $V(\mathbf{r})$) is represented by the black solid circle. When the plane wave reaches the region of influence of the potential, it is scattered. Far from this region, the stationary scattering state $\psi(\mathbf{r})$ can be considered as a superposition of a transmitted plane wave $e^{i\mathbf{k}\cdot\mathbf{z}}$ which continues to propagate along $\hat{\mathbf{z}}$ and a scattered wave with the shape of an "outgoing" spherical wave e^{ikr} represented by the circular orange lines.

Therefore, the wave function $\psi(\mathbf{r})$ associated with the stationary scattering state is the solution of (1.11) whose asymptotic behavior $r \gg r_0$ is of the form

$$\psi(\mathbf{r}) \to e^{i\mathbf{k}\cdot\mathbf{z}} + f(\theta, k)\frac{e^{ikr}}{r}. \tag{1.12}$$

The corresponding asymptotic probability flux is then given by

$$\mathbf{j} = \frac{\hbar}{im_r}\mathrm{Re}\left[\left(e^{i\mathbf{k}\cdot\mathbf{z}} + f(\theta,k)\frac{e^{ikr}}{r}\right)^* \nabla\left(e^{i\mathbf{k}\cdot\mathbf{z}} + f(\theta,k)\frac{e^{ikr}}{r}\right)\right]. \tag{1.13}$$

An expansion leads to two terms with exponential factors of the form $e^{\pm ikr(1-cos\theta)}$ where θ is the angle between $\mathbf{k}$ and $\mathbf{r}$. When $r \to \infty$ it leads to a fast oscillation of this factor and therefore we can then keep only those terms where it is equal to 1 to obtain

$$\mathbf{j} = \frac{\hbar\mathbf{k}}{m_r} + \frac{\hbar k}{m_r}\frac{|f(\theta,k)|^2}{r^2}\hat{r} + ..., \tag{1.14}$$

where the first term represents the incident flux, while the second describes the radial flux of the scattered wave. Thus one can obtain the differential cross-section defined as the ratio of the scattered flux to the incident flux

$$d\sigma = \frac{m_r}{\hbar k}\mathbf{j}\cdot d\mathbf{S} = \frac{|f(\theta,k)|^2}{r^2}r^2 d\Omega = |f(\theta,k)|^2 d\Omega. \tag{1.15}$$

Notice that the total probability flux passing through a sphere of radius r is independent of r. This is due to the $1/r$ factor that we added to the spherical wave in equation (1.12).

But how do we transform these theoretical results into a method to compute the characteristics of a particular scattering problem? Well, in general, for any Hamiltonian with a central potential $V(r)$ (1.11) the wave-function $\psi(\mathbf{r})$ can be expanded as

$$\psi(\mathbf{r}) = \sum_{l=0}^{\infty} R_{k,l}(r)P_l(\cos\theta) = \sum_{l=0}^{\infty}\frac{1}{r}u_{k,l}(r)P_l(\cos\theta) \tag{1.16}$$

where $P_l(\cos\theta)$ are the Legendre polynomials and $R_{k,l}(r)$ are the radial solutions to the radial component of equation (1.11), which are expressed (for practicality reasons) as $\frac{1}{r}u_{k,l}(r)$ to solve the radial equation

$$\frac{\hbar^2\mathbf{k}^2}{2m_r}u_{k,l}(r) = \left(-\frac{\hbar^2}{2m_r}\frac{d^2}{dr^2} + \frac{l(l+1)\hbar^2}{2m_r r^2} + V(r)\right)u_{k,l}(r), \tag{1.17}$$

with the restriction at the origin that $u_{k,l}(0) = 0$.

Each term in the series (1.16) is known as a partial wave. The partial wave is an eigenfunction common to the Hamiltonian and angular momentum operators $\mathbf{L}^2$ and L_z with associated eigenvalues $\hbar^2 l(l+1)$ and 0 respectively. Following standard spectroscopic notation, the values of the angular momentum number $l = 0, 1, 2, ...$ are referred to as the well-known $s, p, d, ...$ waves.

After analyzing the asymptotic behavior $r \gg r_0$ of the radial equation (1.17) [36], substituting it in the partial waves series (1.16) and comparing this asymptotic partial waves expression with equation (1.12), we find that the scattering amplitude to be of the form

$$f(\theta, k) = \frac{1}{2ik} \sum_{l=0}^{\infty} (2l+1)(e^{i2\delta_l(k)} - 1) P_l(\cos\theta) \tag{1.18}$$

which we can use to integrate $d\sigma$ in equation (1.15), obtaining the total cross-section

$$\sigma(k) = \frac{4\pi}{k^2} \sum_{l=0}^{\infty} (2l+1) \sin^2 \delta_l(k), \tag{1.19}$$

where $\delta_l(k)$ is called the phase shift of the partial wave l because it can be interpreted as a phase difference between incoming and outgoing waves. As the incoming wave leaves the region of influence of the potential, it is transformed into an outgoing wave, and it has accumulated a phase shift of $2\delta_l(k)$ relative to the free outgoing wave that would have resulted if the potential $V(r)$ had been identically zero.

Under the conditions of low temperature and large interparticle mean distance required by equation (1.9), the main contribution to the scattering amplitude comes from the $s-$wave state. An extra constraint comes from the antisymmetry of the wave function of identical fermions, which excludes the ocurrence of $s-$wave scattering between same spin particles. This is what we previously referred to as Pauli blocking in section 1.1. As a consequence, only particles in different spin states can interact.

The $s-$wave scattering amplitude $f_0(k)$ loses its angular dependency in equation (1.18) due to $P_0(x) = 1$, so it does not depend on the scattering angle. Therefore that the $s-$wave scattering amplitude can be written as

$$\begin{aligned} f_0(k) &= \frac{1}{2ik}(e^{2i\delta_0(k)} - 1) \\ &= \frac{e^{i\delta_0(k)}}{2ik}(e^{i\delta_0(k)} - e^{-i\delta_0(k)}) \\ &= \frac{\sin(\delta_0(k))}{ke^{-i\delta_0(k)}} \\ &= \frac{\sin(\delta_0(k))}{k[\cos(\delta_0(k)) - i\sin(\delta_0(k))]} \\ &= \frac{1}{k\cot(\delta_0(k)) - ik}. \end{aligned} \tag{1.20}$$

Then applying equation (1.15) directly to $f_0(k)$ results in an s-wave total cross-section

$$\sigma_0(k) = \frac{4\pi}{k^2 \cot^2 \delta_0(k) + k^2} = \frac{4\pi}{k^2} \sin^2 \delta_0(k) \tag{1.21}$$

which is the same result that we obtained with equation (1.19).

Example: Scattering resonance in a spherical well

We fully develop this example to show how to explicitly find the partial s-wave phase shift $\delta_0(k)$ in the problem of quantum scattering from an attractive spherical well potential. This potential is equal to $V(r) = -V_0$ for $r < r_0$ and $V(r) = 0$ everywhere else. As we have already mentioned, at low energies, the scattering is dominated by the s-wave $l = 0$ mode. Therefore the radial equation (1.17) we have to solve is of the the form

$$\left(\frac{d^2}{dr^2} + k_0^2 + k^2\right) u_k(r) = 0, \tag{1.22}$$

where $k_0^2 = \frac{\hbar^2 V_0}{2m_r}$ for $r < r_0$ and $k_0^2 = 0$ everywhere else. Inserting the boundary condition $u_k(0) = 0$ at the origin, the solution is

$$u_k(r) = \begin{cases} C\sin(Kr) & r < r_0 \\ \sin(kr + \delta_0(k)) & r > r_0 \end{cases}, \tag{1.23}$$

where $K^2 = k^2 + k_0^2$ and $\delta_0(k)$ is the partial s-wave phase shift. The continuity condition for the wave-function $C\sin(Kr_0) = \sin(kr_0 + \delta_0(k))$ and its derivative $CK\cos(Kr_0) = k\cos(kr_0 + \delta_0(k))$ at $r = r_0$ implies the relation $\tan(Kr_0)k/K = \tan(kr_0 + \delta_0(k))$. From this last expression, we can solve for the s-wave phase shift

$$\delta_0(k) = \arctan\left[\frac{k}{K}\tan(Kr_0)\right] - kr_0. \tag{1.24}$$

Using the identity for the tangent of an angle difference, we get

$$\tan\delta_0(k) = \frac{\frac{k}{K}\tan(Kr_0) - \tan(kr_0)}{1 + \frac{k}{K}\tan(Kr_0)\tan(kr_0)}, \tag{1.25}$$

or, more conveniently,

$$k\cot\delta_0(k) = \frac{k + \frac{k^2}{K}\tan(Kr_0)\tan(kr_0)}{\frac{k}{K}\tan(Kr_0) - \tan(kr_0)} \equiv -\frac{1}{a_s} + \frac{1}{2}R_0k^2, \tag{1.26}$$

where in the last expression[1] we define the so-called scattering length $a_s = \frac{K\tan(kr_0) - k\tan(Kr_0)}{kK}$ and the effective range of the interaction $R_0 = \frac{2\tan(Kr_0)\tan(kr_0)}{k\tan(Kr_0) - K\tan(kr_0)}$ which is usually of the same order of r_0.

In the low energy regime $k \to 0$, then $K \approx k_0$ and $\tan(kr_0) \approx kr_0$ which can be substituted in the expression for scattering length to obtain

$$a_s \approx r_0\left(1 - \frac{\tan(k_0r_0)}{k_0r_0}\right) \tag{1.27}$$

[1] L. Landau himself proposed a similar expression [37].

which is independent of k. Notice that in this regime $k \to 0$ we can also make the approximations $k \cot \delta_0(k) \approx -1/a_s$ by equation (1.26), then $f_0 = -a_s$ by equation (1.20) and $\sigma_0 = 4\pi a_s^2$ by equation (1.21) which are independent of k as well. Although this cross section has the same form of the one of two coilliding hard sphers with radii equal to the scattering length a_s, we should not forget that we are describing interacting waves. This scattering is isotropic and independent of the particle energy.

Therefore, the scattering length a_s at low energies only depends on the potential characteristics i.e. on r_0 and $k_0 = \sqrt{\frac{\hbar^2 V_0}{2m_r}}$. Therefore, we can calculate the scattering as a function of $k_0 r_0$ as follows. First we plot the functions $\tan(k_0 r_0)$ and $k_0 r_0$ (in blue and red respectively on the left side of figure 1.3). a_s is computed as the substraction of the red an blue lines, divided by $k_0 r_0$, resulting in the purple line on the right side of figure 1.3.

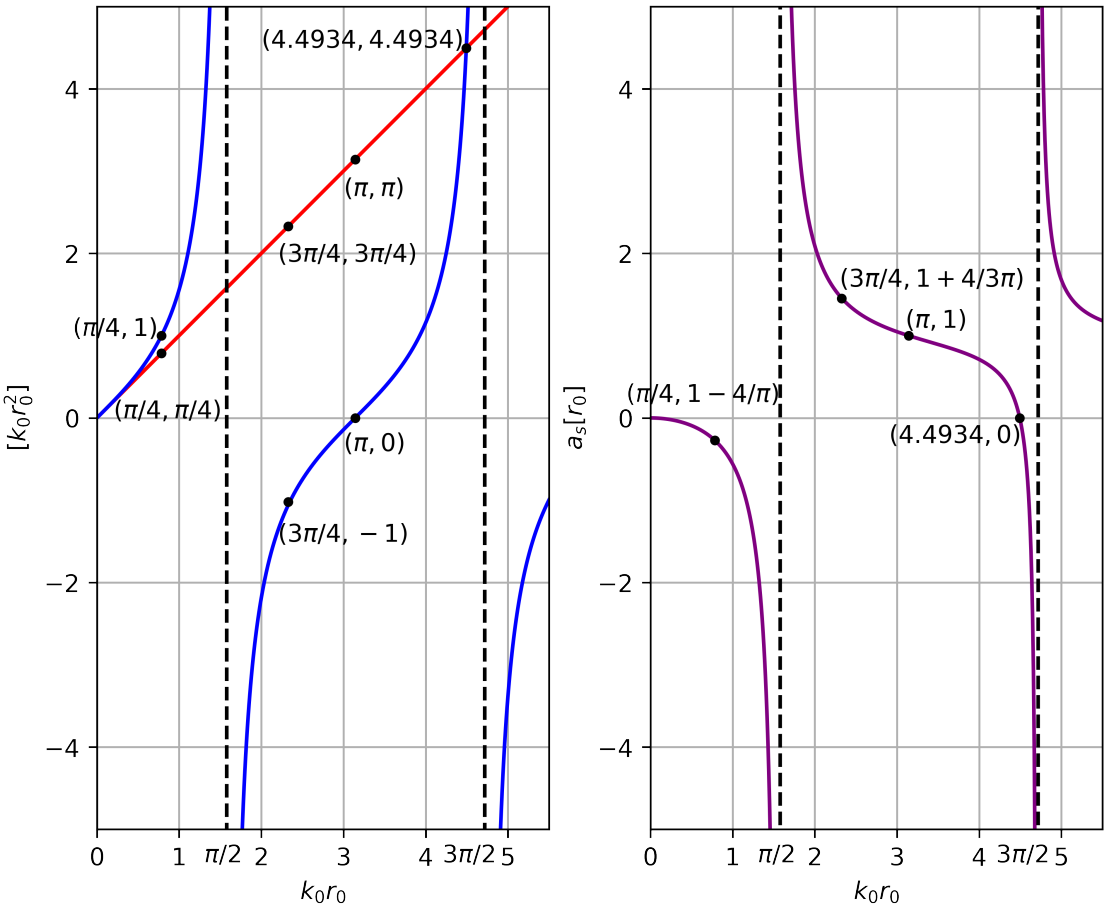

Figure 1.3: Left: the functions $\tan(k_0 r_0)$ and $k_0 r_0$ are shown in blue and red respectively. Right: a_s is computed as the substraction of the red an blue lines, divided by $k_0 r_0$, resulting in the purple line. If $k_0 r_0 < \pi/2$, a_s is negative. As we approach $\pi/2$ from the left; $k_0 r_0 \to (\pi/2)^-$, the scattering length tends to be infinitely negative i.e. $a_s \to -\infty$. On the other hand, as we approach $\pi/2$ from the right; $k_0 r_0 \to (\pi/2)^+$, the scattering length tends to be infinitely positive i.e. $a_s \to +\infty$. Finally, if $\pi/2 < k_0 r_0 < 4.4934$, a_s is positive and tends to zero.

Then, if $k_0 r_0 < \pi/2$, a_s is negative. As we approach $\pi/2$ from the left; $k_0 r_0 \to$

$(\pi/2)^-$, the scattering length tends to be infinitely negative i.e. $a_s \to -\infty$. On the other hand, as we approach $\pi/2$ from the right; $k_0 r_0 \to (\pi/2)^+$, the scattering length tends to be infinitely positive i.e. $a_s \to +\infty$. Finally, if $\pi/2 < k_0 r_0 < 4.4934$, a_s is positive and $a_s = 0$ at the numerical value $k_0 r_0 = 4.4934$.

By analyzing the tangent line of the radial equation (low energies) $u_0(r) = C\sin(k_0 r)$ at the boundary condition $r = r_0$, we obtain (via the point-slope formula) that the linear equation is $y = C\cos(k_0 r_0)(k_0 r - k_0 r_0) + C\sin(k_0 r_0)$. Searching where (r) the line intercepts with the $x-$axis $(y = 0)$ we obtain the same expression as the scattering length (1.27). Therefore we have found a new geometrical interpretation for the scattering length. This geometrical approach is exemplified for 3 values of $k_0 r_0$ (at fixed r_0) in figure 1.4. The radial equation $u_0(r)$ is plotted in green. The dotted purple lines are the tangent lines to $u_0(r)$ at boundary condition $r_0 = 1$. The black dots are the tangent points at $r_0 = 1$.

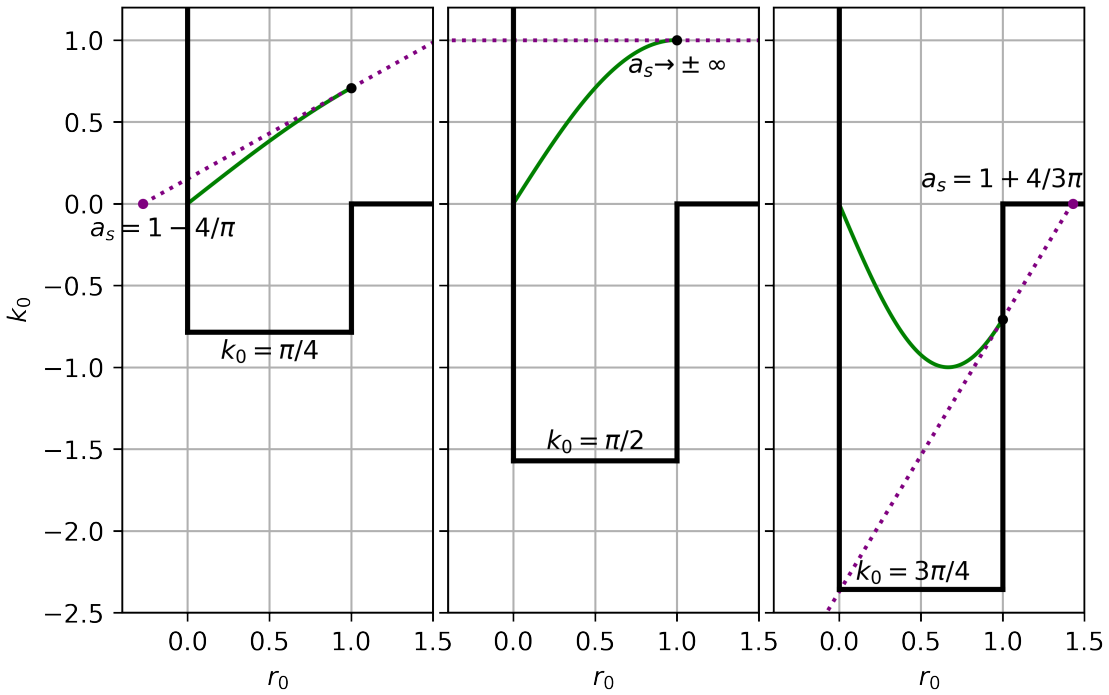

Figure 1.4: Analysis of the tangent line (dotted purple line) of the radial equation with $k \to 0$ and $C = 1$; $u_0(r) = \sin(k_0 r)$ (green lines) at the boundary condition $r = r_0 = 1$ (black dots) for three values of $k_0 r_0 = \pi/4, \pi/2, 3\pi/4$. The point where the tangent line intercepts the $x-$axis turns out to be the scattering length $a_s = r_0\left(1 - \frac{\tan(k_0 r_0)}{k_0 r_0}\right)$. This intercept point is marked as a purple dot. The a_s values correspond with the values displayed to the right of figure 1.3. Note that when the depth of the well is gradually decreased, a_s diverges at $k_0 r_0 = \pi/2$. This phenomenon is called a scattering resonance, and has to do with the fact that the potential well is barely able to support an s-wave bound state.

We can observe from figure 1.4 that when the depth of the well is gradually decreased (at fixed r_0), a_s and in consequence σ_0 diverge at $k_0 r_0 = \pi/2$ (central part of figure 1.4). This phenomenon is called a scattering resonance and has to do with the fact that the potential well is barely able to support an s-wave bound state.. One

important observation is that the scattering length a_s changes its sign when $k_0 r_0$ passes through a bound state. This process repeats itself with the appearance of a second scattering resonance and a second bound state at $k_0 r_0 = 3\pi/2$ (right part of figure 1.3), and in fact it is periodic every odd multiple of $\pi/2$.

In summary, if we are able to change the scattering properties of the atoms $k_0 r_0$, we can control the scattering length a_s of two atoms. But changing the scattering properties would require changing the actual shape of the interatomic potential, which for all practical reasons is impossible.

However there is a different phenomenon that allows us to tune the effective interaction between atoms, the magnetic Feshbach resonance. This phenomenon is more complex to explain theoretically [38], but has many of the characteristics of a resonance presented in this example.

In the next section we introduce the Feshbach resonance, and how the scattering length can be easily controlled experimentally by means of an external magnetic field.

1.2.2 Feshbach resonance and interaction regimes

Up to this point, we have only considered two-body elastic collisions. Elastic scattering refers to an interaction event between free particles that does not change the internal quantum state or quantum numbers of the involved particles. In a simple system composed by two half-spin particles, it turns out that the sum of the spin angular momentum can be $S = 0$ or $S = 1$, called a singlet and a triplet correspondingly. This two possible total spin angular momentum configurations constitute by definition two scattering channels.

In our previous example 1.2.1, we have considered two-body elastic collisions that occur in a single scattering channel in the s-wave limit. This implies that, despite the scattering, the two-particle system remains in the same scattering channel as it was before the interaction.

In the case of multi-channel scattering, various collision channels are possible and they are coupled by the scattering interaction. The importance of multi-channel scattering is that a crucial phenomenon called a Feshbach (or Fano-Feshbach) resonance emerges [39]. Broadly speaking, this resonance occurs when a bound state of one channel becomes degenerate in energy with the scattering state in another channel. The theoretical treatment that describes this process is beyond the scope of what we wish to discuss here but the reader can refer to Stoof [38] where a two-channel model for a Feshbach resonance between two alkali atoms is presented.

From this point on, we are going to explain the Feshbach resonance, in the context of our experiment using ^{6}Li. We first consider two distinguishable half-spin particles labeled as $|1\rangle$ and $|2\rangle$ which correspond to the two lowest energy hyperfine states in the ^{6}Li. As we said in the beginning of this section, there are two channels, the singlet ($S = 0$) and triplet ($S = 1$) configurations. Each channel has different associated interatomic potentials (figure 1.5) which we refer to as "open" (or entrance) and "closed" channels for the triplet and singlet cases respectively.

Similar to our previous scattering resonance example 1.2.1, where the resonance

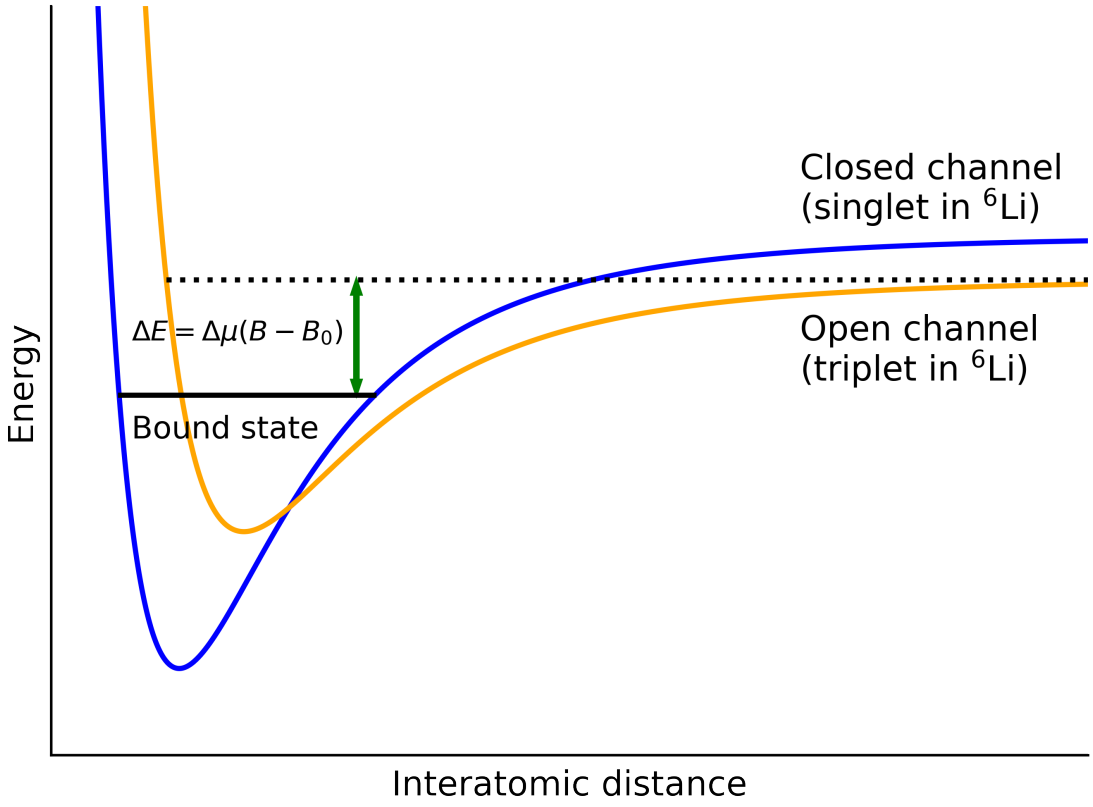

Figure 1.5: Two-channel schematic model of a magnetic Feshbach resonance. The potentials corresponding to each channel are tuned relative to each other using an external magnetic field. When the bound state energy is below the scattering state energy we have that $a > 0$ and viceversa.

appears when a bound state becomes degenerate in energy with the free particle state, the Feshbach resonance phenomenon occurs when the bound state of the closed channel becomes degenerate in energy with the scattering state of the open channel.

The bound state in the case of a Feshbach resonance is a molecular state. This molecular state is created when two free ^{6}Li atoms couple to form a molecule $^6Li_2$ in which the atoms are tightly bound [23]. The closer this molecular level lies with respect to the energy of two free atoms, the stronger the interaction strength between them.

Since the magnetic moments of the pairs of atoms in the two channels are different, the energy difference between the two free atoms and the molecular state can be easily controlled experimentally by means of an external constant magnetic field. Therefore, the magnetic field controls the interatomic interaction strength.

We use this resonances experimentally to tune the interaction between atoms (parametrized by the scattering length) almost at will by changing the value of a constant magnetic field in the system [26]. Close to a Feshbach resonance, the scattering length as a function of the magnetic field B, is described by the formula

$$a_s = a_0 \left(1 - \frac{\Delta_B}{B - B_0}\right), \tag{1.28}$$

where the resonance occurs at a magnetic field B_0 =832G, $\Delta_B \approx$300G is the width of the resonance and a_0 is the background scattering length away from the resonance. One reason to use the Feshbach resonance between state $|1\rangle$ and $|2\rangle$ is that it is very broad (figure 1.6), enabling very fine and precise control of the scattering length.

A very important consequence of having such control over interatomic interactions is the possibility of exploring different interaction regimes. In fermionic systems, the interaction strength is commonly parametrized by introducing the dimensionless interaction parameter $\frac{1}{k_F a_s}$ where k_F is the Fermi wave vector.

On the side of the resonance, where the scattering length is positive $\frac{1}{k_F a_s} > 0$, the molecular energy level is lower in energy than the energy of two unbound atoms. The molecular state is thus"real" and stable, and atoms tend to form molecules. If those atoms are fermions, the resulting diatomic molecule is a bosonic molecule. A gas of these dimers exhibits bosonic statistics making the emergence of Bose-Einstein condensation (BEC) possible after cooling down the sample. This side of the resonance is therefore called the "BEC-side".

On the side of the resonance where the scattering length is negative $\frac{1}{k_F a_s} < 0$, molecules are unstable. Nevertheless, when surrounded by a Fermi sea, two fermions can still form a loosely bound pair (in momentum space), whose size can become comparable to or even larger than the average distance between particles. After cooling down these fragile pairs, a "BCS-state" is formed. This is closely associated to what occurs in superconductors, in which current flows without resistance thanks to electron pairs ("Cooper pairs") well described by BCS theory [25].

Additionally, the Feshbach resonance allows to continuously transit between the BEC and the BCS regimes through the so-called BEC-BCS crossover. This inter-

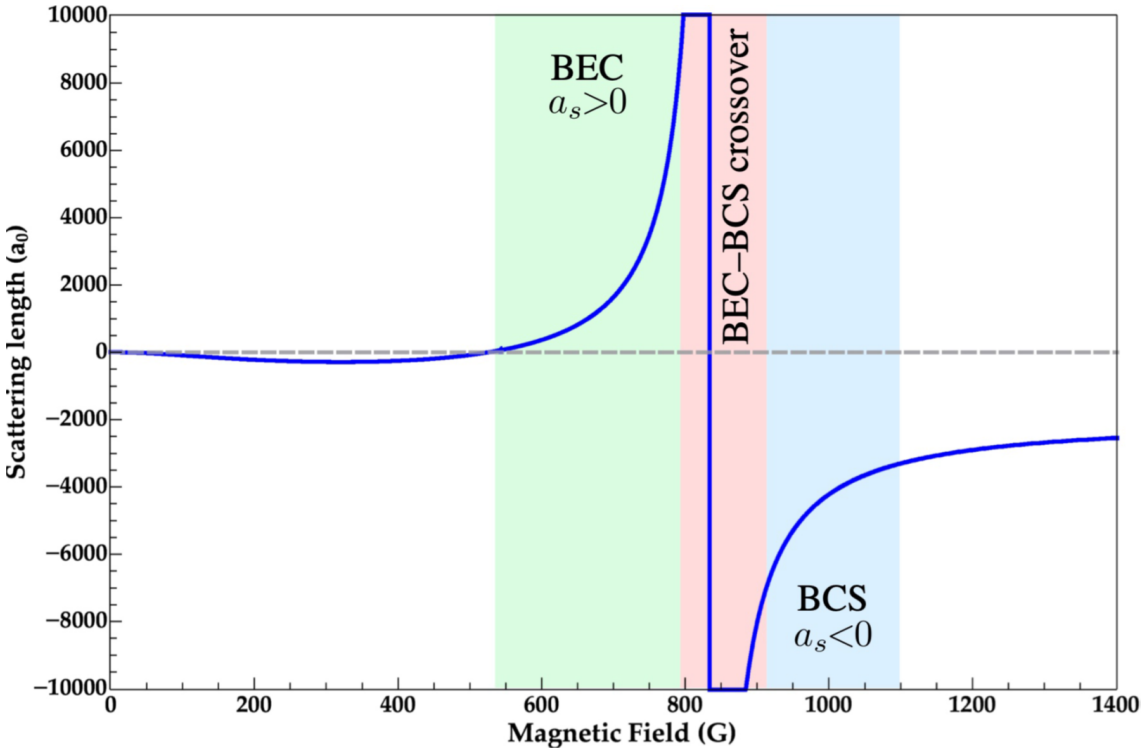

Figure 1.6: Feshbach resonance for the two lowest hyperfine Zeeman levels of ^{6}Li labeled as $|1\rangle$ and $|2\rangle$. Different superfluid regimes are accesible depending on the value of the scattering length a_s.

mediate regime $-1 < \frac{1}{k_F a_s} < 1$ is also known as the "Unitary Limit" and contains the point where the scattering length diverges $\frac{1}{k_F a_s} = 0$. This regime is particularly interesting because the system is strongly interacting and strongly correlated. In fact, in the unitary limit the scattering amplitude (1.20) and (1.26) at wave vectors $k \ll 1/|R_0|$ obey the universal regime $f_0(k) = -i/k$, which is independent of the interaction. Understanding the physics of the BEC-BCS crossover is of profound interest due to its relationship with important phenomena such as high-T_c superconductivity [14] and superfluidity in neutron stars or quark-gluon plasma [40, 41, 42].

Figure 1.6 also shows the different superfluid regimes depending on the value of the scattering length a_s. At the LMU we are able to produce ultracold fermionic superfluid samples of ^{6}Li in the three different interaction regimes presented in section 3.2.2. Absorption images of these samples are shown in figure 3.13.

1.3 Weakly interacting Bose gas

While we are able to produce ultracold fermionic superfluid samples at different interaction regimes, this thesis will focus on the BEC regime. Therefore, a brief description of the weakly interacting Bose gas needs to be introduced.

As we discussed in the last section, in the BEC side of the Feshbach resonance bosonic diatomic molecules are formed. This dimers of size a_s have a binding energy ϵ_b which does not depend on the short-range details of the potential and is simply given by

$$\epsilon_b = \frac{\hbar^2}{2m_r a_s^2}. \tag{1.29}$$

At first glance these molecules can interact either with dimers or with single atoms. Nevertheless the probability of atom-dimer collisions is suppressed by the Pauli principle, because two of the three atoms always have the same spin. According to Petrov [43] the dimer-dimer scattering length is $a_{dd} \approx 0.6a_s$.

Taking into account the low momenta case ($ka_s \ll 1$) where the interaction is weak and expressing the new scattering length between dimers a_{dd} in terms of a_s, this bosonic gas can be described using the mean-field theory developed by Gross and Pitaevskii [44, 45] in 1961. According to this theory, valid at $T = 0$, the BEC can be described by a wave function $\Psi(\mathbf{r}, t)$ which is a solution to the differential equation

$$i\hbar\frac{\partial\Psi(\mathbf{r},t)}{\partial t} = \left(-\frac{\hbar^2}{2M}\nabla^2 + V(\mathbf{r}) + \frac{4\pi\hbar^2 a_{dd}}{M}|\Psi(\mathbf{r},t)|^2\right)\Psi(\mathbf{r},t), \tag{1.30}$$

where M is the mass of the dimer. This wavefunction must fulfill the normalization condition $N = \int |\Psi(\mathbf{r},t)|^2\, d\mathbf{r}$ where N is the total number of particles in the gas.

This equation looks similar to the Schrödinger equation with the addition of an interaction term $g|\Psi(\mathbf{r},t)|^2$. This term transforms the equation into a non-linear differential equation and for this reason it is called a non-linear Schrödinger equation (NLSE) or, more commonly, the Gross-Pitaevskii equation (GPE).

Using separation of variables method one can propose a solution $\Psi(\mathbf{r},t) = \theta(t)\psi(\mathbf{r})$ written as the product of a temporal-function and spatial-function. Substituting this we get that $\theta(t) = e^{-i\mu t/\hbar}$ but to find $\psi(\mathbf{r})$ it is necessary to solve

$$\mu\psi(\mathbf{r}) = \left(-\frac{\hbar^2}{2M}\nabla^2 + V(\mathbf{r}) + g|\psi(\mathbf{r})|^2\right)\psi(\mathbf{r}) \tag{1.31}$$

which is called the time independent GPE. Here μ emerges mathematically from the separation of variables method as an integration constant, but later on it is identified as the chemical potential. Considering the normalization condition $N = \int |\psi(\mathbf{r})|^2\, d\mathbf{r}$ then the BEC density can be calculated simply as $n(\mathbf{r}) = |\psi(\mathbf{r})|^2$.

In the low temperature limit, the kinetic term $-\frac{\hbar^2}{2M}\nabla^2\psi(\mathbf{r})$ can be neglected and then the mean-field interaction term $gn(\mathbf{r})$ determines the dynamics of the BEC. In this limit, the GPE can be trivially solved to find the density, obtaining

$$n(\mathbf{r}) = \frac{1}{g}(\mu - V(\mathbf{r})) \tag{1.32}$$

which is the so called Thomas-Fermi approximation. Then the BEC density only depends on mean-field interactions and the shape of the confinement potential. Now, considering a harmonic potential (1.1), the BEC density is

$$n(x,y,z) = \frac{1}{g}\left(\mu - \frac{1}{2}M(\omega_x^2 x^2 + \omega_y^2 y^2 + \omega_z^2 z^2)\right). \tag{1.33}$$

To make physical sense, this quantity is defined to be strictly positive and hence it is set equal to zero for every point where it results in a negative value. If we plot the density in function of the ith-direction, this expression results in a parabolic profile, plotted as a solid red line in the right panel of figure 1.7. This profile corresponds to the bimodal fit presented in section 3.2.2.

By setting (1.33) equal to zero the maximum extension of the BEC is

$$R_{TF_i} = \frac{1}{\omega_i}\sqrt{\frac{2\mu}{M}} \tag{1.34}$$

These limits along the $i = x, y, z$ directions are known as the Thomas-Fermi radii.

Integrating (1.33) over the three dimensions and using the normalization condition, one finds that the chemical potential is

$$\mu = \frac{\hbar\bar{\omega}}{2}\left(\frac{15a_{dd}N}{a_{ho}}\right)^{2/5} \tag{1.35}$$

where $a_{ho} = \sqrt{\hbar/M\bar{\omega}}$ is the harmonic oscillator length.

After this brief introduction where we have discussed our research topic and motivations, we now move our attention to more practical issues. The next chapter is centered around laser cooling techniques and their theoretical treatment.

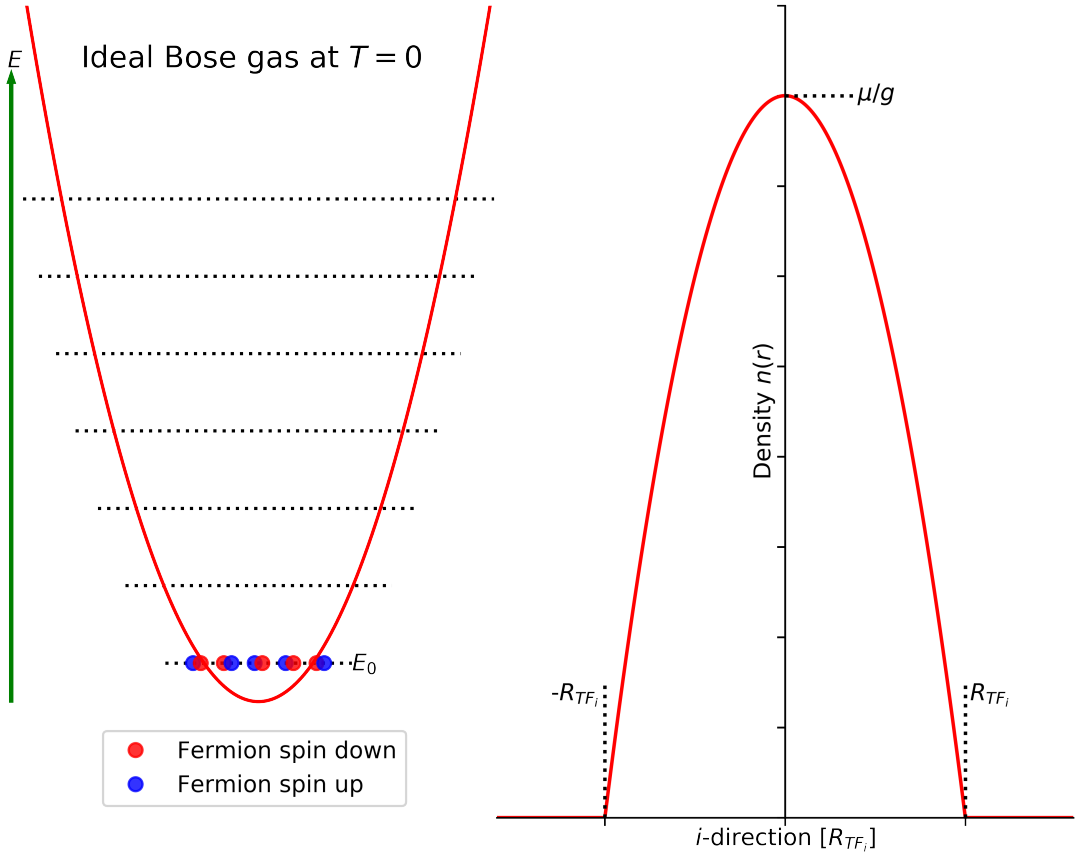

Figure 1.7: Left: pictorial representation of an ideal Bose gas at $T = 0$. Here the so called composite bosons are molecules formed by two fermions with opposite spin. All of the bosons remain at the lowest energy state. Right: density profile of a BEC along one direction according to the Thomas-Fermi approximation.

Chapter 2

Magnetic and optical potentials

Before presenting the implementation of the different cooling techniques employed in our experiment, it is necessary to describe how laser light can be used to slow down the motion of atoms. The theoretical treatment about laser cooling is developed in this chapter following the references [46] and [47]. Additionally, it is important to mention that we are going to describe such cooling stages following the same order in which they are employed in the time sequence of our experiment.

First, we discuss about the concept of radiative force (section 2.2) and how it is used to slow down the atoms. This force is velocity dependent, and therefore it does not confine the atoms in a particular place, it simply slows them down. For this reason, this cooling mechanism must be complemented with additional magnetic fields (see section 2.2.3) to create an electromagnetic "container" to spatially confine the atoms. This combination of optical cooling and magnetic trapping is known as "Magneto-Optical Trap" (MOT). The temperature reached by magneto-optical trapping is typically restricted by the Doppler limit. Therefore, sub-Doppler cooling techniques are necessary to further cool down the sample (see section 2.2.5).

After these first two cooling stages, it is necessary to transfer the atoms into a conservative potential. To do this, a different type of optical force is employed, the so-called dipole force (see section 2.3). This force is used to create a harmonic trap in which the laser cooled atoms are transferred (section 2.3.2). This is known as "Optical Dipole Trap" (ODT). It is in the ODT where the last cooling state can be applied to finally reach quantum degeneracy through the evaporative cooling stage, which we describe in section 2.3.4. We also complement the ODT with additional magnetic fields to create a better confinement (section 2.3.3). We put special emphasis in the theoretical description of the ODT, since it is one of the main topics of this thesis.

2.1 Mechanical effects of light on atoms

Generally speaking, there are two types of mechanical forces that light can exert on atoms [6]. The fist one, the radiation force, is consequence of the absorption and scattering of the incident light and it is related to the imaginary part of the polarizability $\alpha(\omega)$, as can be seen in equation (2.29), where ω is the frequency of the

incident light. The second one, the dipole force, arises from the interaction between the electric dipole moment of the atoms with the electric filed of the light, and it is related to the real part of $\alpha(\omega)$, as shown in eq. (2.57).

In this section we discuss the theoretical background necessary in sections 2.2 and 2.3 to obtain the expression for all these light forces.

2.1.1 Polarizability: Lorentz model

First of all, we will use the following complex notation for the electromagnetic fields:

$$\mathbf{E}(\mathbf{r},t) = \mathbf{E}(\mathbf{r})cos(\omega t + \phi) = \mathbf{E}(\mathbf{r})\frac{e^{-i\phi}}{2}e^{-i\omega t} + \mathbf{E}(\mathbf{r})\frac{e^{i\phi}}{2}e^{i\omega t} \equiv \mathbf{E}^{+}(\mathbf{r}) + \mathbf{E}^{-}(\mathbf{r}). \quad (2.1)$$

Here, we separate them into components with positive and negative frequency, which we denote, respectively, with the superscripts + and −. Notice that one is the complex conjugate of the other. Then, we can always write the physical field as $\mathbf{E}(\mathbf{r},t) = \mathbf{E}^{+}(\mathbf{r}) + c.c.$ which is a convenient mathematical notation.

Now, we obtain an expression for the polarizability $\alpha(\omega)$. Although atoms do not have a permanent electric dipole moment, it can be induced by the electric field of the light with which they interact. To obtain $\alpha(\omega)$, we model the atom as a damped harmonic oscillator. This model is known as the Lorentz model of the atom. In this approximation, we model the atom as an electron harmonically bounded to the nucleus and forced by an electric field. The corresponding equation of motion of the electron is

$$m\ddot{\mathbf{x}}^{+} + m\gamma\dot{\mathbf{x}}^{+} + m\omega_0^2\mathbf{x}^{+} = -\hat{\epsilon}\mathrm{e}E_0^{+}e^{-i\omega t}. \quad (2.2)$$

Here, $\mathbf{x}^{+}$ represent the average position of the electron, ω_0 is the resonant frequency of the harmonic potential, the damping term models radiation due to the charge acceleration and collisions with other atoms. A semi quantum-mechanical calculation shows that for an isolated atom, the damping rate γ can be identified as the spontaneous emission rate (section 2.1.3). The above equation is expressed in the center-of-mass coordinates, thus m is the reduced mass of the electron and also we can ignore the motion of the nucleus. We are considering the dipole approximation in the last term in the above equation, which consists in assuming that the size of the atom is much smaller than the optical wavelength, so that the electron only "sees" the field at the nuclear position. The model also does not consider the spatial dependence or the direction of propagation of the field. Then the force on the electron due to the interaction with a monochromatic field is $\mathbf{F}^{+} = -\mathrm{e}\mathbf{E}^{+} = -\mathrm{e}\hat{\epsilon}E_0^{+}e^{-i\omega t}$ where e is the fundamental electric charge.

Considering an ansatz of the form $\mathbf{x}^{+}(t) = \hat{\epsilon}x_0^{+}e^{-i\omega t}$ that has the same time dependence as the field, the equation (2.2) becomes

$$-m\omega^2x_0^{+} - im\gamma\omega x_0^{+} + m\omega_0^2x_0^{+} = -\mathrm{e}E_0^{+}, \quad (2.3)$$

which we can solve for x_0^{+} to obtain the solution

$$x_0^+ = \frac{\mathrm{e}E_0^+/m}{\omega^2 - \omega_0^2 + i\gamma\omega}. \tag{2.4}$$

The dipole moment of the atom is

$$\mathbf{d}^+ = -\mathrm{e}\mathbf{x}^+ \tag{2.5}$$

where $\mathbf{x} = \hat{\epsilon}x$. Since the dipole moment is induced by the field, we can define the polarizability α to describe how easily the field induces such dipole by

$$\mathbf{d}^+ \equiv \alpha(\omega)\mathbf{E}^+ \tag{2.6}$$

then from equations (2.4) and (2.5), we can write polarizability as

$$\alpha(\omega) = \frac{\mathrm{e}^2/m}{\omega_0^2 - \omega^2 - i\gamma\omega}. \tag{2.7}$$

It is important to emphasize that α is a complex quantity defined for the positive-rotating field by definition.

2.1.2 Dipole Radiation and Damping Coefficient

After finding the polarizability α under the Lorentz model, it is necessary an expression for the damping term γ. To find γ in a classical description, first we need to explain how an oscillating dipole irradiates. The expression of the emitted power will be useful in section 2.2 to explain the radiative force.

In the electric and magnetic fields for an oscillating dipole only the $1/r$ terms transport energy to infinity [48]. These radiation terms are

$$\mathbf{E}^+(\mathbf{r},t) \approx \frac{1}{4\pi\epsilon_0 c^2}[(\hat{\varepsilon}\cdot\hat{r})\hat{r} - \hat{\varepsilon}]\frac{\ddot{d}^+(t_r)}{r}, \tag{2.8}$$

$$\mathbf{H}^+(\mathbf{r},t) \approx \frac{1}{4\pi c}(\hat{\varepsilon}\times\hat{r})\frac{\ddot{d}^+(t_r)}{r}, \tag{2.9}$$

where $t_r = t - r/c$ is the retarded time, and $\hat{\varepsilon}$ is the polarization unit vector of the applied field and, hence, the dipole orientation vector. The energy transport is described by the Poynting vector, which can be written as

$$\begin{aligned}
\langle\mathbf{S}\rangle &= \mathbf{E}^+(\mathbf{r},t)\times\mathbf{H}^-(\mathbf{r},t) + c.c., \\
&= \frac{1}{16\pi^2\epsilon_0 c^3}\frac{|\ddot{d}^+|^2}{r^2}[(\hat{\varepsilon}\cdot\hat{r})\hat{r} - \hat{\varepsilon}]\times(\hat{\varepsilon}^*\times\hat{r}) + c.c., \\
&= \frac{1}{8\pi^2\epsilon_0 c^3}\frac{|\ddot{d}^+|^2}{r^2}\left(1 - |\hat{r}\cdot\hat{\varepsilon}|^2\right)\hat{r},
\end{aligned} \tag{2.10}$$

where we have used that $[(\hat{\varepsilon}\cdot\hat{r})\hat{r} - \hat{\varepsilon}]\times(\hat{\varepsilon}^*\times\hat{r}) = (1 - |\hat{r}\cdot\hat{\varepsilon}|^2)\,\hat{r}$. This term is a real number, so its *c.c.* has the same value and it is taken into account by multiplying by two the first term of $\langle\mathbf{S}\rangle$.

There are two important cases for the polarization vector. The incident light can be linearly or circularly polarized. For the case of linear polarization, $\hat{\varepsilon} = \hat{z}$, we have $1 - |\hat{r} \cdot \hat{\varepsilon}|^2 = \sin^2\theta$. On the other hand, for the case of circular polarization, $\hat{\varepsilon} = (\hat{x} \pm i\hat{y})/\sqrt{2}$, so $1 - |\hat{r} \cdot \hat{\varepsilon}|^2 = (1 + \cos^2\theta)/2$. Note that any arbitrary polarization can be represented as a superposition of these three basis vectors.

The total radiated power is then

$$\begin{aligned} P_{rad} &\equiv \int \frac{dP_{rad}}{d\Omega} d\Omega = \int r^2 \mathbf{S} \cdot \hat{r} d\Omega \\ &= \frac{|\ddot{d}^+|^2}{8\pi^2\epsilon_0 c^3} \int_0^{\pi} \int_0^{2\pi} \left(1 - |\hat{r} \cdot \hat{\varepsilon}|^2\right) \sin\theta d\theta d\phi, \\ &= \frac{|\ddot{d}^+|^2}{3\pi\epsilon_0 c^3} = \frac{\mathrm{e}^2 |\ddot{x}^+|^2}{3\pi\epsilon_0 c^3} \end{aligned} \tag{2.11}$$

where the last equality is obtained using equation (2.5). This result applies to both linearly and circularly polarized light. Also note that the radiated power is the time-averaged power. Calculating the average work done by the complete damping term

$$\int_{x_1}^{x_2} m\gamma \dot{\mathbf{x}} \cdot d\dot{\mathbf{x}}' = \int_{t_1}^{t_2} m\gamma \dot{\mathbf{x}}(t') \cdot \dot{\mathbf{x}}(t') dt' = m\gamma \int_{t_1}^{t_2} 2|\dot{x}^+|^2 dt', \tag{2.12}$$

where in the last equality we use a similar procedure presented in the section 2.3 to calculate the dipole force. This procedure consists in dropping the terms $\dot{\mathbf{x}}^{\pm} \cdot \dot{\mathbf{x}}^{\pm} \sim e^{\pm 2i\omega t}$ because the frequency is too high for the atoms. Instead, the terms of the form $\dot{\mathbf{x}}^{\pm} \cdot \dot{\mathbf{x}}^{\mp} \sim 1$ are kept. These two terms are equal and, then, equivalent to $2|\dot{x}^+|^2$.

Then, the average work done by radiation reaction must balance the energy emitted into the field, giving

$$2m\gamma \int_{t_1}^{t_2} |\dot{x}^+|^2 dt' \equiv \int_{t_1}^{t_2} P_{rad} dt' = \frac{\mathrm{e}^2}{3\pi\epsilon_0 c^3} \int_{t_1}^{t_2} |\ddot{x}^+|^2 dt' \approx \frac{\mathrm{e}^2 \omega_0^2}{3\pi\epsilon_0 c^3} \int_{t_1}^{t_2} |\dot{x}^+|^2 dt' \tag{2.13}$$

where in the last equality we use $x^+(t) = x_0^+ e^{-i\omega t}$ and we can make the approximation $\omega \approx \omega_0$ which implies that the atom is driven close to resonance.

Using equation (2.13), we get a classical expression for the damping coefficient

$$\gamma = \frac{\mathrm{e}^2 \omega_0^2}{6\pi m \epsilon_0 c^3}. \tag{2.14}$$

Although this classical result for the spontaneous emission rate is not strictly correct, it will help to patch our classical expressions for radiative and dipole force to create their semi-classical counterpart.

2.1.3 Quantum Patch: Rate-Equation Model

There is an important feature of the light–matter interaction that this classical model misses; the harmonic oscillator (equation 2.2) can be excited to arbitrarily high amplitudes. We need to introduce some saturation mechanism, this is done using a simple model of the atom that includes discrete energy levels. By discretizing the electromagnetic field the concept of photons emerges, which we can imagine as the energy exchange currency between atoms and light.

However, our next description is not able to reproduce all the phenomena, so the resulting rate equations constitute a sort of "semi-quantum" model of the atom which is enough for our illustrative description.

There are three fundamental interactions between light and atoms which we describe in the following lines. In all cases we will consider only a two-level atom with ground-state energy E_1 and excited-state energy E_2. We will also assume resonant light with frequency $\omega = (E_2 - E_1)/\hbar$.

Absorption (stimulated): This process involves the atom initially being in the ground state. In the absorption process, a photon is destroyed and the atom is promoted to the excited state. More generally, if there are $n + 1$ photons to start with in some resonant mode, after the absorption there will be n photons in the field and the atom will be in the excited state (top panel in figure 2.1).

Stimulated emission: This process involves the atom initially being in the excited state, in the presence of n photons in the resonant mode. After the stimulated-emission event, the atom is demoted to the ground state and the field is left with $n+1$ photons. This emitted photon has the same phase and direction as the incident photons. This process can be seen as a time-reversed stimulated absorption, just with the difference that for the case of stimulated emission beginning with $n = 0$ photons is not possible although absorption ending with $n = 0$ photons is possible (central panel in figure 2.1).

Spontaneous Emission: This process is much like stimulated emission, the atom is demoted to the ground state and a photon is emitted, but the presence of any field is not intrinsically necessary (it can still occur in presence of a field). Also, the phase and direction associated with the emitted photon is random. The excited state of the atom lasts for a characteristic natural time before transitioning to the ground state (bottom panel in figure 2.1).

Now, considering an ensemble of two-level atoms interacting with light. Let N_i denote the number density of atoms with energy E_i. Then the Einstein rate equation for the excited state is

$$\frac{dN_2}{dt} = -A_{21}N_2 - B_{21}\rho(\omega)N_2 + B_{12}\rho(\omega)N_1 \tag{2.15}$$

where $\rho(\omega)$ is the energy density of the electromagnetic field in the frequency interval ω to $\omega + d\omega$. The first term corresponds to spontaneous emission, reducing the excited-state population even in the absence of any field. The second and third terms are proportional to $\rho(\omega)$ and correspond to stimulated emission and absorption respectively.

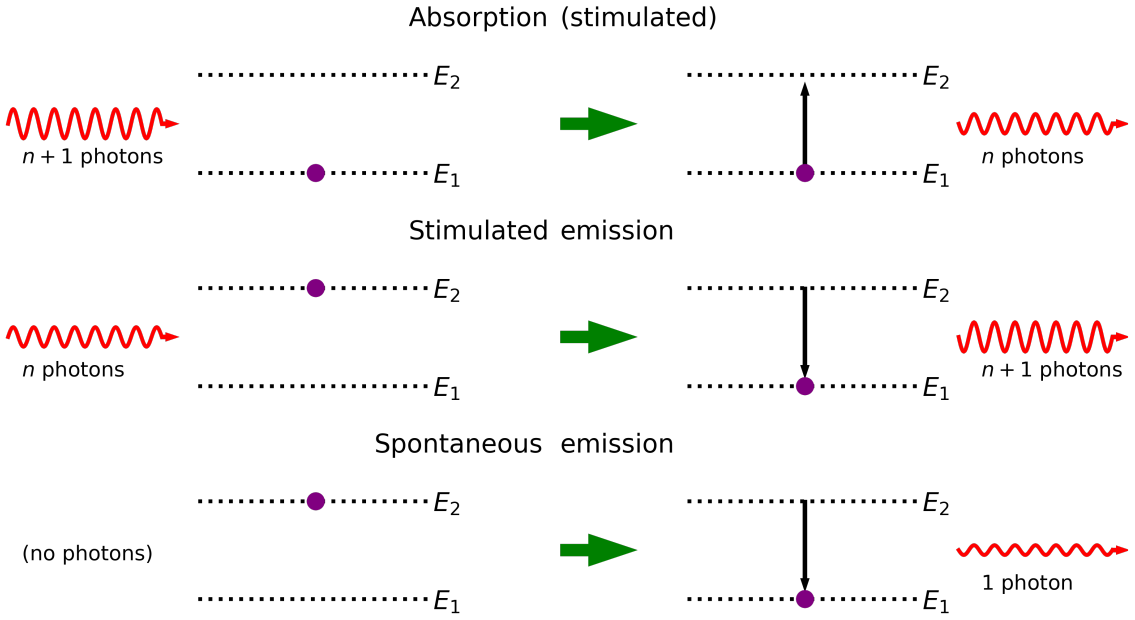

Figure 2.1: Schematic picture for the three fundamental interactions between light (red wavepacket) and atoms (purple dots). Stimulated absorption (top panel); stimulated emission (middle panel), and spontaneous emission (bottom panel). See text for details.

By historical reasons [49], the constant A_{21} is called Einstein A coefficient. Here represents the rate at which energy is lost from the atom and we can identify $A_{21} = \gamma$ as the damping rate in the Lorentz atom model (in the next chapter it will be labeled and referenced as Γ). The constants B_{21} and B_{12} are called Einstein B coefficients.

A steady-state occurs when the change in the number of excited atoms is zero $dN_2/dt = 0$, then the rate equation (2.15) gives

$$\frac{N_2}{N_1} = \frac{B_{12}\rho(\omega)}{A_{21} + B_{21}\rho(\omega)}. \tag{2.16}$$

This steady-state can be thought of as thermodynamic equilibrium between the atoms and the radiation field. Then the ratio N_2/N_1 can be expressed using distribution of the atoms at equilibrium energy as stated by the Maxwell-Boltzmann statistics, giving

$$\frac{N_2}{N_1} = \frac{e^{-E_2/k_BT}}{e^{-E_1/k_BT}} = e^{-\hbar\omega/k_BT}, \tag{2.17}$$

where we assume that the energy levels E_i are no degenerate. Substituting this at equation (2.16) and solving for $\rho(\omega)$ we get

$$\rho(\omega) = \frac{A_{21}}{B_{21}} \frac{1}{\left(\frac{B_{21}}{B_{12}} e^{\hbar\omega/k_BT} - 1\right)}, \tag{2.18}$$

which is equivalent to the Planck law of blackbody radiation if $B_{21} = B_{12}$ and $\frac{A_{21}}{B_{21}} = \frac{8\pi\hbar}{\lambda^3}$. This tell us that the radiation field can be expressed using the distribution

of photons as stated by the blackbody distribution. Again, all this process is based on thermodynamic equilibrium between the atoms and the radiation field.

Although energy generated by stimulated emission is always at the exact frequency of the field which has stimulated it, the rate equation (2.15) refers only to excitation at the particular optical frequency ω_0 corresponding to the energy of the transition. At frequencies around ω_0 the strength of stimulated (or spontaneous) emission will be decreased according to the so-called line shape $s(\omega)$.

The line shape $s(\omega)$ models the fact that the energy levels have some width, usually described by a Lorentzian function of the form

$$s(\omega) = \frac{1}{\pi} \frac{\gamma/2}{(\omega - \omega_0)^2 + (\gamma/2)^2}. \tag{2.19}$$

Then the term $\rho(\omega)$ needs to be substituted by an integral over ω of the product between $\rho(\omega)$ and $s(\omega)$, but in the case of nearly monochromatic light, $s(\omega)$ is much broader than $\rho(\omega)$, then $s(\omega)$ varies slower over the width of $\rho(\omega)$, giving the integral

$$\rho(\omega) \to \int_0^\infty \rho(\omega) s(\omega) d\omega \approx s(\omega) \int_0^\infty \rho(\omega') d\omega' = s(\omega) I/c, \tag{2.20}$$

where the last integral gives the total energy density of the field, which is equal to the total intensity of the field divided by the speed of light.

Substituting this correction and the Einstein coefficients in the steady-state rate equation (2.16) we obtain

$$\frac{N_2}{N_1} = \frac{1}{\frac{A_{21}}{B_{12}\rho(\omega)} + 1} \equiv \frac{1}{\frac{8\pi\hbar}{\lambda^3} \frac{c}{I s(\omega)} + 1} \tag{2.21}$$

where $2\pi c/\lambda = \omega$. We define the absorption cross-section as $\sigma(\omega) \equiv \gamma\lambda^2 s(\omega)/4$ which we substitute in the steady-state rate equation 2.21 giving

$$\frac{N_2}{N_1} = \frac{1}{\frac{\hbar\omega\gamma}{\sigma(\omega) I} + 1} \tag{2.22}$$

where conveniently we can define the saturation intensity as $I_{sat}(\omega) \equiv \frac{\hbar\omega\gamma}{2\sigma(\omega)}$, obtaining the last expression

$$\frac{N_2}{N_1} = \frac{1}{\frac{2I_{sat}(\omega)}{I} + 1}. \tag{2.23}$$

In the limit in which the intensity is very big, $I \to \infty$, the populations are equal. This points to an important effect that is missed by the Lorentz model as we discussed in the beginning of this section: the atomic saturation. Additionally, we can observe that $N_2/N_1 < 1$ for all the intensities, then there is no population inversion in a steady-state of two-level system, but this is another topic that we do not wish to discuss here.

The absorption cross-section and saturation intensity (at resonance) defined in this section will be useful later, $\sigma_0 \equiv \sigma(\omega_0) = \gamma\lambda_0^2 s(\omega_0)/4 = \lambda_0^2/2\pi$ and

$$I_{sat} \equiv \frac{\hbar\omega_0\gamma}{2\sigma_0}. \tag{2.24}$$

Note that $\sigma_0 = \lambda_0^2/2\pi$ is an average over all possible atomic orientations, since the blackbody distribution (2.18) assumes isotropic radiation. For atomic dipole moments aligned with the field polarization, there is just one privileged direction and the resonant cross section is $\sigma_0 = 3\lambda_0^2/2\pi$ due to the coupling that would normally be "distributed" among three orthogonal directions is concentrated into one.

2.2 Radiation force

We will use the simple two-level atom model presented in the last subsection to describe the radiation force in a semi-classic way. Of course, the real world is more complex; in fact, due to the hyperfine structure, the ground state of alkali atoms is split into two levels, and hence, the D_2 transition can be seen as a Λ-type transition (section 2.2.4).

When an atom in the ground state absorbs a photon, it experiences a linear momentum change associated to the photon momentum. Afterwards, the excited atom decays to the ground state and emits a photon due to spontaneous or stimulated emission. This emission results in a second linear momentum change.

As we commented in the last subsection, the emitted photon by stimulated emission has the same phase and direction as the incident photons, contrary to the case of spontaneous emission, where the phase and direction of the emitted photon is random. Then, considering the repetition of many absorption and emission cycles, we can calculate the average change in the linear moment.

Using a continuous source of light with well-defined wave vector $\mathbf{k}$, the photon absorption leads a change in the atom linear momentum of $\Delta\mathbf{p} = \hbar\mathbf{k}$, the stimulated emission of a photon leads a change in the atom linear momentum of $\Delta\mathbf{p} = -\hbar\mathbf{k}$. However, the average change due to spontaneous emission $\langle\Delta\mathbf{p}\rangle = \mathbf{0}$, because the emission occurs randomly along any direction (figure 2.2). Therefore, after adding the contribution of the absorption and spontaneous emission processes which repeats over and over, the atom acquires momentum $\hbar\mathbf{k}$ on average for each absorption-emission process.

Thus, the rate of momentum transfer $\langle\Delta\mathbf{p}\rangle = \hbar\mathbf{k}$ implies a force called radiation pressure which can be expressed as

$$\mathbf{F}_{rad} = \frac{\hbar\mathbf{k}}{\Delta t} \equiv \hbar\mathbf{k}R_{sc} \tag{2.25}$$

where $\mathbf{k}$ is the incident light wave vector, Δt the amount of time to emit the absorbed photon and it can be related to the photon scattering rate $R_{sc} = 1/\Delta t$. Although this description of the radiation force is an oversimplification and it does not consider several important effects, it presents the big picture of the problem [3].

After this semi-classical explanation, we return to our complete classical treatment. The momentum of the classical field is related to the absorbed power P_{abs} by $F =$

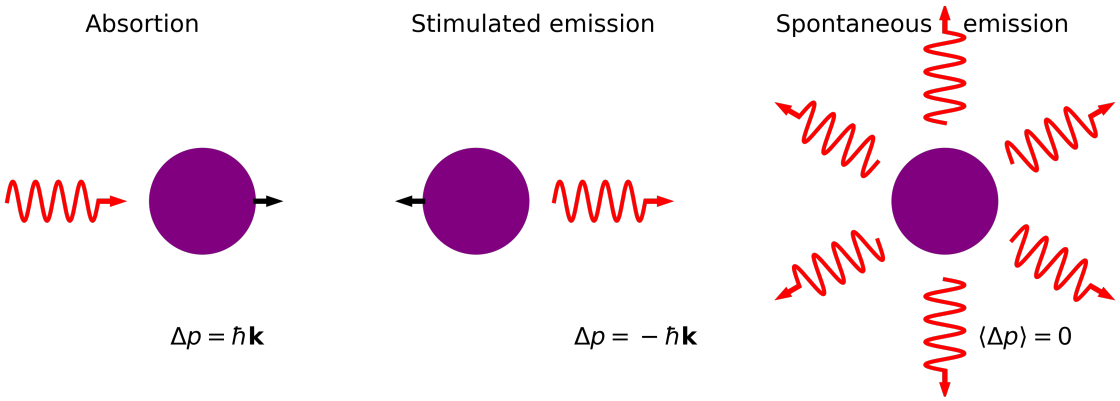

Figure 2.2: Schematic photon-atom interaction. The photon absorption (left panel) leads a change in the atom linear momentum of $\Delta\mathbf{p} = \hbar\mathbf{k}$, the stimulated emission (central panel) of a photon leads a change in the atom linear momentum of $\Delta\mathbf{p} = -\hbar\mathbf{k}$. However, the average change due to spontaneous emission $\langle\Delta\mathbf{p}\rangle = \mathbf{0}$, because the emission occurs in all directions (right part).

$dp/dt = P_{abs}/c$. Due to energy conservation, the absorbed power has to be equal to the radiated power P_{rad} which we already calculated in section 2.1.2. This power radiated by an oscillating dipole P_{rad} is expressed by the equation (2.11).

Rewriting equation (2.11) using the explicit expression $d^+ = \alpha(\omega)E_0^+ e^{-i\omega t}$ from (2.5) and $I = 2\epsilon_0 c|E^+|^2$ we find that

$$P_{rad} = \frac{\omega^4|\alpha(\omega)|^2|E^+|^2}{3\pi\epsilon_0 c^3} = \frac{\omega^4|\alpha(\omega)|^2}{6\pi\epsilon_0^2 c^4} I(\mathbf{r}), \tag{2.26}$$

using the polarizability of equation (2.7), we can write the irradiated power as

$$P_{rad} = \frac{\omega^4 \mathrm{e}^2}{6\pi\epsilon_0^2 c^4 m} \frac{\mathrm{e}^2/m}{\left(\omega_0^2 - \omega^2\right)^2 + \gamma^2\omega^2} I(\mathbf{r}), \tag{2.27}$$

where we recognize the second fraction as the $\mathrm{Im}[\alpha(\omega)]$ divided by a factor $\gamma\omega$. Substituting this we obtain

$$P_{rad} = \frac{\omega^3 \mathrm{e}^2}{6\pi\epsilon_0^2 c^4 m\gamma} \mathrm{Im}[\alpha(\omega)] I(\mathbf{r}) = \frac{\omega^3}{\epsilon_0 c\omega_0^2} \mathrm{Im}[\alpha(\omega)] I(\mathbf{r}) \tag{2.28}$$

where in the last equality we used the expression for γ from equation (2.14).

From here, the photon scattering rate R_{sc} can be defined as the radiated power P_{rad} divided by the photon energy $\hbar\omega$, $R_{sc} = P_{rad}/\hbar\omega$. Again, the physical meaning of this quotient is related to the inverse of the amount of time to emit the absorbed photon, $R_{sc} = 1/\Delta t$. Inserting this into the radiative force expression (2.25) gives

$$\mathbf{F}_{rad} = \frac{\mathbf{k}\omega^2}{\epsilon_0 c\omega_0^2} \mathrm{Im}[\alpha(\omega)] I(\mathbf{r}) \tag{2.29}$$

hence, the radiative force is proportional to the light intensity and the imaginary part of the polarizability $\alpha(\omega)$, as we discussed at the beginning of this chapter.

We can rewrite the expression for the radiative force in a more useful way. First, we use again the polarizability expression from equation (2.7) to find

$$\mathbf{F}_{rad} = \frac{\mathbf{k}\omega^2}{\epsilon_0 c\omega_0^2} \frac{\gamma\omega \mathrm{e}^2/m}{\left(\omega_0^2 - \omega^2\right)^2 + \gamma^2\omega^2} I(\mathbf{r}). \tag{2.30}$$

We need to patch this result with the saturation intensity (2.24), calculated in section 2.1.3 given by

$$I_{sat} \equiv \frac{\hbar\omega_0\gamma}{2\sigma_0} = \frac{\hbar\omega_0\gamma\omega_0^2}{2 \cdot 6\pi c^2}, \tag{2.31}$$

where $\sigma_0 = 3\lambda_0^2/2\pi = 6\pi c^2/\omega_0^2$ is the resonant absorption cross section for an atomic dipole aligned with the field polarization, which is the case because we are considering the power emitted by a dipole (2.11).

Finally, to write this radiative force in a more standard form, we divide and multiply (2.30) by I_{sat}

$$\mathbf{F}_{rad} = \frac{\mathbf{k}\mathrm{e}^2}{m\epsilon_0 c\omega_0^2} \frac{\hbar\omega_0\gamma\omega_0^2}{2 \cdot 6\pi c^2} \frac{\gamma\omega^3}{\left(\omega_0^2 - \omega^2\right)^2 + \gamma^2\omega^2} \frac{I(\mathbf{r})}{I_{sat}}, \tag{2.32}$$

where the constants can be regrouped using expression (2.14) giving

$$\mathbf{F}_{rad} = \frac{\hbar\mathbf{k}}{2\omega_0} \frac{\gamma^3\omega^3}{\left(\omega_0^2 - \omega^2\right)^2 + \gamma^2\omega^2} \frac{I(\mathbf{r})}{I_{sat}} = \frac{\hbar\mathbf{k}}{2\omega_0} \frac{\gamma^3\omega^3}{\left[\left(\omega_0 + \omega\right)\Delta\right]^2 + \gamma^2\omega^2} \frac{I(\mathbf{r})}{I_{sat}}, \tag{2.33}$$

where the last equality is obtained introducing the detuning $\Delta \equiv \omega - \omega_0$. Notice that this force is always positive in the wave vector direction.

After this, some approximations can be taken. Near to resonance $\omega \approx \omega_0$ and $\omega + \omega_0 \approx 2\omega \approx 2\omega_0$, so the radiative force can be written as

$$\mathbf{F}_{rad} = \frac{\hbar\mathbf{k}_0(\gamma/2)^3}{\Delta^2 + (\gamma/2)^2} \frac{I(\mathbf{r})}{I_{sat}}. \tag{2.34}$$

2.2.1 Laser cooling: Optical Molasses

Now let's explore how we can use the radiation-pressure force to cool down an atomic gas [50]. The simplest setup we can consider is an atom moving with velocity v, exposed to identical but counter-propagating laser fields along the velocity direction as shown in figure 2.3.

Using equation (2.34), we have that near resonance, the radiation-pressure force on the atom due to the two fields is

$$F_{mol} = \hbar k(\gamma/2)^3 \left(\frac{1}{\Delta_1^2 + (\gamma/2)^2} - \frac{1}{\Delta_2^2 + (\gamma/2)^2} \right) \frac{I}{I_{sat}}, \tag{2.35}$$

where Δ_i^2 are the effective detunings of the two lasers. The detunings of the two lasers are the same in the laboratory frame, but the idea behind Doppler cooling is

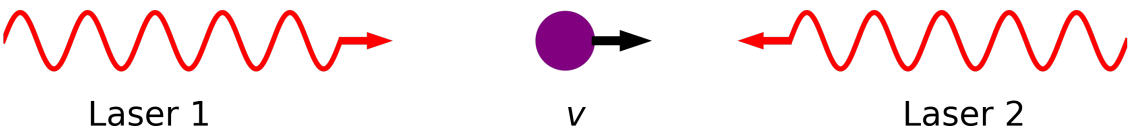

Figure 2.3: One dimension optical molasses scheme. An atom moving with velocity v, exposed to identical but counter-propagating laser fields along the velocity direction.

to tune the lasers below the atomic resonance, so that the beam that opposes the atomic velocity is Doppler shifted into resonance, thus tending to stop the atom.

With the pictured setup of figure 2.3, the frequency of laser 1 is Doppler shifted (red shifted) by $-kv$, while the frequency of laser 2 is Doppler shifted (blue shifted) by $+kv$. Then the corrected detunings are given by

$$\begin{aligned} \Delta_1 &= \Delta - kv \\ \Delta_2 &= \Delta + kv \end{aligned} \tag{2.36}$$

where $\Delta = \omega - \omega_0$ is the detuning in the laboratory frame. Then the force is

$$F_{mol} = \hbar k(\gamma/2)^3 \left(\frac{1}{(\Delta - kv)^2 + (\gamma/2)^2} - \frac{1}{(\Delta + kv)^2 + (\gamma/2)^2} \right) \frac{I}{I_{sat}}. \tag{2.37}$$

For small velocity $kv \ll |\Delta|, \gamma$, we can neglect terms proportional to $(kv)^2$, then

$$\begin{aligned} F_{mol} &\approx \hbar k(\gamma/2)^3 \left(\frac{1}{\Delta^2 - 2\Delta kv + (\gamma/2)^2} - \frac{1}{\Delta^2 + 2\Delta kv + (\gamma/2)^2} \right) \frac{I}{I_{sat}}, \\ &\approx \hbar k(\gamma/2)^3 \left(\frac{2 \cdot 2\Delta kv}{[\Delta^2 + (\gamma/2)^2]^2} \right) \frac{I}{I_{sat}}, \\ &\approx \frac{\hbar k^2 \gamma^3}{2} \frac{\Delta}{[\Delta^2 + (\gamma/2)^2]^2} \frac{I}{I_{sat}} v. \end{aligned} \tag{2.38}$$

Doppler cooling is achieved by tuning the lasers below the atomic resonance, $\Delta < 0$, so the force in equation (2.38) becomes negative, opposing to the velocity direction of the atom. So, the radiative force on atoms of two counter-propagating beams each with equal intensity I, near resonance at $\Delta < 0$ can be written as $F = -\Pi v$ with

$$\Pi = \frac{\hbar k^2 \gamma^3}{2} \frac{|\Delta|}{[\Delta^2 + (\gamma/2)^2]^2} \frac{I}{I_{sat}}. \tag{2.39}$$

This correspond to a viscous force, which is why this configuration is called “optical molasses”.

For implementing a three dimensional optical molasses scheme, we simply combine three of the above one-dimensional setups, one along each axis as shown in figure 2.4.

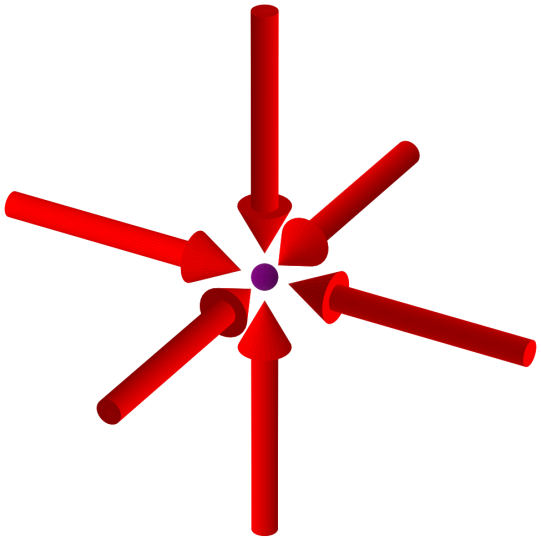

Figure 2.4: Three dimension optical molasses setup scheme. This setup combine three one-dimensional molasses, one along each axis.

Then, the radiative force vector on atoms of three pairs of counter-propagating beams each with equal intensity I, for small velocity $kv \ll |\Delta|, \gamma$ near resonance at $\Delta < 0$ can be written as,

$$\mathbf{F}_{mol} = -\Pi \mathbf{v}. \tag{2.40}$$

2.2.2 Doppler Cooling limit

From the analysis above, we might think that the optical molasses would dampen the speed of the atoms and stop them completely. This, of course, is not possible. Up to now, we have only considered the average cooling force. There are also fluctuations of the cooling force, which become relevant as the temperature decreases. These fluctuation eventually become a source of heating, which lead to a lower temperature limit that can be achieved. This limit is known as Doppler temperature limit [51]. We will now derive the Doppler limit for the optical molasses.

Looking at the variance of the velocity distribution

$$\frac{d}{dt}\langle v^2 \rangle = 2\langle \mathbf{v} \cdot \frac{d\mathbf{v}}{dt} \rangle = \frac{2}{m}\langle \mathbf{v} \cdot \frac{d\mathbf{p}}{dt} \rangle = \frac{2}{m}\langle \mathbf{v} \cdot \mathbf{F}_{mol} \rangle = -\frac{2\Pi}{m}\langle v^2 \rangle \tag{2.41}$$

where the angle brackets denote an ensemble average and we use the force expression from equation(2.40) for small velocities. According to this differential equation, the velocity damps to zero, therefore this rate is associated to cooling.

Now we heuristically include force fluctuations, since we don't have the complete description because we are working with a semi-classical model. As we discussed at

the beginning of this section (2.2), when an atom absorbs a photon, it receives a momentum "kick" $\hbar\mathbf{k}$, followed by a spontaneous emission process which leads to a second momentum "kick" with magnitude $\hbar k$ but at a random direction. However, for 3D optical molasses, the absorption process can occur with the same probability along the direction of any of the six laser beams, which means that the direction of the first momentum kick $\hbar k$ is also random.

Therefore, a scattering event generates two momenta kicks, each of them increases the atom velocity by $\hbar k/m$. Then $\langle v^2\rangle$ has a total change of $2\hbar^2k^2/m^2$ at each scattering event. The rate at which this scattering event occurs is nothing else than the scattering rate R_{sc} defined in (2.29). Using the R_{sc} definition and the radiative force near resonance (2.34) we obtain

$$R_{sc} = \frac{(\gamma/2)^3}{\Delta^2 + (\gamma/2)^2}\frac{I}{I_{sat}} \tag{2.42}$$

for each laser beam. As we have six beams, the $\langle v^2\rangle$ increases at the total rate

$$12R_{sc}\frac{\hbar^2k^2}{m^2}, \tag{2.43}$$

which is called the "heating rate" because, in contrast to the cooling rate (2.41) this term is always positive and, consequently, it increments the kinetic energy of the atoms.

The heating rate can be included by hand in equation (2.41), so we obtain

$$\frac{d}{dt}\langle v^2\rangle = -\frac{2\Pi}{m}\langle v^2\rangle + 12R_{sc}\frac{\hbar^2k^2}{m^2}, \tag{2.44}$$

where we can clearly see the competition between the cooling mechanism, corresponding to the first term, and the heating rate, depicted in the second term. A steady state is reached when $\frac{d}{dt}\langle v^2\rangle = 0$, where the heating and cooling rates equilibrate, resulting in

$$\langle v^2\rangle = \frac{3\hbar}{2m}\frac{\Delta^2 + (\gamma/2)^2}{|\Delta|}. \tag{2.45}$$

The corresponding temperature to this equilibrium kinetic can be obtained by the expression $m\langle v^2\rangle/2 = 3k_BT/2$. In this way, we obtain the minimal temperature reached by the optical molasses at detuning Δ

$$k_BT = \frac{\hbar}{2}\frac{\Delta^2 + (\gamma/2)^2}{|\Delta|}, \tag{2.46}$$

which has a minimum at $\Delta = -\gamma/2$, corresponding to the minimum expected temperature for Doppler cooling, the Doppler temperature T_D

$$k_BT_D = \frac{\hbar\gamma}{2}. \tag{2.47}$$

Using the D_2 line of ^{6}Li, where $\gamma = 2\pi \times 5.87$ MHz, the Doppler temperature is $T_D = 140\mu$K. This temperature is still very high to achieve quantum degeneracy. We can see this through the phase space density (PSD) defined in equation 1.8 with the density at the experiment n in the molasses (section 3.2.1) obtaining PSD= $2 \cdot 10^{-7} \ll 1$.

For this reason, additional cooling techniques must be implemented. In our experiment we employ the sub-Doppler gray molasses cooling technique (see section 2.2.5) and the evaporative cooling technique (see section 2.3.4), which make possible to increase the phase space density of the gas until the quantum regime is reached.

2.2.3 Magneto-Optical Trap

Optical molasses cools the atoms by means of a viscous force, however, this force does not spatially confine the sample. To confine the atoms, it is necessary to add an extra magnetic field to the three-dimensional optical molasses. This arrangement is called "Magneto-Optical Trap" (MOT), it was theoretically proposed by Jean Dalibard in 1986 and experimentally implemented by David E. Pritchard in 1987 [52].

It is created by adding to the 3D optical molasses a magnetic field gradient created by two opposed current loops in "anti-Helmholtz" configuration as shown in figure 2.5, so the magnetic field is zero in the center of the trap and its intensity increases linearly along any radial direction. Dalibard's proposal also modifies the polarization of the molasses beam, by using opposite circularly polarized light in each set of counter-propagating beams (the so-called $\sigma^+ - \sigma^-$ configuration), instead of the linearly polarized light that we considered in our previous discussion.

To understand how this trap works, we consider first the 1D case of two counter-propagating red-detuned beams in presence of a magnetic field as shown in figure 2.6. The two counter-propagating beams have opposite circular polarization σ^+ and σ^-, and the magnetic field is linear along the axis $\mathbf{B}(0,0,z) = bz\hat{\mathbf{z}}$ and it is null at the center of the trap. Here b is the magnetic gradient along the z-direction.

The presence of a magnetic field introduces a shift in the energy levels of the atom due to the linear Zeeman effect. This effect occurs due to the coupling of the atomic magnetic moment $\mu \neq 0$ to the magnetic field. The Zeeman shift can be expressed as $\Delta E = -\mu \cdot \mathbf{B} = -m_j g_j \mu_B B(z)$ where g_j are the Landé factors; j is the total angular momentum of the atom, m_j is its projection along the quantization axis and can take the values $-j, -j+1, ..., j-1, j$.

This Zeeman shift is shown in figure 2.6 by the dotted lines. The linear behavior is due to the magnetic field, which is also linear, $B_z(z) = bz$, as we already stated.

The energy separation between two atomic levels is then $\Delta E_{j \to j'} = -(m_{j'} g_{j'} - m_j g_j)\mu_B B(z) = -\delta\mu B(z)$, which introduces a new contribution to the detuning that depends of the position z

$$\Delta_B(z) = \frac{-\delta\mu B(z)}{\hbar} = \frac{-\delta\mu bz}{\hbar}, \tag{2.48}$$

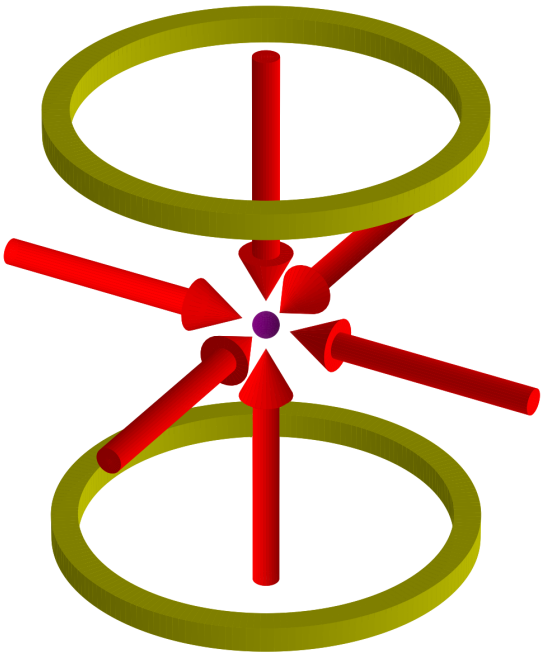

Figure 2.5: The MOT setup scheme. The setup combine a 3D optical molasses with a linear magnetic field (whose zero is at the center of the trap) created by two opposed current loops. In this 3D optical molasses, each counter-propagating beam uses circularly polarized light σ^+ and σ^- respectively, instead linearly polarized.

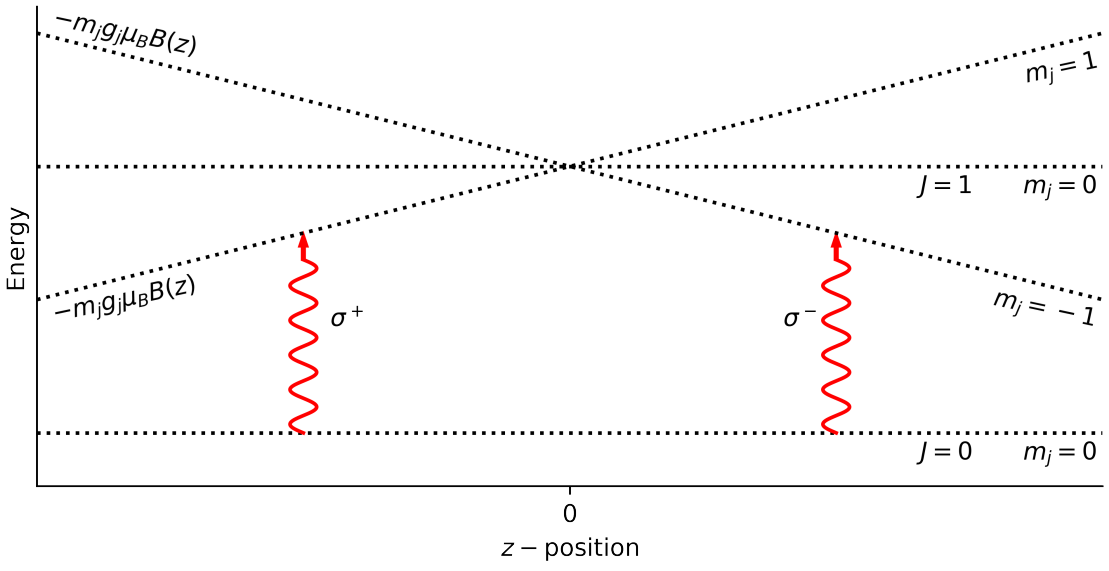

Figure 2.6: The operating principle of the one dimensional MOT for two-level atom, transition $J = 0 \rightarrow J = 1$. The scheme represents the Zeeman shift $\Delta E = -m_j g_j \mu_B B(z)$ by the dotted lines. The lineal behavior is due to the magnetic field, which is linear $B_z(z) = bz$. The red-detuned circularly polarized beams (σ^+ and σ^-) are represented by the red wavy arrows.

which has to be considered when calculating the radiation pressure force. The radiation pressure force in the 1D molasses equation (2.35) is the same except for the corrected detunings of the form

$$\begin{aligned} \Delta_1 &= \Delta - kv - \Delta_B(z) \\ \Delta_2 &= \Delta + kv + \Delta_B(z) \end{aligned} \tag{2.49}$$

where $\Delta = \omega - \omega_0$ is the detuning in the laboratory frame, kv the Doppler shift and $\Delta_B(z)$ the Zeeman shift. For small velocity and small Zeeman shift $kv \ll |\Delta|, \gamma$ and $\Delta_B(z) \ll |\Delta|, \gamma$, we can neglect terms of the order $(kv)^2$, $\Delta_B(z)^2$ and $kv \cdot \Delta_B(z)$; then, following equation (2.38) the force that the atoms experience in the MOT is

$$F_{MOT} \approx \frac{\hbar k^2 \gamma^3}{2} \frac{\Delta}{[\Delta^2 + (\gamma/2)^2]^2} \frac{I}{I_{sat}} \left(kv + \frac{\delta \mu b z}{\hbar} \right). \tag{2.50}$$

When $\Delta < 0$, this force can be written as $F_{MOT} = -\Pi v - \mathrm{P} z$ with Π as in equation (2.39) and $\mathrm{P} = \frac{\delta \mu b z}{k\hbar} \Pi$. Similarly to the case of the optical molasses, Π corresponds to the coefficient of the viscous term of the force, which is responsible for cooling the atoms, and P corresponds to the coefficient of the restorative term, that confines the atoms near the center of the trap.

2.2.4 Repumping

Up to now, we have considered the atom as a two-level system. However, to correctly implement the laser cooling techniques, we need to consider the hyperfine structure of the atoms. As mentioned in section 2.2, the ground state of alkali atoms (such as lithium) is split into two different levels, which we denote as $|1\rangle$ and $|2\rangle$. In this way, the D_2 transition can be better approximated as a Λ-type transition with an excited state that we denote as $|3\rangle$.

Now, if we set the cooling transition between levels $|1\rangle$ and $|3\rangle$, it might happen that the excited state decays into the state $|2\rangle$, and such atom will no longer interact with the cooling light, escaping in this way from the cooling cycle.

This problem can be solved by introducing a second light frequency, corresponding to the transition between the states $|2\rangle$ and $|3\rangle$ as shown in figure 2.7. The addition of this second frequency simply guarantees that the atoms are kept in the cooling cycle. These two frequencies are known as the cooling frequency, for the main frequency, and the repumper frequency, for which it "repumps" the atoms back into the cooling cycle. The light is red detuned by $\Delta = \omega - \omega_0$, necessary for achieving Doppler cooling.

In the experiment, we need the repumper frequency to correctly implement the 3D optical molasses and the magneto-optical trap.

2.2.5 sub-Doppler cooling

All the cooling mechanisms that we have considered up to this point are Doppler limited, and for the case of ^{6}Li, the lowest achievable temperature is $T_D \approx 140\mu$K.

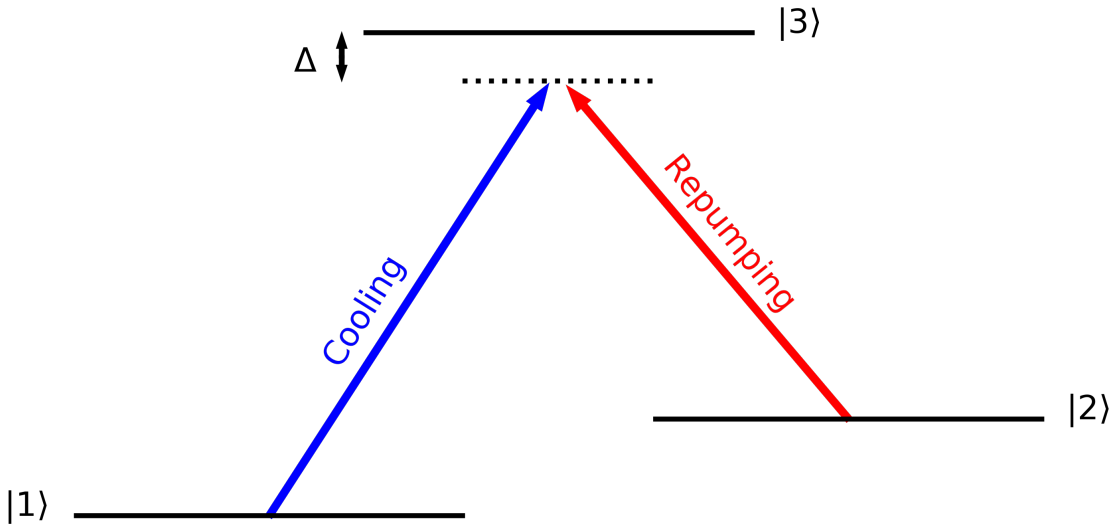

Figure 2.7: Simplified scheme of D_2 Λ transition presented in figure 3.4. The first $|1\rangle$ and second $|2\rangle$ ground states correspond to the lowest energy hyperfine states of ^{6}Li, $2^2S_{1/2}(\mathrm{F} = 3/2)$ and $2^2S_{1/2}(\mathrm{F} = 1/2)$ respectively. The excited state $|3\rangle$ correspond to the level $2^2P_{3/2}$ of D_2 transition which cannot be resolved into hyperfine states. The $\Delta = \omega - \omega_0$ correspond to the detuning to the red of the cooling and repumper frequencies.

Although the first experiments applying optical molasses seemed to be in agreement with this limit, in 1988 the group of W. D. Phillips [53] unexpectedly observed sub-Doppler temperatures in a dilute gas of ^{40}Na. For this species, the Doppler limit is of the order of 240 μK, however, in their experiment a much lower temperature of 43 ± 20 μK was attained.

In 1989, J. Dalibard and C. Cohen-Tannoudji [54] theoretically showed the existence of an additional cooling mechanism originated by the existence of polarization gradients in the optical molasses, this mechanism is known as the Sisyphus effect. Indeed, the Sisyphus effect is able to explain the results obtained by Phillips et.al. [53]. For many atomic species, Sisyphus cooling applied on the D_2 transition is widely used as standard sub-Doppler cooling technique.

However, for this technique to work properly, it is necessary that all the energy levels involved in the cooling cycle are well resolved. This is not the case with the D_2 transition of ^{6}Li, where the hyperfine separation of the levels of the excited state is smaller than the natural linewidth of the transition (such separation is of the order of 4.5 MHz, while the natural linewidth of the transition is of the order of 5.8 MHz). For this reason, standard Sisyphus cooling techniques cannot be applied in our experiment.

Instead, we employ a different sub-Doppler technique known as "gray molasses" [55], which allows to reach in an efficient way temperatures as low as $T \approx 40\mu$K. This cooling scheme is based on the D_1 transition and also employs a Λ-type three-level transition, as shown in figure 2.8.

The gray molasses combines two physical process, Sisyphus cooling and velocity-

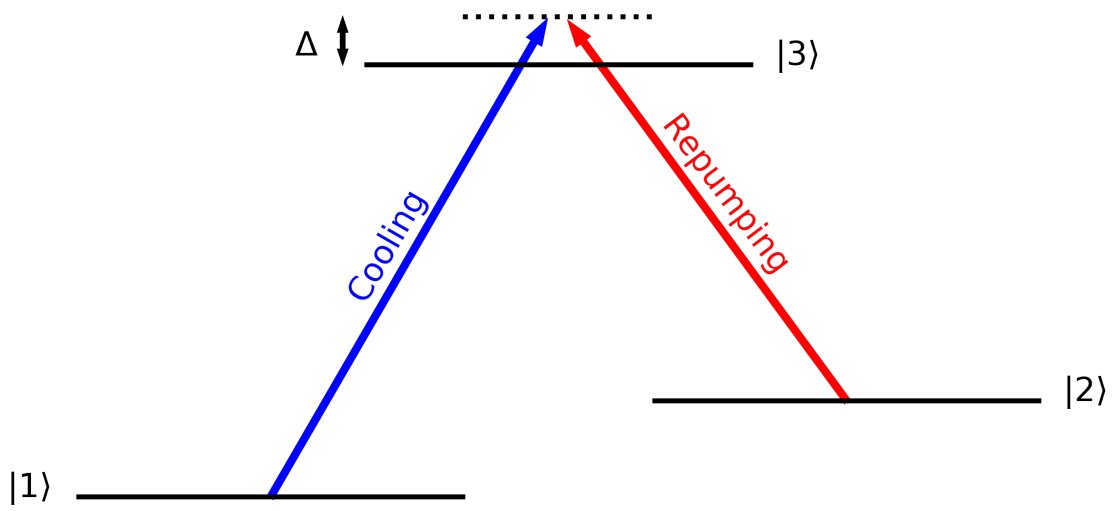

Figure 2.8: Simplified scheme of D_1 Λ transition presented in figure 3.4. The first $|1\rangle$ and second $|2\rangle$ ground states correspond to the lowest energy hyperfine states of ^{6}Li, $2^2S_{1/2}(\mathrm{F} = 3/2)$ and $2^2S_{1/2}(\mathrm{F} = 1/2)$ respectively. The excited state $|3\rangle$ corresponds to the level $2^2P_{1/2}(\mathrm{F'} = 3/2)$ of D_1 transition. The $\Delta = \omega - \omega_0$ corresponds to the detuning (to the blue, in this case). The labels "cooling" and "repumper" are inherited from the D_2 notation.

selective coherent population trapping (VSCPT) [56]. These will be explained below.

Gray molasses cooling is based on the fact that in a three-level transition, it is possible to create dressed states as result of special quantum superpositions between the two ground state levels $|1\rangle$ and $|2\rangle$. In our case, the dressed states of interest are the so-called dark $|\Psi_D\rangle$ and bright $|\Psi_B\rangle$ states. In presence of light, the bright state $|\Psi_B\rangle$ experience a energy shift which depends of the light intensity and polarization. On the other hand, the dark state $|\Psi_D\rangle$ is not sensible to light. That's why they are called dark and bright states. Exploiting this difference is the main idea behind the gray molasses cooling mechanism.

Figure 2.9 shows a simplified scheme of this technique. Using counter-propagating beams with opposite circular polarization (configuration $\sigma^+ - \sigma^-$ which we already have thanks to the MOT configuration), we can create a spatial polarization gradient. Consequently, the light shift experienced by the bright states is spatially modulated [54]. Atoms in the bright state moving along the polarization gradient have to convert their kinetic energy into potential energy in order to climb up the potential hills (left part of figure 2.9). On top of the hills, where the light shift is maximal, it is most probable for the atoms to absorb a photon and populate the excited state.

Once an atom is in the excited state, it has two decay possibilities. On the one hand, the atom might decay into the bright state. In this case, the atoms simply restarts the process, moving along the polarization gradient without any change in its kinetic energy. On the other hand, if the atom decays in the dark state, it will leave the cooling cycle but it will also have lost part of its kinetic energy due to having previously reached the maximum potential energy in the polarization gradient. Now,

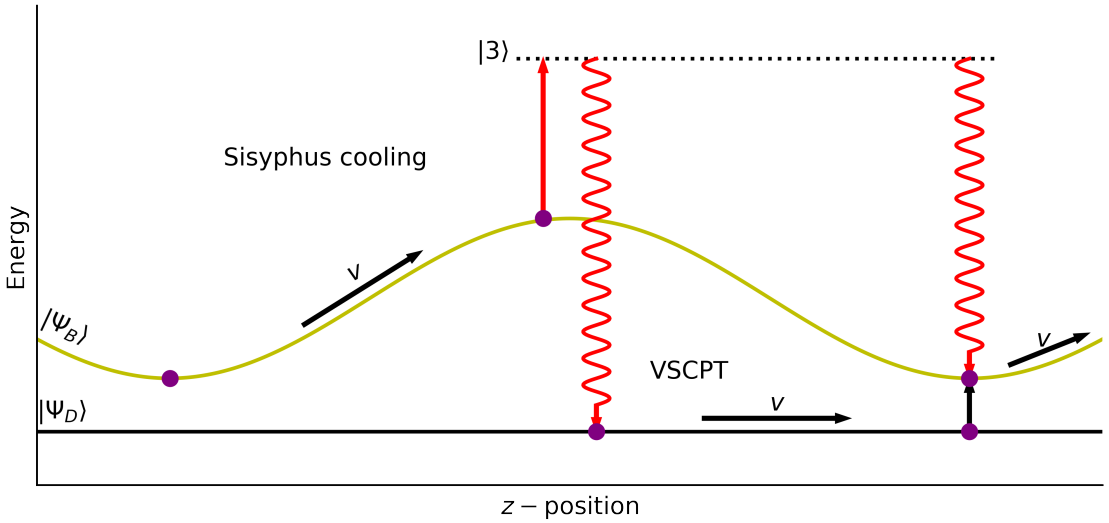

Figure 2.9: One dimension gray molasses cooling schema. There are three states, excited $|3\rangle$, bright $|\Psi_B\rangle$ and dark $|\Psi_D\rangle$. Atoms in bright state have to convert their kinetic energy into potential energy, in order to climb up the potential hills. In the top of the hill, photon absorption is more probable. After photon absorption, the atom reach the excited state, which can decay into two options. If atom decays into bright state, the process can restart, calling Sisyphus cooling to this process. If the atom decays into dark state, it can transferred to the bright state using atom velocity due to VSCPT. This return the atom to the cooling cycle.

to keep this process going, the atom in the dark state has to transition back to the bright state, since this transition cannot occur through absorption of light, the transference is achieved using atomic motion (as illustrated in the right part of figure 2.9). In this way, the atom restarts a new cooling cycle but with less initial kinetic energy, in a similar fashion as the standard Sisyphus cooling mechanism.

Now, the cooling mechanism of gray molasses is so efficient because the probability of this last transition from the dark to the bright state turns out to be proportional to the square of the speed of the atom, in this way, the atom will remain permanently in the dark state (abandoning consequently the transition cycles) only when its speed is very small, leading to samples with very low temperature. The latter process is called velocity-selective coherent population trapping (VSCPT) [56].

In other words, after many cooling cycles, the atoms will accumulate in the dark state with a velocity close to zero. At this point, the probability of transition to the bright state vanishes. Although VSCPT does not have a theoretical limit on the minimum speed that can be reached, in practice, the experimental imperfections of the polarization gradient fields will determine a lower limit on temperature.

The description here presented can be extended to the 3D case. In our experiment, gray molasses is a very important cooling stage since allows to decrease the temperature way below the Doppler limit, reaching values as low as $T = 40$ μK. As will be shown in section 3.2.1, after the gray molasses process the PSD of our sample (equation 1.8) presents an important increase to the order of 1×10^{-6}. At his point, the sample is ready to be transferred into a conservative optical dipole trap where

the very last cooling stage, the evaporative cooling technique, can be applied.

2.3 Dipole force

As discussed in the previous section, after the Doppler and sub-Doppler cooling mechanisms, the temperature of the sample is of the order of tens of microkelvin, which is still few orders of magnitude above the quantum degeneracy temperature, of the order of hundreds of nanokelvin.

In order to implement the last cooling stage, it is necessary to transfer the atoms into a conservative potential where there is no energy exchange between the atoms and the electromagnetic field. This is achieved by using light very far-detuned from atomic resonances, so the atoms will not absorb the light but still interact with its electric field. This interaction is used to create such a conservative potential.

The associated mechanical force to this conservative potential is known as optical dipole force and we devote this section to its description. In particular, at the end of this section, we explain how the last cooling stage is implemented by dynamically reducing the depth of the conservative potential, the so-called evaporative cooling technique.

When a external electromagnetic field interacts with an atom, its electric field induces an electric dipole moment in the atom given by $\mathbf{d} = \alpha\mathbf{E}$ as in (2.6). The potential energy of the induced dipole can be written as

$$U_{dip} = -\frac{1}{2}\mathbf{d}\cdot\mathbf{E} \tag{2.51}$$

where the $1/2$ factor appears because we are considering an *induced* electric dipole rather than a permanent one, so the potential energy can be expressed as $U_{dip} = -\int_0^E \mathbf{d}\cdot d\mathbf{E}' = -\int_0^E \alpha\mathbf{E}'\cdot d\mathbf{E}' = -\frac{1}{2}\alpha E^2$. Writing the potential in terms of the notation employed in (2.1) we get,

$$U_{dip} = -\frac{1}{2}\left(\mathbf{d}^+ + \mathbf{d}^-\right)\cdot\left(\mathbf{E}^+ + \mathbf{E}^-\right), \tag{2.52}$$

we know that $\mathbf{E}^\pm \sim e^{\pm i\omega t}$ and $\mathbf{d}^\pm \sim e^{\pm i\omega t}$, so in Eq. (2.52) there are terms of the form

$$\mathbf{d}^\pm\cdot\mathbf{E}^\pm \sim e^{\pm 2i\omega t}, \tag{2.53}$$

which rotate at twice the optical frequency (terahertz), which is too fast for the atoms to mechanically respond. So we will neglect those terms and keep terms of the form

$$\mathbf{d}^\pm\cdot\mathbf{E}^\mp \sim 1, \tag{2.54}$$

in consequence, the potential energy is rewritten as

$$\begin{aligned} U_{dip} &= -\frac{1}{2}\mathbf{d}^+ \cdot \mathbf{E}^- - \frac{1}{2}\mathbf{d}^- \cdot \mathbf{E}^+ \\ &= -\frac{1}{2}\left[\alpha(\omega)\mathbf{E}^+\right] \cdot \mathbf{E}^- - \frac{1}{2}\left[\alpha^*(\omega)\mathbf{E}^-\right] \cdot \mathbf{E}^+ \\ &= -Re\left[\alpha(\omega)\right]|E^+|^2. \end{aligned} \tag{2.55}$$

Using that the intensity of the electric field in vacuum is $I = \frac{\epsilon_0 c}{2}|E_0|^2 = 2\epsilon_0 c|E^+|^2$ and considering that $E^+(\mathbf{r})$ is a function that slowly varies spatially, the last equation in terms of the intensity is

$$U_{dip} = -\frac{1}{2\epsilon_0 c}\mathrm{Re}\left[\alpha(\omega)\right] I(\mathbf{r}). \tag{2.56}$$

So, the spatial dependence of the potential is determined by the light intensity $I(\mathbf{r})$. The corresponding force is given by the gradient of the potential energy,

$$\mathbf{F}_{dip} = -\nabla U_{dip} = \frac{1}{2\epsilon_0 c}\mathrm{Re}\left[\alpha(\omega)\right] \nabla I(\mathbf{r}). \tag{2.57}$$

hence, the dipole force depends on the gradient of the intensity and on the real part of polarizability $\alpha(\omega)$, as we discussed at the beginning of this chapter.

Returning to the discussion of the dipole potential at equation (2.56), we can substitute the expression for the polarizability from equation (2.7) and write the dipole potential as

$$U_{dip} = \frac{-\mathrm{e}^2}{2m\epsilon_0 c}\frac{\omega_0^2 - \omega^2}{\left(\omega_0^2 - \omega^2\right)^2 + \gamma^2\omega^2} I(\mathbf{r}). \tag{2.58}$$

Using again the detuning $\Delta \equiv \omega - \omega_0$, we can write the dipole potential as

$$U_{dip} = \frac{\mathrm{e}^2}{2m\epsilon_0 c}\frac{(\omega_0 + \omega)\,\Delta}{\left[(\omega_0 + \omega)\,\Delta\right]^2 + \gamma^2\omega^2} I(\mathbf{r}). \tag{2.59}$$

where the sign of the dipole potential is determined only by the detuning of the field from the atomic resonance, because everything in this expression is necessarily positive excepting the detuning Δ in the numerator.

In the case of positive detuning ($\omega > \omega_0$) the dipole potential is positive $U_{dip} > 0$ and we say that the potential is blue-detuned. On the other hand, in the case of negative detuning ($\omega < \omega_0$) the dipole potential is negative $U_{dip} < 0$ and we say that the potential is red-detuned. Therefore, a tightly focused blue-detuned Gaussian beam will repel atoms, forming a potential barrier, while a red-detuned beam will attract atoms, forming a potential well.

It is convenient to express this result in terms of the saturation intensity from equation (2.24),

$$I_{sat} \equiv \frac{\hbar\omega_0\gamma}{2\sigma_0} = \frac{\hbar\omega_0\gamma\omega_0^2}{2 \cdot 6\pi c^2}, \tag{2.60}$$

where $\sigma_0 = 3\lambda_0^2/2\pi = 6\pi c^2/\omega_0^2$ is the resonant absorption cross section for an atomic dipole moment aligned with the field polarization, which is the case because we are working with an induced dipole.

Finally, to write this dipole potential in more standard form, we divide and multiply (2.59) by I_{sat}

$$U_{dip} = \frac{\hbar\omega_0\gamma\omega_0^2}{2\cdot 6\pi c^2}\frac{\mathrm{e}^2}{2m\epsilon_0 c}\frac{(\omega_0+\omega)\,\Delta}{[(\omega_0+\omega)\,\Delta]^2+\gamma^2\omega^2}\frac{I(\mathbf{r})}{I_{sat}}. \tag{2.61}$$

where the constants can be regrouped using γ from expression (2.14) resulting in

$$U_{dip} = \frac{\hbar\omega_0\gamma^2}{4}\frac{(\omega_0+\omega)\,\Delta}{[(\omega_0+\omega)\,\Delta]^2+\gamma^2\omega^2}\frac{I(\mathbf{r})}{I_{sat}} = \frac{\hbar\omega_0\gamma^2}{4}\frac{1/\,(\omega_0+\omega)\,\Delta}{1+\gamma^2\omega^2/\,[(\omega_0+\omega)\,\Delta]^2}\frac{I(\mathbf{r})}{I_{sat}}, \tag{2.62}$$

where in the last equality we rearrange the term to make clear that we are considering that the light is very far away from resonance ($|\Delta| \gg \gamma$). For this reason, we can neglect terms of order γ^2/Δ^2, giving

$$\begin{aligned} U_{dip} &= \frac{\hbar\omega_0\gamma^2}{4}\frac{1}{(\omega_0+\omega)\,\Delta}\frac{I(\mathbf{r})}{I_{sat}} \\ &= \frac{\hbar\gamma^2}{8}\left(\frac{1}{\Delta}-\frac{1}{\omega_0+\omega}\right)\frac{I(\mathbf{r})}{I_{sat}}. \end{aligned} \tag{2.63}$$

Additionally if $|\Delta| \ll \omega_0+\omega$, we can make the so-called rotating-wave approximation and neglect the second counter-rotating term, obtaining a simple formula

$$U_{dip} = \frac{\hbar\gamma^2}{8\Delta}\frac{I(\mathbf{r})}{I_{sat}} \tag{2.64}$$

and consequently,

$$\mathbf{F}_{dip} = -\frac{\hbar\gamma^2}{8\Delta}\frac{\nabla I(\mathbf{r})}{I_{sat}}. \tag{2.65}$$

As we can see, the dipole force is directly proportional to the gradient of the intensity of the light. Broadly speaking, if we focus a red-detuned laser beam using a lens, the focused light is able to create an atom trapping force called optical dipole trap (ODT) [57]. This kind of traps are also known as "far-off resonance trap" (FORT), or as "optical tweezers".

2.3.1 Scaling; Radiative vs dipole force in the ODT

As we concluded in last section, the ODT is created by a focused, red-detuned laser beam. But as we discussed in subsection 2.2.2, a laser beam has an associated heating rate. Therefore, it is reasonable to think that as the atoms scatter the photons from the ODT, they also heat up until they escape from the trap. This

effect is actually substantially suppressed by the fact that the light is very far away from resonance ($|\Delta| \gg \gamma$).

To show this, let us consider the the scaling between the scattering rate (2.42) and the dipole potential (2.64) associated to the radiative and dipole force, respectively, when the detuning of the trap is very big $|\Delta| \gg \gamma$.

The dipole potential at $|\Delta| \gg \gamma$ correspond to (2.64). We use the scattering rate because it is directly related to the heating of the atoms due to the random nature of photon absorption-emission as we discussed in subsection 2.2.2. Then, using the equation (2.42) we obtain

$$R_{sc} = \frac{(\gamma/2)^3}{\Delta^2 + (\gamma/2)^2} \frac{I(\mathbf{r})}{I_{sat}} = \frac{(\gamma/2)^3/\Delta^2}{1 + (\gamma/2)^2/\Delta^2} \frac{I(\mathbf{r})}{I_{sat}}, \tag{2.66}$$

where in the last equality we rearrange the terms to took easily the $|\Delta| \gg \gamma$ approximation. Then, taking the limit in which $(\gamma/\Delta)^2 \ll 1$ we obtain

$$R_{sc} = \frac{\gamma^3}{8\Delta^2} \frac{I(\mathbf{r})}{I_{sat}}. \tag{2.67}$$

Then the scattering rate and dipole potential scale as

$$R_{sc} \propto \frac{I}{\Delta^2}; \quad U_{dip} \propto \frac{I}{\Delta} \tag{2.68}$$

so the scattering rate decreases much faster than the potential depth as the detuning Δ increases, these are important considerations in the design of an optical dipole trap. For a given potential depth, the scattering rate (heating) can be made very small by making the detuning Δ large. The resulting decrease in trap depth is compensated by increasing the intensity of the ODT laser beam.

For example, in our experimental setup, the laser that generates the ODT has a wavelength of 1070nm, while the D-line wavelength for ^{6}Li is of the order of 671 nm. This translates into a detuning of $\Delta \approx 0.6\omega_0$. The focused infrared laser beam for our ODT has a beam waist of 50 μm ($1/e^2$ radius). To transfer the atoms from the sub-Doopler cooling stage, a trap depth of the order of 1 mK is necessary, for which the power of the ODT laser must be around 140 W.

Despite this incredibly high intensity, because the laser is far from resonance, the ODT has a small heating rate R_{sc} and therefore a long lifetime, on the order of several seconds.

2.3.2 Harmonic approximation

As demonstrated in section 2.3, the dipole force is directly proportional to the gradient of the intensity of the light as presented in equation (2.65), then the atoms tend to remain in the focus of a red-detuned laser beam (ODT). The coldest atoms tend to be at the bottom of the dipole potential (2.64). In this subsection we show how, at very low temperatures, this trapping potential is nearly harmonic, the so-called physicists "hobby-horse" potential.

First, we consider the intensity distribution of a focused circular gaussian beam. By "circular" we mean that the beam has radial symmetry. The propagation direction correspond to the x-direction at the laboratory frame (where the z-direction corresponds to the direction of gravity).

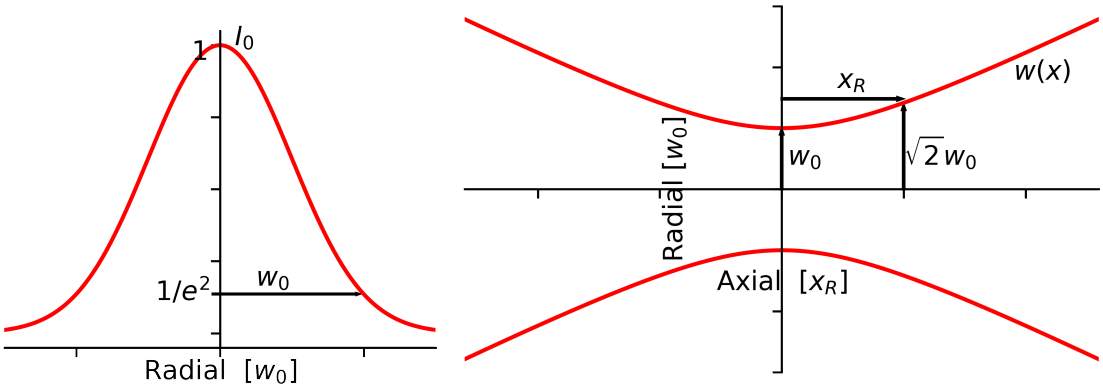

Figure 2.10: Intensity profile of a gaussian beam. At left, the intensity profile (equation 2.69) in a transverse plane at the focus. I_0 is the intensity at the focus, therefore $\frac{2P}{\pi w_0^2}$. Here the $1/e^2$ radius definition is marked by a black arrow, which coincides with beam waist w_0 as the transverse plane is at the focus. At the right, gaussian beam radius $w(x)$ (equation 2.70) as a function of the distance x along the beam. The beam waist w_0 and Rayleigh range x_R are marked by black arrows.

Then, considering that the focus of the beam is at the origin, the intensity of the gaussian beam is given by

$$I(y,z,x) = \frac{2P}{\pi w^2(x)} e^{-2(y^2+z^2)/w^2(x)} \tag{2.69}$$

where P is the power of the laser beam and $w(x)$ is the radius of the beam at position x along the propagation. The radius at position x is defined as the distance from the x-axis to the position where the transverse intensity profile has dropped by a $1/e^2$ factor. The radius $w(x)$ has a functional form given by

$$w(x) = w_0 \sqrt{1 + \left(\frac{x}{x_R}\right)^2}, \tag{2.70}$$

where w_0 is the beam waist and x_R the Rayleigh length. The beam waist ω_0 is the radius of the beam at the focus position (i.e. at $x = 0$) and corresponds to the minimum value of $\omega(x)$. The Rayleigh length $x_R = \pi w_0^2/\lambda$ is the length where the radius of the beam increases by a factor of $\sqrt{2}$ respect the beam waist w_0 and give us the depth of the focus along the beam direction. If the beam is produced by focusing a collimated beam with a lens, $R = w(f) \approx \lambda f/\pi w_0$ is a useful approximation of equation 2.70 which give us an expression to relate the waist, the focal length f and the radius of the collimated beam R.

We need to approximate the intensity distribution from Eq. (2.69) around the focus $(y,z,x) = (0,0,0)$through a Taylor series to obtain a polynomial approximation.

Here we will not present the detailed calculation, but we outline the most important steps.

First, we notice that the first order terms (three of them, one for each spatial variable) are zero at focus. This is because at the beam focus the intensity reaches a maximum value, so the first-order partial derivatives (related to the first order terms) at focus are zero. Therefore, we need to extend the Taylor series approximation to second order terms.

The second order terms are associated to three second-order partial derivatives and six second-order mixed derivatives. The second-order mixed derivatives vanish at focus, while the second-order partial derivatives at focus give $\frac{1}{2}I(0,0,0)(-4/w_0^2)$ for the $y,z-$coordinates and $\frac{1}{2}I(0,0,0)(-2/x_R^2)$ for the $x-$coordinate.

Substituting this second order Taylor series approximation into equation (2.65), the dipole potential can be written as

$$U_{dip}(y,z,x) \approx \frac{\hbar\gamma^2}{8\Delta I_{sat}}\frac{2P}{\pi w_0^2}\left(1-2\frac{y^2+z^2}{w_0^2}-\frac{x^2}{x_R^2}\right) \tag{2.71}$$

which has the form of a harmonic potential $U = U_0 + \frac{1}{2}m(\omega_y^2 y^2 + \omega_z^2 z^2 + \omega_x^2 x^2)$, similar to equation (1.1). The characteristic properties of a harmonic trap are the trap depth U_0 and the trap frequencies ω_i. We will discuss in detail these quantities in the next chapter.

If we compare the harmonic potential with equation (2.71), we find an expression for the trap depth

$$U_0 = \frac{\hbar\gamma^2}{8\Delta I_{sat}}\frac{2P}{\pi w_0^2}, \tag{2.72}$$

and for the trap frequencies

$$\omega_r \equiv \omega_y = \omega_z = \sqrt{\frac{4U_0}{mw_0^2}} \quad \text{and} \quad \omega_x = \sqrt{\frac{2U_0}{mx_R^2}}, \tag{2.73}$$

showing that the radial and axial frequencies are inversely proportional to the beam waist and Rayleigh length, respectively. Another important quantity, that parametrizes the confinement of the trap, is the geometric mean of the trap frequencies, $\bar{\omega} = \sqrt[3]{\omega_x\omega_y\omega_z}$.

In our experiment, the ODT laser has a wavelength of 1070 nm and a beam waist of 50 μm ($1/e^2$ radius),in contrast to the much larger Rayleigh length of 7.34 mm. Since the frequencies are inversely proportional to the trap size, this trap provides a very tight confinement on the radial direction of the beam, in contrast to the axial direction where the confinement is really weak.

The ODT beam power at the end of the evaporative cooling is of the order of 40 mW (see section 2.3.4). At this point, the radial and axial frequencies of the trap are $\omega_r = 2\pi \times 160$ Hz and $\omega_x = 2\pi \times 0.94$ Hz respectively, which correspond to an extremely elongated trap (aspect ratio of the order 1:160). It is desirable to have

extra confinement along the axial direction. As we explain in the following section, we achieve that using an external magnetic field.

2.3.3 Hybrid trap

In order to increase the axial confinement, we add to the optical potential a magnetic curvature that provides a better confinement along the axial direction. To do so, we employ our Feshbach coils, which we set slightly off the Helmholtz configuration to generate a little curvature. Remember that the Feshbach resonance of ^{6}Li is very broad, in consequence, this curvature is enough to generate a good confinement along the axial direction but still very small to produce any noticeable anisotropy in the value of the scattering length (see section 3.1.2). In this way, the created magnetic potential has the shape of a saddle-point which we approximate as

$$U_{mag}(y,z,x) \approx U_{0_{mag}} + \frac{m}{2}\left(\omega_{x_{mag}}^2 x^2 - \omega_{r_{mag}}^2 r^2\right), \tag{2.74}$$

where the trap frequencies are determined by the curvature of the field component along the corresponding direction; then $\omega_{x_{mag}}^2 = \frac{\mu}{m}\frac{\partial^2 B}{\partial x^2}\Big|_0$ and $\omega_{r_{mag}}^2 = \frac{\mu}{m}\frac{\partial^2 B}{\partial r^2}\Big|_0$, being m the mass of the ^{6}Li atom and μ the magnetic moment of the trapped state which, in general for the ground state of alkali atoms, is of the order of the Bohr magneton, $\mu \approx \mu_B$. Note from Eq. (2.74) that along the radial direction we have an "anti-curvature" which will tend to deconfine the atoms along that direction. This does not represent a problem because the radial confinement from the ODT is much stronger. The total frequencies of our hybrid trap will be given by

$$\omega_r = \sqrt{\omega_{r_{ODT}}^2 - \omega_{r_{mag}}^2} \quad \text{and} \quad \omega_x = \sqrt{\omega_{x_{ODT}}^2 + \omega_{x_{mag}}^2}. \tag{2.75}$$

In our experiment, once the quantum sample is produced, we have that the radial optical confinement is much larger than the magnetic one ($\omega_r \approx \omega_{r_{ODT}}$), and vice-versa, along the axial direction the confinement is dominated by the magnetic component ($\omega_x \approx \omega_{x_{ODT}}$).

Using the experimental parameters presented in section 3.1.2, the generated axial curvature is $\frac{\partial^2 B}{\partial x^2}|_0$ =6.2 G/cm^2, which translates into a total axial frequency of $\omega_x \approx 2\pi\times$ 11 Hz. In this way we obtain a cigar-shaped quantum sample whose aspect ratio is 1:15, which is appropriate for our experiments (figure 2.11).

An important observation is that at low power, the radial confinement mainly depends of the light power P, in contrast to the axial confinement which remains almost constant due to the static value of the magnetic curvature $\frac{\partial^2 B}{\partial x^2}|_0$.

For simplicity, from this point on, we will use the term "ODT" to refer to this hybrid trap.

2.3.4 Evaporative cooling

Evaporative cooling is a mechanism that occurs in many cooling processes in nature. For example, it is the operating principle behind sweat, perspiration from plants and even the reason why a cup of coffee cools down when we blow on it. It holds a special

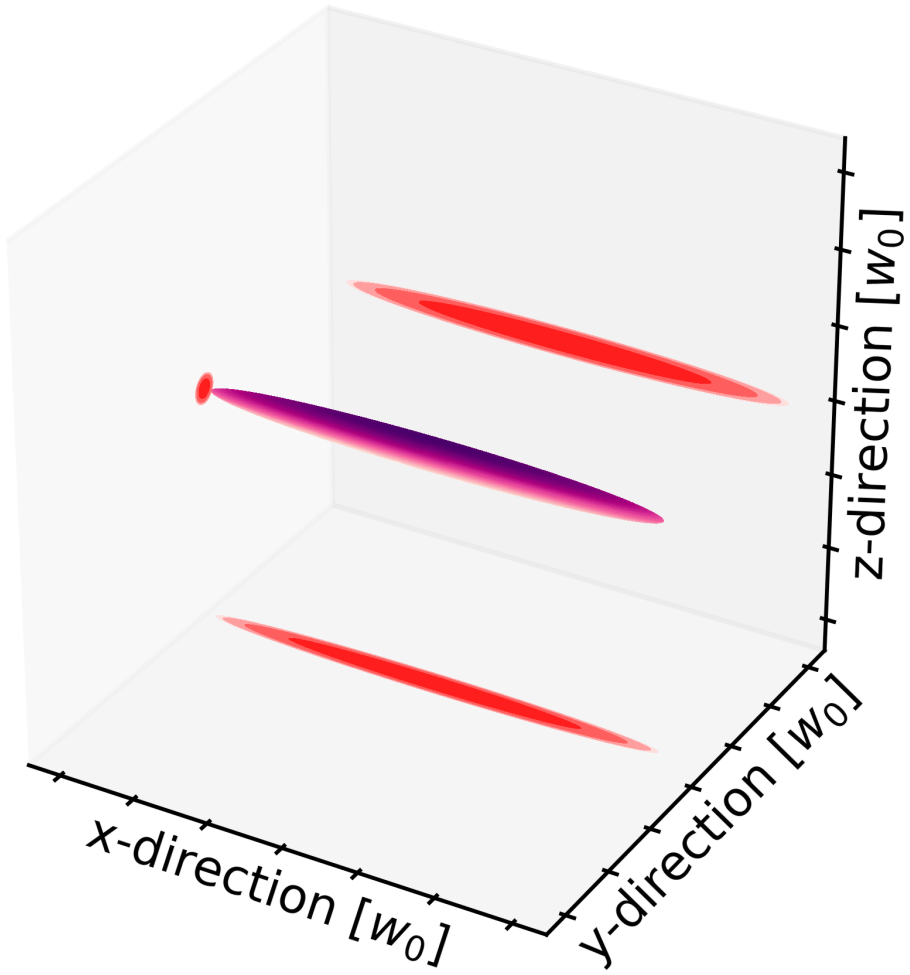

Figure 2.11: Hybrid trap potential surface with lateral projections. In purple, the cigar-shaped hybrid trap whose aspect ratio is 1:15. The lateral projections of the trap are related with the absorption images which we take for the study of the quantum sample.

place in the field of atomic physics. Indeed, in the context of trapped atomic gases, it was essential for the first realization of Bose-Einstein condensation in 1995 [7, 8, 9], and it is still the primary method for producing quantum degenerate gases [58]. After being submitted into the Doppler and sub-Doppler cooling stages, the gas is transferred into the ODT, where evaporative cooling can be applied.

The central idea of evaporative cooling is the selective removal of the most energetic atoms from the sample, in such a way that the sample rethermalizes at a lower temperature. This is illustrated in figure 2.12.

In a more quantitative way, we define a cutting energy $\epsilon_c = \eta k_B T$, such that the particles with energy higher leave the sample. This particles correspond to the high energy tail of the Maxwell-Boltzmann distribution, and therefore the "evaporation" of these particles reduces the average energy of the remaining atoms. The gas rethermalizes by elastic interatomic collisions to a new equilibrium state with lower temperature.

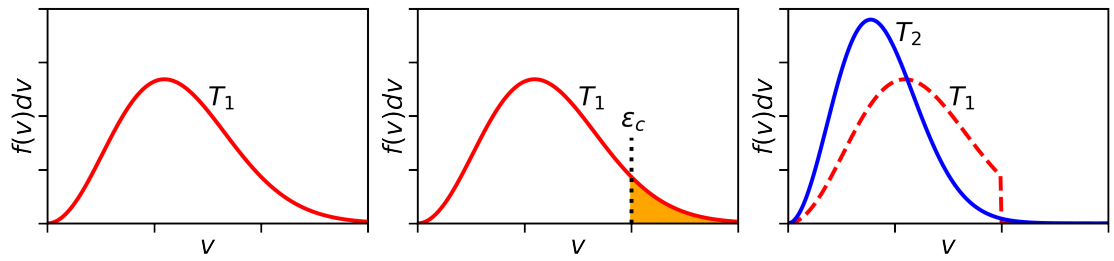

Figure 2.12: Operating principle of evaporative cooling. On the left panel, the red function is the Maxwell-Boltzmann distribution for speed at temperature T_1. The center panel illustrates the selective removal of particles from the sample with energies higher than the cutting energy (filled orange area). This reduces the average energy of the remaining atoms, and after rethermalization the system reach to a new equilibrium state with lower temperature T_2, represented by the blue function on the right panel.

In the case of a trapped thermal gas, the cutting energy can be associated to the trap depth U_0. If we reduce the trap depth to the cutting energy $U_0 = \eta k_B T$, the particles with energy higher than U_0 leave the trap.

We define a parameter to quantify the efficiency of the evaporative cooling process as

$$\varrho = \frac{\dot{T}/T}{\dot{N}/N}, \tag{2.76}$$

which expresses the temperature decrease per particle lost.

Then, analyzing the kinetics of the evaporative process, following the reference [59], for the case of 3D harmonic trap in the limit of a high cutting parameter $\eta \gg 1$, the evaporation loss rate is giving by

$$\dot{N} = -\Gamma_{el}(\eta - 4)e^{-\eta}N, \tag{2.77}$$

where Γ_{el} is the elastic collision rate. The factor $e^{-\eta}$ comes from the Maxwell-Boltzmann distribution. This equation has an exponential solution with an characteristic evaporation time proportional to $1/\Gamma_{el}\eta e^{-\eta}$.

Under the same hypotheses as evaporation loss rate, following the reference [59], the internal energy of the gas has a rate change

$$\dot{E} = \left(U_0 + \frac{\eta - 5}{\eta - 4} k_B T\right) \dot{N} = (\eta + \kappa)\, k_B T \dot{N}, \tag{2.78}$$

and using the equation of state for an ideal gas in a harmonic trap $E = 3Nk_BT$ to connect the internal energy dynamics to temperature, we find that

$$\dot{T} = \frac{\dot{E}}{3k_B N} - T\frac{\dot{N}}{N} = (\eta + \kappa - 3)\, \frac{\dot{N}}{N}\frac{T}{3}. \tag{2.79}$$

Using equation (2.79), we find that evaporative cooling efficiency is

$$\varrho = \frac{\eta + \kappa}{3} - 1. \tag{2.80}$$

This dimensionless quantity ϱ is the ratio between the average energy of an escaping atom $(\eta + \kappa)\, k_BT$ (eq. 2.78) and average energy of an ideal gas in a harmonic trap $3k_BT$ (subtracting one at the end). This characterize how much more than the average energy is removed by the evaporating atoms.

These considerations show that in principle there is no limit for the efficiency of evaporative cooling.

For example, if η is chosen to be extremely large, one just has to wait for the event that one particle has all the energy of the system. Evaporating a single particle then cools the whole system to zero temperature.

Such evaporation would be the most efficient cooling process possible but, unfortunately, this cooling strategy would take an almost infinite amount of time. This due to the exponential factor $e^{-\eta}$ in the characteristic evaporation time $1/\Gamma_{el}\eta e^{-\eta}$.

Then evaporation efficiency ϱ and evaporation time can not be optimized individually for a fixed value of η.

Therefore, we have not other alternative that introduce time as a parameter and dynamically reduce the value of trap depth $U_0(t)$. This process is referred as "forced evaporative cooling", and it is a trade-off between efficiency and cooling speed.

Forced evaporative cooling

The forced evaporative cooling, also called runaway evaporation [58], consist in dynamically reduce the value of the trap depth $U_0(t)$. This results in a time-dependent cutting parameter $\eta(t) = U_0(t)/k_BT(t)$. The situation we keep in mind is forced evaporation at a constant η parameter, i.e. the trap depth $U_0(t)$ is lowered in proportion to the decreasing temperature $T(t)$. Constant η ensures that the energy

distribution is only rescaled during the cooling and does not change its shape. This assumption is reasonably well fulfilled in experiments.

Therefore, schematically, we repeat the process described by figure 2.12, with the new cutting energy $\epsilon_c = \eta k_B T_2$ which is proportional to the new temperature T_2. This process is progressively repeated until quantum degeneracy is achieved.

As the equations of the dynamic evaporation become really complex, we going to keep in mind only two parameters, the elastic collision rate Γ_{el} and phase-space density (PSD).

Elastic collision rate

In the equation (2.77), we expressly omitted to say that the peak elastic collision rate in the harmonic trapped gas Γ_{el} is

$$\Gamma_{el} = n_0 \sigma \bar{v} \propto N\bar{\omega}^3/T, \tag{2.81}$$

where $n_0 = N(m\bar{\omega}^2/2\pi k_B T)^{3/2}$ is the peak density of a classical gas in a harmonic trap, σ the elastic scattering cross section and $\bar{v} = \sqrt{8k_B T/\pi m}$ the mean particle speed.

To achieve sustained evaporation is necessary to maintain or increase the elastic collision rate. Note that as the temperature of the atoms decreases, $\bar{v}$ also decreases, therefore, in order to keep constant or even increase Γ_{el}, the density n_0 must increase as the process occurs.

From $n_0 \propto N\bar{\omega}^3 T^{-3/2}$ and $\bar{v} \propto T^{1/2}$, therefore $\Gamma_{el} \propto N\bar{\omega}^3/T$. Consequently, in order to achieve runaway evaporation the temperature must decrease in a faster rate than the atom losses.

At last, the elastic cross-section σ determines the elastic collision rate as well. As we discussed in section 1.2, the cross-section for indistinguishable fermions is zero due to Pauli blocking, therefore thermalization by s-wave collisions will not be possible, thus evaporation neither. This statistical difference between bosons and fermions led that the quantum degenerate Fermi gas took until 1999 [10], 4 years after the Bose-Einstein condensation was already achieved.

The strategy implemented by D.S. Jin to get the first degenerate Fermi gas was use two spin states of the fermionic atom ^{40}K magnetically trapped. Therefore there is a scattering length and cross-section different from zero between the two spin component, allowing the evaporative cooling.

Recent works use the magnetic Feshbach resonance described in section 1.2.2 for evaporative cooling. Therefore the scattering length and cross-section between the two spin component is tunable, but not only that, the scattering length diverges at B_0. By applying the resonant magnetic field B_0 during evaporation, the inter-atomic collision rate maximizes and thus perform the fastest evaporation. We use this approach in our experiment.

Phase-space density

If we regard evaporation with adiabatic expansion, we realize that temperature does not provide the most qualified variable for quantum degeneracy description, because adiabatic expansion trades in temperature against density. We therefore now focus on PSD, which is invariant with respect to adiabatic changes of the trapping potential.

The PSD is described by

$$D = n_0 \lambda_{dB}^3 \propto N\bar{\omega}^3/T^3 \tag{2.82}$$

with $\lambda_{dB} = (2\pi\hbar^2/mk_BT)^{1/2}$ the de Broglie wavelength and $n_0 = N(m\bar{\omega}^2/2\pi k_BT)^{3/2}$ is the peak density of a classical gas in a harmonic trap.

The best evaporation is achieved when we obtain the maximum increase in PSD with the smallest loss in the number (to reach quantum degeneracy with the largest number of atoms possible). This efficiency can be quantified by the parameter

$$\gamma = \frac{\ln(D_f/D_i)}{\ln(N_f/N_i)} \tag{2.83}$$

where sub-indices quantities i and f indicates before (initial) and after (final) the evaporation.

At the experiment, decreasing the trap depth U_0 for forced evaporation is equivalent to decreasing the ODT laser power over time (eq. (2.72)). This function $U_0(t)$ ($P(t)$) is called evaporation ramp.

If evaporation ramp is performed too slowly, in practice, loss and heating mechanisms, as those presented in section 2.3.1, could dominate. On the contrary, if this is done too fast, the thermalization processes will not have enough time to re-distribute energy, making evaporation inefficient as well.

Despite the fact that there are theoretical proposals to analytical evaporation ramp should have to optimize eq. (2.83) to achieve the most efficient forced evaporation [60], in practice, the most used evaporation ramps are the linear, exponential or a concatenation of them which are optimized experimentally to maximize γ at any time.

Adiabatic expansion during forced evaporation

For a Gaussian-shaped optical trapping beam of fixed waist, there is a reduction of the trap frequencies associated with the decreasing trap depth $U_0(t)$, observed from equation 2.73.

Since the harmonic confinement decreases while performing forced evaporative cooling, the trap extends spatially, presented in the Thomas-Fermi radius equation (1.34). This expansion can be considered adiabatic, and this adiabatic expansion has a contribution to decrease the temperature.

It is important to note here that although the adiabatic reduction of temperature associated with the trap expansion can achieved impressively low temperatures, there is no associated gain in phase-space density since the change is adiabatic.

Unfortunately, these trap frequencies $\bar{\omega}$ reduction has associated a decreasing in the density n_0. This results a very small collision rates at lowest depths, due to eq. (2.81).

In chapter 4 of this thesis we will discuss how to overcome this problem implementing the time-averaged potentials technique (see section 4.4). In short, one can change the size of the waist trapping beam to achieve independent control over the trap depth U_0 and frequency $\bar{\omega}$.

At this point we finish the most important theoretical background to understand the cooling techniques. Therefore in the next chapter we describe the experimental procedure to the quantum gases production.

Chapter 3

Quantum gases production

This chapter is devoted to present our experimental setup and employed methods to produce quantum degenerate samples of ^{6}Li. It is divided as follows, in section 3.1 we describe the different systems that compose our setup, this includes the ultra-high vacuum system, the laser cooling system, the magnetic field generation system, and finally, the optical trapping system, which is of particular importance in this thesis. Section 3.2 is dedicated to explain the procedures that we employ to implement the laser and evaporative cooling techniques, as well as the production of a superfluid sample in different interaction regimes across the BEC-BCS crossover.

It is important to mention that this entire chapter is strongly based on the reference [61], which is a recently published article by our group where a detailed description of our experiment is presented. This article represents one of the important products of my master's project and that is why we reproduce parts of it here.

3.1 Experimental setup

3.1.1 Ultra-high vacuum system

Ultracold quantum gases are considered the coldest objects in the universe. They are also a rather fragile system. For this reason, they can only be created in a completely isolated environment, to avoid heating and any other spurious interaction with the environment. For this reason, we employ an ultra-high vacuum (UHV) system specially designed for our experiment, in which all the cooling and probing techniques can be implemented. This system was designed by a former student of the group, Eduardo Ibarra, to obtain his bachelor's degree, all the details can be found in his thesis, in reference [62].

Our UHV system (figure 3.1) is divided in three main sections, namely (i) the effusive oven; (ii) the differential pumping stage, and (iii) the Zeeman slower system and the main chamber where the sample is produced and the experiments performed. Each of these sections is pumped by 200 L/s pumping system composed by a combination of an ion pump and a non-evaporable getter (model NEXTorr R D200-5 from SAES getters Inc).

The effusive oven consists of a cylindrical recipient which is heated to a temperature

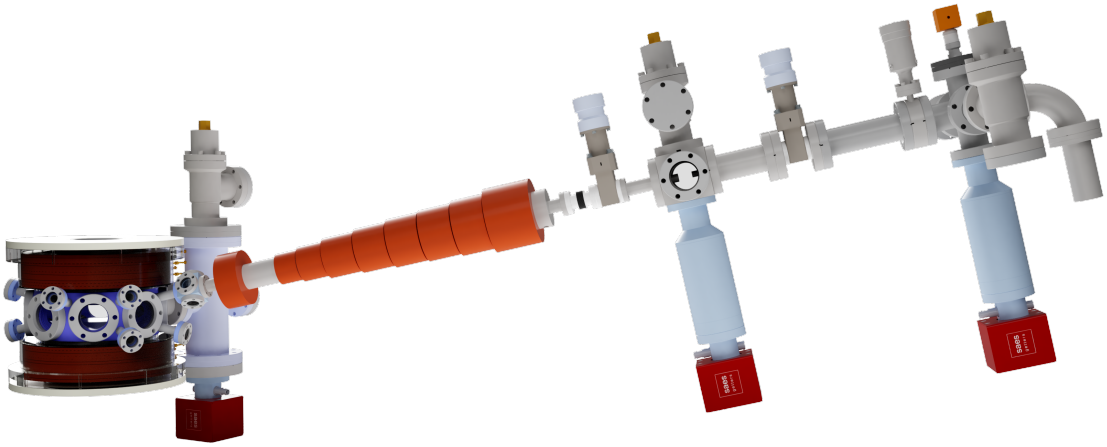

Figure 3.1: Scheme of the ultra-high vacuum system including the Zeeman and the Feshbach coil systems. See section 3.1.1 for details. Image taken from [61].

of 450°C. The oven contains 5 gr of purified ^{6}Li, which at this temperature the vapor pressure is about 1×10^{-9} Torr. The oven is connected to the rest of the UHV system through a 4mm diameter nozzle, where the vapor passes through and propagates to the rest of the system.

Since the pressure right after the nozzle is too high for producing quantum degenerate samples (which require to be at the UHV regime, below 10^{-10}Torr), we need a differential pumping stage to keep a continuous pressure difference between the oven and the region in which experiments are performed. The differential pumping consists of two aligned tubes separated by 25mm from each other. The first one, facing the oven, has a 4.6 mm inner diameter and a second one, facing the Zeeman slower, is 7.7 mm inner diameter. This scheme was designed to keep a pressure difference as large as five orders of magnitude [62]. In this way, the pressure in the main chamber is of the order of 10^{-11} Torr.

The Zeeman slower system consist in a tube of 16.5 mm inner diameter and 56 cm long which connect the main chamber to the differential pumping stage. Around this tube there is a conical solenoid which is used to create a spatially inhomogeneous magnetic field which is required to implement a Zeeman slower (more details in section 3.1.2).

Finally, the main chamber is a stainless steel custom-made octagon chamber from Kimball Physics Inc. This chamber contains eight CF40 viewports on its sides; two CF100 vertical viewports; and ten CF16 viewports connected to the chamber by arms extruded from it at an angle of 13° from the horizontal plane. The Zeeman slower tube is connected to the main chamber by one of these arms. All viewports have anti-reflection coating for all the wavelengths used in our experiment (532 nm, 671 nm and 1064 nm).

We have placed on both CF100 flanges reentrant viewports of high optical quality whose inner face is very close to the atoms, at a distance of only half an inch. This opens the possibility of building a large numerical aperture optical system to produce high resolution images of the sample.

3.1.2 Magnetic field generation system

We employ three different sets of coils to generate all the required magnetic fields to trap and manipulate the atoms. We describe each of them in the following sections.

Zeeman slower magnetic field

Atoms coming from the oven move at surprisingly high speeds, given by the Maxwell-Boltzmann distribution at 450°C, the mean speed of the atoms is of the order of 1540 m/s, while the capture speed of the MOT is around 60 m/s. For this reason, we use a Zeeman slower stage to decelerate the atomic beam before they reach the main chamber.

This cooling stage uses the radiative force (see section 2.2) of a red-detuned laser beam which counter-propagates respect to the atoms coming from the oven. But there is a problem: as the atoms interact with the Zeeman slower beam, they start

to decelerate and, due to Doppler effect, the light is no longer in resonance with them. So the deceleration mechanism stops working.

To overcome this issue, in a similar fashion as done with the MOT (section 2.2.3), we can use the Zeeman shift produced by a magnetic field to change the relative detuning between the light frequency and the atomic transitions. In this way, the Zeeman slower consists of a series of coils, which generate an inhomogeneous magnetic field $B(z)$ along z, the axis of propagation of the atomic beam. But unlike the MOT case, the purpose of this is to keep the atoms in resonance as they slow down, not to trap them. Then, using this in equation (2.49), the condition for atoms to remain in resonance with light is

$$\Delta_Z = \frac{\mu_B}{\hbar} B(z) - kv(z) \tag{3.1}$$

where μ_B is the Bohr magneton, k is the wavevector of the cooling frequency of the slower light and Δ_Z is the detuning of the Zeeman slower laser beam. In this formula we only consider the cooling frequency as we discuss at the beginning of section 2.2.5, however, the beam also contains a repumper frequency which keeps the atoms in the cooling cycle.

Assuming the radiative force from equation (2.34) to be constant (which means that the magnetic field $B(z)$ is such that the atoms remains at constant detuning with the light), then, the deceleration $a \approx \hbar k\gamma/2m$ is also constant [1]. Then, the atoms follow a uniformly decelerated motion with an initial speed v_0. The analytical expression for magnetic the field $B(z)$ with these conditions is obtained from equation 3.1 giving

$$B(z) = \frac{\hbar}{\mu_B}\left(\Delta_Z + kv_0\sqrt{1 - \frac{z}{L_0}}\right) \tag{3.2}$$

where L_0 is the length of the Zeeman slower solenoid. The initial speed for our system was designed to be $v_0 = 960$ m/s, which comes approximately from the uniformly accelerated motion formula $v_0 = \sqrt{2aL_0}$. This speed is much lower than mean speed of the atoms coming from the oven, about 1540 m/s; however, this is not a problem since the flux of atoms effusing from the oven is very large, about 6×10^{15} atoms/s, so we still are able to decelerate enough atoms to efficiently load our MOT.

Our Zeeman slower produces the desired magnetic field employing a succession of eight size-decreasing coils connected in series and an extra ninth coil at the end in which the current circulates in opposite direction, inverting in this way the magnetic field sign. This is known as "spin-flip configuration". All nine coils are wound directly onto the slower UHV tube using 1 mm diameter cooper wire. The coils are held together using a thermal conducting and electric insulating ceramic epoxy (Duralco$^{\text{TM}}$ 128). The total current passing through each coil is of the order of 2.0

[1] This deceleration depends on the parameters of the cooling frequency of the Zeeman slower light as $a = \frac{\hbar k\Gamma}{2m}\frac{s}{1+s}$ (which is slightly different from our equation (2.34) because it comes from the Optical Bloch equations), where $s = I/I_s$ is the saturation parameter, being I the intensity of the light and I_s= 2.54mW/cm^2 the saturation intensity of the D_2 line. For our experimental conditions $s \approx 10$, so we are close to the maximum attainable deceleration.

A to generate a field which goes from a maximum around 600G to a minimum of about -250 G.

Figure 3.2(a) shows a scheme of the coil configuration of our Zeeman slower. Figure 3.2(b) presents the generated magnetic field. Finally, Figure3.2(c) exhibits the calculated velocity profile of the decelerated atoms through their propagation along the slower.

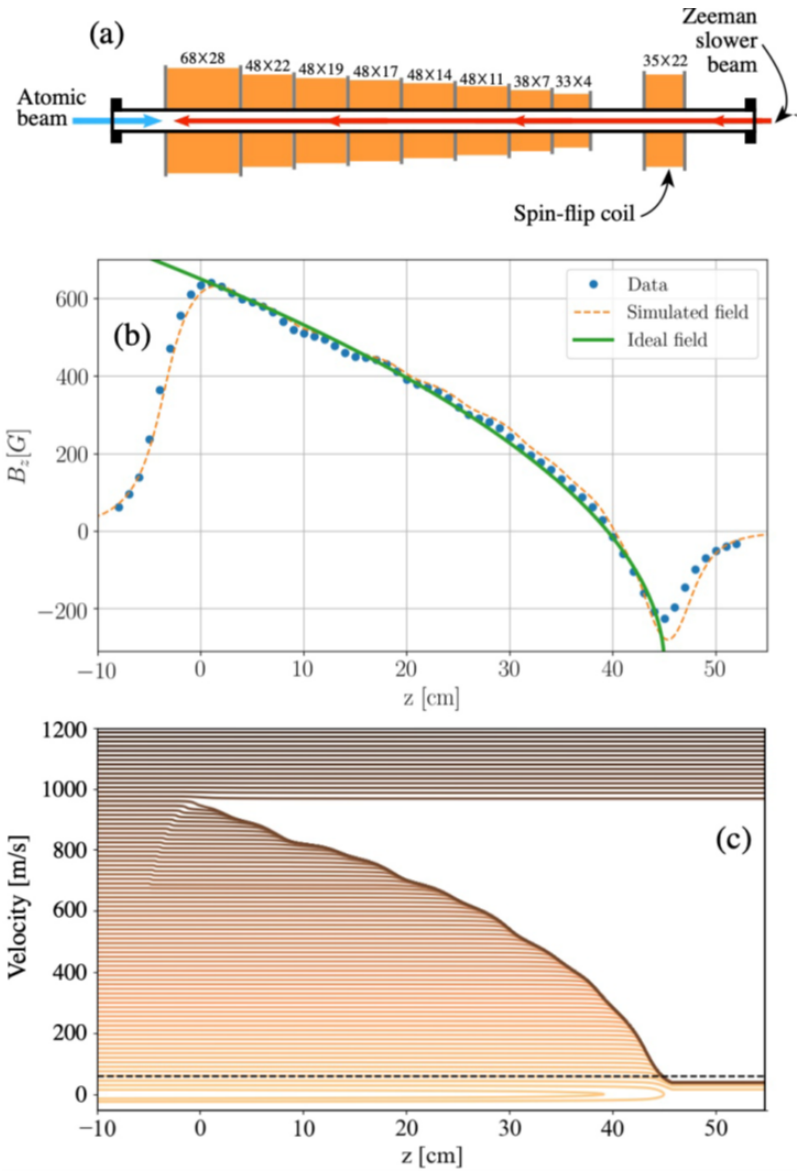

Figure 3.2: (a) Scheme of our Zeeman slower coil set, the number of windings of each coil is indicated in the format $H \times V$, where V denotes the number of layers in the vertical direction and H provides the number of turns in each layer. (b) Axial component of the magnetic field generated along the Zeeman slower, the blue dots are the experimental data, the orange dashed line is the simulated field for this coil configuration and the solid green curve is the ideal magnetic field obtained through equation 3.2. The data uncertainty is of 1%, however the corresponding error bars are not visible at this scale. (c) Evolution of the speed of the atoms propagating through the Zeeman slower, the dashed horizontal line indicates the capture velocity of the MOT. Image taken from [61].

Magnetic quadrupole for MOT

To produce the proposed linear magnetic field for the MOT (section 2.2.3) we use a quadrupole magnetic field whose axial gradient at the center of the trap is $\left.\frac{\partial B(z)}{\partial z}\right|_0 =$ 28 G/cm. This field is generated by two small coils of 6×4 windings connected in anti-Helmholtz configuration. Each of these coils is mounted in a cylindrical water-cooled support to prevent them from heating. This support is made of Teflon^{TM} which is a machineable amagnetic and insulating material that prevents the induction of eddy currents on it when the quadrupole field is abruptly switched off. The two supports are mounted inside the reentrant viewports of the main chamber, along the vertical direction. The coils are wound with strip-shaped copper wire of 4 mm×1 mm and held together with ceramic epoxy (Duralco^{TM} 128). The left panel of figure 3.3 shows the position of these coils in relation to the main chamber.

Feshbach resonance magnetic field

As already discussed in section 1.2.2, one of the important advantages of ultracold lithium gases is the possibility of precisely controlling the interatomic interactions by means of a very broad Feshbach resonance. In our experiment, we use the resonance between the states $|1\rangle$ and $|2\rangle$, shown in figure 1.6, centered at 832 G. So we need an extra set of coils able to produce an uniform magnetic field with any value from zero to 1000 G in order to have full control of all interaction regimes.

To do so, we use a pair of coils connected in Helmholtz configuration. We intentionally set the coils slightly away from the Helmholtz configuration so the magnetic field is almost uniform with a small curvature, a saddle-point magnetic potential. This curvature is useful to confine the atoms along the weak direction of our optical dipole trap, as presented in section 2.3.3. Right at the Feshbach resonance, at 832 G, this curvature along the coils axis direction is $\frac{\partial^2 B}{\partial x^2}|_0 = 6.2\mathrm{G/cm}^2$, while the corresponding magnetic gradient $\frac{\partial B}{\partial x}|_0$ is nearly zero.

The Feshbach coils are made by 4 mm square section copper wire. This wire is hollow, with an internal diameter of 2 mm, which allows cooling the coil by circulating cold water inside the wire. These coils were fabricated by the company Oswald Elektromotoren GmbH and each of them is embedded in an insulating resin that avoids the induction of undesired eddy currents. We can circulate a current above 200 A without noticing any significant heating of the coils. This thermal stability together with a PID feedback loop makes possible to produce magnetic fields stable in one part in 10,000. We place these coils along the vertical direction, colinear to the quadrupole field coils. The left panel of figure 3.3 shows each of the employed set of coils and their position in the experimental setup.

3.1.3 Laser system

Optical cooling scheme

We use the D_2 and D_1 optical transitions of ^{6}Li to implement the different laser cooling techniques in our experiment. The D_2 and D_1 transitions correspond to 670.997 nm and 670.992 nm wavelength respectively [63]. The main optical frequencies employed in our experiment are shown in figure 3.4. The natural linewidth of

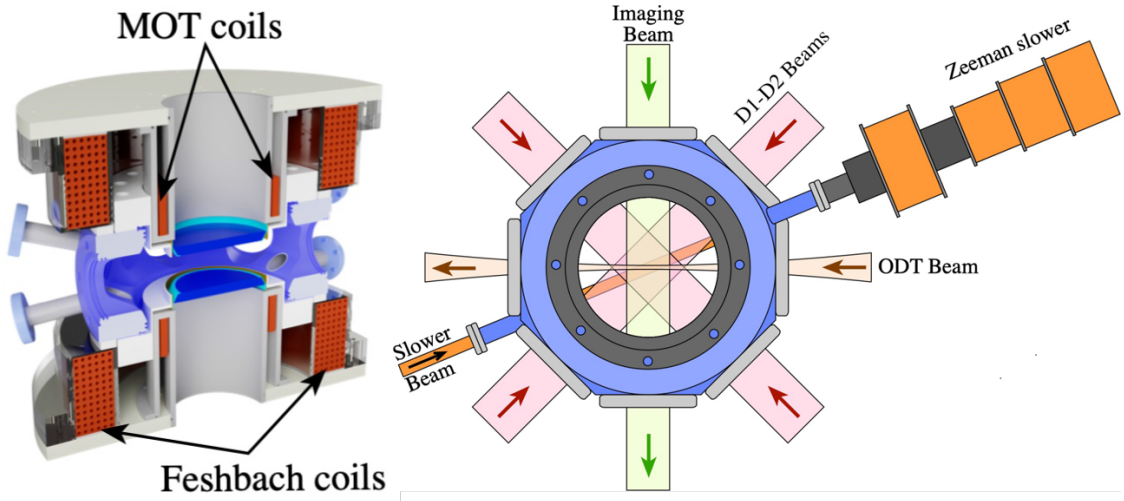

Figure 3.3: On the left we show a cut of the main chamber, exhibiting the distribution of the Feshbach and MOT coils. On the right, top view scheme of the main chamber, showing the configuration of the MOT beams (D_1 and D_2 beams), the imaging beam, the Zeeman slower beam and the ODT beam. MOT and Feshbach coils were omitted for clarity. The third pair of MOT beams is perpendicular to the plane of this scheme and, hence, not shown.Image taken from [61].

both lines is $\Gamma = 2\pi \times 5.87$ MHz (referenced as γ in the past chapter) [64].

As discussed in section 2.2.5, since the ground state splits into two hyperfine levels, it is necessary for the D_2 Doppler cooling to have and extra frequency to repump the atoms into the cooling cycle. This additional frequency called repumper in contrast with the main frequency called cooling. The D_1 sub-Doppler cooling intrinsically needs two frequencies, which by D_2 inheritance are called cooling and repumper frecuencies. Then D_2 Doppler cooling is used first to implement the MOT and later an optical molasses cooling stage in the experiment. The D_1 sub-Doppler cooling is subsequently used to apply a gray molasses cooling stage.

In this section, we explain how to produce the light of the D_2 and D_1 optical transitions of ^{6}Li to implement the different laser cooling techniques in our experiment. Figure 3.5 presents a simplified scheme of the laser setup. This scheme will be used to explain the light production.

We use two extended cavity diode lasers (cat-eye configuration, model CEL002 from MOGLabs), one for each D-transition line. The emission frequency of these lasers is locked-in into an atomic reference using a standard saturated absorption spectroscopy (SAS) [65]. Our atomic reference is purified ^{6}Li heated at 320°C in a spectroscopy cell.

Let us start by considering only the the D_2 cooling and repumper frequencies, leaving aside for a moment the D_1 line. The light produced by the diode laser locked-in into D_2 transition is pumped into an optical tapered amplifier (model MOA002 from MOGLabs) called main TA. The amplified beam is divided into two beams and independently shift to cooling and repumper frequency using two different acousto-optic modulators (AOM). The frequency difference between them is 228.2 MHz, which corresponds to the hyperfine splitting of the ground state $2^2S_{1/2}$ of ^{6}Li.

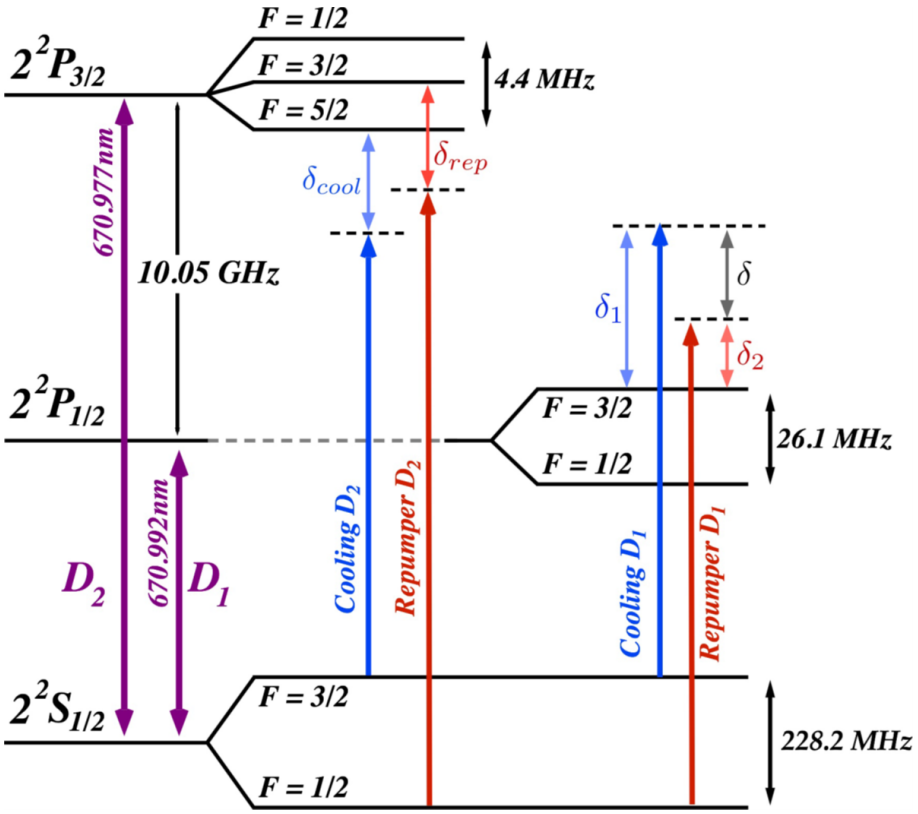

Figure 3.4: Level scheme (not to scale) for ^{6}Li showing (left) the D_2 and (right) the D_1 hyperfine structures and the transitions used for the laser cooling processes. See section 3.1.3 for details. Image taken from [61].

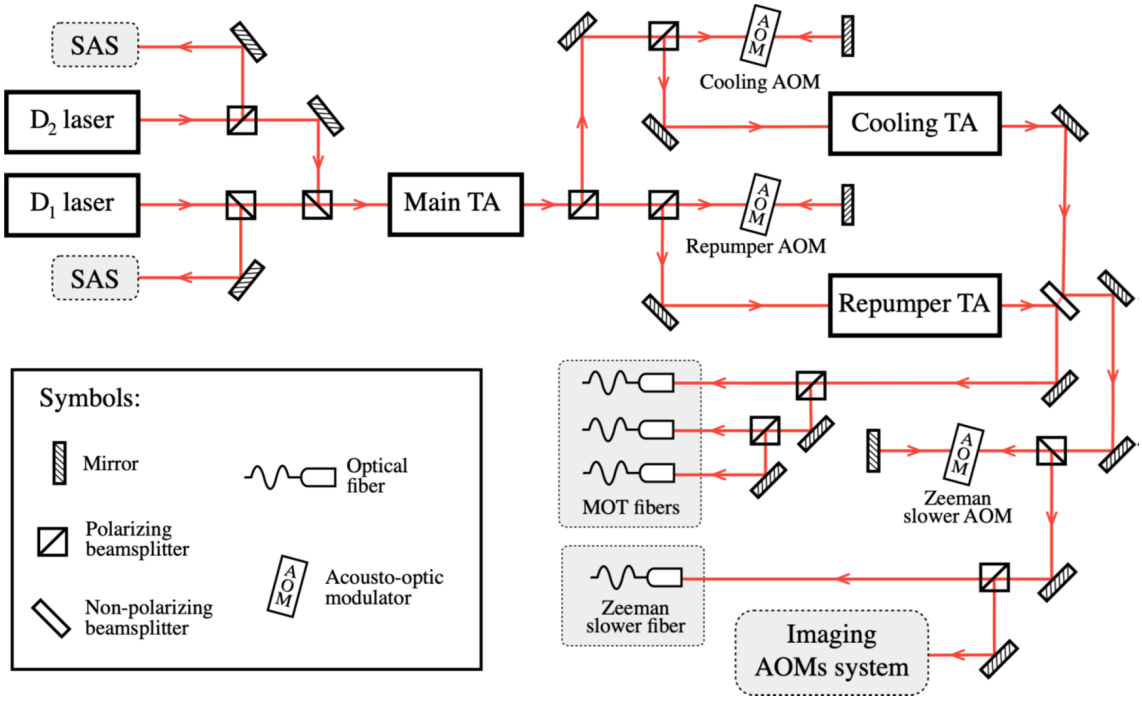

Figure 3.5: Simplified scheme of the laser cooling and imaging optical setup showing the main features of the system. Lenses and waveplates have been omitted for clarity. See 3.1.3 for details. Image taken from [61].

Next, each one of these beams separately pumps another TA, generating two high power beams (∼500mW each). One of these beams, the one with lower frequency, corresponds to the cooling frequency which is red-detuned from the $2^2S_{1/2}$(F = 3/2) $\rightarrow 2^2P_{3/2}$ transition by 8.5 Γ (about 50 MHz). The second beam is used as repumper frequency and is red-detuned from the $2^2S_{1/2}$(F = 1/2) $\rightarrow 2^2P_{3/2}$ transition by 8.5 Γ. Note that we cannot specify the hyperfine level of the excited state $2^2P_{3/2}$, because the energy separation of these hyperfine levels is less than Γ, and therefore we can not resolve them in our spectroscopy cell.

We superimpose both beams using a 50:50 non-polarizing beam splitter which produces two beams with the same power, each one carrying both, cooling and repumper frequencies. One of these beams is used to generate the light for the MOT. To do so we subsequently divide it into three equally powered beams and couple each one into a polarization maintaining optical fiber which brings the light directly to the experiment region. The second beam coming from this 50:50 beam splitter is additionally red-shifted by $\Delta_Z = 76$ Γ using an additional AOM. In this way we produce the Zeeman slower beam (which also arrives into the experiment by a polarization maintaining optical fiber). The Δ_Z frequency shift is chosen to correspond to $v_0 = 960$ m/s, the designed maximum velocity we can decelerate in our slower, as explained in section 3.1.2.

Now we can consider the D_1 line, which we use to implement the gray molasses cooling stage. As we discussed in section 2.2.5, the D_2 Λ transition is very similar to the D_1 Λ transition. The cooling and repumper frequencies of the D_2 and D_1 line are separated in both cases by 228.2 MHz. Additionally, during the experimental sequence, we never use both D_2 and D_1 lines at the same time. This enables us to use exactly the same optical setup to generate the D_2 and D_1 frequencies.

The light produced by a second diode laser locked-in into the D_1 line is superimposed (using a polarizing beam splitter cube) onto the very same optical path of the D_2 line laser. Then, we obtain the high power D_1 cooling and repumper beams. The cooling frequency is blue-detuned from the transition $2^2S_{1/2}$(F = 3/2) $\rightarrow 2^2P_{1/2}$(F' = 3/2) by 5 Γ (about 30 MHz), and the repumper frequency is blue-detuned from the transition $2^2S_{1/2}$(F = 1/2) $\rightarrow 2^2P_{1/2}$(F' = 3/2) also by 5 Γ. Finally, the D_1 cooling and repumper beams reach the sample using the same optical fibers that were used for the MOT.

As can be seen, we essentially set all the required frequencies using three AOMs in double-pass configuration [66]. These AOMs are also used to dynamically change the frequency of these beams and implement the D_2 optical molasses and D_1 sub-Doppler cooling stages, as explained in section 3.2.1.

Generation of probing light

The most important diagnostic tool in cold atoms experiments is imaging the samples using laser light. In our case the preferred technique is absorption imaging due to its simplicity and reliability [67, 68].

Absorption imaging consists in probing the sample using a collimated laser beam whose frequency is resonant to some atomic transition. To perform the image, we pulse this light on the atoms during a short time (of the order of 5 μs). The atoms will

absorb some of the light of this beam, casting a "shadow" on it, which corresponds to the absorption profile of the gas. After passing through the atoms, the light is collected by a telescope that creates an image of such absorption profile on a CCD camera (model MANTA G-145 NIR from Allied Vision Technology GmbH). The density profile of the gas can be extracted from this image.

In our experiment we want to produce samples at different interaction regimes across the BEC-BCS crossover. This is done by applying an external magnetic field that changes the value of the scattering length by means of a Feshbach resonance. This magnetic field, in turn, will also cause a Zeeman splitting on the electronic levels of the atoms. Hence, probing the atoms at different interaction regimes poses the necessity of generating different light frequencies to keep the imaging light resonant with the atoms.

To do so, we use the Zeeman slower beam which already has a considerable shift of 76 Γ. We deviate a fraction of this beam using a polarizing beam splitter before it is coupled into the Zeeman slower optical fiber, as shown in figure 3.5. Next, this deviated beam passes through additional AOMs that will further shift the frequency to match it to the specific magnetic field in which we want to probe the atoms. This configuration of AOMs allows to tune the frequency of the probing light at different values within the range from 0 to -220 Γ from the D_2 transitions. In this way, we are able to produce images at practically any magnetic field from 200 to 1200 G and also at the vicinity of zero magnetic field. In this way, as can be seen in figure 1.6, we can image the sample in all the superfluid regimes across the BEC-BCS crossover.

Finally, it is important to mention that the magnetic field used to access the BEC-BCS crossover is high enough to ensure that the hyperfine splitting of the atoms is well within the Paschen-Back regime, where the separation between the $|1\rangle$ and $|2\rangle$ states remains almost constant at approximately 76 MHz. For this reason, we can probe both spin states in any magnetic field through the Feshbach resonance.

3.1.4 Conservative trapping potential ODT

As we discuss in section 2.3.3, we produce the quantum degenerate fermionic system in a conservative trap generated by the combination of an optical potential and a magnetic curvature. The optical potential consists in a far red-detuned single-beam ODT created by focusing a gaussian infrared laser beam [57]. The magnetic curvature is produced by setting the Feshbach coils slightly off the Helmholtz configuration, as discussed in section 3.1.2.

The complete ODT laser setup is presented in figure 3.6. This setup is very versatile as it allows us to produce tunable and moldable potentials. In this Section we will focus on how we use it to generate a simple ODT in which the quantum degenerate sample is produced. Later, in chapter 4, we will explain how this setup can be employed to create time-averaged optical potentials.

To produce the ODT light we use a single mode ytterbium-doped fiber laser from IPG Photonics Corp. (model YLR-200-LP), which delivers up to 200W of continuum linearly polarized infrared light at $\lambda = 1070$ nm.

The beam of this laser is coupled into a quartz crystal AOM from the company Gooch

& Housego (model I-M080-2C10G-4-AM3), which resists very high intensities, above 1 GW/cm^2. We use the first diffracted order to produce the optical trap.

Therefore, to implement the evaporative cooling (section 2.3.4), it is necessary to be able to precisely control the power of this diffracted beam. This is done by controlling the AOM input RF-signal amplitude. The RF-signal is produced by a circuit based on a voltage controlled oscillator (VCO) whose output amplitude can be easily controlled using an external analog signal. Hence, the evaporative cooling stage is performed by changing this analog signal.

To stabilize the power of this diffracted order we employ a PID circuit driven by the signal of a photodiode (Thorlabs, model DET36A) which detects the small fraction of the light transmitted by a 99.9% reflection mirror (indicated as "beam up" in figure 3.6).

With our setup, we are able to generate an infrared collimated beam with $R = 2.75$ mm radius which we focus on the atoms using a $f = 40$ cm focal length lens, as indicated in figure 3.6. The beam waist at focus is $w_0 = 50\mu$m, with a Rayleigh length $x_R = 7.34$ mm respectively.

3.2 Methods for quantum gases production

As we discussed at the beginning of Chapter 2, in a very general way, the production of the quantum sample can be divided into two main processes: an initial laser cooling stage mediated by absorption and re-emission of light (section 2.2), and the transference into a conservative potential to apply the cooling by forced evaporation (section 2.3).

We provide details on the experimental procedures employed to produce ultracold samples, divided according to these two main processes in sections 3.2.1 and 3.2.2.

3.2.1 Implementation of laser cooling technique

In this first cooling process we are able to produce atomic samples at temperatures as low as 40 μK containing 4.5 $\times 10^8$ atoms with a density of the order of 4.5 $\times 10^9$ atoms/cm^3, which correspond to a phase-space density of about 6.6×10^{-6}. We provide details on the laser cooling procedure in the next sections.

Zeeman slower and magneto-optical trapping

Zeeman slower operation: The quantum sample generation process starts by heating the lithium sample contained in the oven of our UHV system to 450°C. This generates a high temperature atomic beam that propagates along the UHV system which is decelerated by our Zeeman slower. Along the magnetic coils counter-propagates (in relation to the atomic beam) a laser beam carrying two different frequencies, both of them red-detuned by 76 Γ ($\approx$ 446 MHz) from the cooling and repumper transitions of the D_2 line, carrying positive circular polarization σ^+ and having a power of 40 mW each. In this way, we are able to decelerate all the atoms from velocities classes below 960 m/s to speeds of the order of 40 m/s, well below the 60 m/s capture velocity of the MOT, as shown in figure 3.2(c).

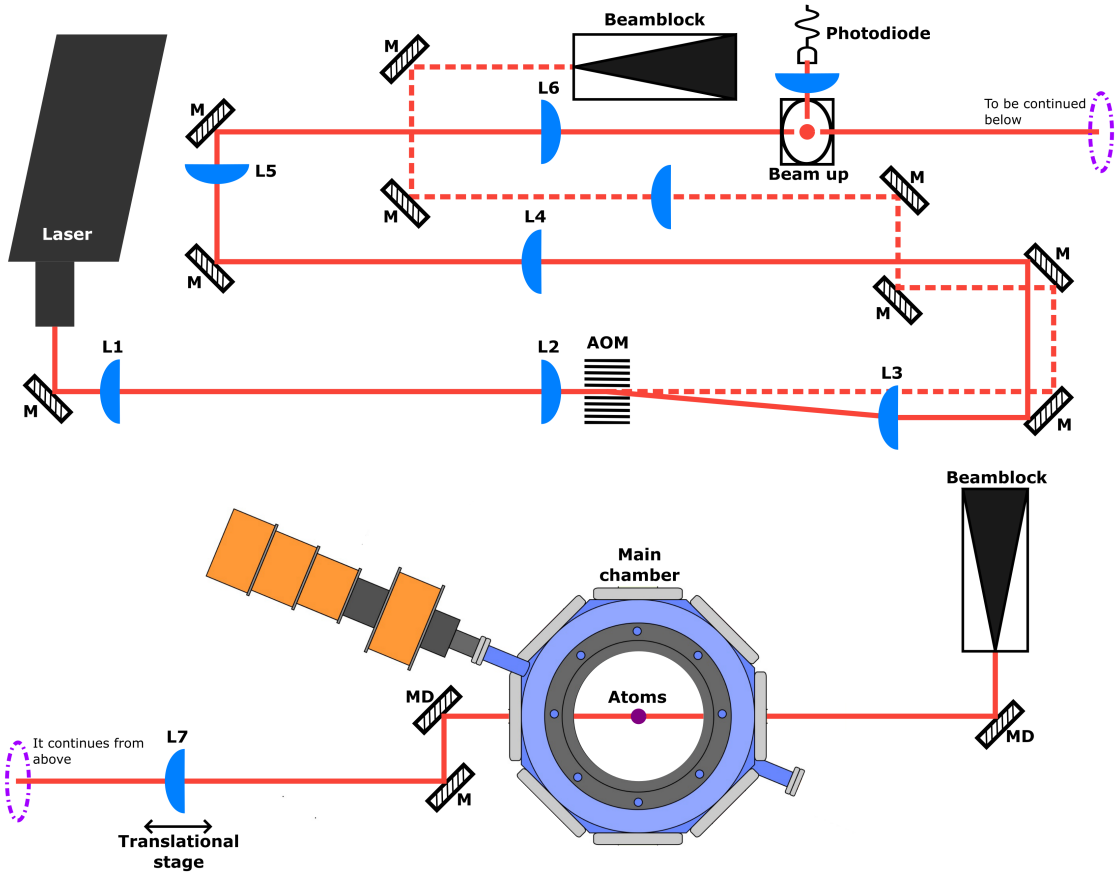

Figure 3.6: The detailed ODT laser setup, which is divided in two parts. The upper part of the scheme shows how to prepare the laser beam with the required characteristics to produce the ODT. The beam radius outgoing from the laser (IPG Photonics Corp. model YLR-200-LP) is 3740 μm, which is subsequently collimated to 795 μm radius by the telescope formed by two lenses indicated as L1-L2 with 254 mm and 54 mm focal lengths respectively. The beam is coupled into an AOM (Gooch & Housego model I-M080-2C10G-4-AM3), we keep the first diffracted order (red solid line) and we reject the zeroth diffracted order (red dashed line) redirecting it to a beam block. The first order is collimated to 2750 μm radius by two telescopes formed by L3-L4 and L5-L6 with 234 mm, 293 mm, 54 mm and 179 mm focal lengths respectively. The beam-up is composed by two mirrors placed like in a periscope, which has the purpose to change the beam height to the height of the main chamber center. A 99.9% reflection mirror (piece of the beam-up) transmits a small fraction of the light, which is collected and focused in a photodiode (Thorlabs, model DET36A). The photodiode signal feeds a PID circuit which is employed to stabilize the power of this diffracted order. The bottom part of the scheme shows how the laser beam is focused in the main chamber center in order to create the ODT. The lens L7 which focuses the light on the atoms has a 400 mm focal length. L7 is mounted in a translational stage, which helps to have a fine control of the focus position in the main chamber. Finally, the light is deviated to a beamblock. All mirrors are dielectric infrared mirrors and marked with M, however the two MD marked are dichroic plates, which reflect infrared light but transmit visible light.

We found that controlling independently the electric current of the spin-flip coil provides better results. Best results are obtained using a current of 2.0 A for the spin-flip coil and 2.9 A for all other coils, which optimize the number of loaded atoms into the MOT and minimize the corresponding loading time.

Loading of the magneto-optical trap: The decelerated atoms arrive into the main chamber where we capture them and further cool them in a MOT (section 2.2.3. To implement the MOT we use three retroreflected mutually perpendicular laser beams with a diameter of $D = 2.3$ cm, as shown at the right of figure 3.3.

The MOT beams carry two frequencies: a cooling frequency, red-detuned from the $2^2S_{1/2}(\mathrm{F} = 3/2) \rightarrow 2^2P_{3/2}$ transition, and a repumper frequency, red-detuned from the $2^2S_{1/2}(\mathrm{F} = 1/2) \rightarrow 2^2P_{3/2}$ transition. We use the standard $\sigma^+ - \sigma^-$ polarization configuration. We determine the value of the detunings by maximizing the number of atoms N loaded into the MOT and by trying to keep the temperature of the sample T as low as possible. Figure 3.7(a) shows N and T as a function of the cooling light detuning δ_{cool}. From these measurements we determine $\delta_{cool} = -8.6\ \Gamma$ (≈ 50 MHz) and $\delta_{rep} = -8.4\ \Gamma$ as the optimal values.

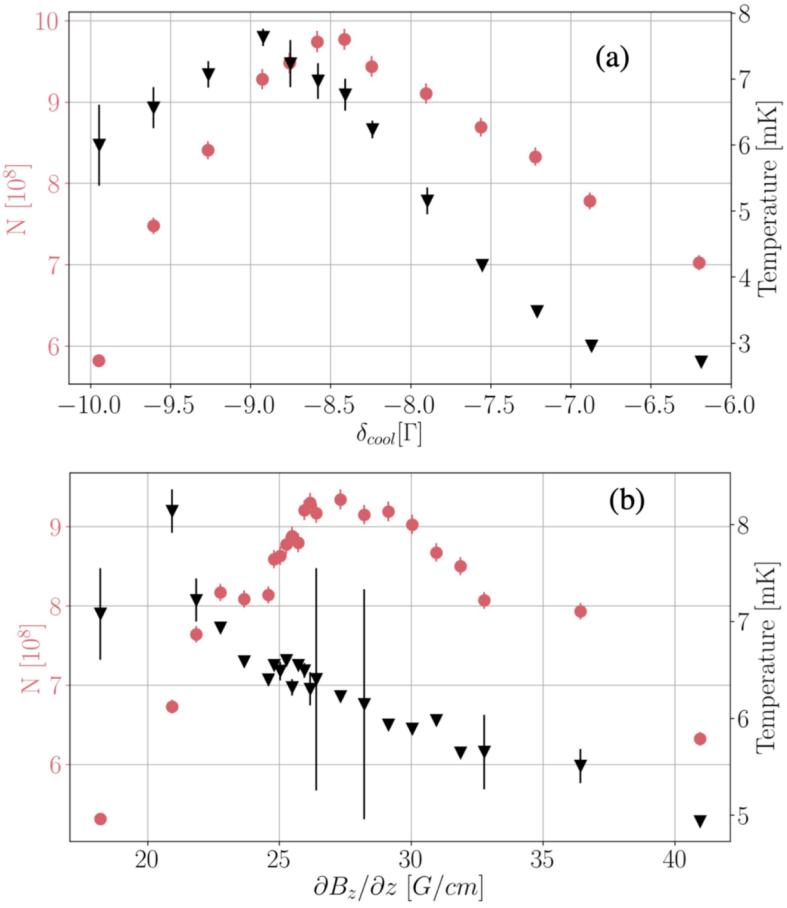

Figure 3.7: Number of atoms N (red dots) and temperature T (black triangles) of the atoms of the MOT as a function of (a) the detuning of the cooling light and (b) the axial gradient of the quadrupole magnetic field. In these plots, the error bars correspond to one standard deviation of ten independent measurements. Image taken from [61].

The power of each MOT beam is about $P = 33$ mW for each frequency, whose intensity $I_{MOT} = 4P/\pi D^2 \approx 7.9$ mW/cm^2 is well above the saturation intensity of these transitions ($I_{sat}^{D_2} = 2.54$ mW/cm^2). The magnetic field of the magneto-optical trap is generated by the coils in anti-Helmholtz configuration described in section 3.1.2 which generate a quadrupole magnetic field. We also determine the optimal parameters of this field by maximizing the number of atoms in the sample while keeping its temperature as low as possible. Figure 3.7(b) shows a measurement of N and T as a function of the axial gradient of the quadrupole field, showing that the value $\frac{\partial B(z)}{\partial z}\Big|_0 = 28$ G/cm is optimal.

As result, after a loading time of 8.6 s we manage to capture up to $N = 5 \times 10^9$ atoms in the MOT at a temperature, still relatively high, of $T = 7$ mK and atomic density of $n = 7.5 \times 10^{10}$ atoms/cm^3. The phase space density of the system is still very low, of the order of PSD $= 4.7 \times 10^{-8}$. In these measurements, as well as in all those presented in this paper, the temperature is obtained using the time-of-flight technique [67].

Doppler and sub-Doppler cooling

In order to further cool down the sample and increase its phase space density, the gas undergoes two different additional laser cooling processes. We first apply an optical molasses cooling process based on the D_2 laser line (section 2.2.1) that allows approaching the Doppler limit temperature (section 2.2.2). Next, we implement a gray-molasses technique, employing the D_1 line transitions to reach sub-Doppler temperatures (section 2.2.5) [55]. We provide experimental details in the two following sections.

D_2 optical molasses cooling: The theoretical Doppler temperature limit for our sample is given by $T_D = 140.9$ μK (equation 2.47). To reach this limit it is necessary to lower the intensity of the MOT light to minimize light-scattering heating, so the MOT light intensity should be much lower than the saturation intensity $I_{sat}^{D_2} = 2.54$ mW/cm^2. Also, the cooling light must be approached to resonance, having an optimal value at $\delta_{cool} = -\Gamma/2$. The process needs to be done in absence of any magnetic field.

After loading the MOT we abruptly switch off the quadrupole magnetic field (we also switch off the Zeeman slower magnetic field 400 ms before to guarantee the absence of any magnetic field in the sample region). Simultaneously, we decrease the intensity of the MOT beams and shift the value of cooling and repumper frequencies towards resonance. Figure 3.8(a) shows the effect on N and T of the intensity reduction, while figure 3.8(b) and (c) present the corresponding effect of the frequency shift of both MOT frequencies.

As we can see, an important temperature drop is observed when the intensity of the light decreases. Concerning the frequency shift, as long as we keep the detuning below -2Γ the number of atoms remains approximately constant while temperature decreases. We determine that the best values for intensity are $I_{cool} \approx 0.35 I_{sat}^{D_2}$ for cooling light and $I_{rep} \approx 0.3 I_{sat}^{D_2}$ for repumper, while the optimal frequency detuning is $\delta_{cool} = \delta_{rep} = -2\Gamma$. We also found that the optimal duration of this molasses process is 850 μs; if shorter, the temperature does not reach the minimum possible

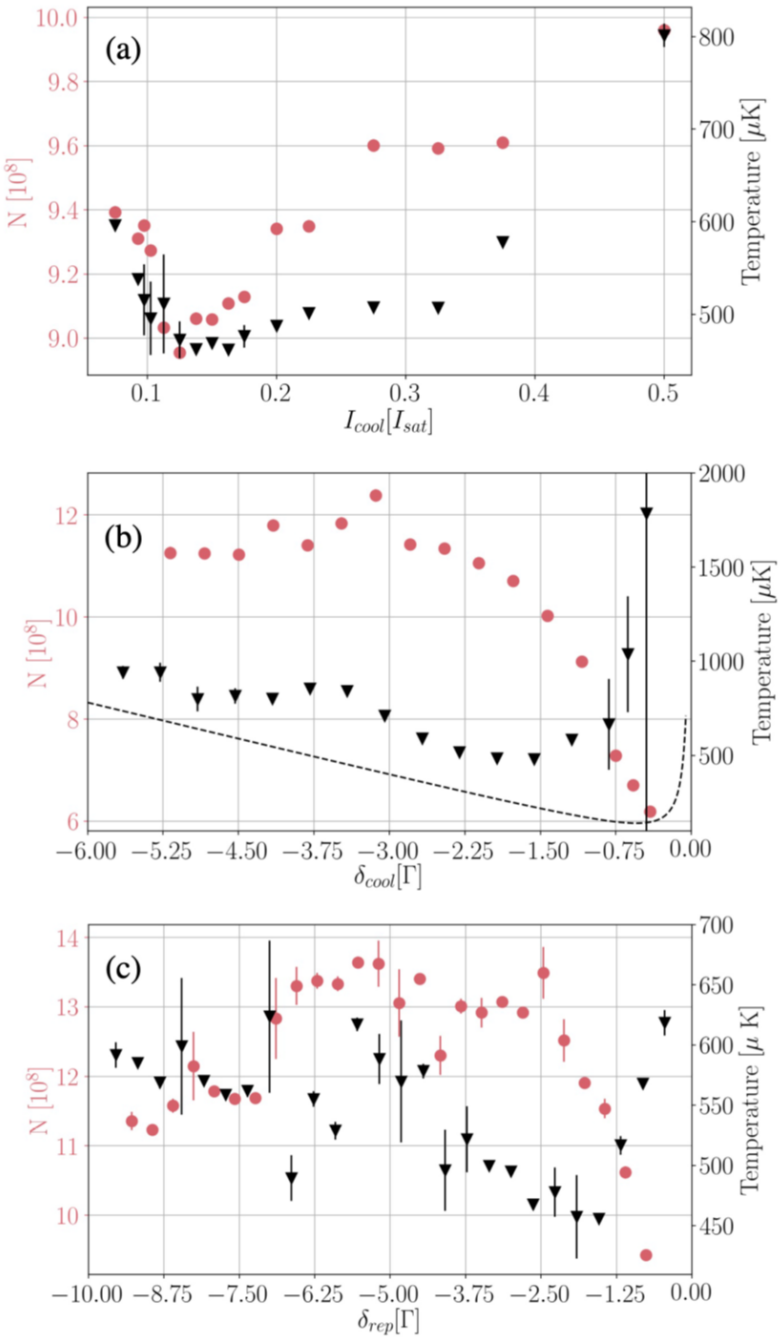

Figure 3.8: Number of atoms N (red dots) and temperature T (black triangles) of the atoms of the MOT after the D_2 optical molasses as a function of (a) the intensity of the cooling light and the detuning of (b) the cooling light and (c) the repumper light. The dashed black curve in (b) corresponds to the theoretical Doppler limit for the temperature of our sample. In these plots, the error bars correspond to one standard deviation of ten independent measurements. Image taken from [61].

value, and if longer we start losing atoms.

Under these conditions, we are able to cool down about 6 $\times 10^8$ atoms at approximately 500 μK. The dashed black curve in figure 3.8(b) shows the theoretical Doppler limit (equation 2.46), our experimental points are always above it. As discussed in section 2.2.5, for other elements such as rubidium or cesium, it is observed not only that the Doppler limit is reached but even sub-Doppler temperatures are attained due to the emergence of the Sisyphus sub-Doppler cooling mechanism [53][54]. For lithium, this molasses scheme is not very efficient because the hyperfine levels of the state $2^2P_{3/2}$ cannot be well resolved, since their separation is smaller than Γ. This limits the efficiency of the cooling process and keeps the sample well above the Doppler limit. The increase of the phase space density is also not very good, and we improve only by a factor of 2, being of the order of PSD $= 1 \times 10^{-7}$. For this reason, we apply a second laser cooling technique that utilizes the transitions of the D_1 line, known as gray molasses, that allows true sub-Doppler cooling [55].

D1 gray molasses sub-Doppler cooling: Gray-molasses cooling is a two-photon process in Λ-configuration (see figure 3.4) which combines both, Sisyphus cooling [54] and Velocity Selective Coherent Population Trapping (VSCPT) [56] as cooling mechanisms (more details in section 2.2.5).

In our experiment, we implement this cooling stage immediately after the D_2 molasses stage. We specifically use the D_1 transition frequencies $2^2S_{1/2}$(F = 3/2) $\rightarrow$ $2^2P_{1/2}$(F' = 3/2), which we call "cooling" frequency, and $2^2S_{1/2}$(F = 1/2) $\rightarrow$ $2^2P_{1/2}$(F' = 3/2), which we call "repumper". This nomenclature is inherited by the standard molasses. Both frequencies will be detuned, the cooling frequency by δ_1 and the repumper light by δ_2. Another important parameter is the difference between these detunings that we define as $\delta = \delta_1 - \delta_2$.

To characterize the gray-molasses we start by fixing $\delta_1 = +5.7\ \Gamma$ and keeping the repumper intensity low, at about $I_{rep} \approx 0.06 I_{sat}^{D_1}$, while the cooling intensity at its maximum value of the order of $I_{cool} \approx I_{sat}^{D_1}$. The saturation intensity for the D_1 line is $I_{sat}^{D_1} = 7.59\ \mathrm{mW/cm^2}$. We next measure the number of atoms and the temperature of the sample as the detuning difference δ varies. The results are shown in figure 3.9.

We can see that the temperature follows a Fano-like profile, reaching a minimum at $\delta = 0$ (i.e. at $\delta_1 = \delta_2$), the so called Raman condition, in which the temperature is as low as 40 μK. Although the number of atoms does not reach its maximum at the Raman condition but at $\delta \approx -0.25\ \Gamma$, we still have a very good efficiency of the process at $\delta = 0$, being able to cool about 75% of the atoms. These results are expected, as previously reported for the case of ^{6}Li [55]. Notice that the graph figure 3.9 has no data points in the interval $0.4 < \delta < 0.8$, as explained in reference [55], in this range the energy of the dark state becomes larger than the energy of the bright state and in consequence the VSCPT process significantly heats the cloud. In this range the temperature becomes so high that time-of-flight measurements become very difficult to analyze and the measurement of N and T cannot be performed. Notice how the error bars of the data around that range consistently increase.

We also measure the effect of changing the cooling detuning δ_1 while keeping the Raman condition $\delta = 0$. Both the number of atoms and the temperature remain con-

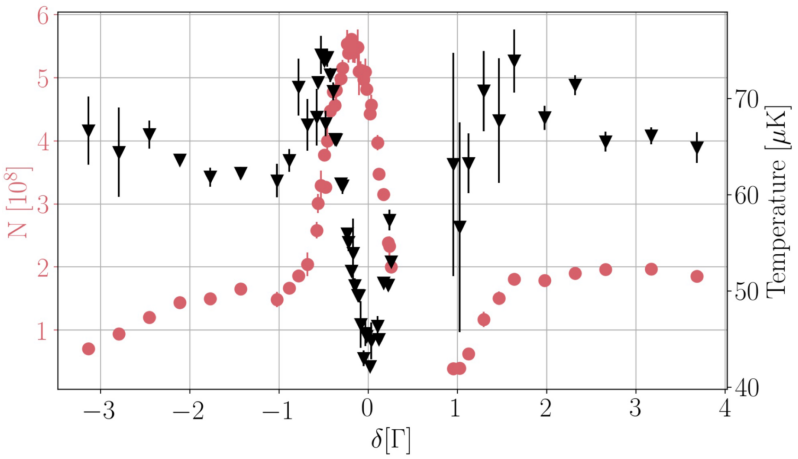

Figure 3.9: Number of atoms (red dots) and temperature (black triangles) of the sample as a function of the detuning between cooling and repumper light during gray molasses sub-Doppler cooling stage. The error bars correspond to one standard deviation of ten independent measurements. Image taken from [61].

stant in a wide interval of frequencies, showing the robustness of the gray-molasses process. We keep $\delta_1 = +5.7\ \Gamma$ because the efficiency of our acousto-optic modulators is maximum at that value.

The duration of the gray molasses is also an important parameter. We observe that after 400 μs the efficiency of the process becomes nearly constant and obtain better results for a duration time of 1 ms.

For the next stages it is important to have all the atoms of the sample in the $F = 1/2$ hyperfine state of the ground state $2^2S_{1/2}$ because the Feshbach resonance that we will use is present between its two magnetic sublevels. To do so, we switch off the D_1 repumper light 50 μs before than the D_1 cooling light, so we manage to concentrate nearly 95% of the atoms in the $F = 1/2$ hyperfine level.

To summarize, all the important steps of the laser cooling procedure are presented in Table 3.1. At the end of all these processes, we are able to produce a sample containing about 4.5×10^8 atoms in the hyperfine $F = 1/2$ state at a temperature of 40 μK. The phase space density increased considerably to PSD $= 6.6 \times 10^{-6}$. This represents an excellent starting point for the subsequent cooling stages.

3.2.2 Cooling toward quantum degeneracy

After the D_2 and D_1 cooling stages the sample is ready to be transferred into a conservative potential (section 2.3.3) in which evaporative cooling (section 2.3.4) can be applied and quantum degeneracy is achieved. In the following sections we explain how this process is done in our setup.

Transference into the conservative trap

As explained in section 2.3.3, our trap is created as the composition of a single-beam optical dipole trap and a magnetic curvature, which provide, respectively, radial and axial confinement.

Cooling stage	**Parameter**	**Optimal Value**
MOT	$\partial B_z(z)/\partial z\|_{z=0}$	$28\,\mathrm{G/cm}$
	δ_{cool}	-8.6 Γ
	δ_{rep}	-8.4 Γ
	Loading time	8.6 s
	N	5×10^9 atoms
	T	7 mK
	PSD	4.7×10^{-8}
D_2 Molasses	δ_{cool}	-2 Γ
	δ_{rep}	-2 Γ
	I_{cool}	0.35 $I_s^{D_2}$
	I_{rep}	0.30 $I_s^{D_2}$
	Duration	$850\,\mu$s
	N	6×10^8 atoms
	T	$500\,\mu$K
	PSD	1×10^{-7}
D_1 Gray molasses	δ_1	+5.7 Γ
	δ_2	+5.7 Γ
	I_{cool}	$I_s^{D_1}$
	I_{rep}	0.06 $I_s^{D_1}$
	Duration	1 ms
	N	4.5×10^8 atoms
	T	$40\,\mu$K
	PSD	6.6×10^{-6}

Table 3.1: Optimized parameters of the optical cooling stages.

During the D_1 cooling process we ramp the optical dipole trap (ODT) from zero to 150 W in 7 ms. The beam is focused right at the center of the atomic cloud, as shown at the right figure 3.3. Once the power of the optical beam has reached its maximum value we ramp the Feshbach magnetic field to 832 G in 50 ms. This field corresponds to the unitary limit in which the scattering length diverges, which is optimal for the following evaporative cooling stage because the collision rate is maximized and the thermalization process is optimized as discussed at section 2.3.4.

When the magnetic field is ramped up, the $F = 1/2$ hyperfine state splits into the two states $|1\rangle$ and $|2\rangle$, where $|1\rangle$ has lowest energy for all magnetic fields. In the magnetic fields that we employ these states are well within the Paschen-Back regime, so the energy difference between them remains almost unchanged. Moreover, if the ramp of the magnetic field is adiabatic, both states are nearly equally populated, so we create a well balanced mixture.

The Feshbach field curvature provides an axial harmonic confinement of about $\omega_{x_{mag}} \approx 2\pi \times 11$ Hz. This confinement, of course, is negligible at the beginning of the ODT loading since at 150 W power the confinement provided by the optical trap is much higher, $\omega_{r_{ODT}} \approx 2\pi \times 10$ kHz and $\omega_{x_{ODT}} \approx 2\pi \times 87$ Hz (see equation 2.75), however, the magnetic confinement becomes more and more important as we apply the evaporative cooling process in which the power of the ODT laser beam is gradually decreased.

After the optical and magnetic fields have been ramped up we trap about 3×10^6 atoms in the conservative potential, which means that our trapping efficiency is of the order of 1%. We hold the atoms in this trap for 20 ms more to let them settle in the minimum of the potential. At this point we can implement the evaporative cooling process (section 2.3.4), which is the last step before reaching quantum degeneracy. The temperature of the sample is difficult to measure because the geometry of the trap is very elongated so time-of-flight imaging is impractical. However, since the trap increases the density of the sample, we estimate a considerable increase of the temperature of the sample to about 200 μK. Figure 3.10 shows an absorption image of the atoms from the sub-Doppler cooled sample transferred into the ODT beam.

Evaporative cooling

Evaporative cooling is performed by ramping down the ODT power while keeping the magnetic field at 832 G. As we discussed in section 2.3.4, to achieve runaway evaporation it is fundamental that the collision rate does not decrease as the atoms are evaporated, this means that the density of the cloud needs to increase as its temperature is reduced. To guarantee this condition the evaporation process must be performed slow enough for thermalization to occur. At the same time, the evaporation has to be the main loss process, so it cannot be too slow for the background-vapor collisions with the sample to be important. A good quantity to evaluate the effectiveness of the evaporation process is the phase space density PSD, which must increase as the evaporation is applied [58].

The evaporative process is performed by concatenating three exponential ramps, as shown in the blue curves of figure 3.11. The first ramp goes from 160W to 35W in 300 ms having a characteristic time of $\tau_1 = 125$ ms (dotted curve); the second ramp, from 35 W to 10 W in 1000 ms, with $\tau_2 = 440$ ms (dashed curve), and finally,

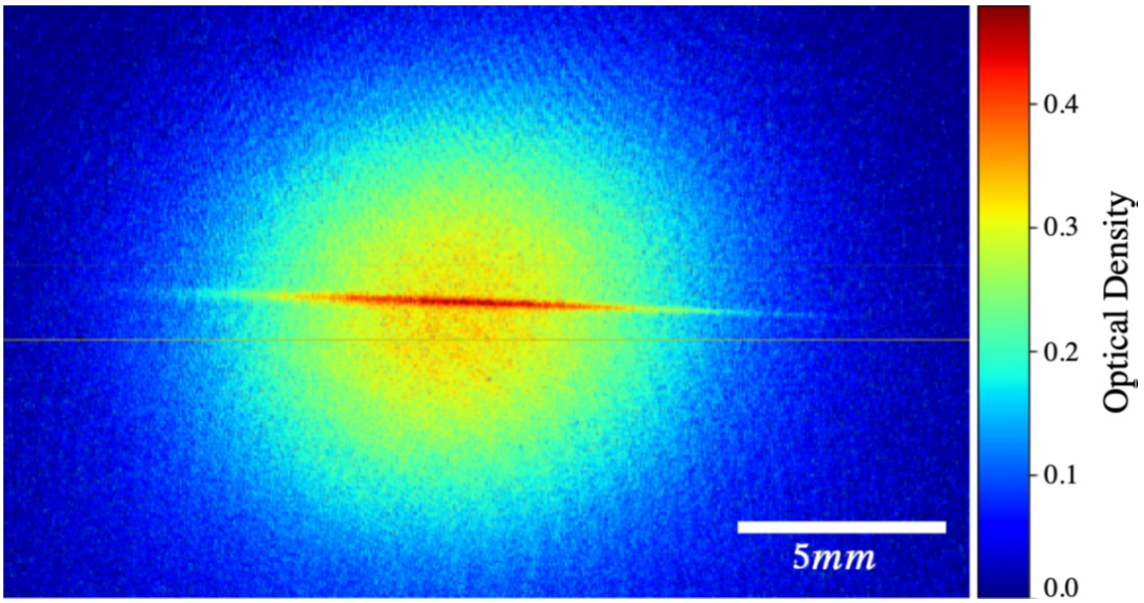

Figure 3.10: Absorption imaging of the atoms transferred to the optical dipole trap (horizontal darker region) from the laser sub-Doppler cooled sample (round lighter region). The color gradient corresponds to the optical density of the sample according to the color bar on the right. Image taken from [61].

a very slow ramp from 10 W to $P_0 = 35$ mW in 2.6 s, with $\tau_3 = 2000$ ms (solid curve). The value of P_0 is variable, depending the target sample temperature as we will discuss, but around the order of 35 mW. The total duration of the evaporation process is 3.8 s. These parameters are determined by maximizing the phase density of the system. The black data points in figure 3.11 shows how the measured PSD increases as the evaporation proceeds. Notice that PSD ≥ 1 at the end of the last ramp, indicating the onset of quantum degeneracy.

At the end of the third evaporation ramp we adiabatically ramp the Feshbach field to the corresponding value in order to produce a sample in any desired interaction regime across the Feshbach resonance, this magnetic ramp lasts about 300 ms. The regimes that we explore are within the interval of 670 to 900 G, which contains the BEC-BCS crossover.

By changing the value of the Feshbach field we also modify the curvature of the magnetic field, however it changes less than a 10% within the mentioned interval of interest, which means that we do not significantly modify the geometry of the trap as we change the scattering length. Of course, as can be seen in equation 2.73, the frequencies of the trap depend on the power P_0 of the ODT, which, in turns determines the temperature and degree of degeneracy of the sample.

After the evaporative cooling process we are able to produce quantum degenerate superfluid samples containing about $N = 5 \times 10^4$ atomic pairs at a temperature of the order of $T/T_F = 0.1$ (which corresponds for this value of N to approximately 20 nK) and a phase space density well above the unity, of the order of PSD ≈ 10, demonstrating the fully degenerate nature of our sample. The trap frequencies are $\omega_r \approx 2\pi\times$ 163 Hz and $\omega_x \approx 2\pi\times$ 11 Hz, which means that our sample is cigar-shaped with an aspect ratio of the order of 1:15 (figure 2.11). The duty cycle of our

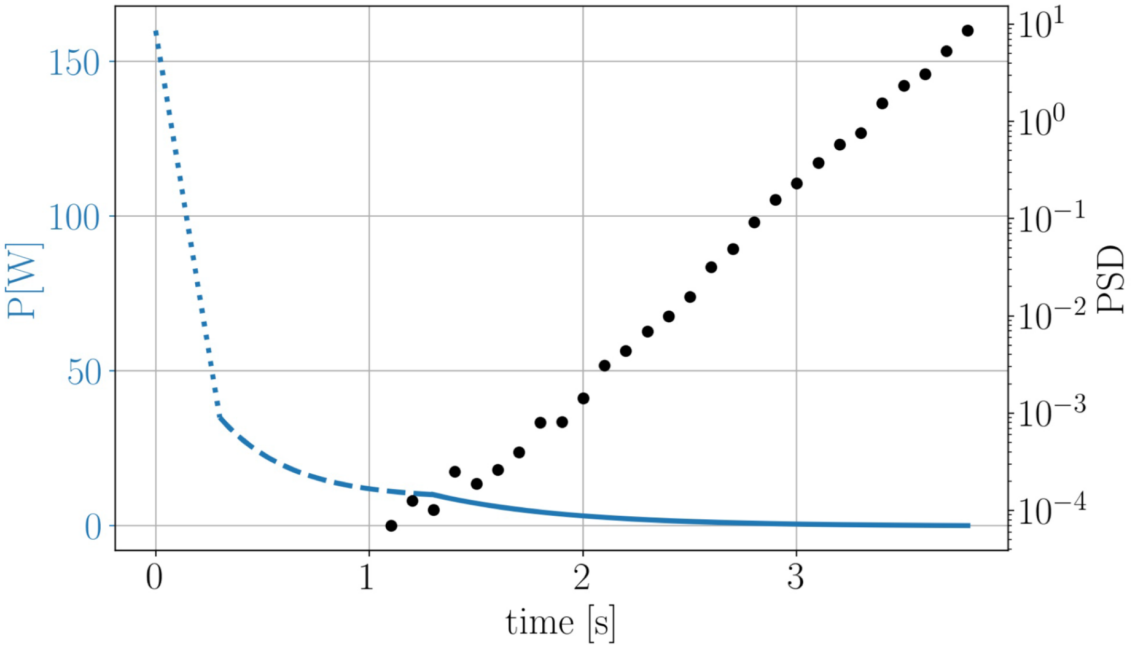

Figure 3.11: Evaporation ramps performed by decreasing the power of the optical dipole trap (blue curves). See text for details. Measurement of the phase space density of the system during evaporation (black data points). The error bars, although not visible at this scale, correspond to one standard deviation of ten independent measurements. Image taken from [61].

experiment is shorter than 14s.

Superfluids across the BEC-BCS crossover

As mentioned in the previous section, we select the interacting regime of the produced sample at the end of the last evaporation ramp by means of the Feshbach resonance that allows us to set the value of the scattering length a_s. As explained in Section , we are able to produce and probe samples at practically any magnetic field up to 1200 G. Specifically, as we explain below, we are able to produce ultracold superfluid samples within the interaction range of $7.6 \geq \frac{1}{k_F a_s} \geq -0.65$, which means that we can produce samples from the deep (weakly interacting) BEC regime to the strongly interacting BCS regime, passing, of course, through unitarity at $\frac{1}{k_F a_s} = 0$. Clearly, we have access to most of the crossover region, $1 > \frac{1}{k_F a_s} > -1$, corresponding to the magnetic field interval 790 to 900 G.

Evidently, the most important point here is to achieve, at every interacting regime, temperatures that are below the critical superfluid temperature, T_C. On the deep BEC side, $\frac{1}{k_F a_s} > 1$, the critical temperature is approximately T_C^{BEC}=$0.52T_F$ and it is nearly independent of the scattering length [69]. The minimum temperature attainable in our experiment, $T/T_F = 0.1$, remains well below T_C^{BEC}. In this case, the density profile of the cloud exhibits the very characteristic bimodal distribution. The condensed fraction presents a parabolic sharp density profile that arises from the Thomas-Fermi approximation (section 1.3), while the non-condensed thermal atoms follow a gaussian Maxwell-Boltzmann distribution, which we use to estimate the temperature of the cloud in time-of-flight (TOF) imaging [67]. These features

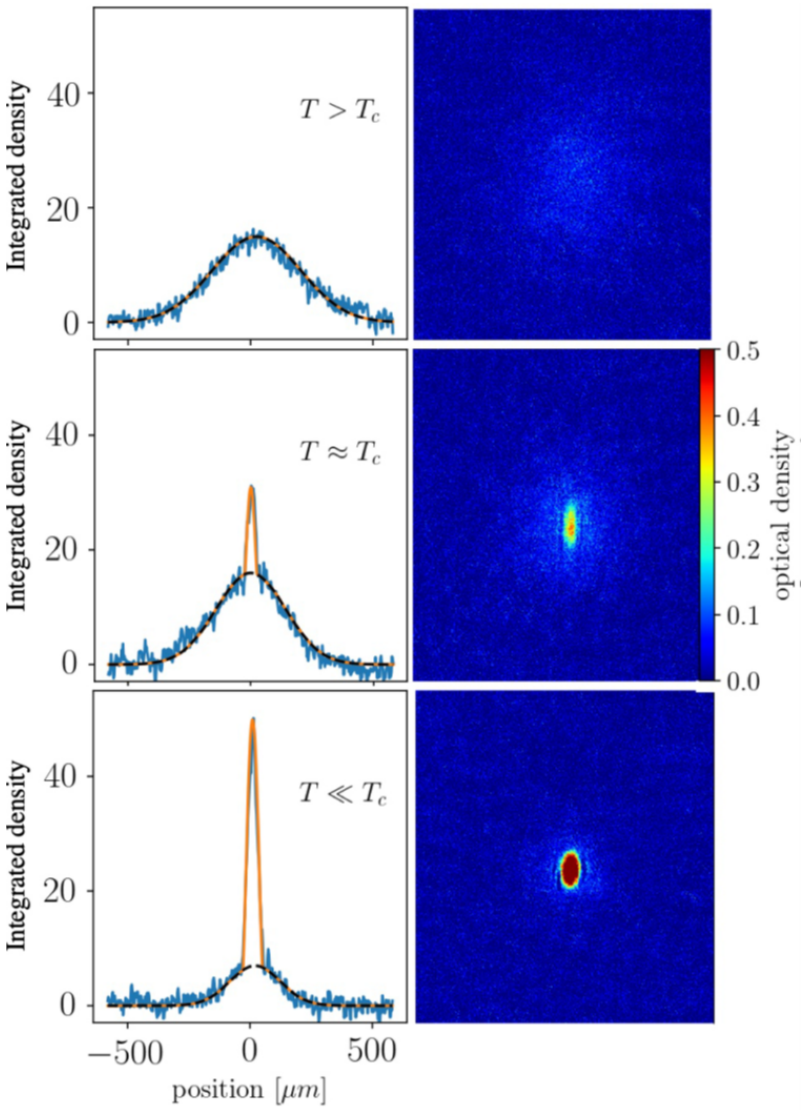

Figure 3.12: Absorption images of the atomic samples (right pictures) and their corresponding integrated density profile (left graphs) as temperature is decrease. Upper panels: thermal gas above critical temperature T_C. Middle panels: gas just below the critical temperature, notice the bimodal gaussian-parabolic distribution. Lower panels: molecular Bose-Einstein condensate well below the critical temperature, the parabolic distribution is dominant and the gaussian one is barely noticeable. The color gradient corresponds to the optical density of the gas. All pictures were taken after a time-of-flight of 15ms. In the graphs, the dashed black line corresponds to a fitting of only the gaussian wings, while the orange solid line to the bimodal distribution. Image taken from [61].

can be seen in figure 3.12. The weakest interacting BEC that we can produce corresponds to a magnetic field of 670G for which $a_s = 1080\ a_0$ and $\frac{1}{k_F a_s} = 7.6$. For lower magnetic fields the lifetime of the molecular condensate is too short to perform any typical experiment (it is shorter than 100 ms, while in any other regime described here, it is of the order of 1.5 s).

As the scattering length increases, within the BEC-BCS crossover range, and specially right at unitarity, this well defined bimodal distribution starts to wash out and becomes broader due to strong interactions [35, 70]. In this regime, it is not possible to discriminate between the superfluid fraction and the thermal fraction, and the density profile looks nearly Gaussian. However, we know that we are in the superfluid regime due to the following consideration. On the vicinity of the unitary limit the critical temperature is given by $T_C^U \approx 0.167\ T_F$ [71], which again, is above the temperature of our sample.

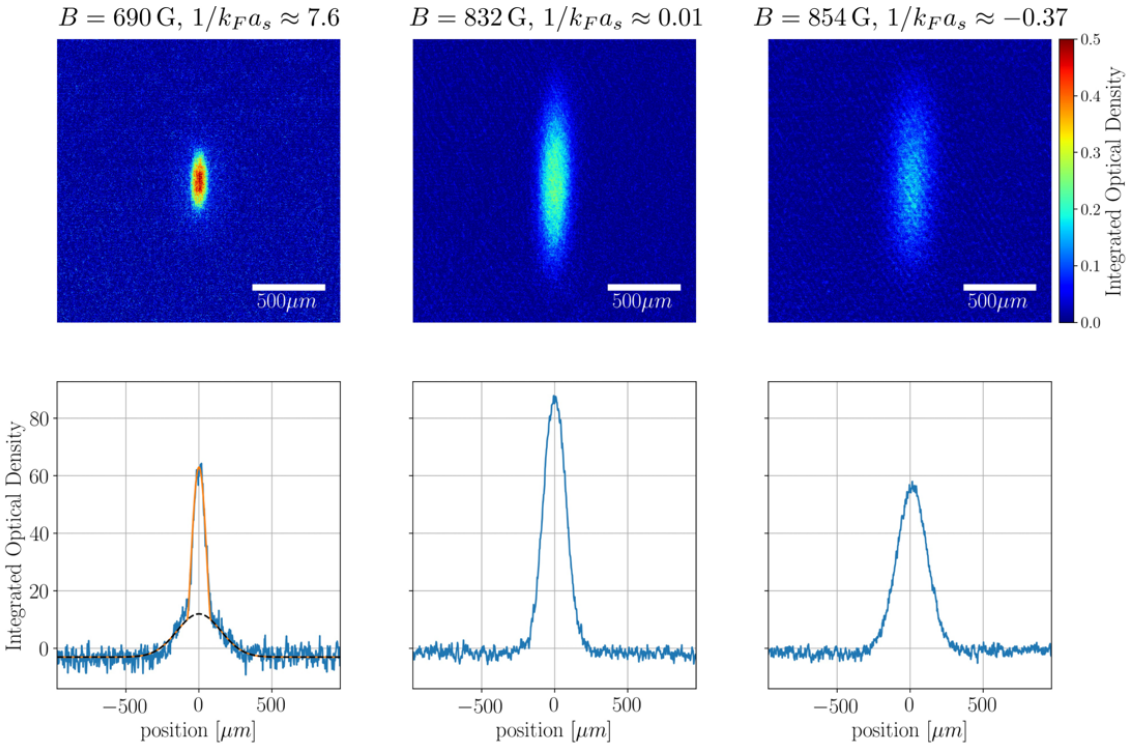

Figure 3.13: Absorption images of quantum degenerate atomic samples (upper pictures) and their corresponding integrated density profile (lower graphs) as the scattering length is varied across the BEC-BCS crossover. Left panels: Bose-Einstein condensate of molecules at $\frac{1}{k_F a_s} \approx 7.6$, the bimodal and gaussian fits are shown as a orange solid and black dashed lines, respectively. Middle panels: superfluid gas at unitarity at $\frac{1}{k_F a_s} \approx 0.01$. Right panels: ultracold gas at the BCS side of the Feshbach resonance at $\frac{1}{k_F a_s} \approx -0.37$. The color gradient corresponds to the optical density of the gas. All pictures were taken after a time-of-flight of 20 ms. Image taken from [61].

In contrast, on the BCS side of the crossover, the critical temperature is given by [23][24] $T_C^{BCS} \approx 0.28\ T_F e^{-\pi/2|k_F a_s|}$ so it exponentially decays as the quantity $|k_F a_s|$ increases. For instance, at $\frac{1}{k_F a_s} = -0.65$, the critical temperature for the superfluid state is $T_C^{BCS}/T_F \approx 0.1$, which is comparable to the minimum achievable tempera-

ture of our setup. In consequence, we cannot access the deep (weakly interacting) BCS superfluid regime because the critical temperature is below the technical limit of our experiment. This means that in our setup, superfluid regimes are attainable within the range $7.6 \geq \frac{1}{k_F a_s} \geq -0.65$. Figure 3.13 shows a sequence of absorption images of a superfluid at $T_C^{BCS}/T_F = 0.1$ containing $N = 5 \times 10^4$ atomic pairs, as the scattering length changes from the BEC to the BCS regimes across the crossover.

Besides the considerations concerning the critical temperature that we have presented here, we have also performed an additional measurement that ensures that all the observed regimes present superfluidity. Right after releasing the atoms from the trap, we have performed a fast Feshbach magnetic field ramp from the strongly interacting regimes into the deep BEC side [23][24]. As result of this ramp, the many-body wave function of the system is projected onto the far BEC side of the resonance. In all cases we observe the characteristic BEC bimodal distribution in the density profile, indicating that at unitarity and its vicinity we always have condensation of atomic pairs.

We have presented the experimental setup and methods we use to produce and study ultracold fermionic superfluid samples of ^{6}Li. We are able to generate samples containing 5×10^4 atomic pairs at temperatures as low as $T/T_F = 0.1$ at any superfluid regime across the BEC-BCS crossover within a duty cycle shorter than 14 s. Our setup combines versatile and state-of-art techniques, such as the TAP technique, which is the main topic of this thesis.

As we discuss in the following chapters, we develop and implement time-averaged optical potentials which permit us to change the size of the optical trap, allowing us to have more control in the density variable. Also the TAP technique allow us to alter the geometry of the trap precisely. It is possible to "paint" different trapping potentials, for example a double-well, a box potential and a harmonic potential, which will allow us to study different aspects of quantum matter.

Chapter 4

Time-averaged optical potentials

Efficient transference of atoms into the ODT is needed to produce large enough quantum gases. An important variable to have an efficient transfer is the size of the trap. On the one hand, a tight trap will not overlap sufficiently with the initial atom cloud and it can even heat up the atoms due to the high intensity as we discuss at section 2.3.1. On the other hand, wide traps have low trapping frequencies which translate to low densities of the sample. This is disadvantageous as we conclude at the end of section 2.3.4, since high collisional rates necessary for evaporative cooling requires high densities.

By considering equation 2.73 one can see that the only free parameter that allows manipulation (other than the laser's power which is used to do the evaporation) is the beam's waist. Hence, finely changing the waist size allows us to have both the advantages of narrow and wide traps. Nevertheless the waist size is intrinsically related to the focal length of the lens that creates the ODT so it cannot be changed so simply. A clever solution to this is to create a time-averaged potential, in order to control the size of beam waist.

The basic idea to control the size of the beam waist involves rapidly modulating the position of the laser beam focus. The timescale of the modulation is much faster than the radial trap frequency. By doing so the atoms do not respond to the "instantaneous" motion of the beam and instead "see" a potential proportional to the time-averaged intensity profile. We will refer to this method as TAP, from "Time-Averaged Potential". The modulation, which we call modulation function $f(t)$, has a specific form for each desired TAP. The inspiration for this technique is based on the article of Gupta et. al. [72].

In this chapter we discuss in detail the TAP technique and its experimental implementation in section 4.1. Later, in section 4.2, we discuss how calculate TAP for some basic modulation functions $f(t)$. In section 4.3 we develop a method to calculate the modulation function $f(t)$ necessary to obtain any desired TAP, with special emphasis to the harmonic potential. At the end, in the case of harmonic potential, we observe that the trap depth is reduced depending the modulation. We characterize this behavior in section 4.4.

4.1 TAP technique

The ODT frequencies at high power (150 W), which are used during the beginning of evaporation, are $\omega_{r_{ODT}} \approx 2\pi \times 10$ kHz and $\omega_{x_{ODT}} \approx 2\pi \times 87$ Hz (see equation 2.75). The frequency of the modulation $f(t)$ need to be at least some order of magnitude larger than this trap frequencies to ensure a time-averaged potential [72].

There are different methods to modulate the center position of the beam at time-scales faster than the trap frequencies of the ODT. One useful approach is using active optical devices like acousto-optic modulators (AOM), acousto-optic deflectors (AOD) or electro-optical deflectors (EOD).

Since AOMs are suitable for high power (in contrast to EODs) and we already have an AOM in our experiment, which is used to control the evaporative cooling process, we decided to use this AOM in order to implement the TAP technique.

A briefly introduction about the physics of the AOM is given at subsection 4.1.1.

4.1.1 AOM

An AOM consists of a crystal (e.g. TeO_2) attached to a radio-frequency (RF) transducer, which in turn is connected to a high-power RF source. This setup produces high-frequency sound waves in the crystal i.e. a density modulation associated to the sound wave vector $\vec{k}_s$ as shown in the left side of figure 4.1. Effectively the RF makes the crystal behave as a diffraction grating with lattice pattern $D = 2\pi/k_s$ then, an incident laser beam with wavelength $\lambda = 2\pi/k_L$ will experience Bragg diffraction $m\lambda = 2D \sin\theta_B$, with the first-order ($m = 1$) diffracted beam travelling at an angle $\theta_B = \arcsin(k_s/2k_L)$ with respect to the incident beam, where θ_B is called the Bragg angle. Hence, for small angles we find that the deflection is proportional to the RF frequency $\theta_B \propto c_s k_s \equiv \omega_{RF}$, where c_s is the speed of sound in the crystal (section 14.10 of [73]).

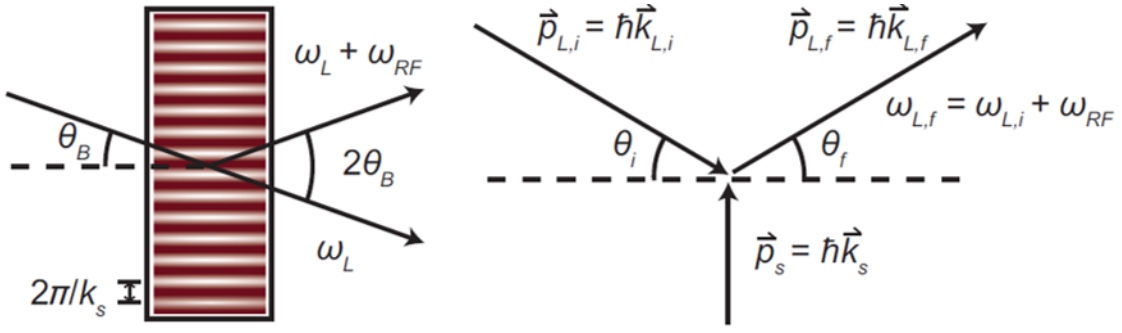

Figure 4.1: Bragg scaterring in an AOM (left). A sound wave in the crystal creates a periodic modulation of the refractive index, which produces Bragg diffraction in a laser beam with angle θ_B for the first order. This process can be analyzed through the photon-phonon picture (right). Here a initial photon of frequency $\omega_{L,i}$ and momentum $\hbar\vec{k}_{L,i}$ experiences Bragg diffraction by the absorption of a phonon of frequency ω_{RF} and momentum $\hbar\vec{k}_s$.

As seen in the right side of figure 4.1, this process can also be analyzed at the level of photon-phonon interactions. An incident photon with wave vector $\vec{k}_{L,i}$ absorbs

a phonon with wave vector $\vec{k}_s$, resulting in a scattered photon with wave vector $\vec{k}_{L,f}$. The momentum and energy conservation conditions imply that $\vec{k}_{L,i}\cos\theta_i = \vec{k}_{L,i}\cos\theta_f$, $\vec{k}_s - \vec{k}_{L,i}\sin\theta_i = \vec{k}_{L,i}\sin\theta_f$ and $\omega_{L,f} = \omega_{L,i} + \omega_{RF}$. Using the approximation that $\omega_{L,f} = \omega_{L,i}$ due to $\omega_{RF}/\omega_{L,i} \approx 90\text{MHz}/300\text{THz} \approx 3 \times 10^{-7}$ we get that $k_{L,f} = k_{L,i}$ which results, through the first momentum conservation equation, in $\theta_i = \theta_f \equiv \theta_B$. Under this theoretical frame, we can understand higher-order diffraction as multi-phonon absorption, and negative-order diffraction as phonon-emission into the crystal by photons (section 14.10 of [73]).

4.1.2 TAP technique

As a summary from the previous section, we have that an AOM with an induced acoustic wave diffracts a laser beam at an angle θ_B proportional to the frequency of such wave, ω_{RF}.

If we dynamical change the signal $\omega_{RF}(t)$, we get a time-dependent Bragg angle $\theta_B(t)$. Let us consider that we vary the frequency of the RF signal through the formula $\omega_{RF}(t) = \omega_{RF,0} + \delta\omega_{RF} f(t)$, so we vary ω_{RF} around a central value $\omega_{RF,0}$ through a periodic modulation function $f(t)$ and with an amplitude $\delta\omega_{RF}$. Then, we get a time-dependent Bragg angle of the form $\theta_B(t) = \theta_{B,0} + \delta\theta_B f(t)$. In other words,

$$\theta_B(t) \propto \omega_{RF}(t) = \omega_{RF,0} + \delta\omega_{RF} f(t)$$

Now, we can employ a lens to transform the angular displacement $\theta_B(t)$ into a transverse displacement $d(t)$ from the focal point. Suppose we use a lens with a focal length f_1. If we place such lens along the optical path of the diffracted beam of the AOM at a distance f_1 apart from the AOM, the diffracted beam will be focused on the focal plane of the lens, which is orthogonal to the beam and separated from the lens by exactly a focal length f_1. As we change the frequency ω_{RF}, the angle of the diffracted beam will change accordingly but the beam will remain focused on same focal plane, translated by a distance d from the original focal point. Hence, we can dynamically control d by changing the value of ω_{RF}. In other words, this special configuration has the property to transform angular displacement $\delta\omega_{RF} f(t)$ into transverse displacement $d(t)$.

We use this idea with the ODT beam to implement a time-averaged potential. In this case, if the modulation function $f(t)$ is fast enough (i.e. if the characteristic time of $f(t)$ is much shorter than the inverse of the trap frequencies), the trapped atoms will experience a static trap spread over the distance d, rather than a moving trap.

Figure 4.2 illustrates these ideas. In this scheme, the initial Gaussian beam is collimated before the AOM. Here, we show two paths of the first-order beam deflected at time t and $t + \delta t$, which varies in time due to time-dependent Bragg angle $\theta_B(t) \propto \omega_{RF}(t) = \omega_{RF,0} + \delta\omega_{RF} f(t)$.

The next step is to establish an algorithm to calculate the form of the modulation $\omega_{RF}(t)$ to create any desired potential.

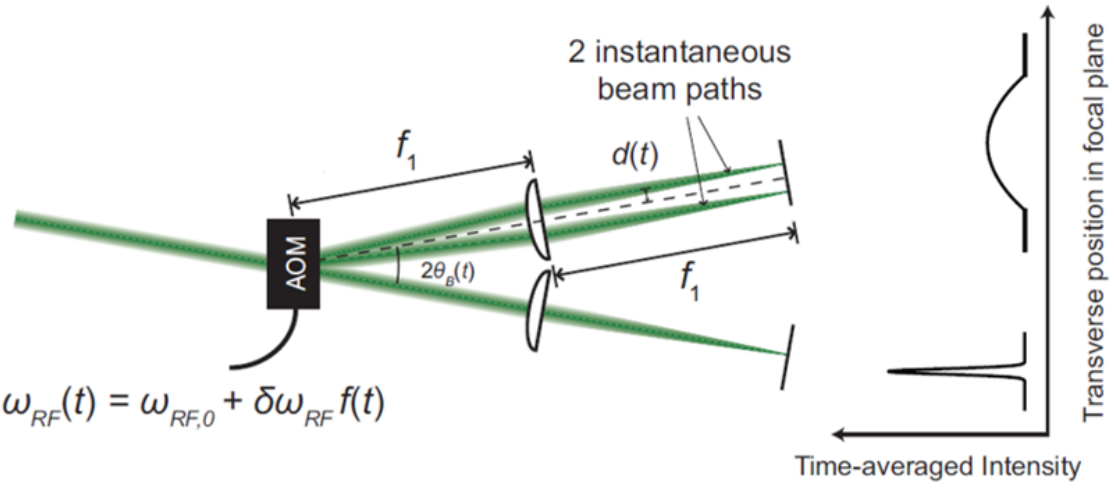

Figure 4.2: Painting with an AOM. The time-dependent AOM driving frequency $\omega_{RF}(t)$ results in a time-dependent Bragg diffraction angle $\omega_B(t)$. Through a suitable FM waveform $f(t)$, one can create arbitrary time-averaged intensity profiles. The focal length f_1 of the lens placed after the AOM determines the conversion of amplitude $\delta\omega_{RF} f(t)$ to amplitude $d(t)$.

4.2 Calculating time-averaged potentials

We now move on to calculate the form of the resulting time-averaged intensity profile. Without loss of generality, we assume that the TAP displacement takes place along the y-direction. Consider an AOM driving RF signal with carrier frequency $\omega_{RF,0}$, FM waveform $f(t)$ and amplitude $\delta\omega_{RF}$. This results in time-dependent transverse shift in the position of the focus described by $\tilde{y}(t) = y - hf(t)$ in the focal plane. The function $f(t)$ is periodic with frequency ω_{mod} (which has to be much faster than the trap's radial frequency) bounded between -1 and 1. Also, we will refer to h as the TAP amplitude. That said, the time-average intensity profile is given by

$$\bar{I}(y,z,x) = \frac{\omega_{mod}}{2\pi} \int_0^{2\pi/\omega_{mod}} I(y - hf(\tau), z, x) d\tau, \tag{4.1}$$

where $I(y,z,x)$ is the intensity of a Gaussian beam given by the equation 2.69. As we will discuss later on, the conditions over $f(t)$ ensure that it is equivalent to calculate the TAP for half an oscillation period π/ω_{mod} (and trivially, for multiples of that quantity $n\pi/\omega_{mod}$).

A general analytic integration of equation (4.1) for every modulation function $f(t)$ does not exist, therefore it needs to be calculated numerically, as we present at the end of this section.

In particular, there are some particular solvable examples such as the triangular- and square-wave modulation, which we will now explore.

4.2.1 Analytical calculations

Substituting the gaussian beam intensity given by equation 2.69 we can compute the time-average profile at equation (4.1) over two triangular-wave periods obtaining

$$\begin{aligned}\bar{I}(y,0,0) &= \frac{I_0}{2T}\int_{-T}^{T} e^{-2(y-h\tau/T)^2/w_0^2}d\tau \\ &= \sqrt{\frac{\pi}{2}}\frac{I_0 w_0}{4h}\left[\mathrm{erf}\left(\frac{\sqrt{2}(y+h)}{w_0}\right) - \mathrm{erf}\left(\frac{\sqrt{2}(y-h)}{w_0}\right)\right], \end{aligned} \tag{4.2}$$

which is plotted in figure 4.3. We see that for large values of h the triangular wave creates a one-dimensional box potential near the center.

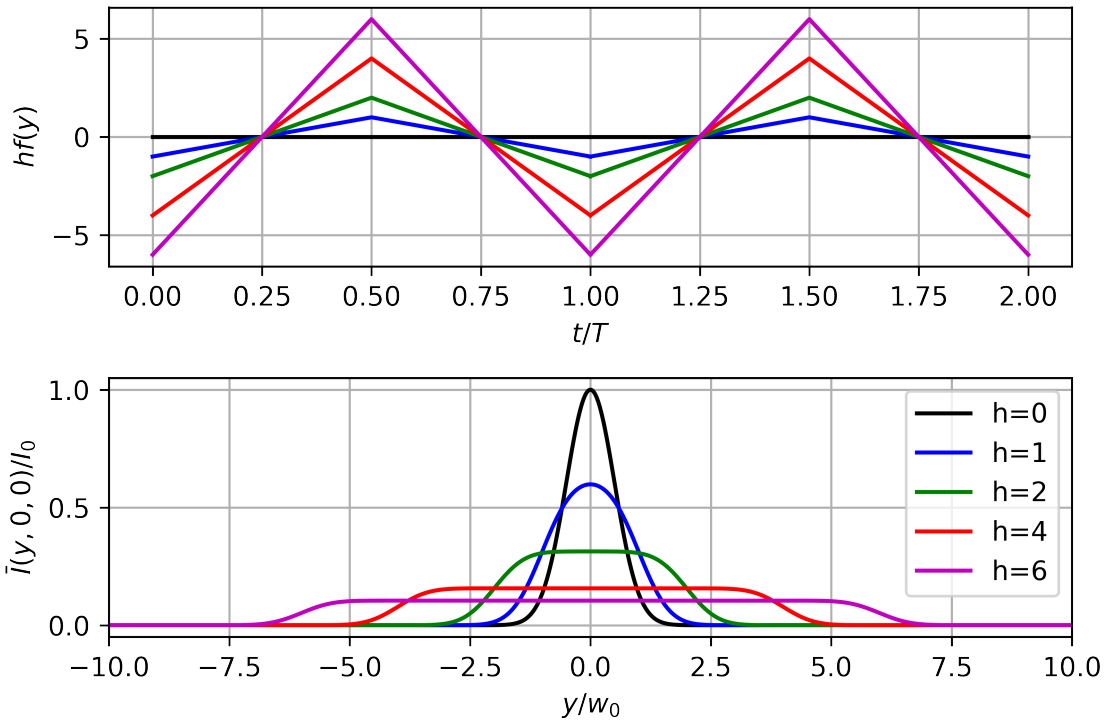

Figure 4.3: Analytically calculated time-averaged potential for a triangular wave modulation at different amplitudes (below). For large values of h (above) the triangular wave produces a box-like potential. The amplitude h for each triangular wave modulation is given in units of the Gaussian beam waist w_0.

Another time-averaged potential that can be calculated analytically is using the square-wave modulation. A square-wave over the first half-period can be analytical expressed as $h\mathrm{sgn}(\tau - T/4)$ where $\mathrm{sgn}(t)$ is a sign function. Integrating equation (4.1) over the first half-period results in

$$\begin{aligned}\bar{I}(y,0,0) &= \frac{I_0}{T/2}\int_{0}^{T/2} e^{-2(y-h\mathrm{sgn}(\tau-T/4))^2/w_0^2}d\tau \\ &= \frac{I_0}{T/2}\left[\int_{0}^{T/4} e^{-2(y+h)^2/w_0^2}d\tau + \int_{T/4}^{T/2} e^{-2(y-h)^2/w_0^2}d\tau\right] \\ &= \frac{I_0}{2}\left[e^{-2(y+h)^2/w_0^2} + e^{-2(y-h)^2/w_0^2}\right], \end{aligned} \tag{4.3}$$

which is the sum of two Gaussian beam profiles with the same waist size as the original one, centered in $-h$ and h respectively. Nevertheless each profile has only half of the original center-intensity I_0. This profile is of particular interest because it can be used to generate a double-well trap, as shown in figure 4.4.

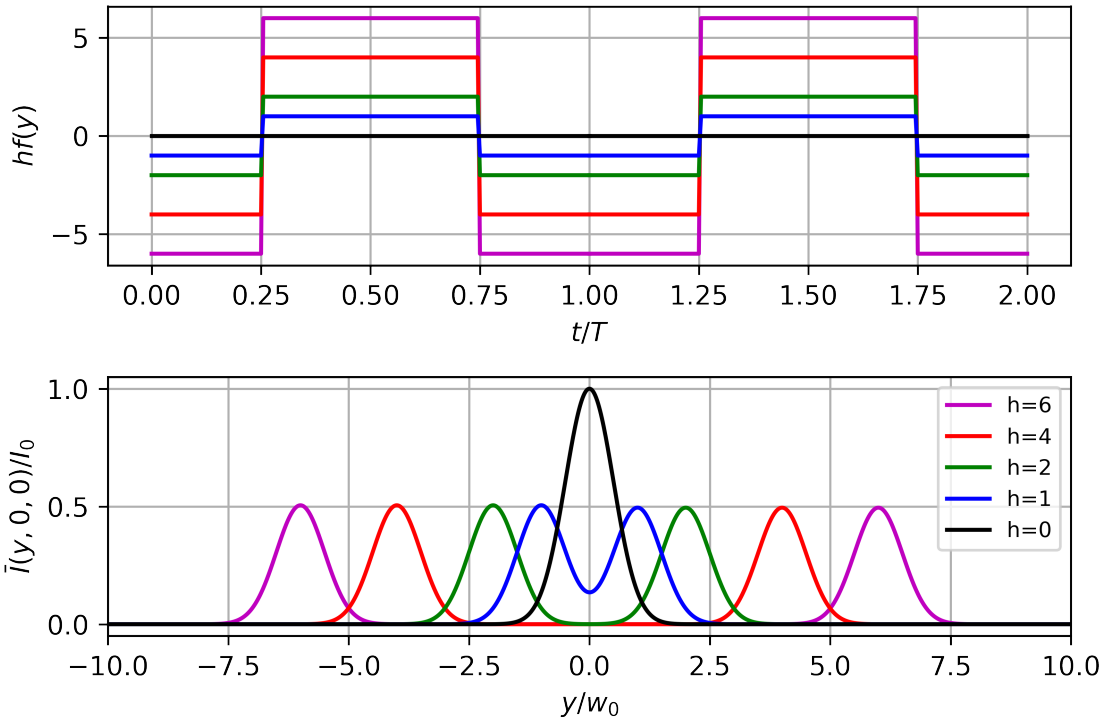

Figure 4.4: Analytically calculated time-averaged potential for a square wave modulation at different amplitudes (below). The amplitude h for each square-wave modulation (above) is given in units of the Gaussian beam waist w_0. For $h \gtrapprox 1$ the square-wave produces a double-well trap.

4.2.2 Numerical calculations

Alternatively we can calculate integral 4.1 numerically. If we do so for a sinusoidal-wave modulation it results in a double well-like trap which is plotted in figure 4.5.

4.3 Calculating the painting function

We have already shown how to calculate $\bar{I}$ using basic (and simple to experimentally implement) $f(t)$ waveforms (i.e. $f(t) \rightarrow \bar{I}$), but our goal is to do it the other way around. We want a method that allows us to determine the function $f(t)$ needed to create an arbitrary potential shape $\bar{I}$ (i.e. $\bar{I} \rightarrow f(t)$).

To find a recipe to determine the painting function $f(t)$ for a given $\bar{I}$, we use an approximate method where we consider the unpainted beam (the "paintbrush") to be a delta function in the y-dimension. Under that approximation, equation 4.1 integrated over a half period becomes

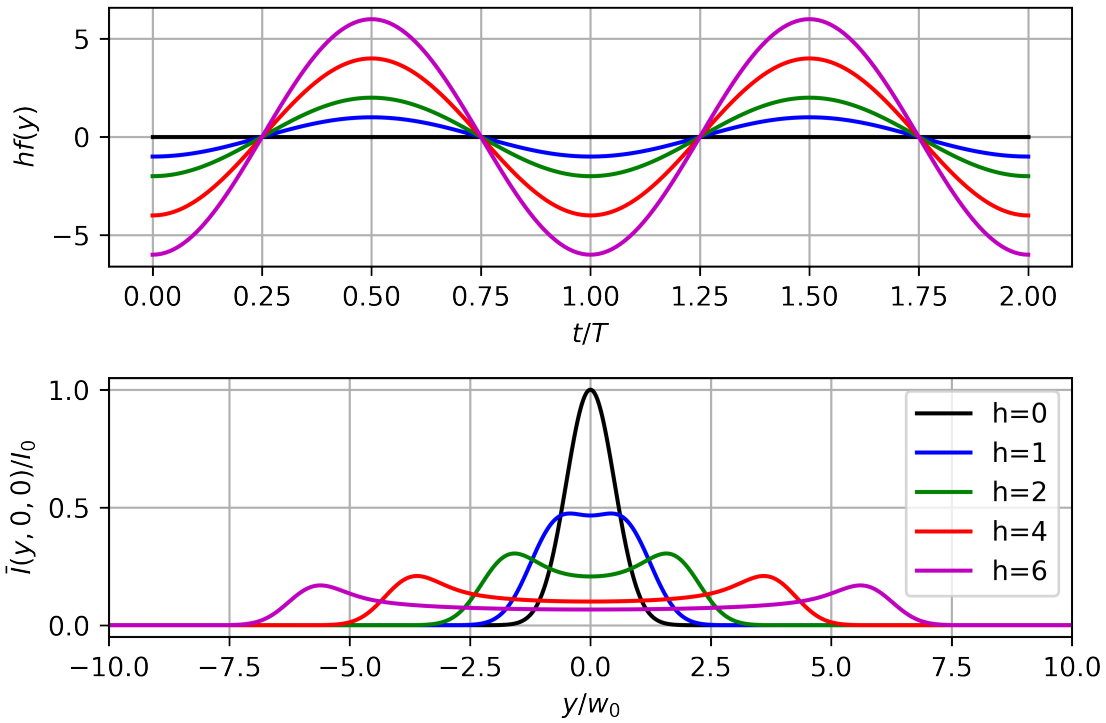

Figure 4.5: Numerically calculated time-averaged potential for a sinusoidal modulation at different amplitudes (below). The amplitude h for each sinusoidal-wave modulation (above) is given in units of the Gaussian beam waist w_0. For large values of h the sinusoidal wave produces a double well-like trap.

$$\bar{I}(y,0,0) = \frac{I_0}{T/2}\int_0^{T/2} \delta(y - hf(\tau))d\tau, \tag{4.4}$$

integrating by substitution where $u = y - hf(\tau)$ and using differentiation of the inverse function we get

$$\bar{I}(y,0,0) = \frac{I_0}{T/2}\int_{y+h}^{y-h} \delta(u)\frac{du}{-h\dot{f}(f^{-1}(\frac{y-u}{h}))} = \frac{2I_0}{T}\frac{1}{h\dot{f}(t)}. \tag{4.5}$$

In the last term we return to the original variables where t satisfies $u = 0 = y - hf(t)$. The expression $y = hf(t)$ seems pretty innocent but under our delta-paintbrush approximation it acquires meaning. It implies that the relation between the spatial coordinate y and time t of our paintbrush is no other than f scaled by a factor of h), which is what we wanted in the beginning.

Then, if we force make the equation (4.5) to be equal to our desired function g, we get

$$g(y) = \frac{\bar{I}(y,0,0)}{I_0} = \frac{2}{T}\frac{1}{h\dot{f}(t)}, \tag{4.6}$$

rearranging the terms and using again that $y = hf(t)$ we get

$$g(hf(t))h\dot{f}(t) = \frac{2}{T}, \tag{4.7}$$

integrating over t (using a dummy variable) and introducing the variable c to ensure "normalization" (needed to satisfy the conditions we imposed over g and f) we get

$$c\int_0^t g(hf(\tau))h\dot{f}(\tau)d\tau = c\int_{-h}^{y=hf(t)} g(Y)dY = \frac{2}{T}t. \tag{4.8}$$

Therefore our main goal is to solve equation 4.8 in order to find y. Once we have $y = hf(t)$, one must remember that, by hypothesis, the solution we obtained corresponds only to half a period, so we need to mirror that solution over the y-axis to obtain the other half thus creating a continuous function (following our analogy here *continuous* means that the paintbrush never separates from the canvas). Equation 4.8 can be solved analytically for some profiles. In the next subsection we exemplify how to analytically search for a particular waveform.

4.3.1 Analytical example

Our target function is $g(y) = (1+ay/h)\Theta(1-|y/h|)$ where Θ is a Heaviside function and $-1 \leq a \leq 1$. First we calculate the normalization constant c and then we integrate equation 4.8 at $t = T/2$

$$c\int_{-h}^{h=hf(T/2)} g(Y)dY = c\int_{-h}^{h}(1+aY/h)dY \tag{4.9}$$

$$\frac{2}{T}\frac{T}{2} = c\left[\frac{(1+a)^2}{2a/h} - \frac{(1-a)^2}{2a/h}\right] \tag{4.10}$$

$$1 = c\frac{h}{2a}\left[4a\right]. \tag{4.11}$$

So $c = 1/2h$. We now have everything we need to calculate $y = hf(t)$

$$\frac{1}{2h}\int_{-h}^{y}(1+aY/h)dY = \frac{1}{2h}\int_{-h}^{y}(1+aY/h)dY \tag{4.12}$$

$$\frac{2}{T}t = \frac{1}{2h}\left[\frac{(1+ay/h)^2}{2a/h} - \frac{(1-a)^2}{2a/h}\right] \tag{4.13}$$

$$4a\frac{2}{T}t + (1-a)^2 = (1+ay/h)^2 \tag{4.14}$$

$$\sqrt{4a\frac{2}{T}t + (1-a)^2} - 1 = ay/h \tag{4.15}$$

$$y = \frac{h}{a}\left(\sqrt{4a\frac{2}{T}t + (1-a)^2} - 1\right). \tag{4.16}$$

Where the time interval goes from $0 < 2t/T < 1$ (half a period). As we said before, we have to mirror our solution over the y-axis to obtain the other half of the function i.e. to complete the full period. The analytical waveform we calculated is plotted in figure 4.6. We also calculate the integral 4.1 numerically for the waveform and plot the resulting potentials shapes with solid-lines in figure 4.6. Dashed line curves are calculated using the delta-paintbrush approximation which, by construction, is the desired function $g(y) = \frac{w_0\sqrt{\pi/2}}{2h}(1+ay/h)\Theta(1-|y/h|)$ with its corresponding normalization factor. Notice that in the limit $a \to 0$ the FM waveform becomes a triangular wave as expected (black curve). This potential shape is of particular interest as the linear slope can be tuned to cancel the effect of gravity within the trapping region.

4.3.2 Numerical method and paramount example

Additionally, a situation where analytic solutions may not exist is possible. Therefore, we wish to have a generally applicable numerical algorithm for determining the desired function f.With this in mind we use $c\int_{-1}^{y} g(Y)dY = t$ (equation 4.8 with $T = 2$ and $h = 1$) as a guide. First we create a partition `Y=[y0,y1,...,yN]` which goes from `y0=-1.0` to `yN=1.0`. Then we calculate the integral of the desired function `g` numerically from `y0=-1.0` to each `Y[i]` and save that value as `T'[i]` in an array `T'`. In synthesis the algorithm is:

```
for i in [0,...,N]
     T'[i]=integrate(g,-1.0,Y[i])
end
```

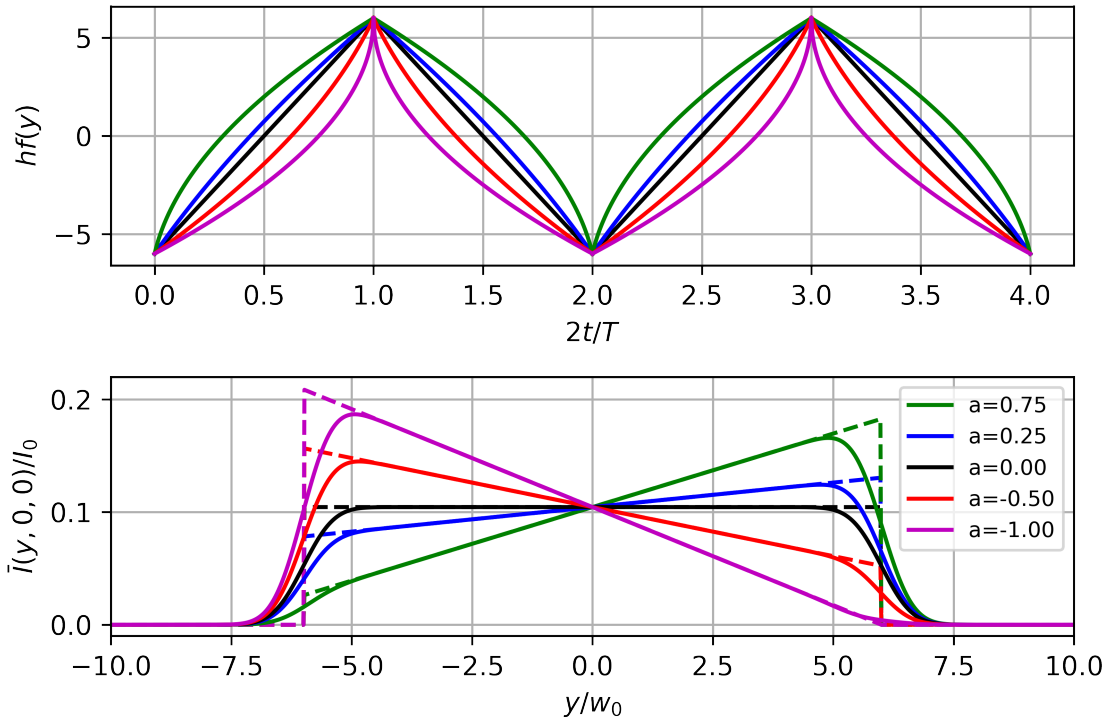

Figure 4.6: Analytically calculated waveform (above) used to obtain a linear-slope time-averaged potential with different inclinations (below). The resulting waveform is $y = \frac{h}{a}\left(\sqrt{4a\frac{2}{T}t + (1-a)^2} - 1\right)$ over half a period $0 < 2t/T < 1$ and then it is simply mirrored over the y-axis. We can create linear-slopes with negative and positive inclinations a. The amplitude of all the waveforms is $h = 6$ given in units of the Gaussian beam waist w_0. The solid line time-averaged potentials are calculated numerically from equation 4.1 and the dashed lines are calculated using the delta-paintbrush approximation. This potential shape is of particular interest because the linear slope can be tuned to cancel the effect of gravity within the trapping region.

Likewise, we need a normalization constant `c` just as in equation 4.8. Analogously `c` is equal to the integral over all the defined interval, i.e. from `-1.0` to `1.0` which corresponds to the last value of the array `T'` i.e. `T'[N]`. We normalize dividing all the elements in the array `T'` by `T'[N]` obtaining the normalized array, which we will call `T` and goes from `t0=0.0` to `tN=1.0`. Thus, we have obtained a binary relation between each element `Y[i]` and `T[i]`. This binary relation is our desired painting-function $f(t)$ defined as $f : \mathtt{T} \to \mathtt{Y}$.

To exemplify this method we will now calculate the waveform $f(t)$ needed to obtain a time-averaged potential with shape $g(y) = (1-(y/h)^2)\Theta(1-|y/h|)$ i.e. a parabolic potential. This waveform is of great relevance to us because we use a parabolic potential in most of our experiments. The main reason for this choice lies in the convenience to model the trap as a harmonic potential, as presented in section 2.3.2.

If we apply the delta-paintbrush approximation and use equation 4.8, we find that we need to solve the equation

$$\frac{3y}{4h} - \frac{y^3}{4h^3} + \frac{1}{2} = \frac{2}{T}t, \tag{4.17}$$

for y, which needs to be solved numerically since there is no analytical solution. Therefore we have to follow the algorithm presented above to find the solution over half a period which is plotted in figure 4.7 (see appendix for the code). The numerically obtained TAPs resulting from different values of $hf(t)$ are also plotted in figure 4.7. The potentials drawn with dotted lines are calculated via the delta-paintbrush approximation, which, by construction, is the desired function $g(y) = \sqrt{\frac{\pi}{2}}\frac{3w_0}{4h}(1-(y/h)^2)\Theta(1-|y/h|)$ with its corresponding normalization factor.

Notice that with increasing amplitude (larger values of h), the painted potential better approximates a parabolic potential, but at the cost of losing intensity in the center of the trap.

This numerical algorithm allows us to modify the geometry and volume of the atom trap at will. In particular, we numerically calculate a waveform that results in the harmonic potential used for trapping atoms in our experiment. Additionally, this waveform allows us to modify the volume of the trap without straying from the harmonic approximation. Because of this pivotal property we selected this waveform to be implemented in our laboratory. The experimental results of this technique are presented in the next chapter.

4.3.3 Paintbrush with inhomogeneous intensity

To solve a more general problem, we will explore the situation where the intensity of the beam is not the same in every position, as shown in figure 4.8. These irregularities are frequent because the AOM's efficiency depends on the RF input which, as we said in section 4.1.1, results in spatial dependence produced by the optical array. If we calculate the parabolic time-averaged potential using the waveform discussed in section 4.3.2 for $h = 4$ but taking into account the paintbrush's inhomogeneous intensity, we see a big discrepancy from the target function as shown in figure 4.8.

To solve this problem we developed a method using the following numerical approach. We first include the positional dependence of the intensity as a factor $I(y)$

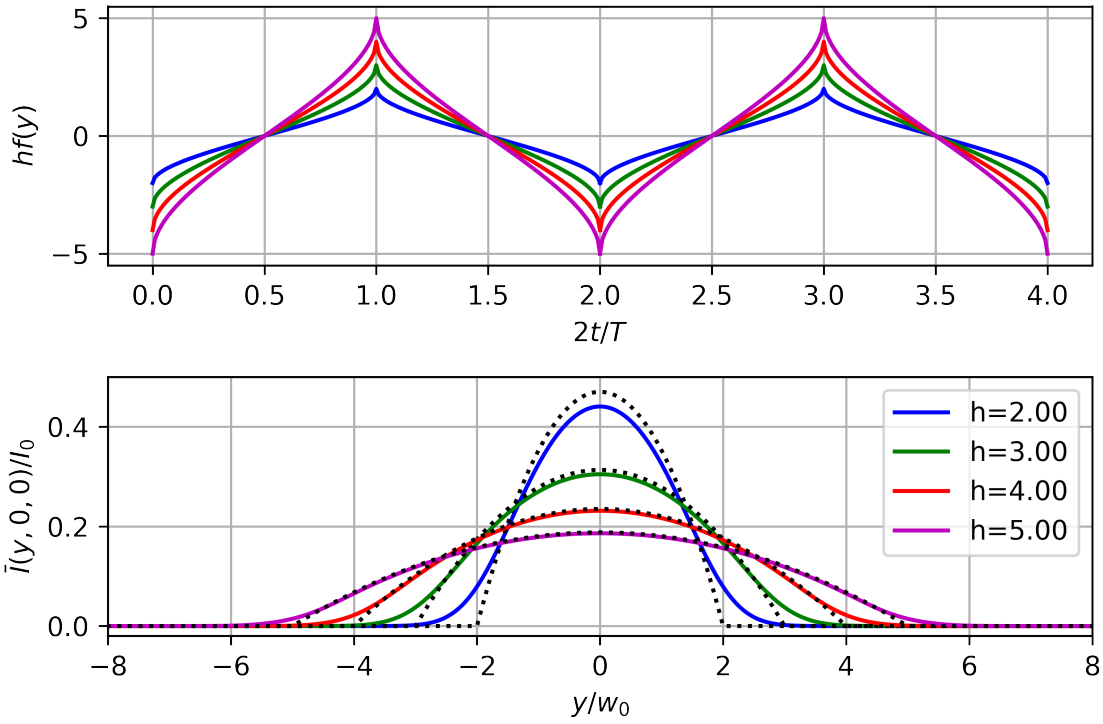

Figure 4.7: Numerically calculated waveforms (above) that produce parabolic time-averaged potentials of different widths (below). The resulting waveform is the obtained through the algorithm presented in this section. We calculate the solution over half a period $0 < 2t/T < 1$ and later mirror it over the y-axis. Amplitudes for all waveforms are given in units of the Gaussian beam waist w_0. The solid line time-averaged potentials are calculated numerically from equation 4.1 while the dotted line potentials are calculated using the delta-paintbrush approximation. This waveform is of great relevance to us because we use a parabolic potential in most of our experiments.

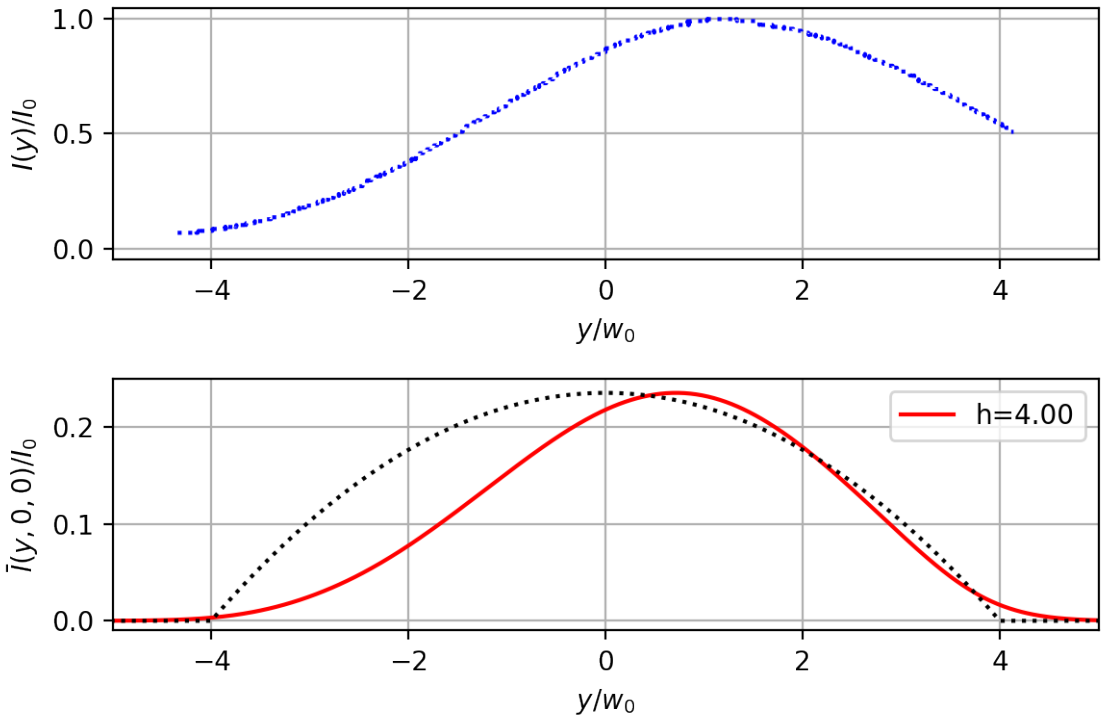

Figure 4.8: A parabolic time-averaged potential (red line below) considering the inhomogeneous intensity profile of the paintbrush (above). The numerically calculated parabolic time-averaged potential (solid line) results from the waveform in section 4.3.2 (shown in figure 4.7 for $h = 4$) but considering the inhomogeneity as pictured above. The dotted-line is calculated using the delta-paintbrush approximation and therefore corresponds to the target function g. The inhomogeneous intensity profile (above) was measured using a probe system.

in equation 4.5 and obtain

$$\bar{I}(y,0,0) = \frac{2I(y)}{T}\frac{1}{h\dot{f}(t)}, \tag{4.18}$$

we then normalize $I(y)$ by the maximum intensity I_0 in 4.18 and equate this to our desired function

$$g(y) = \frac{\bar{I}(y,0,0)}{I_0} = \frac{2}{T}\frac{I(y)}{I_0}\frac{1}{h\dot{f}(t)}. \tag{4.19}$$

Rearranging terms, using $y = hf(t)$, integrating over t and introducing the normalization constant c we get

$$c\int_0^t \frac{I_0}{I(hf(\tau))}g(hf(\tau))h\dot{f}(\tau)d\tau = c\int_{-h}^{y=hf(t)} \frac{I_0}{I(Y)}g(Y)dY = \frac{2}{T}t. \tag{4.20}$$

As the intensity $I(y)$ is a non analytical function because it is measured directly from the experiment, the best approach to solve the integral 4.20 is numerical, using a similar algorithm as the one obtained in section 4.3.2

```
gs=g/I

for i in [0,...,N]
     T'[i]=integrate(gs,-h,Y[i])
end

T=T'/T[N]
```

where `gs` is simply the target function `g` divided by the normalized calibration function `I`, which is measured experimentally (upper half of figure 4.8). The integration runs over the full interval `Y=[-h,...,h]` because the inhomogeneous intensity profile is not symmetric and therefore we cannot multiply the resulting function f by h for the interval $(-1, 1)$ as in figure 4.7.

After we apply this algorithm to the measured calibration curve $I(y)/I_0$ shown in the upper panel of figure 4.8 we obtain waveform $f(t)$. This function is plotted with a solid line in figure 4.9, in contrast to the uncorrected function plotted with a black dashed line. The TAP obtained from this waveform is plotted in the lower panel of figure 4.8 with a solid line. Notice the center of the corrected TAP is very close to the center of the target function, which itself is plotted with a dotted-line.

4.4 Modulation dependent trap depth and frequencies

Some important characterizations and measurements should be performed before testing the TAP technique on the atoms.

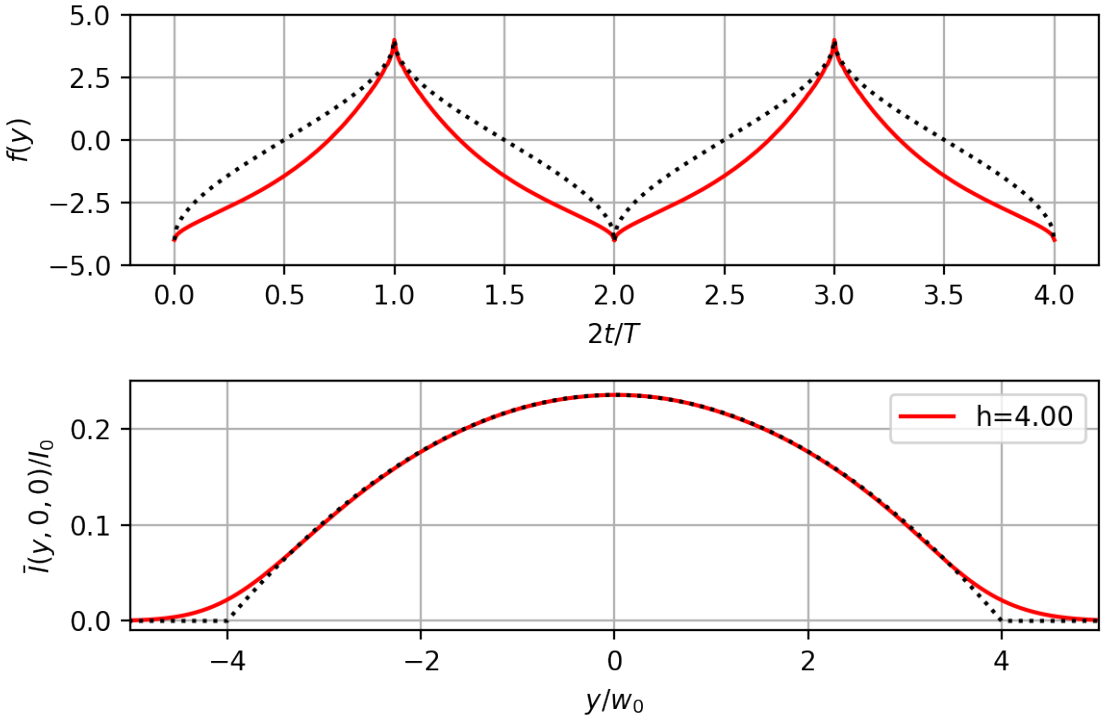

Figure 4.9: A parabolic time-averaged potential (red line below) calculated using our new waveform, which corrects for the inhomogeneous intensity of the paintbrush (red line above). The dotted-line above is the numerically calculated waveform in section 4.3.2 (shown in figure 4.7 for $h = 4$) associated to the target function g (dotted-line below). The dotted-line below is calculated using the delta-paintbrush approximation and therefore corresponds to the target function g. The solid-line above is the numerically calculated waveform using the algorithm presented in this section.

For example, as we can see in figure 4.7, the central intensity of the parabolic TAP is inversely proportional to the modulation amplitude h. Therefore, both the depth U_0 and the frequencies ω_i of the trap (eq. 2.73) change because they are intensity dependent.

In order to conduct future experiments, such as the thermodynamics of global variables proposed by V. Romero [32, 33, 34], we would like to precisely know said dependence as a function of the modulation amplitude of the Gaussian beam paintbrush.

Since the production of a TAP for the Gaussian beam is a numerical procedure (fig. 4.7), we do not have access to an analytical expression from which to calculate them directly. Instead, we can extract these quantities from the numerically calculated profiles.

We can use the numerically calculated peak value of the intensity to determine $I_0(h/w_0)$, and then, by fitting a Gaussian in the neighborhood of $y = 0$ we can determine the waist $w_0(h/w_0)$.

Then, we define the following fractional relations:

$$Q_I(h/w_0) = \frac{I_0(h/w_0)}{I_0(0)}; \quad \text{and} \quad Q_w(h/w_0) = \frac{w_0(h/w_0)}{w_0(0)}, \tag{4.21}$$

which are the normalization of the modulated intensity $I_0(h/w_0)$ and waist $w_0(h/w_0)$ between its initial values (i.e. with zero modulation). This numerically variables are plotted with solid lines in figure 4.10.

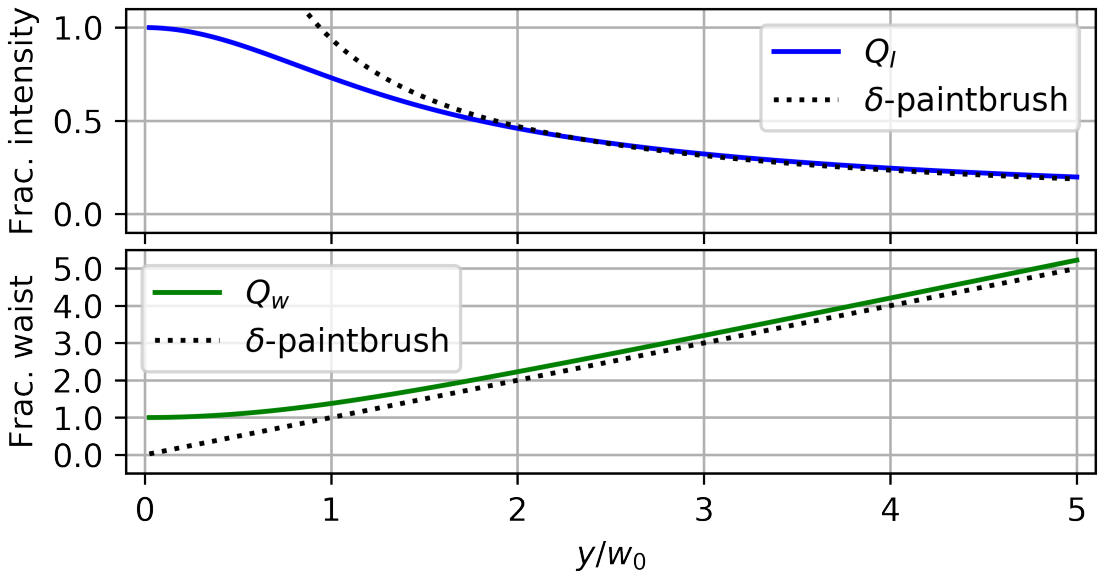

Figure 4.10:

To connect these values to the depth U_0 and the frequencies ω_i of the trap (eq. 2.73), we define the following relations:

$$Q_U(h/w_0) = \frac{U_0(h/w_0)}{U_0(0)} = Q_I(h/w_0), \tag{4.22}$$

$$Q_{\omega_z}(h/w_0) = \frac{\omega_z(h/w_0)}{\omega_z(0)} = \sqrt{Q_U(h/w_0)} \tag{4.23}$$

$$Q_{\omega_y}(h/w_0) = \frac{\omega_y(h/w_0)}{\omega_0(0)} = \sqrt{\frac{Q_U(h/w_0)}{Q_w^2(h/w_0)}} \quad \text{and} \tag{4.24}$$

$$Q_{\bar{\omega}}(h/w_0) = \frac{\bar{\omega}(h/w_0)}{\bar{\omega}(0)} = \sqrt[3]{\frac{Q_U(h/w_0)}{Q_w(h/w_0)}} \tag{4.25}$$

Note that the trap frequency in x direction is not affected because it corresponds to the magnetic component of the hybrid trap. Clearly, all the factors must satisfy $Q_i(0) = 1$.

The trap frequency factor Q_{ω_z} in z direction is only affected by the decreasing of the central intensity, which is quantified by the factor Q_U. The trap frequency factor Q_{ω_y} in the y direction is determined by the composition between the decreasing of the central intensity and the waist increasing quantified by the factors Q_U and Q_w respectively.

The frequency factor $Q_{\bar{\omega}}$ is the reduction factor for the geometric mean frequency $\bar{\omega}$. An important observation has to be made here. We can see that to change the geometric frequency trap $\bar{\omega}$ (related with volume) we have two parameters, Q_U and Q_w. Before TAP, the only free parameter to change $\bar{\omega}$ was the power, i.e. the trap depth related with Q_U. Now we have an extra parameter, the modulation, related with Q_w, that allows us to have more trap control. We return to this discussion at section 5.2.3.

All these frequencies, which are plotted with solid lines in figure 4.11, are calculated using the numerically values $Q_I(h/w_0)$ and $Q_w(h/w_0)$.

We want to compare this numerically calculated functions with those of the delta-approximation TAP. Using the peak value and the harmonic expansion near $y = 0$ of the expression $g(y) = \sqrt{\frac{\pi}{2}}\frac{3w_0}{4h}(1-(y/h)^2)\Theta(1-|y/h|)$, calculated in section 4.3.2 for delta-approximation, it can be shown that

$$q_U(h/w_0) = \frac{U^\delta(h/w_0)}{U_0(0)} = \sqrt{\frac{\pi}{2}}\frac{3w_0}{4h},$$

$$q_{\omega_z}(h/w_0) = \frac{\omega_z^\delta(h/w_0)}{\omega_z(0)} = \sqrt{\sqrt{\frac{\pi}{2}}\frac{3w_0}{4h}},$$

$$q_{\omega_y}(h/w_0) = \frac{\omega_y^\delta(h/w_0)}{\omega_0(0)} = \sqrt{\sqrt{\frac{\pi}{2}}\frac{3w_0^3}{4h^3}} \quad \text{and}$$

$$q_{\bar{\omega}}(h/w_0) = \frac{\bar{\omega}(h/w_0)}{\bar{\omega}(0)} = \sqrt[3]{\sqrt{\frac{\pi}{2}}\frac{3w_0^2}{4h^2}}$$

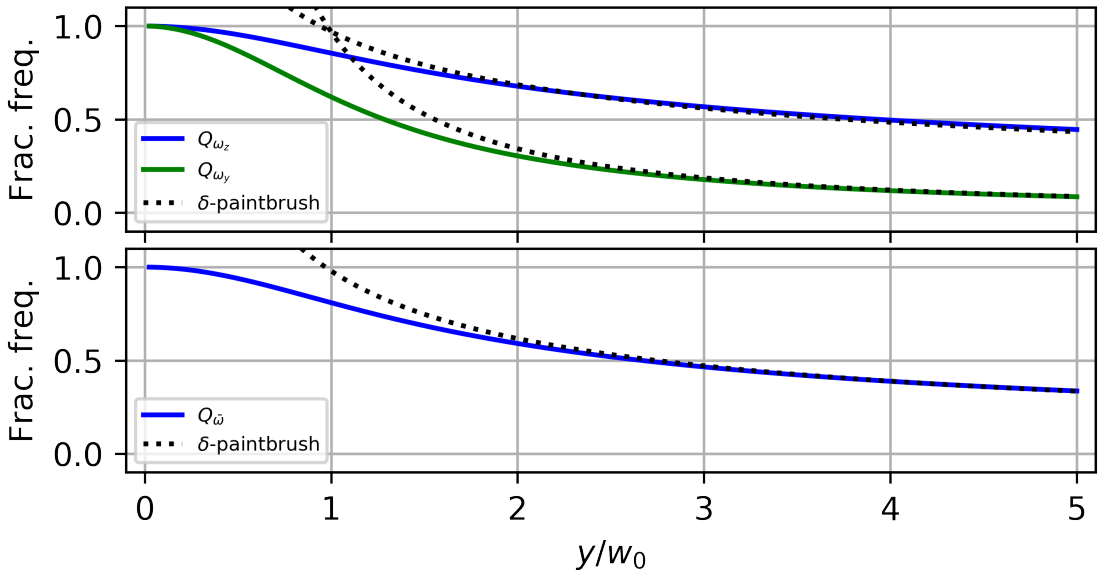

Figure 4.11:

where $U^{\delta}(h/w_0)$ is the trap depth and $\omega_i^{\delta}(h/w_0)$ are the trap frequencies in the delta-approximation for TAP with amplitude h. The frequency factor $q_{\bar{\omega}}$ is the reduction factor for the geometric mean frequency $\bar{\omega}$.

This fractional variables are plotted with dotted lines in figures 4.10 and 4.11. There is shown the comparison between the delta-function and the numerical calculated Gaussian paintbrushes. As we expected for TAP amplitudes much greater than the beam waist $h \gg w_0$, the depth and frequency of the trap in the painted direction will approach those of the delta-approximation TAP as discussed in section 4.3.2.

4.5 Experimental implementation

After the theoretical treatment to obtain the desired geometry for the ODT, the next step is to implement the optical setup and the control system for experiment automation.

4.5.1 Optical setup

The detailed ODT optical setup is already presented at figure 3.6. The upper part of figure 3.6 shows how to prepare the laser beam with the required characteristics to produce the ODT. This part is schematically equivalent to all components before the f_1 lens at figure 4.2. The lower part of figure 3.6 shows how to produce the ODT using the focusing L7 lens. This part is schematically equivalent to the focusing f_1 lens in scheme at figure 4.2. There is some comments and technical details about this optical array which we want to discuss here for future references from lab users.

For example, the telescope formed by the two lenses indicated as L1-L2 is constructed to obtain a collimated beam around 800 μm radius, which is the optimum radius for the AOM input beam. The L3 lens is centered to the first diffracted order and it has a tiny inclination to ensure the lens is perpendicular to the first diffracted

order. Additionally, this L3 lens was finely placed at a focal distance from the AOM to ensure that the angular displacement $\theta_B(t)$ can be transformed into a transverse displacement $d(t)$. The way to align this critical property was varies the L3 lens position until the zeroth and first diffracted order travel parallel the longest possible distance.

The mirror which separates the zeroth and first diffracted order is almost at the focus of the L3 lens. This is placed in this position because there the beams are the thinnest and easiest to separate. The two telescopes formed by L3-L4 and L5-L6 are necessary to collimate and magnified the first diffracted order from around 800 μm to 2750 μm radius. This magnification is in order to achieve with the L7 lens, the last lens, a beam waist around 50 μm at the focus, ideal for our ODT.

Just as technical comment, perhaps the optical setup at figure 3.6 looks pretty simple, it has a high degree of difficulty. Their complexity remains at the necessity of place all the lenses after the AOM at $2f$ configuration, which means that the distance between them is equivalent to the sum of their focal distances. This is necessary (besides the collimation) to ensure that the angular displacement $\theta_B(t)$ can be transformed into a transverse displacement $d(t)$. Therefore, all the optical lenses after the AOM become positionally fixed, and then the beam focus after the L7 lens, which forms the ODT, becomes also fixed. Thus we need to put the AOM at some position to ensure the ODT is near the center of the magnetic Feshbach fields, to create the hybrid trap described at section 2.3.3. A finely adjustment to center perfectly the ODT with magnetic Feshbach fields can be done using the translational stage where the L7 lens is mounted.

4.5.2 Control system

The TAP technique need to be controller by our control system which handles all the experiment. For a given painting function $f(t)$, the only two free parameters that we can change are the amplitude h and the center position.

An important feature not discussed previously is the possibility of moving the potential center finely along the $y-$direction. Despite this was not explicitly said at section 4.1.2, the Bragg angle without modulation $\theta_{B,0}$ after the lens correspond to the center position of the painted potential d_0. Then, the d_0 "constant" for the potential center can be finely moved.

Other way to see this concept is that every value of the waveform $f(y)$ maps into a specific beam position. For instance, let's consider the double well potential (fig.4.4). If we keep only the high value of the square signal, the trap is at the right; otherwise if we keep the low value, the trap is at the left. Therefore, adding a constant signal (or offset) to a waveform is equivalent to shifting the center of the time-averaged potential.

Then the scheme for the control system is presented at figure 4.12. The radio frequency (RF) signal is produced by a voltage-controlled oscillator (VCO), then this RF signal is amplified to 14 W for the AOM. The RF signal generated by the VCO can be controlled by the amplitude (AM) and frequency (FM) channels. As we are interested to change the frequency $\omega_{RF}(t)$, the channel which we need to control is the FM.

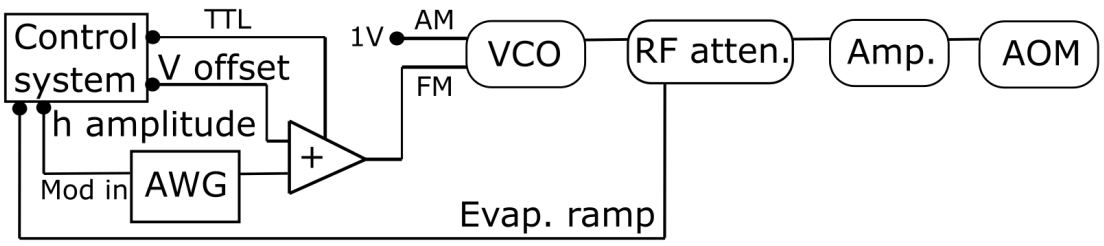

Figure 4.12: Scheme of the experimental control system for TAP technique.

The signal which goes to FM channel is prepared as follows. The painting function $f(t)$ is pre-charged (using the code presented at B.1) in the Arbitrary Wave Generator (AWG) Standford DS345, then its amplitude h is controlled by the MOD IN channel in the AWG. Then this signal is added with a voltage OFFSET, which control the center potential position, and then this complete signal is sent to the FM VCO channel. The special electronic adder was designed and developed in the Electronic Lab by Carlos Gardea, because it needs to add high frequency signals.

In this way, the TAP technique is just controlled by two voltage signals, the h amplitude and the offset. These signals are programmed into the central control system which handles all the experiment.

Chapter 5

Results

After the construction of the experimental setup, some important characterizations and calibrations should be performed before testing the TAP technique on the atoms. We need to be able to fully characterize the beam, with and without modulation. The procedure to characterize the beam is presented in the section 5.1. Next, in section 5.2 we finally test the beam on the atoms. Some important technical parameters can only be determined once the atoms are transferred into the trap, such as the minimum modulation frequency to the TAP technique. In addition, the protocol to measure the trap frequencies ω_i in all directions is presented. This helps to characterize the dependency between the trap frequencies ω_i and the modulation, which must agree with our numerical calculations. Finally, it is also discussed how a TAP expansion can be used as an additional fine evaporation curve for cooling, allowing an additional experimental parameter for the generation of quantum gases.

The thermodynamic theory of global variables [32, 33, 34] establishes that the volume can be taken as the inverse of the cube of the geometric mean of the trap frequencies $V = \frac{1}{\omega_x \omega_y \omega_z}$. A first insight of this proposal by means of an experiment is presented in section 5.3. Basically, we achieve the BEC phase transition by changing the volume while keeping the temperature constant. This is interesting, since in the vast majority of experiments with ultracold atoms around the world, quantum degeneracy is achieved by lowering the value of the temperature as much as possible.

The last section 5.4 is devoted to present the flexibility of TAP to generate trapping potentials. There, we present an implementation of a the double well potential and how it can be used to produce a matter wave diffraction pattern, an important indicator of the onset of the quantum regime.

5.1 Characterizing the beam

The first step is to characterize the beam when no modulation is employed. This consists in measuring the beam intensity profile as it propagates, with special emphasis at the focus position. To make this discussion easier, let us consider that the beam propagates along the x-direction, so each measurement of the intensity profile at a given x is a function of y and z. From this profile, we extract the beam waists ω_y and ω_z along these two directions at each x-position. In other words, we

measure $\omega_y = \omega_y(x)$ and $\omega_z = \omega_z(x)$. In an ideal circular gaussian beam, we have that $\omega_y(x) = \omega_z(x)$ at every value of x. Which means that the focus position, i.e. the x-position in which ω_y and ω_z reach a minimum value, is the same for both of them. However, in practice this is not the case: the beam is imperfect and little misalignments can accumulate as the beam propagates across the several employed optical components such as mirrors and lenses. This might derive in the presence of two focal points: an x-position where ω_y reaches its minimum value, and a different one for ω_z. In this case, it is said that the beam is "astigmatic", an optical aberration that we want to avoid because it significantly decreases the trapping efficiency of the ODT.

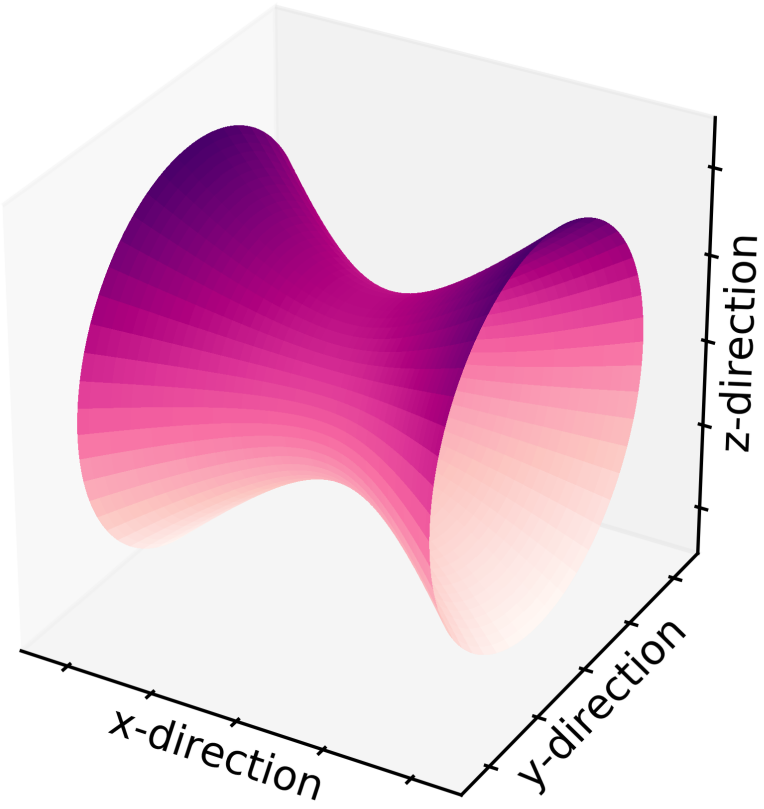

Figure 5.1: The radius $w(x)$ of a focused Gaussian beam as a function of the distance x along the beam (equation 2.70). This is a no-scale 3D version of the right panel of figure 2.10.

In subsection 5.1.1 we discuss how to eliminate the astigmatism from our beam. After solving this problem, we show that, in a well-aligned optic setup, the modulation does not introduces any astigmatism into the beam.

In subsection 5.1.2, we discuss that the TAP technique allows to finely move the trap along the y-direction. We use this to calibrate the conversion between modulation voltage to modulation displacement.

Finally, in subsection 5.1.3, we measure the waist and intensity dependency on the

modulation. We find that our measurements agree with our numerical calculations presented in section 4.4.

5.1.1 Astigmatism

The characterization of the intensity profile of the beam as a function of x is done in a tomographic fashion. We use a CCD camera (Thorlabs DCC1645C) mounted on a translational stage to image the beam at different positions along its propagation direction. To do this, we set the power of the laser at a very low value to prevent any damage on the CCD. This does not alter in any way our measurements because the beam waists do not depend on the laser power. Thanks to the translational stage, we can move the CCD and obtain several "slices" of the beam along the x direction. So we can fully characterize the focus of the beam.

After obtaining about 50 of these slices, we save all images in a computer and use a Python script to fit a 2D Gaussian function in every picture. This gives us, for each x-position, the beam waist along y and z axes, in a similar way as shown in the right panel of figure 2.10. This reconstruction help us to determine whether the beam is astigmatic.

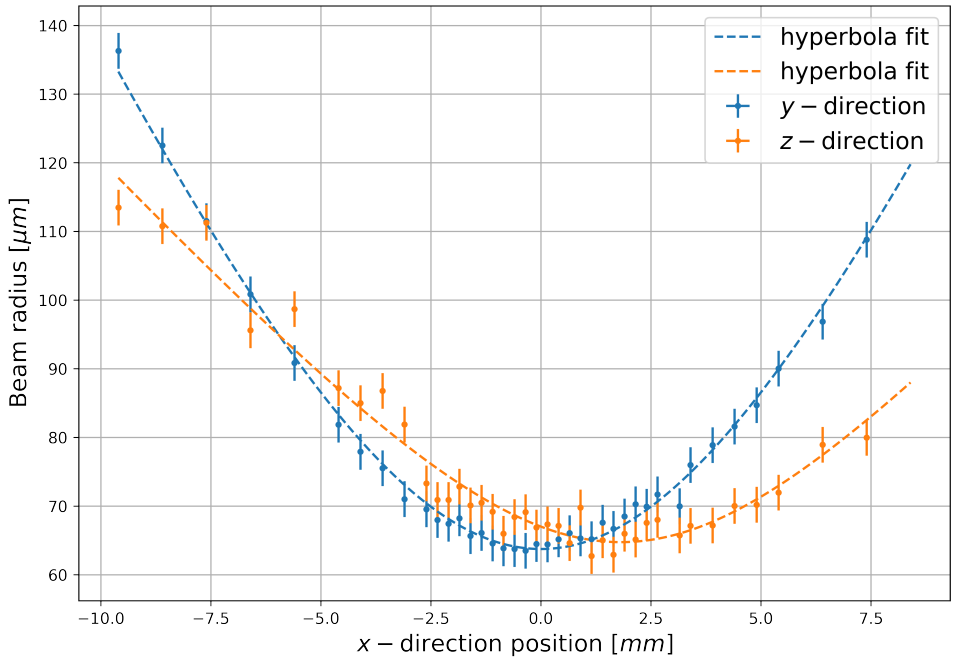

Figure 5.2: Beam waists of an astigmatic beam along propagation direction. The y-focus is at 12.61(39) mm and the z-focus at 14.39(14) mm. This give us a difference of around 1800 μm, big enough for preventing efficient trapping. At their respective foci, the beam waists are $\omega_y = 63.1(26)\mu m$ and $\omega_z = 64.6(26)\mu m$. The uncertainty associated to the data is given by the function `scipy.optimize.curve_fit` used in the Python fitting program, however, the error bars are not visible at the scale of the graph.

For example, the beam characterized in figure 5.2 presents almost 1800 μm of astigmatism, this means that the distance between the y and z foci is 1800 μm. This

difference is big enough to prevent an efficient optical trapping and we lost nearly all the atoms during the transference process between gray molasses and ODT trapping.

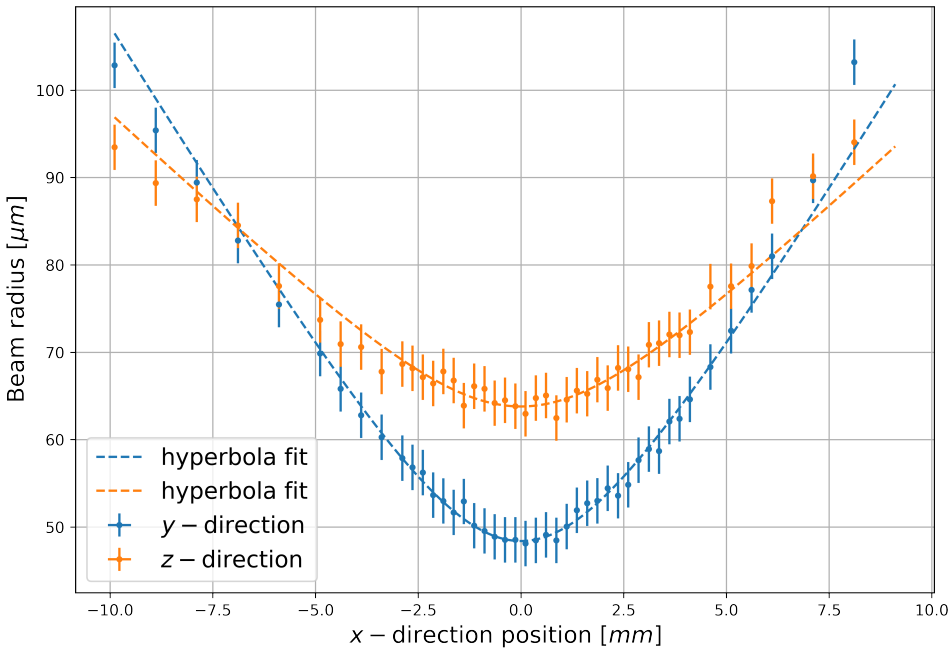

Figure 5.3: Beam waists of a non-astigmatic beam along propagation direction. The y-focus is at 10.89(29) mm and the z-focus at 10.73(89) mm. This give us a difference of around 160 μm, this small value of the astigmatism can be neglected. At their respective foci, the beam waists are $\omega_y = 48.8(26)\mu m$ and $\omega_z = 62.9(26)\mu m$. The uncertainty associated to the data is given by the function `scipy.optimize.curve_fit` used in the Python fitting program, however, the error bars are not visible at the scale of the graph.

To get rid of this problem we have intensively worked in improving the quality of the alignment of our ODT optical setup, trying numerous strategies. At the end of this process, we found out that we could eliminate the astigmatism by introducing a little misalignment on the beam by slightly tilting, in a very controlled fashion, one of the lenses of the setup (labeled as "L6" in fig. 3.6). To do so, we mounted such lens in an opto-mechanical mount, which allows micrometric control. The result is presented in figure 5.3. As we can see, the beam is not symmetrically cylindrical, because the beam waists along y and z directions differ, respectively being 48.8(26) μm and 62.9(26) μm. This asymmetry is not an ideal condition, however, it completely solves the astigmatism problem and does not represent any real disadvantage in the production of the ultracold sample.

Up to this point, we have characterized the beam without introducing the modulation. The next step is to characterize the beam at different values of modulation amplitude to ensure that our TAP technique does not introduce further misalignment or astigmatism. It is convenient to remember that the modulation is performed along the y-direction.

The result, after an exhaustive study, is that the astigmatism remains very small and nearly constant for all the modulation conditions of interest.

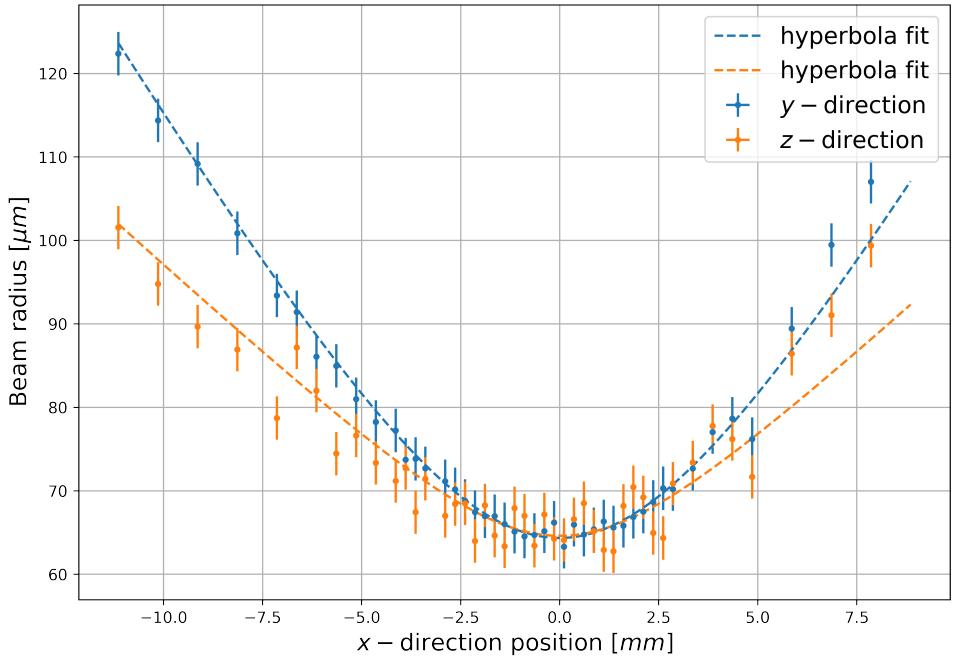

Figure 5.4: Beam waists of a non-astigmatic modulated beam along propagation direction. The value of modulation is 35.3 μm. The x-focus is at 11.14(51) mm and the y-focus at 11.00(14) mm. This give us a difference of around 140 μm, this small value of the astigmatism can be neglected. At their respective foci, the beam waists are $\omega_x = 64.3(26)\mu m$ and $\omega_y = 64.5(26)\mu m$. The uncertainty associated to the data is given by the function `scipy.optimize.curve_fit` used in the Python fitting program, however, the error bars are not visible at the scale of the graph.

This allows us for example, to use the modulation to compensate the asymmetry of the not-modulated beam. The result of modulating 35.3(26) μm the beam is presented in figure 5.4, where the beam is symmetric with a beam waist around 64 μm for the two directions.

5.1.2 Offset

An important feature discussed previously at section 4.5.2 is the possibility of moving the potential center finely along the $y-$direction.

We can characterize this displacement using the tomographic technique described in the previous section. We place our CCD camera at the focus position and take an image for each offset voltage. Then, from our Gaussian fit we extract the central position of the beam.

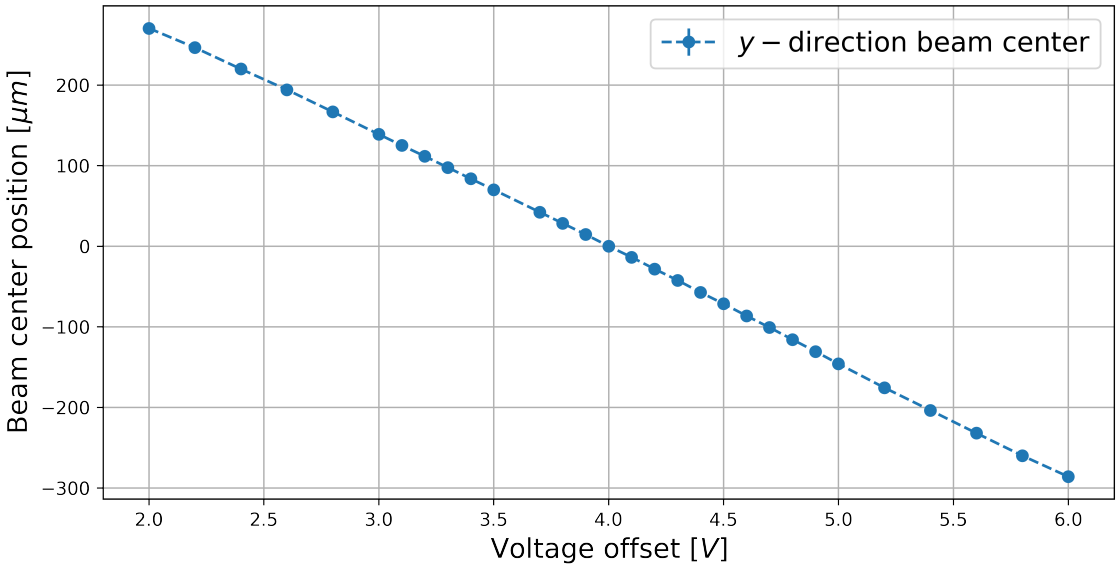

Figure 5.5: Calibration of the offset voltage versus the position of the center of the beam. The center of the beam moves 140 μm per offset Volt, approximately. The uncertainty associated to the data is given by the function `scipy.optimize.curve_fit` used in the Python fitting program, however, the error bars are not visible at the scale of the graph.

The results of offset voltage versus the center position of the beam are presented in figure 5.5. This calibration is very useful to convert modulation voltage into beam displacement h. From this point on, all the results we present use this calibration curve.

It is also important to mention that the capability of changing the trap position is also very important to measure the trap frequency ω_y. This is done by abruptly changing the trap frequency by a small quantity. In consequence, the atoms are "pushed" from the center and start to oscillate at the corresponding frequency (sec. 5.2.2). Finally, we can use this to calibrate the pixel size of the imaging system along the vertical direction.

5.1.3 Intensity and waists modulation-dependency

As discussed in section 4.4, the intensity at the center of the parabolic TAP falls depending on the modulation amplitude h. Therefore, the trap depth U_0 and the trap frequencies ω_i (eq. 2.73) change because they are intensity-dependent.

At this point we are able to characterize the modulated beam. These experimental results are compared with the numerical calculation presented in section 4.4.

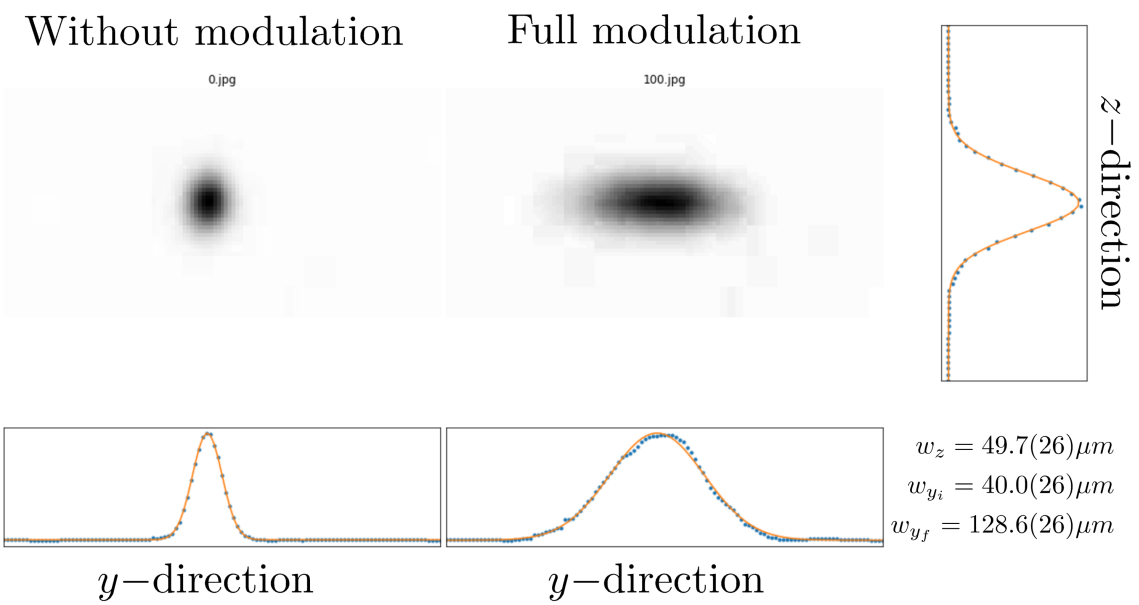

Figure 5.6: Images of the beam at focus, with their corresponding Gaussian fit. On the left we have the unmodulated beam, and on the right we have the beam with the maximal achievable modulation (about 140 μm). We are capable to increment the beam waist at $y-$direction around 3 times its original size. The error associated to the data is given by the function `scipy.optimize.curve_fit` used in the Python fitting program.

Again, we place the CCD camera at the focus position and image the beam for each value of the modulation amplitude. Next, we apply to each image a Gaussian fit and extract from it the maximum intensity, and the $y-$ and $z-$ waists.

As an example, in figure 5.6 we present two images of the beam at focus for two different values of the modulation amplitude.

The fractional amplitude reduction and the waist increment are shown in figures 5.7 and 5.8 respectively, showing a good agreement with the numerical calculations (dotted lines) previously presented in fig. 4.10.

Additionally, we observe that at certain amplitude modulation (35.3 μm), both waists are equal, so the trap becomes radially symmetric. Hence, this modulation becomes our new trap standard for loading the atoms in our experiments.

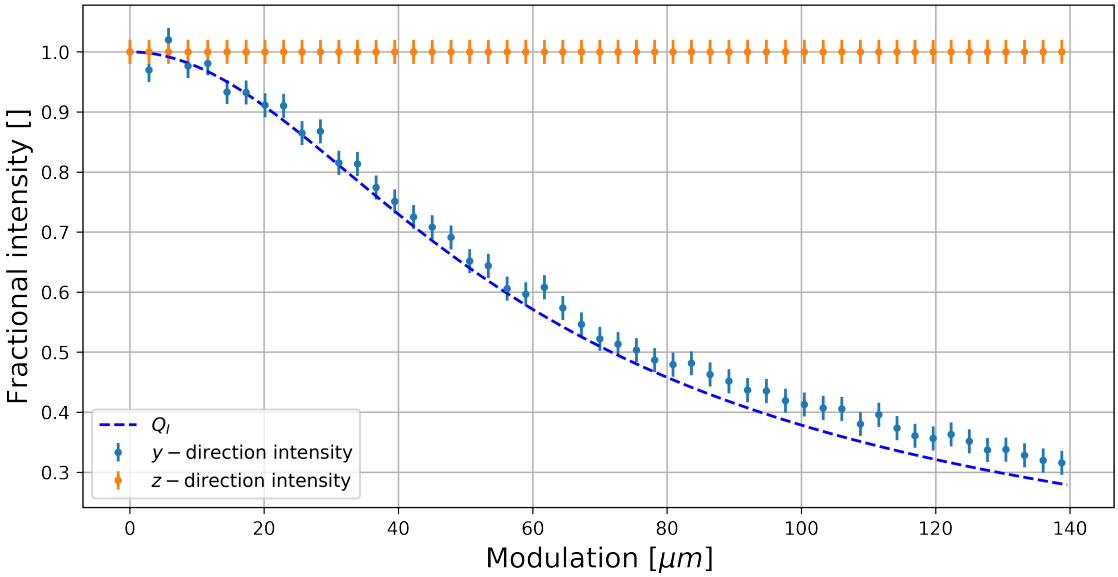

Figure 5.7: Measurement of the evolution of the average normalized intensity in the centre of the beam (dots) with increasing modulation amplitude h. The dotted line is the numerical calculation presented in section 4.4. The error bar (smaller the dot) associated to the data is given by the function `scipy.optimize.curve_fit` used in the Python fitting program.

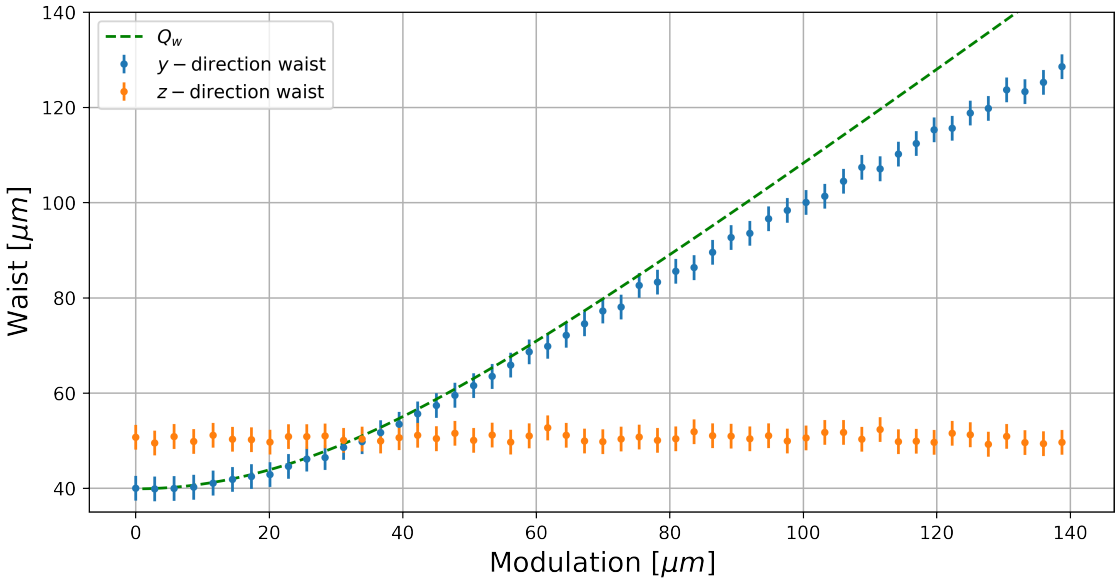

Figure 5.8: Measured waist in $y-$direction (blue dots) and $z-$direction (orange dots) of the parabolic TAP as a function of the modulation amplitude h. The dotted line is the numerical calculation presented in section 4.4. The error bar (smaller the dot) associated to the data is given by the function `scipy.optimize.curve_fit` used in the Python fitting program.

5.2 Using the atoms as a probe

After the beam characterization, we are finally able to employ it to trap the atoms in it. After aligning the beam at the center of the atomic cloud, we can follow the experimental procedure presented in section 3.2.2 to obtain the quantum sample.

After loading the MOT, we apply D_1 cooling process and during it we ramp the ODT power from zero to 150 W in 7 ms. Once the ODT power has reached its maximum value, we ramp the Feshbach magnetic field to 832 G in 50 ms. At this value of the magnetic field, evaporative cooling is performed by ramping down the ODT power following the evaporation ramps shown in figure 3.11 (blue curves).

At the end of the evaporative cooling we adiabatically ramp (300 ms duration) the Feshbach field to 690 G in order to produce molecular BEC of ^{6}Li. We are interested to work in this chapter with the BEC phase because it is the easiest to detect and diagnose.

After producing the BEC in the TAP, we need to determine which is the minimum modulation frequency at which the atoms really interact with a time-averaged potential. For too low modulation frequencies, the atoms won't "see" a static potential, but a dynamic one. This is presented in section5.2.1.

Next, we present in section 5.2.2 a technique to measure the trap frequencies along each direction. Additionally, this technique allows us to verify that the ODT focus is truly at the center of the magnetic Feshbach field.

In section 5.2.3 we discuss the dependency of the trap frequencies on the modulation. We show that our measurements agree with the numerical calculations presented in 4.4. The capability of varying the trap frequencies is important to perform experiments on thermodynamics, specially within the context of the theory of global variables, which defines a global volume parameters as the inverse of the cube of the geometric mean of the trap frequencies $V = \frac{1}{\omega_x \omega_y \omega_z}$.

Finally, we show how the TAP technique can be used to finely expand the volume of the trap, contributing to the evaporative cooling process. In this way, we have an additional experimental parameter for the generation of quantum gases. As a plot twist, in the data presented at Chapter 3 (for example, fig. 3.12) we were already using the TAP parameters to improve the evaporation ramp. Additionally, we use the modulation to make a cylindrical symmetric trap.

5.2.1 Frequency modulation

One of the first tests to probe the TAP on the atoms is to determine the modulation frequency above which the TAP technique really works as a time-average potential for the atoms. To do so, after producing the quantum sample, we change the modulation frequency and measure the number of atoms remaining in the trap. We observe an abrupt change of the atom number at 10 kHz, which is the frequency correspond to the trap frequency expected at high power, discussed at section 3.2.2. Below that frequency the modulation heats the sample and the atoms escape from the trap.

For very large modulation frequencies the bandwidth of the employed electronics

and the wave generator become a limitation, so that the safe zone were we decided to maintain the modulation frequency is at 200 kHz.

5.2.2 Measuring the trap frequencies

For measuring the trap frequencies, we use the atoms as a weight in a simple pendulum. We give the atoms an initial "kick" to transfer momentum to them. Then, since the ODT is harmonic, the sample oscillates sinusoidally around the center of the trap. We track the center of mass of the cloud by taking a series of images at different times, appealing to the repeatability of the experiment.

Just as a technical comment, when the ODT is not centered with the magnetic curvature of the Feshbach field, we observe an undesired oscillatory movement along the axial direction. By moving the translational stage where the last lens is attached (labeled as "L7" in fig. 3.6), we finely center the ODT with the Feshbach field until the oscillatory movement along the axial direction is suppressed.

The initial " kick " is different for each direction, so we divide the procedure for the different axes as described below.

Trap frequency in the z-direction

For measuring the frequency along the gravity direction, we turn off the ODT (50 ms after finishing the evaporative process) to leave the atoms to fall freely. After 1 ms of free fall, we turn on the ODT. Next, we wait 5 ms after which a series of images of the cloud in situ are taken using the horizontal imaging system. Finally, in each image the center of mass of the cloud is determined. The measurement is concluded after 4 or 5 oscillation cycles.

We plot the z-position of the sample as a function of time. We fit the data with a sinusoidal function to obtain the trap frequency. The oscillation is presented at the upper panel of figure 5.9, where the ODT beam has 35 mW of power; with no TAP modulation, a frequency of $\omega_z = 2\pi \times 185.33(310)$ Hz is obtained.

Trap frequency in the y-direction

For measuring the frequency along the modulation direction, we abruptly move by 50 μm the ODT center position along the y-direction (50 ms after finishing the evaporative process), 1 ms later we bring the trap back to its original position. This is done using our TAP technique by just changing the value of the offset of the modulation signal (see section 5.1.2). We then wait 5 ms after which a series of images of the cloud in situ are taken using the vertical imaging system. Finally, in each image the center of mass of the cloud is determined. The measurement is concluded after 4 or 5 oscillation cycles.

We plot the y-position of the sample as a function of time. We fit the data with a sinusoidal function to obtain the trap frequency. The oscillation is presented at the middle panel of figure 5.9, where the ODT beam has 35 mW of power; with no TAP modulation, a frequency of $\omega_y = 2\pi \times 223.95(321)$ Hz is obtained.

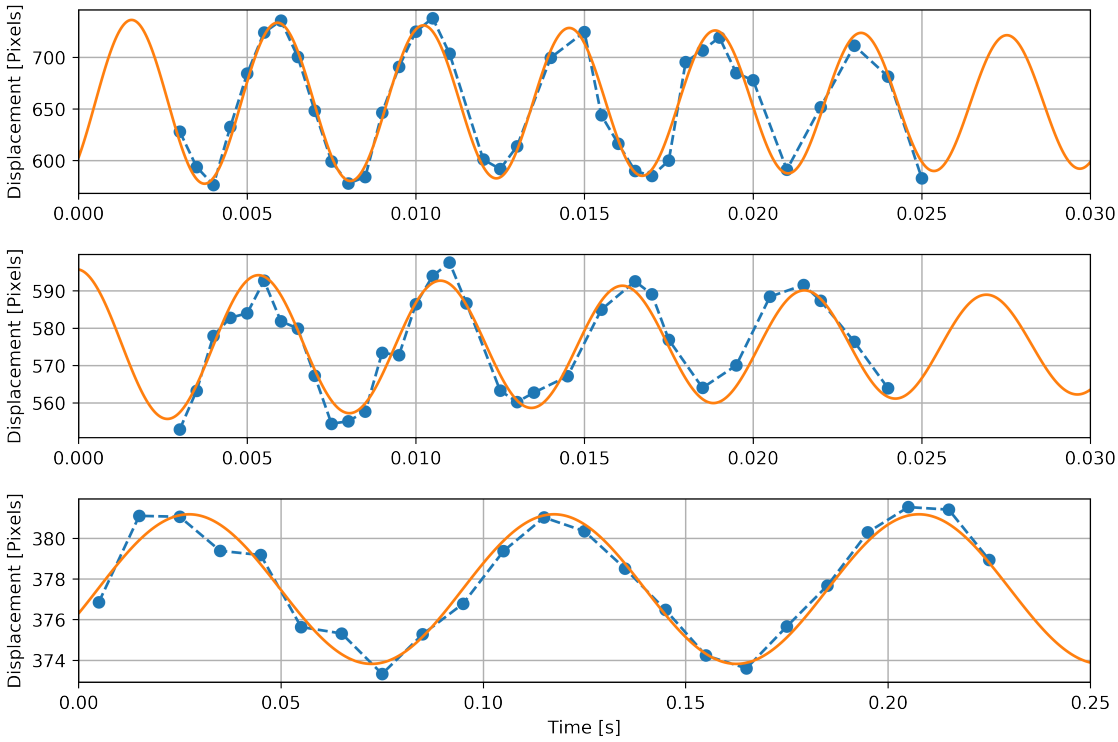

Figure 5.9: Center of mass position at $z-$,$y-$ and $x-$direction, from the upper to the lower panel respectively, after an initial displacement from the center of the ODT. The centers of mass are extracted from a series of absorption images in situ of the ^{6}Li atoms. The oscillation is fitted with a sinusoidal function, giving the frequencies $\omega_z = 2\pi \times 185.33(30)$ Hz, $\omega_y = 2\pi \times 223.95(32)$ Hz, and $\omega_x = 2\pi \times 10.75(28)$ Hz. The characteristics of the ODT beam is 35 mW of power without TAP modulation for the ω_z and ω_y and 90 mW of power with TAP modulation $h = 2.5$ for the ω_x. The error bar associated to the data is given by the standard deviation for 5 independent measurements, such bars are not visible at this scale.

Trap frequency in the x-direction

For measuring the frequency along the propagation direction, we abruptly turn on the MOT coils at 1 A during a period of 2 ms after which they are turned off again. This is done 50 ms after finishing the evaporative process. We then wait 5 ms and next a series of images of the cloud in situ are taken using the vertical imaging system. Finally, in each image the center of mass of the cloud is determined. The measurement is concluded after 3 or 4 oscillation cycles, in this case, the oscillation period is longer than in the previous cases.

We plot the x-position of the sample as a function of time. We fit the data with a sinusoidal function to obtain the trap frequency. The oscillation is presented at the lower panel of figure 5.9, where the ODT beam has 90 mW of power; with a TAP modulation amplitude of $h = 2.5$, a frequency of $\omega_x = 2\pi \times 10.754(28)$ Hz is obtained.

At this point, we emphasize that this trap frequency only depends on the curvature of the Feshbach magnetic field, as discussed in section 2.3.3. Indeed, we have experimentally confirmed that ω_x remains constant for any ODT/TAP parameters as long as the magnetic field is unchanged. The measurements reported in fig. 5.9 were all taken at a Feshbach field of 690 G.

5.2.3 Changing the volume with TAP

At this point, we can use the TAP technique to change the volume of the atomic sample. To do so, we keep the ODT power constant (at approximately 32 mW), and then we change the amplitude of the modulation. We take absorption images of the $^6Li_2$ BEC in situ employing the vertical imaging system at different modulation amplitudes, we observe that the trap geometry change as we increase the modulation. This change is shown in figure 5.10.

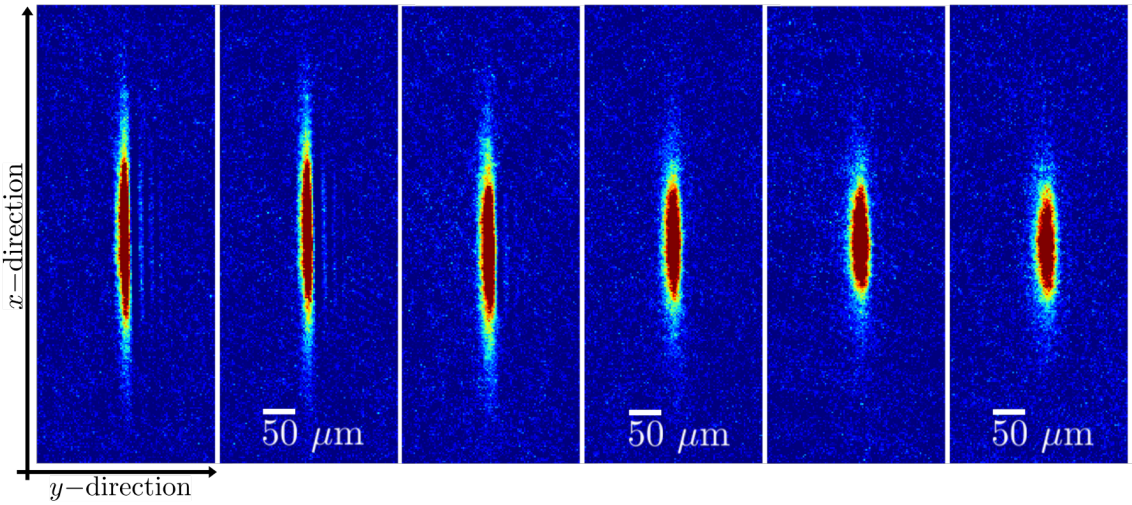

Figure 5.10: Absorption images of the $^6Li_2$ BEC in situ using the vertical imaging system at different modulation amplitudes. The images from the left to the right correspond to modulation amplitudes of 0, 28.4, 56.2, 83.6, 111.5 and 138.8 μm, respectively.

To quantitatively characterize the change in the sample volume we measure the trap frequencies ω_z and ω_y as a function of the amplitude of the modulation. This is done using the protocol describe at section 5.2.2.

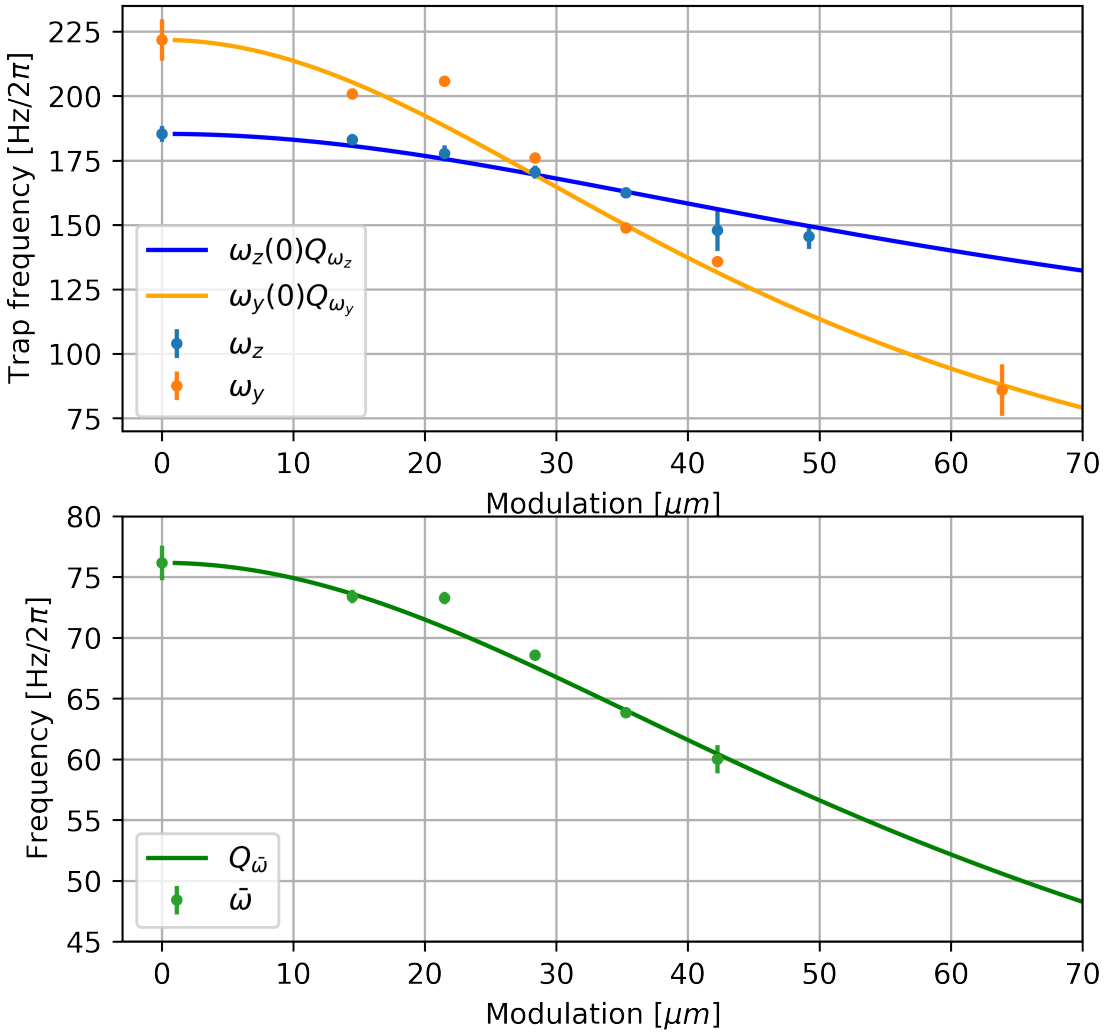

Figure 5.11: Measured ODT trap frequencies for different modulation amplitudes (upper panel) and its correspondent calculated geometric mean frequency (lower panel). The error bar associated to the data in the upper panel is given by the function `scipy.optimize.curve_fit` used in the Python fitting progra, in the lower panel the error is calculated by distribution. The theoretical curves (solid lines) come from the equations presented in section 4.4.

In figure 5.11, we compare the measured trap frequencies (upper panel) and its corresponding geometric mean frequency $\bar{\omega}$ (lower panel) with those predicted by the numerical model for TAP frequencies presented in section 4.4.

It is worth remembering that this technique can also be used not only to vary the sample volume but also as a fine control in the evaporative cooling process. The decreasing of the center trap intensity (fig. 5.7) during the modulation results into the decreasing of the trap depth, lowering the temperature of the gas by evaporative cooling. In fact, this is already used in the data presented in Chapter 3. We already

use TAP to improve the evaporation ramp, for example, in the absorption images presented in fig. 3.12).

Since the thermodynamic global variable theory establishes that the volume depends on these frequencies through the expression $V = \frac{1}{\bar{\omega}^3}$, decreasing the trap frequencies and trap depth due to modulation is equivalent respectively to increase the volume and decrease the temperature simultaneously.

An important feature of TAP is that it have decoupled the trap frequencies values from the trap depth. This can be seen in expression $Q_{\bar{\omega}}(h/w_0) = \sqrt[3]{\frac{Q_U(h/w_0)}{Q_w(h/w_0)}}$ (4.25) presented in section 4.4. We can compensate the intrinsically trap depth decreasing factor due to modulation $Q_U(h/w_0)$ by increasing the power beam.

Compensating $Q_U(h/w_0)$ for each increasing modulation allows us, for example, to decrease the trap frequencies at the same trap depth. This is translated to increase the sample volume (due to $V = \frac{1}{\bar{\omega}^3}$) maintaining its temperature and atom number constant.

We develop an experiment using this isothermal expansion (or compression if we reverse the process) to achieve a BEC phase transition maintaining the temperature constant, presented in the next section. For this reason, the TAP technique is a useful instrument to explore the thermodynamic properties of ultracold gases. We go a little deeper into this aspect in the next section.

5.3 BEC phase transition at constant T

To show the usefulness of the TAP, we carried out an experiment whose objective is to observe the BEC phase transition by increasing the density (decreasing the volume) while maintaining the temperature and number of atoms constant.

This makes sense, since as we discussed before at equation (1.8), the important variable that defines the quantum phase transition is the phase space density, $\rho = n\lambda_T^3$, where λ_T is the de Broglie thermal wavelength associated to the atoms, and n the atom density. The PSD measures the atom number inside a cube whose side is λ_T. When $\rho > 1$, i.e. low temperature and large density n, the system is degenerate.

Then, working theoretically with an ideal gas of bosons harmonically trapped [74], we find that the average number of particles is $N = (k_B T/\hbar\bar{\omega})^3 \, g_3(z)$, with $g_3(z)$ the Bose function (polylogarithm) and $z = e^{\mu/k_B T}$ the fugacity. Imposing that at the transition, the condensed part is zero and the fugacity $z = 1$, we get an expression for the critical temperature T_c for the phase transition between the ideal gas and ideal Bose gas is expected in a harmonic potential

$$k_B T_c = \left(\frac{N}{\zeta(3)}\right)^{1/3} \hbar\bar{\omega} \approx 0.94 N^{1/3} \hbar\bar{\omega}, \tag{5.1}$$

with $\zeta(3) \approx 1.202$ the Riemann function valued at 3.

This experiment presents a new perspective in the way that instead of lowering the temperature until T_c, as is usually done in the vast majority of the quantum gas experiments, we increase the trap frequencies geometric mean until a critical value

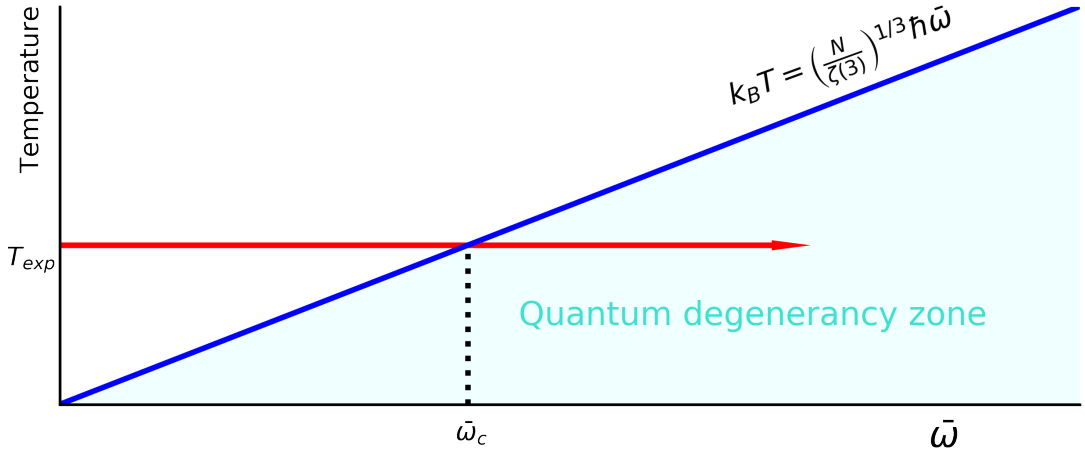

Figure 5.12: A schematic diagram to achieve the BEC phase transition at constant temperature. The red arrow is equivalent to an isothermal compression process. The blue line is the expected temperature at which the phase transition of an ideal Bose gas occurs in a harmonic potential.

$\bar{\omega}_c$. This, under the global variable theory, is equivalent to decrease the volume $V = \frac{1}{\bar{\omega}^3}$, and therefore it is a compression where the density n increase.

Therefore, if we make a process following the red arrow in figure 5.12, which is equivalent to an isothermal compression process, we eventually cross a critical geometric mean frequency $\bar{\omega}_c$ at which the quantum degenerancy is reached and the BEC phase transition is observed. The critical geometric mean frequency is the result of solving for $\bar{\omega}$ from the linear relation (5.1) with a experimental temperature T_{exp}.

Then, we first need to find the experimental process, the isothermal compression (red arrow), which maintain temperature and number of atoms constant. This process is presented in section 5.3.1 and we show the corresponding results in section 5.3.2.

5.3.1 Isotherms

Despite we find at section 5.2.3 that the frequencies decreases as the amplitude modulation increases, the trap depth also decreases and consequently the temperature decreases (section 2.3.4). Then, the TAP technique at constant power of the ODT laser beam inevitably reduces the sample temperature.

Since we want to keep the temperature and number of atoms constant to achieve an isothermal compression, we must compensate the trap depth reduction by increasing the power of the ODT laser beam. We already know how much we need to compensate the power due to the result shown in the figure 5.7. For example, if we modulate 80 μm the trap, we can estimate that it is necessary to double the power to have the same trap depth U_0 as the original unmodulated beam. Same trap depth is equivalent to have the same final temperature.

Therefore, the way to proceed is to select a modulation amplitude, then evaporate for different final ODT powers around the expected value given by the figure 5.7. At each final power the sample temperature and atom number are measured, as

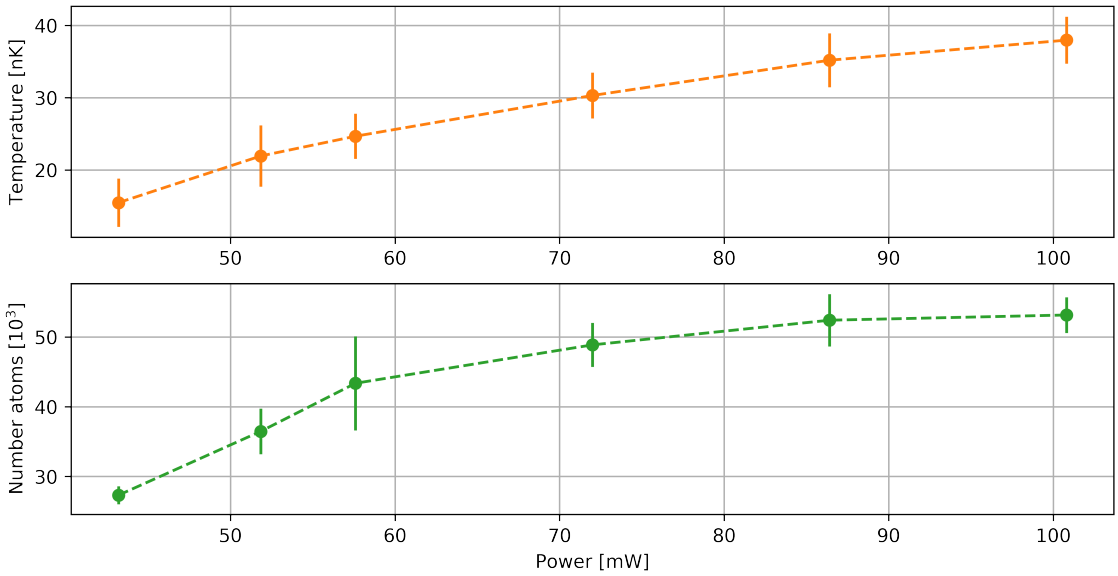

Figure 5.13: Sample temperature and atom number for different evaporation final ODT powers, for a modulation of 70 μm. These are extracted from absorption images after 20 ms of TOF using vertical imaging. As expected, the number of atoms and the temperature are proportional. The error bar associated to the data is given by the standard deviation for 3 or 4 measurements per power.

presented in fig. 5.13.

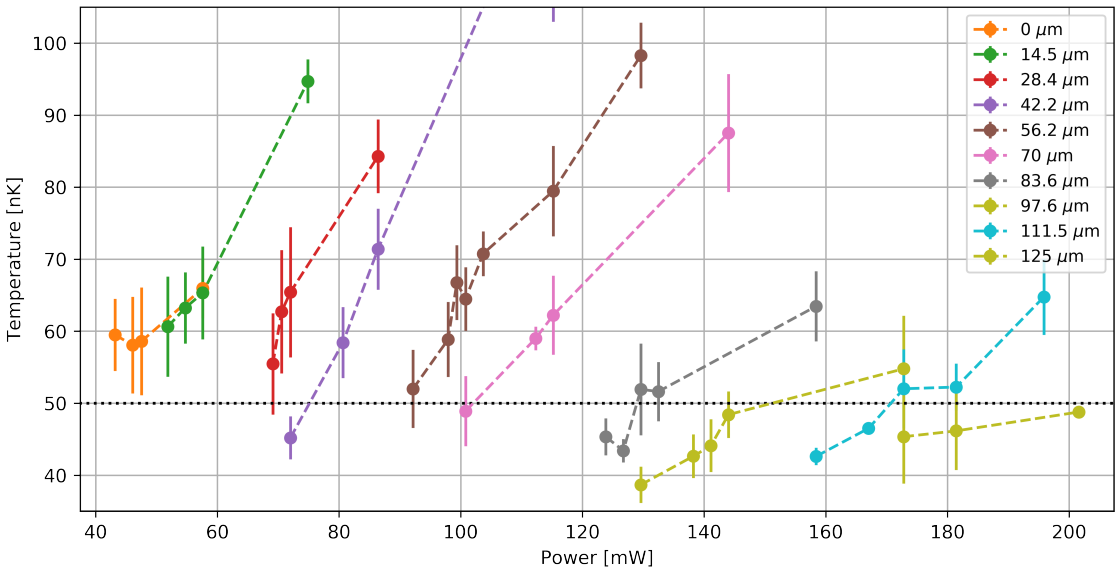

Figure 5.14: The BEC temperature for different evaporation final ODT powers, for 10 different modulation values. These are extracted from absorption images after 20 ms of TOF using vertical imaging. The black dotted line is the desired temperature 50 nK, at which we want to maintain the compression. The set of ODT powers at which the intersection between coloured dotted lines and black dotted line takes place, makes up our isothermal compression. The error bar associated to the data is given by the standard deviation for 3 or 4 measurements per power.

After obtaining this curve for ten different modulation amplitudes, we select the common temperature for all the amplitudes, and practically the same atom number $4.0{\times}10^4(3)$. We select for this experiment the temperature 50(6) nK. Then for each modulation amplitude we search in its respectively curve, shown in figure 5.14, the corresponding ODT power at which the sample temperature is 50 nK (black dotted line).

Therefore, with this information was possible to construct an isothermal compression, shown in figure 5.15, given by a column of ten experimental data pairs, modulation and beam power (h, P). Using this compression we achieve isothermal BEC phase transition, shown in figure 5.15

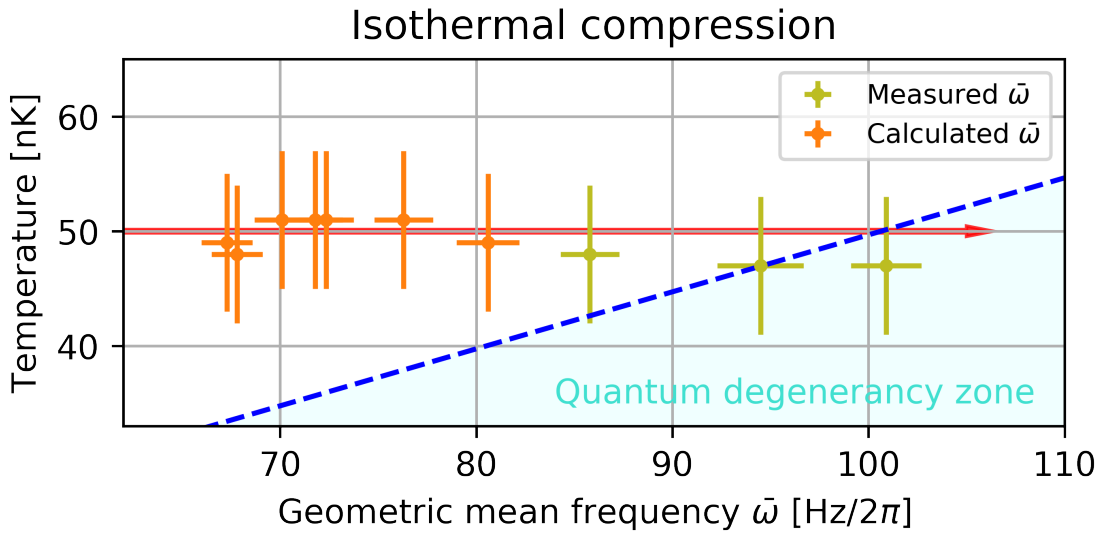

Figure 5.15: Experimental isothermal compression. The green data points has the $\bar{\omega}$ measured using the method described in section 5.2.2. The orange data points has the $\bar{\omega}$ calculated using the laser power beam and the numerical calculation represented by green line in figure 5.11.

5.3.2 Transition

We carry out an experiment to achieve a isothermal BEC phase transition following an isothermal compression process composed by 10 different $\bar{\omega}$, presented in the past section. The BEC phase transition is shown in figure 5.12.

The only thing left to measure for this isothermal process is some of the trap frequencies. We follow the procedure described in section 5.2.2 to measure the trap frequencies at all the directions. It is only possible to measure the trap frequencies for the three last modulation amplitudes because since we are far from the BEC transition, the sample is a rather large thermal cloud whose center of mass is difficult to track.

The geometric mean $\bar{\omega}$ are calculated for the three last modulation amplitudes, and they are indicated in their corresponding absorption image in figure 5.11.

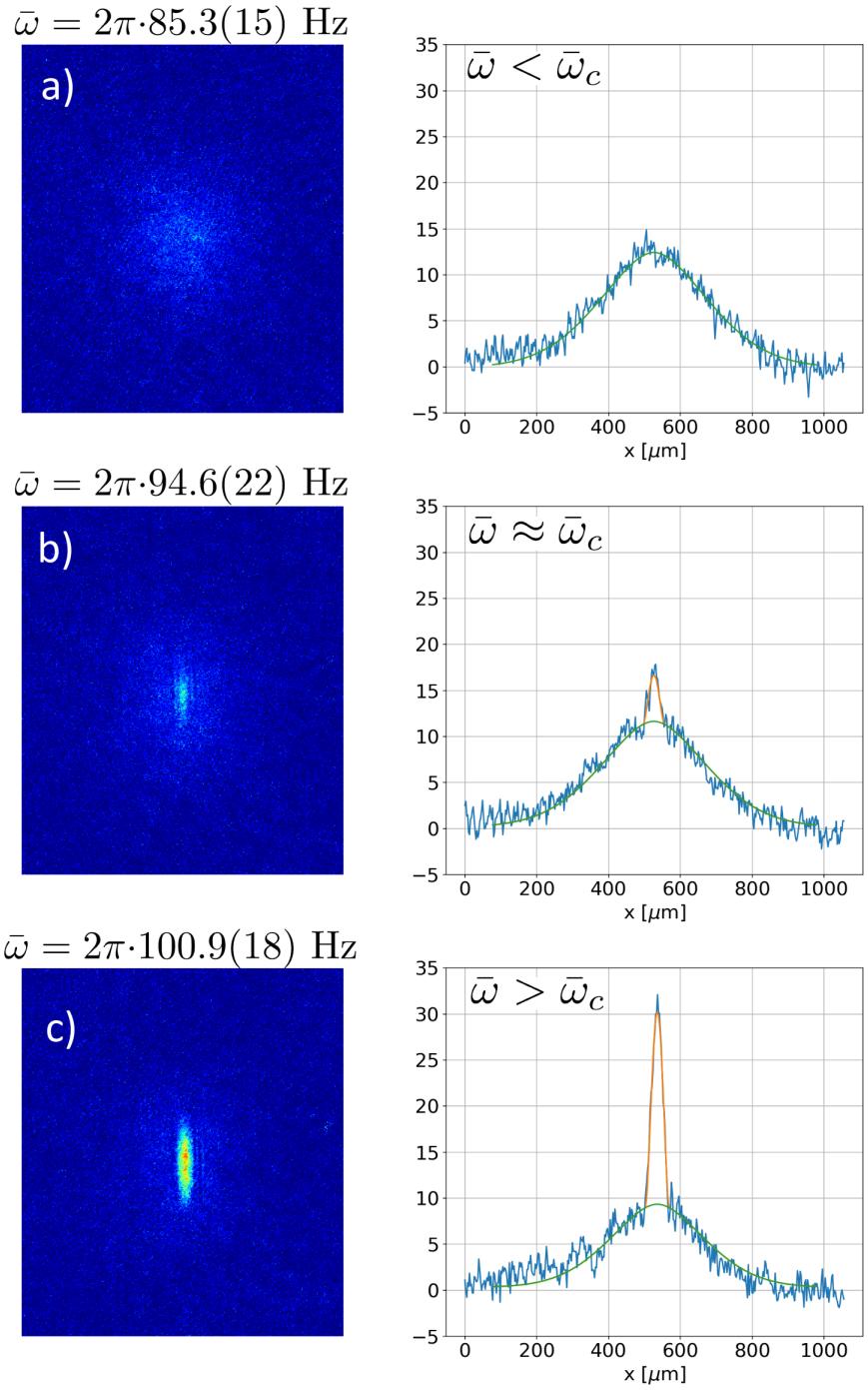

Figure 5.16: Absorption images of ^{6}Li atomic samples after evaporative cooling (left panel) and their corresponding integrated density profiles (right panel, optical density in arbitrary units) as the volume decreases, at constant temperature 50.0(3) nK and constant number of molecules $4.0\times10^4(3)$. (a) Thermal gas where the black dotted line is a Gaussian fit. (b) A gas starting with the transition, showing a bimodal Gaussian-parabolic distribution marked by the orange line. (c) Bose-Einstein molecular condensate, the parabolic distribution is dominant to the Gaussian in the bimodal and the Gaussian distribution decreases appreciably. The color gradient at absorption images corresponds to the optical density of the gas. All images have 15 ms TOF.

5.4 TAP flexibility

As we discussed in section 4.2, it is possible to use the TAP technique to create other trap geometries, for example a double well potential, a nearly box potential, or even a constant-gradient potential.

As an example, we have selected to show here some results for the double-well potential. The waveform signal to create this potential is a square signal. This potential geometry was tested and characterized, and we show the results in in figure 5.17.

Finally, if we left the two quantum sample at time of flight, they interact, showing a matter wave diffraction pattern. This help us to conclude that our sample is in quantum regime.

To summarize this section, we must mention that all these results show the great flexibility and usefulness of the TAP technique, making it an important tool for carrying out all of our experiments. Indeed, in section 6.2.1 we will present another application of this technique in the generation and study of collective excitations in our sample.

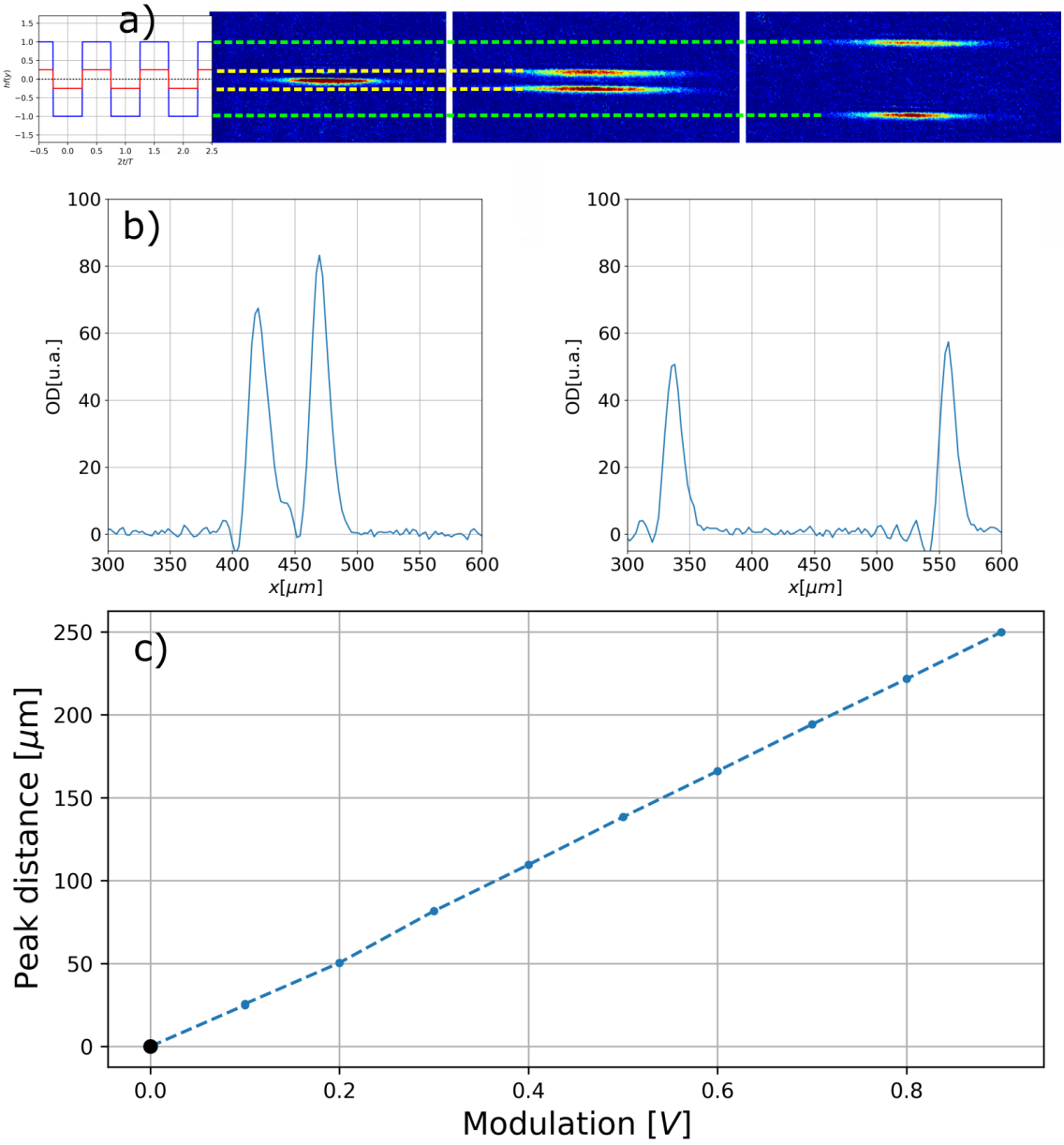

Figure 5.17: (a) Scheme that illustrates how to generate a double well trap from a square signal. (b) The density profile, at optical density arbitrary units, for modulation of 0.2 V and 0.8 V from the left to the right respectively. The distance between the double well increase as we increase the modulation voltage. (c) The characterization of the distance between the double wells as a function of a control voltage.

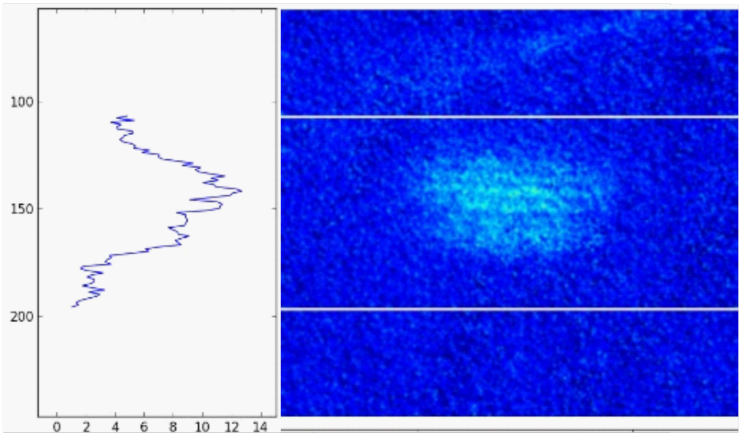

Figure 5.18: An interference pattern (seen in the density profile) generated by releasing the atoms from the double well trap after a TOF of 5ms.

Chapter 6

Conclusions and perspectives

6.1 Conclusions

The main result of this thesis is the design and implementation of an optical system that allows the creation of time-averaged optical potentials (TAP) for the capture and manipulation of ^{6}Li quantum gases.

The basic idea to control the size of the beam waist involves rapidly modulating the position of the trapping laser beam focus. The timescale of the modulation is much faster than the radial trap frequency. By doing so the atoms do not respond to the "instantaneous" motion of the beam and instead "see" a potential proportional to the time-averaged intensity profile.

The implementation of the TAP technique allows us to create a moldable optical dipole trap (ODT). In this trap the last stage of cooling is carried out, evaporative cooling, which allows us to obtain a degenerate ultracold Fermi gas ($T \approx 20$ nK). Evaporative cooling was optimized and complemented with TAP, which is documented and characterized in this thesis.

The different geometries for ODT that TAP allows us to create are very flexible. By means of an algorithm that we have developed as part of this thesis, we can generate arbitrary geometries, from a double well to a box or a harmonic potential.

Once the geometry is selected, it is also possible to scale its dimensions. This allows us to control the size and volume of the trap. For example, using harmonic geometry, it is possible to manipulate the ODT waist to go from 40.0(26) μm to 128.6(26) μm in a fine way.

This is an important characteristic of the TAP technique, because it allows to modify the size and volume of the trap independently from the trap depth. This provides an additional tool for thermodynamics experiments. For example, in this work we have presented the design and study of an experiment whose objective is to observe the BEC phase transition decreasing the volume, but keeping the temperature and the number of atoms constant.

This experiment, in addition to showing the usefulness of TAP, offers a new perspective on what is usually done in the field of ultracold atoms, where it is the trap volume, rather than the temperature of the sample, the variable that is controlled

to achive quantum degeneracy. This experiment also give us an insight of how to measure the volume of a three dimensional harmonic trap.

Additionally, the double-well geometry trap is tested on the atoms, which allows us to obtain two quantum samples whose separation we can finely control, showing the versatility of the TAP technique. With this configuration it was possible to carry out an experiment in which we definitively concluded that we have samples in the quantum regime. This was achieved by allowing the two samples to interact and since they behave like matter waves, a diffraction pattern was obtained.

Finally, our setup has also been very useful to perform the experiments that are currently in progress in our laboratory. In particular, as explained in the following section, it has played an important role for the production and study of parametric excitations in the superfluid, since it provides an extra degree of control on the sample.

6.2 Perspectives

As a first experiment, we have started the study of parametric excitations in the superfluid, in particular, we have studied the phenomenon of Faraday waves.

In this section we present the type of physics that we want to explore in the Ultracold Matter Laboratory (LMU) as well as some of the preliminary results of our research in this direction. In particular, we discuss the role that the TAP technique has played to obtain these results.

6.2.1 Faraday Waves

Faraday waves (FW) are non-linear parametric excitations in continuous media that manifest as a spatial and temporal periodic modulation on the density of the fluid. They were first reported by Michael Faraday in 1831, while studying the emergence of waves on the surface of liquids in a container forced to oscillate along the vertical direction [75].

These excitations are parametric in the sense that they are produced by varying (at a excitation frequency) a parameter of the system, which in consequence changes the oscillation frequency of the system at other than its natural frequency.

FW are specially interesting in the context of atomic superfluids due to the extraordinary level of control that these systems offer. In particular, the possibility of controlling the dimensionality of the system and varying the interatomic interactions present interesting scenarios in which this old phenomenon can be explored under new conditions. Besides, the absence of viscosity causes the collective modes of oscillation to be much less damped than in normal fluids, making parametric conditions easier to achieve. Moreover, the theoretical framework to describe atomic superfluids is simpler than its classical counterpart, enabling an easier theoretical and computational research of this topic.

As we explain below, Faraday waves are connected with microscopic properties of the system such as the superfluid sound velocity, so FW can be employed to measure this important quantity. Exploring deeper this phenomenon might provide a new way

to access more elusive quantities, such as the condensed or the superfluid fractions in both, Bose and Fermi ultracold systems.

Furthermore, in classical fluids it has been shown that FW can decay into other excitations, such as shock waves or vortices [REFERENCE]. It would be very interesting if FW could be employed to generate other more complex phenomena, such as quantized vorticity and quantum turbulence, two topics that we are very interested in exploring at the LMU. Indeed, on the quantum counterpart, recent work shows that in BECs there is a connection between Faraday waves and more complex phenomena, such as highly disordered regimes [76] and granulation [77].

From all atomic superfluids, weakly interacting Bose-Einstein condensates offer the simplest theoretical description. In this case, the excitations are well described by theory since most of the system is in the ground state and the produced FW can be treated as a disturbance [78, 79]. Indeed, FW have already been observed in BECs in several experiments of which we mention three important examples.

The first observation of Faraday patterns in a weakly interacting BEC was reported by Engels et al. [80] in 2007, where the wave is generated by modulating periodically the radial confinement of a cigar-shaped BEC of ^{87}Rb confined in a magnetic trap. More recently, in 2018, van der Straten et al. [81] have also produced Faraday waves, in this case in a ^{23}Na cigar-shaped BEC, modulating the radial frequency of the magnetic trap that contains it. However, these authors do not identify the excitation as a Faraday wave but as a *space-time crystal*. Finally, in 2019, Hulet et al. report on the production of Faraday waves in a cigar-shaped BEC of ^{7}Li [77], in this case, the excitation is not generated by modulating the trap but the scattering length of the sample by means of a Feshbach resonance.

All these experiments share two important features:

1. Faraday waves were observed in a cigar-shaped trap.
2. The sample is in a weakly interacting regime, in which the $T = 0$ Gross-Pitaevskii equation correctly describes the dynamics of the system.

Concerning the point (1), the cigar-shaped geometry of the BEC is essential for observing Faraday waves. To obtain this BEC shape, the role of radial symmetry of the trap is fundamental. This is where the main result of this thesis comes in handy. The TAP technique is capable of creating a trap with a highly symmetric radial coordinate. In this way, this thesis makes a fundamental contribution to perform these experiments in our laboratory.

Regarding the point (2), it is important to mention that there is much less research on Faraday waves in more strongly interacting regimes, such as the BEC-BCS crossover in Fermi superfluids. Indeed, there are just few theoretical predictions and simulations of their occurrence along the BEC-BCS crossover [82, 83] and, what is more, Faraday patterns have never been observed in Fermi superfluids. This opens up interesting research opportunities.

Indeed, strongly interacting superfluids are much more difficult to model and, in general, their microscopic properties much more difficult to measure. One of the main differences between Fermi and Bose superfluids is that in a Fermi system the microscopic features of the superfluid state depend on the nonlinear term, i.e. on the

interaction strength. For this reason, it is very important to count with robust and universal methods to probe the superfluid accross the whole BEC-BCS crossover.

It is in this context that we have chosen the investigation of FW across the BEC-BCS crossover as one of the first research topics to be addressed at the LMU. We are particularly interested in exploring the possibility of using these waves to address microscopic quantities of the system. Indeed, as shown in[82], the superfluid sound velocity can be extracted from the FW pattern.

To obtain the formation of FW it is necessary to drive the non-linearity of the system. In ultracold gases, it can be driven either by varying the scattering length, for example via Feshbach resonances, as experimentally realized by Hulet et al. [9], or by varying the radial trap frequency as done by Engels et al. [80] and van der Straten et al. [81].

At the LMU we currently have the ability to produce FW in the deep BEC regime of the Feshbach resonance. First, we prepare the cigar-shape BEC, where we use the TAP technique described in this thesis to obtain a highly symmetric radial trap frequency. Then we drive sinusoidally, with frequency Ω, the power of the laser around a offset power P_0. The radial frequency ω_r is proportional to the square root of the beam power and, under the small perturbation amplitude approximation $\alpha \ll 0$, we get that $\omega_r \propto \sqrt{P} \propto 1 + \alpha\cos(\Omega t)/2$ under a Taylor expansion.

However, by varying the radial trap frequency it's not entirely clear that the non-linear term in the Gross-Pitaevskii equation (GPE), given by eq. (A.3), is modulated. It's not until the 3D GPE is reduced to 1D GPE (section A.5) that we observe that modulating the radial frequency of the BEC cigar-shape translates into modulating the non-linear term in the 1D effective equation. Another way to understand this process from a less mathematical perspective is to think that the radial frequency modulation in the 3D GPE creates a volume modulation of the trap, which in turn modulates the density $|\psi(x,t)|^2$ and therefore the non-linear term.

By setting the excitation frequency Ω to the frequency of the breathing mode [REFERENCIA] and setting the number of excitation cycles to 10, we vary α until we find the Faraday pattern. As we increas α, we observe overlapping patterns with different wavelength k.

To describe theoretically the Faraday waves, the process is detailed in the Appendix, at section A.7. Broadly speaking, after a linear stability analysis the dynamics of the BEC is mapped from 1D GPE to a Mathieu equation. This Mathieu equation under the analysis in terms of the Floquet stability theory, gives us values of α and Ω at which the solutions are or are not stable. When they are presented graphically, this gives the so-called stability chart with regions of stability and regions of instability separated by the so-called transition curves. This instability regions where the solution is unstable, and therefore where the FW exists, form the well-known "resonances tongues" [84].

When the parameters α and Ω are such that the excitation is unstable and therefore where the FW exists, the density profile is given by

$$\rho(x,t) \approx |\psi_0(x)|^2 \left[1 + 2\mathrm{Re}[A(t)]\cos(kx)\right]$$

where $|\psi_0(x)|^2$ is the density under the Thomas-Fermi approximation, similar to eq. (1.33), summed to a sinusoidal spatial pattern with wavelength k and whose amplitude oscillates $\mathrm{Re}[A(t)]$ in time. This result is observed in the first measurements made in our laboratory (figure 6.1).

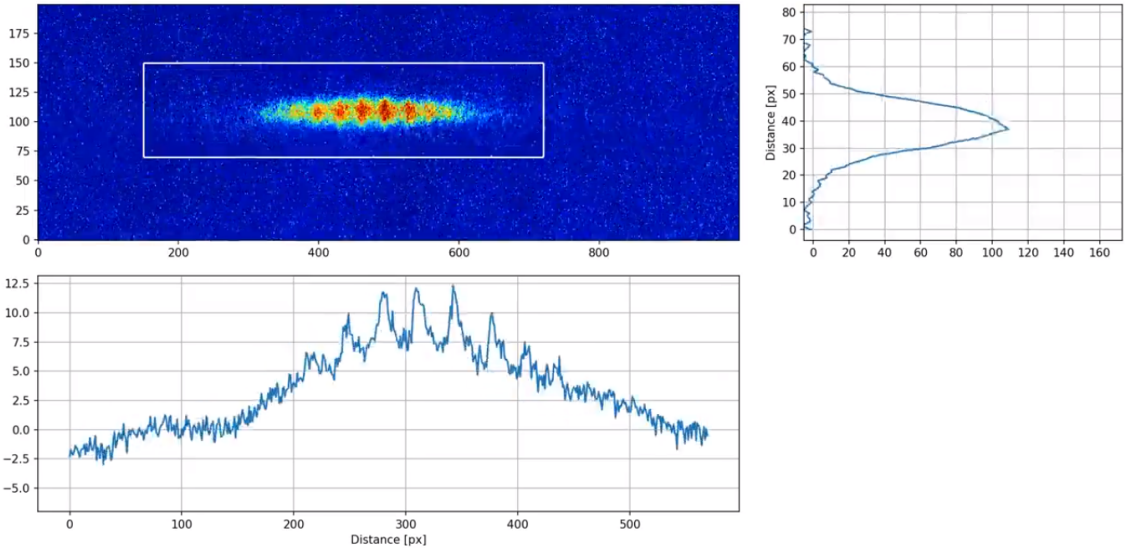

Figure 6.1: Absorption image of a Faraday wave in a Bose-Einstein condensate at 690 G.

In the LMU we have produced this Faraday waves for different magnetic field values, and therefore different scattering lengths, all on the BEC side of the Feshbach resonance. For some reason that we still do not understand, these excitations have not been generated in the unitary regime, under any combination of frequency and amplitude of modulation.

Our optimistic hypothesis is that the specific value of the excitation frequency at the unitary regime is critical, so perhaps we have not excited with the precise frequency. Another hypothesis is that the pattern is formed but the non-condensed fraction fills the pattern's minima, not allowing us to see the FW on the most strongly interacting regimes (remember that as the interaction strength increases, the condensed fraction decreases [REFERENCIA]). Finally, it is important to consider the possibility that for some unknown reason FW are simply not physically possible at unitarity, we consider this very unlikely since the patterns are theoretically predicted by two different models [82, 83].

Consequently, the objective of our research will be to analyze under which conditions Faraday waves occur. In particular, we will seek to determine if they occur in the unitary regime and on the BCS side of the Feshbach resonance since, to our knowledge, they have never been observed in those regions. Likewise, we seek to build the first experimental Floquet stability diagram ("stability chart") along the BEC-BCS crossover. At last, we want to extract the superfluid sound velocity from the FW pattern. This motivates us to propose the use of FW parametric excitation as a probe to measure the superfluid sound velocity. We certainly expect to generate new and exciting results in the near future.

Appendix A

Faraday Waves

This appendix is a result of a strong collaboration with Victor Manuel Romero Rochin, with the target to describe theoretically the Faraday waves.

A.1 Dynamical trap

We create a dynamical trap, modulating sinusoidally the power of the laser with frequency Ω around a offset power P_0, following the function

$$P(t) = P_0 \left[1 + \alpha \cos(\Omega t)\right],$$

where α is the amplitude of the perturbation, which is small compared to P_0.

As we conclude at the section 2.3.3, we have a 3D harmonic hybrid trap. The axial trap frequency ω_x depends of the magnetic curvature, which for our purposes it is static and constant. The radial frequency ω_r depends proportionally to the square root of the beam power $\omega_r \propto \sqrt{P}$. As we are modulating dynamically the power $P(t)$, then the 3D harmonic trap can expressed as

$$V(r, x, t) = V_0(t) + \frac{1}{2} m(\omega_r(t)^2 r^2 + \omega_x^2 x^2), \tag{A.1}$$

with dynamical trap depth $V_0(t) = V_0^0 \left[1 + \alpha \cos(\Omega t)\right]$ and radial trap frequency $\omega_r(t) = \omega_r^0 \sqrt{1 + \alpha \cos(\Omega t)}$. The terms V_0^0 and ω_r^0 correspond to the trap depth and radial trap frequency when there is no perturbation, respectively; therefore using expressions 2.72 and 2.73 we get $V_0^0 = \frac{\hbar \gamma^2}{8 \Delta I_{sat}} \frac{2P_0}{\pi w_0^2}$ and $\omega_r^0 = \sqrt{\frac{4V_0^0}{m w_0^2}}$. With a Taylor series around small α perturbation, the dynamical radial frequency trap can be approximated by $\omega_r(t) \approx \omega_r^0 \left[1 + \alpha \cos(\Omega t)/2\right]$.

A.2 Weakly interacting Bose gas

As we discuss in section 1.3, the BEC can be described by a wave function $\Psi(\mathbf{r}, t)$ which solves the Gross-Pitaevskii equation (GPE), given by eq. 1.30. At this case, as the potential now is time-dependent, the expression becomes

$$i\hbar\frac{\partial\Psi(\mathbf{r},t)}{\partial t} = \left(-\frac{\hbar^2}{2m}\nabla^2 + V(\mathbf{r},t) + \frac{4\pi\hbar^2 a_{dd}}{m}|\Psi(\mathbf{r},t)|^2\right)\Psi(\mathbf{r},t). \tag{A.2}$$

with a normalization condition $N = \int |\Psi(\mathbf{r},t)|^2\, d\mathbf{r}$ with N the total particles number in the gas and m the mass of the dimer. This differential equation looks similar to the Schrödinger equation with the addition of the interaction term $g|\Psi(\mathbf{r},t)|^2$ with $g = \frac{4\pi\hbar^2 a_{dd}}{m}$, which is a non-linear term. For this reason the GPE is also known as "non-linear Schrödinger equation".

Substituting in eq. (A.2) the potential described by eq. (A.1), and reordering the terms, we get

$$i\hbar\frac{\partial\Psi(\mathbf{r},t)}{\partial t} = \left[-\frac{\hbar^2}{2m}\nabla^2 + V_0(t) + \frac{1}{2}m(\omega_r(t)^2 r^2 + \omega_x^2 x^2)\right]\Psi(\mathbf{r},t) + g|\Psi(\mathbf{r},t)|^2\Psi(\mathbf{r},t), \tag{A.3}$$

where the term in square bracket is called lineal term, and the term $g|\Psi(\mathbf{r},t)|^2$ is called non-lineal term.

A.3 Dimensionless Gross-Pitaevskii equation

It is useful to work with a dimensionless version of eq. (A.3), following the reference [85] to do so, we introduce the dimensionless variables

$$\bar{t} \equiv t/t_s \quad \text{and} \quad \bar{\mathbf{r}} \equiv \mathbf{r}/r_s, \tag{A.4}$$

where $t_s = 1/\omega_r^0 = 1/\omega_r$ and $r_s = \sqrt{\frac{\hbar}{m\omega_r}}$. In this section, for simplicity, we going to change the symbol ω_r^0 to ω_r.

Dividing by N the normalization condition, gives

$$1 = \int |\Psi(\mathbf{r},t)|^2 \frac{1}{N}\, d\mathbf{r} = \int |\Psi(\mathbf{r},t)|^2 \frac{r_s^3}{N}\, d\bar{\mathbf{r}} \equiv \int |\bar{\Psi}(\bar{\mathbf{r}},\bar{t}))|^2\, d\bar{\mathbf{r}}$$

where we get the definition $\bar{\Psi}(\bar{\mathbf{r}},\bar{t}) \equiv r_s^{3/2}/N^{1/2}\Psi(\mathbf{r},t)$.

To begin substituting these new variables into the GPE, we need to develop relations for their derivatives. Using the chain rule,

$$\frac{1}{dt} = \frac{1}{t_s}\frac{1}{d\bar{t}}, \quad \frac{1}{dr} = \frac{1}{r_s}\frac{1}{d\bar{r}} \quad \text{and} \quad \nabla = \frac{1}{r_s}\bar{\nabla}.$$

Introducing these relations into eq. (A.3) we obtain

$$i\hbar\omega_r\frac{\partial\bar{\Psi}(\bar{\mathbf{r}},\bar{t})}{\partial\bar{t}} = \left(-\frac{\hbar^2}{2mr_s^2}\bar{\nabla}^2 + \frac{1}{2}mr_s^2\omega_r^2\left(\frac{\omega_r(\bar{t})^2}{\omega_r^2}\bar{r}^2 + \frac{\omega_x^2}{\omega_r^2}\bar{x}^2\right) + V_0(t) + g\frac{N}{r_s^3}|\bar{\Psi}(\bar{\mathbf{r}},\bar{t})|^2\right)\bar{\Psi}(\bar{\mathbf{r}},\bar{t}),$$

which we divide by $\hbar\omega_r$ to finally obtain the following dimensionless GPE,

$$i\frac{\partial\bar{\Psi}(\bar{\mathbf{r}},\bar{t})}{\partial\bar{t}} = \left(-\frac{1}{2}\bar{\nabla}^2+\frac{1}{2}\left(\bar{\omega}_r(\bar{t})^2\bar{r}^2+\bar{\omega}_x^2\bar{x}^2\right)+\bar{V}_0(\bar{t})+k|\bar{\Psi}(\bar{\mathbf{r}},\bar{t})|^2\right)\bar{\Psi}(\bar{\mathbf{r}},\bar{t}), \quad \text{(A.5)}$$

where $\bar{\omega}_x=\omega_x/\omega_r$, $k=4\pi a_{dd}N/r_s$, $\bar{V}_0(\bar{t})=\left[1+\alpha\cos(\Omega/\omega_r\bar{t})\right]V_0^0/\omega_r$ and $\bar{\omega}_r(\bar{t})^2=1+\alpha\cos(\Omega/\omega_r\bar{t})$. We highly recommend check this coefficients.

From this point, we are going to work exclusively with equation (A.5) (unless we explicitly state otherwise) so we are going to refer to it as dimensionless GPE, or simply GPE. Also, for the sake of notation simplicity, we remove all the "bars" $\bar{\cdot}$ from all variables in this equation.

A.4 Gross-Pitaevskii equation in two dimensions

If we have a disk-shape condensate with strong confinement along the x-direction (that is $\omega_x \gg \omega_r$) the 3D GPE can be reduced to a two-dimensional (2D) GPE.

This can be done assuming that the time evolution does not generate excitations along the x-axis since these excitations require much larger energies, of the order of $\hbar\omega_x$ to be generated, in contrast to excitations along the y and z-axis whose energies are of the order of $\hbar\omega_r$.

In this case and assuming that the system is weakly interacting, an useful ansatz for the GPE wavefunction is written in the following way

$$\Psi(x,y,z,t)\equiv\psi_1(x)\psi_2(y,z,t)=\left(\frac{\omega_x}{\pi}\right)^{1/4}e^{-\omega_x x^2/2}\psi_2(y,z,t) \quad \text{(A.6)}$$

where $\psi_1(x)$ is the ground state of the harmonic oscillator in x-dimension.

Substituting eq. (A.6) in the dimensionless GPE eq. (A.5) we find

$$i\psi_1\frac{\partial\psi_2}{\partial t} = -\frac{\psi_1}{2}\nabla^2\psi_2-\frac{\psi_2}{2}\frac{\partial^2\psi_1}{\partial x^2}+\frac{\psi_2}{2}\omega_x^2x^2\psi_1+\left(\frac{1}{2}\omega_r(t)^2r^2+V_0(t)+k|\psi_1|^2|\psi_2|^2\right)\psi_1\psi_2,$$

which we multiply by ψ_1^*, the conjugate of ψ_1. After we integrate over x and using that $\int|\psi_1(x)|^2\,dx=1$ we obtain

$$i\frac{\partial\psi_2}{\partial t}=\left(-\frac{1}{2}\nabla^2+C+\frac{1}{2}\omega_r(t)^2r^2+V_0(t)+\beta|\psi_2|^2\right)\psi_2, \quad \text{(A.7)}$$

where

$$C=-\frac{1}{2}\int_{-\infty}^{\infty}\psi_1^*\frac{\partial^2\psi_1}{\partial x^2}dx+\frac{\omega_x^2}{2}\int_{-\infty}^{\infty}x^2|\psi_1|^2dx \quad \text{and} \quad \beta=k\int_{-\infty}^{\infty}|\psi_1|^4dx=k\sqrt{\frac{\omega_x}{2\pi}}.$$

It is no necessary to calculate C, because this GPE is time-transverse invariant. Therefore we can replace $\psi_2 \to \psi e^{-iCt}$ and drop the constant C in the right equation part.

A.5 Gross-Pitaevskii equation in one dimension

In the case in which radial confinement is much stronger than the axial confinement (that is, $\omega_r \gg \omega_x$), the corresponding condensate is very elongated along the x-direction, the so called cigar-shaped condensate (figure 2.11). In this situation, the 3D GPE can be reduced to a 1D GPE.

Just as in the 2D case, this can be done assuming that the time evolution does not generate excitations along the r-axis since these excitations have much larger energies, of the order of $\hbar\omega_r$, compared to excitations along the x-axis with energies of the order of $\hbar\omega_x$.

Once again, a useful ansatz for Ψ is of the form

$$\Psi(x,y,z,t) \equiv \psi_1(x,t)\psi_2(y,z,t) = \psi_1(x,t)\left(\frac{\omega_r(t)}{\pi}\right)^{1/2} e^{-\omega_r(t)(y^2+z^2)/2} \tag{A.8}$$

where $\psi_2(y,z,t)$ is the ground state of the 2D harmonic oscillator, which is just the product of the 1D harmonic oscillator for y and z-dimension with $\int |\psi_2(y,z,t)|^2\, dydz = 1$.

Substituting eq. (A.8) in (A.5) we find

$$\begin{aligned} &i\psi_1\frac{\partial\psi_2}{\partial t} + i\psi_2\frac{\partial\psi_1}{\partial t} = \\ &\quad -\frac{\psi_2}{2}\frac{\partial^2\psi_1}{\partial x^2} - \frac{\psi_1}{2}\nabla^2\psi_2 + \frac{\psi_1}{2}\omega_r(t)^2 r^2\psi_2 + \left(\frac{1}{2}\omega_x^2x^2 + V_0(t) + k|\psi_1|^2|\psi_2|^2\right)\psi_1\psi_2, \end{aligned}$$

which we multiply by ψ_2^*, the conjugate of ψ_2. After we integrate over y and z, using $\int |\psi_2(y,z,t)|^2\, dydz = 1$ we obtain

$$i\frac{\partial\psi_1}{\partial t} = \left(-\frac{1}{2}\frac{\partial^2}{\partial x^2} + C + \frac{1}{2}\omega_x^2x^2 + V_0(t) + \beta|\psi_1|^2\right)\psi_1,$$

where

$$\begin{aligned} C = &-\frac{1}{2}\int_{-\infty}^{\infty}\int_{-\infty}^{\infty}\psi_2^*\left(\frac{\partial^2\psi_2}{\partial y^2} + \frac{\partial^2\psi_2}{\partial z^2}\right)dydz \\ &+ \frac{\omega_r(t)^2}{2}\int_{-\infty}^{\infty}\int_{-\infty}^{\infty}|\psi_2|^2(y^2+z^2)dydz - i\int_{-\infty}^{\infty}\int_{-\infty}^{\infty}\psi_2^*\frac{\partial\psi_2}{\partial t}dydz \end{aligned}$$

$$\text{and} \quad \beta = k\int_{-\infty}^{\infty}\int_{-\infty}^{\infty}|\psi_2|^4 dydz = \frac{k\omega_r(t)}{2\pi}.$$

It is no necessary to calculate C because this GPE is time-transverse invariant. Therefore we can replace $\psi_1 \to \psi e^{-i\int C dt}$ and drop C in the right part of the equation. After this point, we are going to substitute β as simply $\beta\omega_r(t)$ with $\beta = \frac{2a_{dd}N}{r_s}$, to obtain the very important equation

$$i\frac{\partial\psi(x,t)}{\partial t} = \left[-\frac{1}{2}\frac{\partial^2}{\partial x^2} + \frac{1}{2}\omega_x^2 x^2 + V_0(t)\right]\psi(x,t) + \beta\omega_r(t)|\psi(x,t)|^2\psi(x,t). \quad \text{(A.9)}$$

A.6 GPE 1D solutions

A.6.1 GPE 1D stationary solution under Thomas-Fermi approximation

Before to start to applying linear stability analysis, which lead to dynamic solutions, we present the stationary solution ($\alpha = 0$) under the Thomas-Fermi approximation.

In the absence of modulation $\alpha = 0$, taking in mind that we are under the dimensionless frame, we get that the factors in equation (A.9) become $\omega_r(t) = 1$ and $V_0(t) \equiv V_0 = V_0^0/\omega_r$.

Similar to the procedure presented in section 1.3, we use separation of variables method to propose a solution of the form $\psi(x,t) = \psi_0(x)e^{-i\mu t/\hbar}$ written as the product of a time-function and space-function. From the separation of variables method the integration constant μ emerges, but later it is identified as the chemical potential. Here we define the dimensionless parameter $\mu = \hbar\omega_r\bar{\mu}$ so we get $\psi(\bar{x},\bar{t}) = \psi_0(\bar{x})e^{-i\bar{\mu}\bar{t}}$.

The separable variable solution is possible because we are searching the ground state $\psi_0(x)$, which is stationary and therefore time-independent. Here the exponential term carries the time dependence of the wavefunction.

The resulting time-independent GPE after substituting this separable variable solution in the 1D GPE equation (A.9) is

$$\mu\psi_0(x) = \left[-\frac{1}{2}\frac{\partial^2}{\partial x^2} + \frac{1}{2}\omega_x^2 x^2 + V_0\right]\psi_0(x) + \beta|\psi_0(x)|^2\psi_0(x) \quad \text{(A.10)}$$

which is time independent.

The Thomas-Fermi approximation consists in neglecting the kinetic term in equation (A.10), that is, the second derivative with respect to x, resulting into an algebraic equation.

After the Thomas-Fermi approximation, we get the following analytic solution for the density $n(x) = |\psi_0(x)|^2$,

$$|\psi_0(x)|^2 = n(x) = \frac{1}{\beta}(\mu - V_0 - \frac{1}{2}\omega_x^2 x^2). \quad \text{(A.11)}$$

To make physical sense, this quantity is defined to be strictly positive and hence it is set equal to zero for every point where it results in a negative value. Then the density is zero when the absolute value of x is greater than

$$R_{TF} = \frac{1}{\omega_x}\sqrt{2(\mu - V_0)} \tag{A.12}$$

which is called Thomas-Fermi radius.

This approximation, although somehow rough, provides a very good description of a stationary BEC. Evidently, it can be avoided to obtain better results, but the solution should be computed numerically to solve equation (A.10).

A.6.2 GPE homogeneous solution

Now we consider the case with the modulation of the radial frequency, therefore $\alpha \neq 0$. Although the modulation α is different from zero, it always remains small, therefore we can approximate $\omega_r(t) = \sqrt{1 + \alpha\cos(\Omega t)} \approx 1 + \alpha\cos(\Omega t)/2$ with Taylor series around $\alpha = 0$.

With this approximation and additionally the Thomas-Fermi approximation to neglect the kinetic term $-\frac{1}{2}\frac{\partial^2}{\partial x^2}\psi(x,t)$, we obtain an analytic solution for equation (A.9) as

$$\psi_h(x,t) = \psi_0(x)\exp\left[-i\mu t - iV_0\alpha\sin(\Omega t)/\Omega - i\beta|\psi_0(x)|^2\alpha\sin(\Omega t)/2\Omega\right]. \tag{A.13}$$

The subscript h stands for "homogeneous", or rather "spatially homogeneous", which is another way of stating that we are neglecting the kinetic term. To verify that it is a solution, we substitute the homogeneous solution in both sides of equation (A.9), neglecting the kinetic term, we find that

$$i\psi_0(x)\exp[*]\left[-i\mu - iV_0\alpha\cos(\Omega t) - i\beta|\psi_0(x)|^2\alpha\cos(\Omega t)/2\right] =$$
$$\left[\frac{1}{2}\omega_x^2x^2 + V_0(1+\alpha\cos(\Omega t))\right]\psi_0(x)\exp[*] + \beta(1+\alpha\cos(\Omega t)/2)|\psi_0(x)|^2\psi_0(x)\exp[*],$$

where we have defined $\exp[*] \equiv \exp\left[-i\mu t - iV_0\alpha\sin(\Omega t)/\Omega - i\beta|\psi_0(x)|^2\alpha\sin(\Omega t)/2\Omega\right]$. After rearranging the terms we finally obtain

$$\mu\psi_0(x) = \left[\frac{1}{2}\omega_x^2x^2 + V_0\right]\psi_0(x) + \beta|\psi_0(x)|^2\psi_0(x).$$

which is true by equation (A.10) under the Thomas-Fermi approximation.

A.7 Linear stability analysis

We phenomenologically know that the periodic modulation of the non-lineal term can induce a spontaneous spatial-symmetry breaking of this "homogeneous" state, resulting in a spatial pattern whose amplitude is time-dependent [78]. This pattern is proposed of the form

$$\psi(x,t) = \psi_h(x,t)\psi_p(x,t) = \psi_h(x,t)\left[1 + A(t)\cos(kx)\right] \tag{A.14}$$

where $A(t)$ is complex function which is time-dependent only and its amplitude is small $|A(t)| \ll 1$. The $k = 2\pi/\lambda$ is vector wave of the spatial pattern.

The next step is to substitute the proposal (A.14) into the equation (A.9), giving

$$\begin{aligned} i\psi_h\frac{\partial\psi_p}{\partial t} + i\psi_p\frac{\partial\psi_h}{\partial t} &= \left[-\frac{1}{2}\frac{\partial^2}{\partial x^2} + \frac{1}{2}\omega_x^2x^2 + V_0(t)\right]\psi_p\psi_h + \beta\omega_r(t)|\psi_h|^2|\psi_p|^2\psi_p\psi_h \\ &= \psi_p\left[-\frac{1}{2}\frac{\partial^2}{\partial x^2} + \frac{1}{2}\omega_x^2x^2 + V_0(t)\right]\psi_h + \beta\omega_r(t)|\psi_h|^2\psi_p\psi_h \\ &\quad - \frac{\partial\psi_h}{\partial x}\frac{\partial\psi_p}{\partial x} - \frac{\psi_h}{2}\frac{\partial^2\psi_p}{\partial x^2} + \beta\omega_r(t)|\psi_h|^2(|\psi_p|^2 - 1)\psi_p\psi_h \end{aligned}$$

where the two penultimate terms of the last equation comes from applying the Laplacian $\partial^2(\psi_p\psi_h)/\partial x^2$ and the second and last terms of the last equation are a decomposition which sum up to the second term of the right side of the first equation.

If we observe carefully this last expression, the homogeneous part ψ_h follows the equation (A.9), then we can cancel the second term of the left side with the first line of the right hand, giving

$$i\psi_h\frac{\partial\psi_p}{\partial t} = -\frac{\partial\psi_h}{\partial x}\frac{\partial\psi_p}{\partial x} - \frac{\psi_h}{2}\frac{\partial^2\psi_p}{\partial x^2} + \beta\omega_r(t)|\psi_h|^2(|\psi_p|^2 - 1)\psi_p\psi_h$$

here, we can approximate $\partial\psi_h/\partial x = 0$, and we can substitute $\partial\psi_p/\partial t = \dot{A(t)}\cos(kx)$, $\partial^2\psi_p/\partial x^2 = -A(t)k^2\cos(kx)$, $|\psi_h|^2 = |\psi_0(x)|^2$, $|\psi_p|^2 = 1 + 2\mathrm{Re}[A(t)]\cos(kx) + A^2(t)\cos^2(kx)$ and $\psi_p = 1 + A(t)\cos(kx)$ resulting in

$$\begin{aligned} &i\dot{A(t)}\cos(kx) = \\ &\frac{k^2}{2}A(t)\cos(kx) + \beta\omega_r(t)|\psi_0(x)|^2(2\mathrm{Re}[A(t)]\cos(kx) + A^2(t)\cos^2(kx))(1 + A(t)\cos(kx)) \end{aligned}$$

$$i\dot{A(t)} = \frac{k^2}{2}A(t) + \beta\omega_r(t)|\psi_0(x)|^2(2\mathrm{Re}[A(t)] + A^2(t)\cos(kx))(1 + A(t)\cos(kx)),$$

then, we perform a linear stability analysis which consist to keep the first order elements respect to $A(t)$, we obtain

$$i\dot{A(t)} \approx \frac{k^2}{2}A(t) + 2\beta|\psi_0(x)|^2\omega_r(t)\mathrm{Re}[A(t)].$$

At this point we have an inconsistency, the left side only depends on time, while the right side depends on both time and x, due to the presence of the term $|\psi_0(x)|^2$.

We can patch this problem by assuming that $A(t)$ "interacts" only with the average density of the condensate, then $|\psi_0(x)|^2 \approx \bar{\rho}$. We will calculate this average density later. Then, we get

$$i\dot{A(t)} \approx \frac{k^2}{2}A(t) + 2\beta\bar{\rho}\omega_r(t)\mathrm{Re}[A(t)].$$

Since $A(t)$ is a complex function, we separate it into its real and imaginary parts $A(t) = \mathrm{Re}[A(t)] + i\mathrm{Im}[A(t)]$ and we get the following two equations

$$\begin{aligned} \frac{d}{dt}\mathrm{Re}[A(t)] &= \frac{k^2}{2}\mathrm{Im}[A(t)] \\ -\frac{d}{dt}\mathrm{Im}[A(t)] &= \frac{k^2}{2}\mathrm{Re}[A(t)] + 2\beta\bar{\rho}\omega_r(t)\mathrm{Re}[A(t)]. \end{aligned}$$

Applying time derivation to the first equation, and then substituting the second into the first after derivation, we get

$$\begin{aligned} \frac{d^2}{dt^2}\mathrm{Re}[A(t)] &= \frac{k^2}{2}\left(-\frac{k^2}{2}\mathrm{Re}[A(t)] - 2\beta\bar{\rho}\omega_r(t)\right)\mathrm{Re}[A(t)] \\ &= \left(-\frac{k^4}{4} - k^2\beta\bar{\rho} - k^2\beta\bar{\rho}\frac{\alpha}{2}\cos(\Omega t)\right)\mathrm{Re}[A(t)]. \end{aligned}$$

Rearranging the terms, to the left side we obtain

$$\frac{d^2}{dt^2}\mathrm{Re}[A(t)] + \left(\frac{k^4}{4} + k^2\beta\bar{\rho} + k^2\beta\bar{\rho}\frac{\alpha}{2}\cos(\Omega t)\right)\mathrm{Re}[A(t)] = 0, \tag{A.15}$$

which is an equation similar to the standard Mathieu equation

$$\frac{d^2x}{d\tau^2} + (a + \epsilon\cos(2\tau))\,x = 0, \tag{A.16}$$

identifying

$$\begin{aligned} x &= \mathrm{Re}[A(t)] \\ \tau &= \frac{\Omega t}{2} \\ a &= \frac{k^4}{4} + k^2\beta\bar{\rho} \\ \epsilon &= \frac{k^2}{2}\beta\bar{\rho}\alpha. \end{aligned}$$

where a and ϵ are constant parameters, while x is a dependent variable and τ is time.

The only term which is missing to calculate is the average density of the condensate $\bar{\rho}$ which we calculate as follows

$$\bar{\rho} = \frac{1}{2R_{TF}} \int_{-R_{TF}}^{R_{TF}} |\psi_0(x)|^2 \mathrm{d}x = \frac{2}{3\beta}(\mu - V_0), \tag{A.17}$$

which we can substitute where it is necessary.

A.8 Mathieu equation and the stability chart

The form of Mathieu's equation (A.16) is very simple, it is a linear second-order ordinary differential equation (ODE), which differs from the one corresponding to a simple harmonic oscillator in the existence of a time-varying (periodic) forcing of the stiffness coefficient a.

So, the simple harmonic oscillator is obtained for $\epsilon = 0$, and the stiffness parameter a corresponds then to the square of its natural frequency, therefore $\sqrt{a}$. This oscillator performs free vibrations around the stable equilibrium position $x = 0$. However, if the stiffness term contains the parametric excitation $\epsilon \neq 0$, the motion can stay bounded (this case is referred to as stable) or the motion becomes unbounded (this case is referred to as unstable). The occurrence of one of these two outcomes depends on the combination of the parameters a and ϵ. When presented graphically, this gives the so-called stability chart with regions of stability and regions of instability (tongues) separated by the so-called transition curves, enabling one to clearly determine the resulting behavior and the stability property mentioned.

The stability chart of Mathieu's equation with several tongues can be obtained by using numerical integration in conjunction with Floquet theory as presented in reference [84].

In this section, we will just present some analytically expressions for the first and second tongues transition curves (contours) at small excitation $\epsilon \approx 0$. All these under the Poincaré-Lindstedt method, which allows to find convergent series approximations of periodic solutions by using a series expansion and the periodicity of the solution [86].

After apply Floquet theory (appendix 2 of [86]) to Mathieu's equation (eq. A.16), we conclude that for $\sqrt{a} = m, m = 1, 2, ...$ we have stability for ϵ in the neighbourhood of zero. These points works as seeds where the stability tongues will grown.

If $\epsilon = 0$, the solutions of Mathieu's equation (eq. A.16) are known, a linear combination of $\cos(mt)$ and $\sin(mt)$ which are $2\pi/m$-periodic, then

$$\begin{aligned} x(t) &= y_1 \cos(mt) + y_2 \sin(mt) \\ \dot{x}(t) &= -my_1 \sin(mt) + my_2 \cos(mt), \end{aligned}$$

where theirs respective amplitudes y_1 and y_2 are constants determined by the initial values.

For $\epsilon \approx 0$, we propose the solution can still be written in this form where both amplitudes are now functions of time. So the proposed solution is

$$\begin{aligned} x(t) &= y_1(t)\cos(mt) + y_2(t)\sin(mt) && \text{(A.18)} \\ \dot{x}(t) &= -my_1(t)\sin(mt) + my_2(t)\cos(mt). && \text{(A.19)} \end{aligned}$$

Here, we are assuming that these Mathieu's equation (eq. A.16) solutions are periodic into the neighborhood of $\epsilon \approx 0$. But the period $T(\epsilon)$ will depend on the small parameter ϵ. Then, we shall expand the period with respect to the small parameter ϵ. For convenience, we express this period ϵ-dependence as $a = m^2 - \epsilon\beta$ with β a constant independent of ϵ.

For solve this equations system, we need transform it into two first-order ODEs. The process we need to follow is transform $x, \dot{x} \rightarrow y_1, y_2$. First, we substitute the expressions for x and $\dot{x}$ (after applying another differentiation) into Mathieu's equation (eq. A.16) to produce an equation for the amplitudes $y_1(t)$ and $y_2(t)$

$$\begin{aligned} - \quad & m^2\left[y_1\cos(mt) + y_2\sin(mt)\right] \\ + \quad & m\left[-\dot{y_1}\sin(mt) + \dot{y_2}\cos(mt)\right] \\ + \quad & a\left[y_1\cos(mt) + y_2\sin(mt)\right] = \epsilon\cos(2t)\left[y_1\cos(mt) + y_2\sin(mt)\right]. \end{aligned}$$

Before to continue, we can use $a = m^2 - \epsilon\beta$ to reduce the first and third left-handed terms. After that, we obtain the first transformed equation. Another requirement from we can obtain the second transformed equation is that the differentiation of x must produce an expression which equals $\dot{x}$. So we find that

$$\dot{y_1}\cos(mt) + \dot{y_2}\sin(mt) = 0.$$

Solving this last equation for $\dot{y_2}$ or $\dot{y_1}$, and substituting into the first transformed equation, allow us to find expressions for $\dot{y_1}$ or $\dot{y_2}$ respectively as

$$\begin{aligned} \dot{y_1} &= -\frac{\epsilon}{m}\left[\beta - \cos(2t)\right]\left[y_1\cos(mt) + y_2\sin(mt)\right]\sin(mt) && \text{(A.20)} \\ \dot{y_2} &= \frac{\epsilon}{m}\left[\beta - \cos(2t)\right]\left[y_1\cos(mt) + y_2\sin(mt)\right]\cos(mt) && \text{(A.21)} \end{aligned}$$

which are equivalent to the Mathieu's equation.

Then we can integrate them to obtain

$$\begin{aligned} y_1(\tau) &= y_1(0) - \frac{\epsilon}{m}\int_0^\tau \left[\beta - \cos(2t)\right]\left[y_1\cos(mt) + y_2\sin(mt)\right]\sin(mt)\mathrm{d}t \\ y_2(\tau) &= y_2(0) + \frac{\epsilon}{m}\int_0^\tau \left[\beta - \cos(2t)\right]\left[y_1\cos(mt) + y_2\sin(mt)\right]\cos(mt)\mathrm{d}t, \end{aligned}$$

but we appeal for the periodicity of the the solution $y(\tau) = y(\tau + 2\pi/m)$ we obtain then two conditions

$$\int_0^{2\pi/m} [\beta - \cos(2t)] [y_1 \cos(mt) + y_2 \sin(mt)] \sin(mt) \mathrm{d}t = 0 \quad \text{(A.22)}$$

$$\int_0^{2\pi/m} [\beta - \cos(2t)] [y_1 \cos(mt) + y_2 \sin(mt)] \cos(mt) \mathrm{d}t = 0. \quad \text{(A.23)}$$

For the fist tongue we have that $m = 1$, solving the integrals supposing y_1 and y_2 are constants, we obtain that $y_2(\beta + 1/2) = 0$ and $y_1(\beta - 1/2) = 0$, then the periodic solutions exist if $a \approx 1 \pm 1/2\epsilon$. For the second tongue we have that $m = 2$, solving the integrals supposing y_1 and y_2 are constants, we obtain that $\beta = 0$. Then we need to expand the period to the next order, expressed as $a \approx 1 - \epsilon\beta - \epsilon^2\gamma$. After apply this condition to the system equation, we obtain the periodic solutions exist if $a \approx 4 - 1/48\epsilon^2$ and $a \approx 4 + 5/48\epsilon^2$.

A.9 Faraday Waves

Assuming then that the values of α and Ω of the modulation of the radial frequency are appropriate such that the excitation is stable and therefore, they generate a value of the valid wave number k, the solution is finally observed as equation (A.14), then the density profile of the condensate, observable in the experiments, is given by

$$\rho(x,t) \approx |\psi_0(x)|^2 (1 + 2\mathrm{Re}[A(t)] \cos(kx)) \quad \text{(A.24)}$$

which is the Faraday wave, a spatial pattern which in time its amplitude oscillates as a function of $\mathrm{Re}[A(t)]$.

Appendix B

Codes

B.1 Algorithm to calculate the painting function

The code for the calculation of the painting function $f(t)$ to the case to obtain a harmonic potential is included. Also this algorithm loads the points to an Arbitrary Wave Generator Standford DS345 due to the GPIB conector.

```
1
2  import visa
3  import numpy as np
4  import pylab as pl
5  import struct
6  from scipy.integrate import quad
7  from scipy.interpolate import interp1d
8
9  #Code developed by Eduardo Padilla at the LMU-IFUNAM
10 #Version 1.0
11
12 #Number of points in the total waveform
13 Np = 50
14
15 #Heavside
16 def Heav(x):
17     return 1 * (x > 0)
18
19 #Target painting function
20 def ThomasFermi(x):
21    return (1-x**2)*Heav(1-abs(x))
22
23 #Waveform generation
24 X=np.linspace(-1,1,Np)
25 Z=np.zeros(Np)
26
27 for i in range(Np):
28     Z[i]=quad(ThomasFermi,-1,X[i])[0]
29
30 res=np.concatenate((X,list(reversed(X))[1:Np]))
31 res2=np.concatenate((Z/Z[-1],1+Z[1:Np]/Z[-1]))
32
33 #Visualization part, to generate a graph in JupyterNotebook
34 f2 = interp1d(res2,res, kind='cubic')
```

```
35
36 xnew = np.linspace(0, 2, num=Np+1, endpoint=True)
37 xnew = xnew[0:Np]
38 ynew = f2(xnew)
39
40 #We prepare the information that we are going to send to Standford
      WaveGenerator
41
42 samplerate = 40e6 # Samples per second
43 #amplitude = 5.0 # V
44 #offset = 3.0 # V
45
46 V = np.around(2047.0*ynew)
47 pl.plot(np.arange(len(ynew))/samplerate*1e9,V,'.')
48 pl.xlabel("Time [ns]")
49 pl.ylabel("Voltage [V]")
50
51 pl.show()
52
53 #Begins the remote comunication
54 rm = visa.ResourceManager()
55 #Yo can change the default adress
56 inst = rm.open_resource('GPIB0::19::INSTR')
57
58 # Query the ID string of the signal generator to check
59 # whether the remote communication is normal
60 print("Informacion del generador")
61 print(inst.query("*IDN?"))
62
63 AMP=1.0
64 OFFSET=1.5
65
66 inst.write("*CLS") # clears registers
67 inst.write("*SRE 16") # enables "message available bit"
68
69 inst.write("AMPL " + str(AMP) + "VP") # sets amplitude
70 inst.write("OFFS %f" % OFFSET) # sets offset
71
72 #creates binary data from V, including the checksum
73 #creates the first byte
74 chksum = int(V[0])
75 b = struct.pack('h', int(V[0]))
76 #then the others bytes
77 for i in range (1,len(V)):
78     b += struct.pack('h', int(V[i]))
79     chksum += V[i]
80 #Add the checksum to the data
81 b += struct.pack('h', int(chksum))
82
83 # the first 0 tells the format will be point (1 to be vector format
      )
84 # tells the machine that Np points will be sent
85 inst.write("LDWF? 0,%i"%Np)
86 #It's necessary to read the anwser befores to send the data
87 print("El generador esta listo para recibir=%s"%inst.read())
88
89 #Send the binary data to the generator
90 r=inst.write_raw(b)
```

```
91
92 print("El generador recibio %i bytes (2 byte por dato mas checksum)
       de manera correcta."%r[0])
93
94 # Turn on the output
95 inst.write("FUNC5\n")
```

Bibliography

[1] Heavner, T. P., Jefferts, S. R., Donley, E. A., Shirley, J. H. & Parker, T. E. NIST-f1: recent improvements and accuracy evaluations. *Metrologia* **42**, 411–422 (2005). URL https://doi.org/10.1088/0026-1394/42/5/012.

[2] Gerginov, V. *et al.* Uncertainty evaluation of the caesium fountain clock PTB-CSF2. *Metrologia* **47**, 65–79 (2009). URL https://doi.org/10.1088/0026-1394/47/1/008.

[3] Hänsch, T. & Schawlow, A. Cooling of gases by laser radiation. *Optics Communications* **13**, 68–69 (1975). URL http://www.sciencedirect.com/science/article/pii/0030401875901595.

[4] Phillips, W. D. Nobel lecture: Laser cooling and trapping of neutral atoms. *Rev. Mod. Phys.* **70**, 721–741 (1998). URL https://link.aps.org/doi/10.1103/RevModPhys.70.721.

[5] Chu, S. Nobel lecture: The manipulation of neutral particles. *Rev. Mod. Phys.* **70**, 685–706 (1998). URL https://link.aps.org/doi/10.1103/RevModPhys.70.685.

[6] Cohen-Tannoudji, C. N. Nobel lecture: Manipulating atoms with photons. *Rev. Mod. Phys.* **70**, 707–719 (1998). URL https://link.aps.org/doi/10.1103/RevModPhys.70.707.

[7] Anderson, M. H., Ensher, J. R., Matthews, M. R., Wieman, C. E. & Cornell, E. A. Observation of bose-einstein condensation in a dilute atomic vapor. *Science* **269**, 198–201 (1995). URL https://science.sciencemag.org/content/269/5221/198.

[8] Davis, K. B. *et al.* Bose-einstein condensation in a gas of sodium atoms. *Phys. Rev. Lett.* **75**, 3969–3973 (1995). URL https://link.aps.org/doi/10.1103/PhysRevLett.75.3969.

[9] Bradley, C. C., Sackett, C. A., Tollett, J. J. & Hulet, R. G. Evidence of bose-einstein condensation in an atomic gas with attractive interactions. *Phys. Rev. Lett.* **75**, 1687–1690 (1995). URL https://link.aps.org/doi/10.1103/PhysRevLett.75.1687.

[10] DeMarco, B. & Jin, D. S. Onset of fermi degeneracy in a trapped atomic gas. *Science* **285**, 1703–1706 (1999). URL https://science.sciencemag.org/content/285/5434/1703.

[11] Abo-Shaeer, J. R., Raman, C., Vogels, J. M. & Ketterle, W. Observation of vortex lattices in bose-einstein condensates. *Science* **292**, 476–479 (2001). URL https://science.sciencemag.org/content/292/5516/476.

[12] Zwierlein, M. W., Abo-Shaeer, J. R., Schirotzek, A., Schunck, C. H. & Ketterle, W. Vortices and superfluidity in a strongly interacting fermi gas. *Nature* **435**, 1047–1051 (2005). URL https://doi.org/10.1038/nature03858.

[13] Bloch, I., Dalibard, J. & Zwerger, W. Many-body physics with ultracold gases. *Rev. Mod. Phys.* **80**, 885–964 (2008). URL https://link.aps.org/doi/10.1103/RevModPhys.80.885.

[14] Chen, Q., Stajic, J., Tan, S. & Levin, K. Bcs–bec crossover: From high temperature superconductors to ultracold superfluids. *Physics Reports* **412**, 1 – 88 (2005). URL http://www.sciencedirect.com/science/article/pii/S0370157305001067.

[15] Cataliotti, F. S. *et al.* Josephson junction arrays with bose-einstein condensates. *Science* **293**, 843–846 (2001). URL https://science.sciencemag.org/content/293/5531/843.

[16] Greiner, M., Mandel, O., Esslinger, T., Häensch, T. & Bloch, I. Quantum phase transition from a superfluid to a mott insulator in a gas of ultracold atoms. *Nature* **415**, 39–44 (2002). URL https://www.nature.com/articles/415039a.

[17] Baumann, K., Guerlin, C., Brennecke, F. & Esslinger, T. Dicke quantum phase transition with a superfluid gas in an optical cavity. *Nature* **464**, 1301–1306 (2010). URL http://dx.doi.org/10.1038/nature09009.

[18] Stamper-Kurn, D. M. *et al.* Optical confinement of a bose-einstein condensate. *Phys. Rev. Lett.* **80**, 2027–2030 (1998). URL https://link.aps.org/doi/10.1103/PhysRevLett.80.2027.

[19] Inouye, S. *et al.* Observation of feshbach resonances in a bose–einstein condensate. *Nature* **392**, 151–154 (1998). URL https://www.nature.com/articles/32354.

[20] O'Hara, K. M., Hemmer, S. L., Gehm, M. E., Granade, S. R. & Thomas, J. E. Observation of a strongly interacting degenerate fermi gas of atoms. *Science* **298**, 2179–2182 (2002). URL https://science.sciencemag.org/content/298/5601/2179.

[21] Bartenstein, M. *et al.* Precise determination of ^{6}Li cold collision parameters by radio-frequency spectroscopy on weakly bound molecules. *Phys. Rev. Lett.* **94**, 103201 (2005). URL https://link.aps.org/doi/10.1103/PhysRevLett.94.103201.

[22] Pollack, S. E. *et al.* Extreme tunability of interactions in a ^{7}Li bose-einstein condensate. *Phys. Rev. Lett.* **102**, 090402 (2009). URL https://link.aps.org/doi/10.1103/PhysRevLett.102.090402.

[23] Regal, C. A., Greiner, M. & Jin, D. S. Observation of resonance condensation of fermionic atom pairs. *Phys. Rev. Lett.* **92**, 040403 (2004). URL https://link.aps.org/doi/10.1103/PhysRevLett.92.040403.

[24] Zwierlein, M. W. *et al.* Condensation of pairs of fermionic atoms near a feshbach resonance. *Phys. Rev. Lett.* **92**, 120403 (2004). URL https://link.aps.org/doi/10.1103/PhysRevLett.92.120403.

[25] Bardeen, J., Cooper, L. N. & Schrieffer, J. R. Theory of superconductivity. *Phys. Rev.* **108**, 1175–1204 (1957). URL https://link.aps.org/doi/10.1103/PhysRev.108.1175.

[26] Bourdel, T. *et al.* Experimental study of the bec-bcs crossover region in lithium 6. *Phys. Rev. Lett.* **93**, 050401 (2004). URL https://link.aps.org/doi/10.1103/PhysRevLett.93.050401.

[27] Bartenstein, M. *et al.* Collective excitations of a degenerate gas at the bec-bcs crossover. *Phys. Rev. Lett.* **92**, 203201 (2004). URL https://link.aps.org/doi/10.1103/PhysRevLett.92.203201.

[28] Valtolina, G. *et al.* Josephson effect in fermionic superfluids across the bec-bcs crossover. *Science* **350**, 1505–1508 (2015). URL http://dx.doi.org/10.1126/science.aac9725.

[29] Vinen, W. & Niemela, J. Quantum turbulence. *Journal of Low Temperature Physics* **128**, 167–231 (2002). URL https://link.springer.com/article/10.1023/A:1019695418590.

[30] Henn, E. A. L., Seman, J. A., Roati, G., Magalhães, K. M. F. & Bagnato, V. S. Emergence of turbulence in an oscillating bose-einstein condensate. *Phys. Rev. Lett.* **103**, 045301 (2009). URL https://link.aps.org/doi/10.1103/PhysRevLett.103.045301.

[31] Seman, J. *et al.* Route to turbulence in a trapped bose-einstein condensate. *Laser Physics Letters* n/a–n/a (2011). URL https://doi.org/10.1002/lapl.201110052.

[32] Romero-Rochín, V. Equation of state of an interacting bose gas confined by a harmonic trap: The role of the "harmonic" pressure. *Phys. Rev. Lett.* **94**, 130601 (2005). URL https://link.aps.org/doi/10.1103/PhysRevLett.94.130601.

[33] Romero-Rochin, V. *et al.* Observation of bose-einstein condensation in an atomic trap in terms of macroscopic thermodynamic parameters. *Phys. Rev. A* **85**, 023632 (2012). URL https://link.aps.org/doi/10.1103/PhysRevA.85.023632.

[34] Poveda-Cuevas, F. J., Reyes-Ayala, I., Seman, J. A. & Romero-Rochín, V. Global thermodynamics of confined inhomogeneous dilute gases: A semiclassical approach. *AIP Conference Proceedings* **1950**, 030006 (2018). URL https://aip.scitation.org/doi/abs/10.1063/1.5031698.

[35] Giorgini, S., Pitaevskii, L. P. & Stringari, S. Theory of ultracold atomic fermi gases. *Rev. Mod. Phys.* **80**, 1215–1274 (2008). URL https://link.aps.org/doi/10.1103/RevModPhys.80.1215.

[36] Cohen-Tannoudji, C., Diu, B. & Laloe, F. *Quantum Mechanics, 2 Volume Set* (Wiley, 1992), 2 edn.

[37] Landau, L. & Lifshitz, E. *Quantum Mechanics: Non-Relativistic Theory.* Course of Theoretical Physics (Elsevier Science, 1981).

[38] Stoof, H., Gubbels, K. & Dickerscheid, D. *Ultracold Quantum Fields* (Springer Netherlands, 2009). URL https://doi.org/10.1007/978-1-4020-8763-9_17.

[39] Chin, C., Grimm, R., Julienne, P. & Tiesinga, E. Feshbach resonances in ultracold gases. *Reviews of Modern Physics* **82**, 1225–1286 (2010). URL http://dx.doi.org/10.1103/RevModPhys.82.1225.

[40] Adams, A., Carr, L. D., Schäfer, T., Steinberg, P. & Thomas, J. E. Strongly correlated quantum fluids: ultracold quantum gases, quantum chromodynamic plasmas and holographic duality. *New Journal of Physics* **14**, 115009 (2012). URL https://doi.org/10.1088/1367-2630/14/11/115009.

[41] Salasnich, L. Fermionic condensation in ultracold atoms, nuclear matter and neutron stars. *Journal of Physics: Conference Series* **497**, 012026 (2014). URL https://doi.org/10.1088/1742-6596/497/1/012026.

[42] van Wyk, P., Tajima, H., Inotani, D., Ohnishi, A. & Ohashi, Y. Superfluid fermi atomic gas as a quantum simulator for the study of the neutron-star equation of state in the low-density region. *Phys. Rev. A* **97**, 013601 (2018). URL https://link.aps.org/doi/10.1103/PhysRevA.97.013601.

[43] Petrov, D. S., Salomon, C. & Shlyapnikov, G. V. Weakly bound dimers of fermionic atoms. *Phys. Rev. Lett.* **93**, 090404 (2004). URL https://link.aps.org/doi/10.1103/PhysRevLett.93.090404.

[44] Gross, E. P. Structure of a quantized vortex in boson systems. *Il Nuovo Cimento (1955-1965)* **20**, 454–477 (1961). URL https://link.springer.com/article/10.1007/BF02731494.

[45] Pitaevskii, L. P. Vortex lines in an imperfect bose gas. *Sov. Phys. JETP* **13**, 451–454 (1961). URL http://www.jetp.ac.ru/cgi-bin/dn/e_013_02_0451.pdf.

[46] Steck, D. A. *Quantum and Atom Optics* (revision 0.13.3, 2020). URL http://steck.us/teaching.

[47] Metcalf, H. & van der Straten, P. *Laser Cooling and Trapping.* Graduate Texts in Contemporary Physics (Springer New York, 2001).

[48] Jackson, J. D. *Classical Electrodynamics* (Wiley, 1999).

[49] Einstein, A. Zur Quantentheorie der Strahlung (in German). *Physikalische Zeitschrift* **18**, 121–128 (1917). URL http://www.sciencedirect.com/

science/article/pii/B9780080121024500188. Translated in "On the Quantum Theory of Radiation". The Old Quantum Theory. Elsevier. 1967. pp. 167–183.

[50] Chu, S., Hollberg, L., Bjorkholm, J. E., Cable, A. & Ashkin, A. Three-dimensional viscous confinement and cooling of atoms by resonance radiation pressure. *Phys. Rev. Lett.* **55**, 48–51 (1985). URL https://link.aps.org/doi/10.1103/PhysRevLett.55.48.

[51] Castin, Y., Wallis, H. & Dalibard, J. Limit of doppler cooling. *J. Opt. Soc. Am. B* **6**, 2046–2057 (1989). URL http://josab.osa.org/abstract.cfm?URI=josab-6-11-2046.

[52] Raab, E. L., Prentiss, M., Cable, A., Chu, S. & Pritchard, D. E. Trapping of neutral sodium atoms with radiation pressure. *Phys. Rev. Lett.* **59**, 2631–2634 (1987). URL https://link.aps.org/doi/10.1103/PhysRevLett.59.2631.

[53] Lett, P. D. *et al.* Observation of atoms laser cooled below the doppler limit. *Phys. Rev. Lett.* **61**, 169–172 (1988). URL https://link.aps.org/doi/10.1103/PhysRevLett.61.169.

[54] Dalibard, J. & Cohen-Tannoudji, C. Laser cooling below the doppler limit by polarization gradients: simple theoretical models. *J. Opt. Soc. Am. B* **6**, 2023–2045 (1989). URL http://josab.osa.org/abstract.cfm?URI=josab-6-11-2023.

[55] Burchianti, A. *et al.* Efficient all-optical production of large ^{6}Li quantum gases using D_1 gray-molasses cooling. *Phys. Rev. A* **90**, 043408 (2014). URL https://link.aps.org/doi/10.1103/PhysRevA.90.043408.

[56] Aspect, A., Arimondo, E., Kaiser, R., Vansteenkiste, N. & Cohen-Tannoudji, C. Laser cooling below the one-photon recoil energy by velocity-selective coherent population trapping. *Phys. Rev. Lett.* **61**, 826–829 (1988). URL https://link.aps.org/doi/10.1103/PhysRevLett.61.826.

[57] Grimm, R., Weidemüller, M. & Ovchinnikov, Y. B. Optical dipole traps for neutral atoms. In Bederson, B. & Walther, H. (eds.) *Advances In Atomic, Molecular, and Optical Physics*, vol. 42, 95 – 170 (Academic Press, 2000). URL http://www.sciencedirect.com/science/article/pii/S1049250X0860186X.

[58] Ketterle, W. & Druten, N. V. Evaporative cooling of trapped atoms. In Bederson, B. & Walther, H. (eds.) *Advances In Atomic, Molecular, and Optical Physics*, vol. 37, 181 – 236 (Academic Press, 1996). URL http://www.sciencedirect.com/science/article/pii/S1049250X08601019.

[59] Luiten, O. J., Reynolds, M. W. & Walraven, J. T. M. Kinetic theory of the evaporative cooling of a trapped gas. *Phys. Rev. A* **53**, 381–389 (1996). URL https://link.aps.org/doi/10.1103/PhysRevA.53.381.

[60] Luo, L. *et al.* Evaporative cooling of unitary fermi gas mixtures in optical traps. *New Journal of Physics* **8**, 213–213 (2006). URL https://doi.org/10.1088/1367-2630/8/9/213/.

[61] Hernandez-Rajkov, D. *et al.* Experimental setup for the production of ultracold strongly correlated fermionic superfluids of 6li. *Revista Mexicana de Física* **66**, 388–403 (2020). URL https://rmf.smf.mx/ojs/rmf/article/view/Vol.%2066%2C%20issue%204%2C%20pp.%20388-403.

[62] Ibarra García-Padilla, E. *Diseño de los sistemas de ultra-alto vacío y de control para experimentos con gases ultrafríos de Litio (Spanish).* (Bachelor's thesis, Facultad de Ciencias, UNAM, 2016).

[63] Das, D. & Natarajan, V. Absolute frequency measurement of the lithium d lines: Precise determination of isotope shifts and fine-structure intervals. *Phys. Rev. A* **75**, 052508 (2007). URL https://link.aps.org/doi/10.1103/PhysRevA.75.052508.

[64] McAlexander, W. I., Abraham, E. R. I. & Hulet, R. G. Radiative lifetime of the $2p$ state of lithium. *Phys. Rev. A* **54**, R5–R8 (1996). URL https://link.aps.org/doi/10.1103/PhysRevA.54.R5.

[65] Letokhov, V. S. *Saturation spectroscopy. In: Shimoda K. (eds) High-Resolution Laser Spectroscopy*, 95–171 (Springer Berlin Heidelberg, Berlin, Heidelberg, 1976). URL https://doi.org/10.1007/3540077197_20.

[66] Donley, E. A., Heavner, T. P., Levi, F., Tataw, M. O. & Jefferts, S. R. Double-pass acousto-optic modulator system. *Review of Scientific Instruments* **76**, 063112 (2005). URL https://doi.org/10.1063/1.1930095.

[67] Ketterle, W., Durfee, D. S. & Stamper-Kurn, D. M. Making, probing and understanding bose-einstein condensates. *Proceedings of the International School of Physics "Enrico Fermi", Course CLV, IOS Press* 67–176 (1999). URL https://doi.org/10.3254/978-1-61499-225-7-67.

[68] Ketterle, W. & Zwierlein, M. W. Making, probing and understanding ultracold fermi gases. *Proceedings of the International School of Physics "Enrico Fermi", Course CLXIV, IOS Press* 95–287 (2008). URL https://doi.org/10.1393/ncr/i2008-10033-1.

[69] Giorgini, S., Pitaevskii, L. P. & Stringari, S. Condensate fraction and critical temperature of a trapped interacting bose gas. *Phys. Rev. A* **54**, R4633–R4636 (1996). URL https://link.aps.org/doi/10.1103/PhysRevA.54.R4633.

[70] Regal, C. A., Greiner, M., Giorgini, S., Holland, M. & Jin, D. S. Momentum distribution of a fermi gas of atoms in the bcs-bec crossover. *Phys. Rev. Lett.* **95**, 250404 (2005). URL https://link.aps.org/doi/10.1103/PhysRevLett.95.250404.

[71] Ku, M. J. H., Sommer, A. T., Cheuk, L. W. & Zwierlein, M. W. Revealing the superfluid lambda transition in the universal thermodynamics of a unitary fermi gas. *Science* **335**, 563–567 (2012). URL https://science.sciencemag.org/content/335/6068/563.

[72] Roy, R., Green, A., Bowler, R. & Gupta, S. Rapid cooling to quantum degeneracy in dynamically shaped atom traps. *Phys. Rev. A* **93**, 043403 (2016). URL https://link.aps.org/doi/10.1103/PhysRevA.93.043403.

[73] Yariv, A. *Quantum Electronics* (Wiley, 1989), 3 edn.

[74] Romero-Rochín, V. & Bagnato, V. S. Thermodynamics of an ideal gas of bosons harmonically trapped: equation of state and susceptibilities. *Brazilian Journal of Physics* **35**, 607 – 613 (2005). URL https://doi.org/10.1590/S0103-97332005000400004.

[75] Faraday, M. On a Peculiar Class of Acoustical Figures; and on Certain Forms Assumed by Groups of Particles upon Vibrating Elastic Surfaces. *Philosophical Transactions of the Royal Society of London* **121**, 299–340 (1831). URL http://www.jstor.org/stable/107936.

[76] Okazaki, K., Han, J. & Tsubota, M. Faraday waves in bose–einstein condensate: From instability to nonlinear dynamics (2021). 2012.02391.

[77] Nguyen, J. H. V. *et al.* Parametric Excitation of a Bose-Einstein Condensate: From Faraday Waves to Granulation. *Phys. Rev. X* **9**, 011052 (2019). URL https://link.aps.org/doi/10.1103/PhysRevX.9.011052.

[78] Staliunas, K., Longhi, S. & de Valcárcel, G. J. Faraday Patterns in Bose-Einstein Condensates. *Phys. Rev. Lett.* **89**, 210406 (2002). URL https://link.aps.org/doi/10.1103/PhysRevLett.89.210406.

[79] Nicolin, A. I., Carretero-González, R. & Kevrekidis, P. G. Faraday waves in Bose-Einstein condensates. *Phys. Rev. A* **76**, 063609 (2007). URL https://link.aps.org/doi/10.1103/PhysRevA.76.063609.

[80] Engels, P., Atherton, C. & Hoefer, M. A. Observation of Faraday Waves in a Bose-Einstein Condensate. *Phys. Rev. Lett.* **98**, 095301 (2007). URL https://link.aps.org/doi/10.1103/PhysRevLett.98.095301.

[81] Smits, J., Liao, L., Stoof, H. T. C. & van der Straten, P. Observation of a Space-Time Crystal in a Superfluid Quantum Gas. *Phys. Rev. Lett.* **121**, 185301 (2018). URL https://link.aps.org/doi/10.1103/PhysRevLett.121.185301.

[82] Capuzzi, P. & Vignolo, P. Faraday waves in elongated superfluid fermionic clouds. *Phys. Rev. A* **78**, 043613 (2008). URL https://link.aps.org/doi/10.1103/PhysRevA.78.043613.

[83] Tang, R.-A., Li, H.-C. & Xue, J.-K. Faraday instability and Faraday patterns in a superfluid Fermi gas. *Journal of Physics B: Atomic, Molecular and Optical Physics* **44**, 115303 (2011). URL https://doi.org/10.1088.

[84] Kovacic, I., Rand, R. & Sah, S. Mathieu's equation and its generalizations: Overview of stability charts and their features. *Applied Mechanics Reviews* **70** (2018).

[85] Bao, W., Jaksch, D. & Markowich, P. A. Numerical solution of the gross–pitaevskii equation for bose–einstein condensation. *Journal of Computational Physics* **187**, 318–342 (2003). URL https://www.sciencedirect.com/science/article/pii/S0021999103001025.

[86] Verhulst, F. *Nonlinear Differential Equations and Dynamical Systems* (Springer-Verlag Berlin Heidelberg, 1996), 2 edn.